Springer Theses
Recognizing Outstanding Ph.D. Research

Daniel O'Hanlon

Studies of *CP*-Violation in Charmless Three-Body *b*-Hadron Decays

Springer

Springer Theses

Recognizing Outstanding Ph.D. Research

Aims and Scope

The series "Springer Theses" brings together a selection of the very best Ph.D. theses from around the world and across the physical sciences. Nominated and endorsed by two recognized specialists, each published volume has been selected for its scientific excellence and the high impact of its contents for the pertinent field of research. For greater accessibility to non-specialists, the published versions include an extended introduction, as well as a foreword by the student's supervisor explaining the special relevance of the work for the field. As a whole, the series will provide a valuable resource both for newcomers to the research fields described, and for other scientists seeking detailed background information on special questions. Finally, it provides an accredited documentation of the valuable contributions made by today's younger generation of scientists.

Theses are accepted into the series by invited nomination only and must fulfill all of the following criteria

- They must be written in good English.
- The topic should fall within the confines of Chemistry, Physics, Earth Sciences, Engineering and related interdisciplinary fields such as Materials, Nanoscience, Chemical Engineering, Complex Systems and Biophysics.
- The work reported in the thesis must represent a significant scientific advance.
- If the thesis includes previously published material, permission to reproduce this must be gained from the respective copyright holder.
- They must have been examined and passed during the 12 months prior to nomination.
- Each thesis should include a foreword by the supervisor outlining the significance of its content.
- The theses should have a clearly defined structure including an introduction accessible to scientists not expert in that particular field.

More information about this series at http://www.springer.com/series/8790

Daniel O'Hanlon

Studies of *CP*-Violation in Charmless Three-Body *b*-Hadron Decays

Doctoral Thesis accepted by
the University of Warwick, Coventry, UK

Springer

Author
Dr. Daniel O'Hanlon
Department of Physics
University of Warwick
Coventry, UK

Supervisor
Prof. Tim Gershon
Department of Physics
University of Warwick
Coventry, UK

ISSN 2190-5053 ISSN 2190-5061 (electronic)
Springer Theses
ISBN 978-3-030-02205-1 ISBN 978-3-030-02206-8 (eBook)
https://doi.org/10.1007/978-3-030-02206-8

Library of Congress Control Number: 2018957248

© Springer Nature Switzerland AG 2018
This work is subject to copyright. All rights are reserved by the Publisher, whether the whole or part of the material is concerned, specifically the rights of translation, reprinting, reuse of illustrations, recitation, broadcasting, reproduction on microfilms or in any other physical way, and transmission or information storage and retrieval, electronic adaptation, computer software, or by similar or dissimilar methodology now known or hereafter developed.
The use of general descriptive names, registered names, trademarks, service marks, etc. in this publication does not imply, even in the absence of a specific statement, that such names are exempt from the relevant protective laws and regulations and therefore free for general use.
The publisher, the authors and the editors are safe to assume that the advice and information in this book are believed to be true and accurate at the date of publication. Neither the publisher nor the authors or the editors give a warranty, express or implied, with respect to the material contained herein or for any errors or omissions that may have been made. The publisher remains neutral with regard to jurisdictional claims in published maps and institutional affiliations.

This Springer imprint is published by the registered company Springer Nature Switzerland AG
The registered company address is: Gewerbestrasse 11, 6330 Cham, Switzerland

All you really need to know for the moment is that the universe is a lot more complicated than you might think, even if you start from a position of thinking it's pretty damn complicated in the first place.

—Douglas Adams, *Mostly Harmless*

Supervisor's Foreword

The LHCb detector at CERN is designed to allow detailed investigations of hadrons containing beauty or charm quarks. This is achieved by collecting copious samples of these hadrons, which are produced in large quantities in the Large Hadron Collider's high energy proton–proton collisions. By studying the properties and decays of beauty and charm hadrons, it is possible to test the Standard Model (SM) of particle physics, and potentially to reveal sources of "new physics", not described by the SM.

One of the most interesting branches of particle physics research concerns the phenomenon known as *CP* violation, which involves studying differences in behaviour between matter and antimatter particles. We live in a Universe that consists only of matter, with negligible amounts of antimatter. Yet at and very shortly after the Big Bang, the Universe contained equal amounts of matter and antimatter. Clearly, understanding the violation of this symmetry is essential to know why the Universe turned out the way it did, which remains an unsolved problem in physics. By studying beauty and charm hadrons in laboratory experiments such as LHCb, we hope to find new manifestations of *CP* violation and thus to improve our understanding of the Universe.

Like all large particle physics experiments, LHCb is operated by an international collaboration, in this case comprised of around 1000 researchers. The collaboration constructed and now maintains and operates the detector, which thanks to the smooth running of the LHC accelerator as well as dedicated effort from LHCb collaborators, has collected much larger samples of beauty and charm hadrons compared to previous experiments. The volume of data collected is so large that a complicated computing infrastructure, including a worldwide grid, is necessary to access it. In order to allow efficient studies of its data, the LHCb collaboration provides a variety of software packages and tools.

Although such an environment may be daunting for a new Ph.D. student to enter, our best students learn rapidly and thrive on the interactions with colleagues from around the globe. This was the case for Daniel O'Hanlon, who started his Ph.D. studies under my supervision at the University of Warwick in October 2013, having obtained his undergraduate degree from the University of Exeter. Daniel carried out

some extremely important work during his studies, the most visible aspects of which are his physics analyses. He worked on two somewhat different studies of decays of beauty hadrons (states containing a b quark) to three final state particles. The first concerned previously unobserved decays of b baryons. Daniel carried out this analysis more-or-less single-handedly, with supervision from myself and technical assistance from a PDRA in my group. His work resulted in first observations of two new decay modes, and was published in JHEP 05 (2016) 081. Daniel's results add to the currently rather sparse knowledge of b baryon decays, and open the door to possible future studies of matter-antimatter asymmetries in these modes.

The majority of Ph.D. students in experimental particle physics complete at most one journal publication during their studentship, but since Daniel had made such strong progress I asked him to follow up with a more challenging topic, namely, an amplitude analysis of the decay of the charged B meson to three pions. Large matter-antimatter asymmetries in the resonant structure of this decay had previously been seen, but not understood. Understanding these effects is a high priority topic in quark flavour physics, and therefore several groups within LHCb are working together in this area. Daniel implemented a particularly sophisticated method, known as the "K-matrix formalism" to allow a physical description of the amplitude. This is the first ever implementation of the K-matrix approach to study matter-antimatter asymmetries. He was able to complete this extraordinarily challenging measurement only by having a detailed understanding of both the physics, which involves complicated and subtle hadronic effects, and the detector response, as well as being technically proficient. The results of Daniel's work are documented in this thesis, and will be published later in 2018 in peer-reviewed journal articles that are currently in preparation.

In addition to his analysis work, Daniel carried out "service tasks" for the LHCb collaboration related to Monte Carlo simulation and particle identification. He was responsible for validating the large number of user-submitted configuration files for the EvtGen simulation package. This is a truly thankless task that is nonetheless essential for people working on analyses across the LHCb physics programme. He carried this work out efficiently and uncomplainingly for several years. He also served as particle identification liaison for the charmless b hadron decays working group, in which capacity he made several important contributions, in particular toward improving understanding of the proton identification performance.

Daniel submitted his thesis at the start of September 2017, passed his viva examination with only very minor corrections on 4 October, and submitted the revised version (approved by the examiners) on 12 October. I have had the fortune of working with some excellent students, but Daniel is one of the two or three most impressive. It was a pleasure to supervise him and to watch him gain in experience and develop into an excellent young researcher. We continue to collaborate as he is now working on LHCb as a PDRA on an INFN fellowship in Bologna, and I look forward to following his next career steps.

Coventry, UK
July 2018

Prof. Tim Gershon

Abstract

Violation of combined charge and parity inversion (*CP*) is a property of the Standard Model that results in a fundamental difference between particles and anti-particles. The single source of *CP*-violation in the Standard Model is insufficient to explain the dominance of matter over antimatter in the contemporary universe; however, thus far, there has been no clear observation of *CP*-violation beyond the Standard Model. Constraints on various *CP*-violating observables are now precise enough that these represent sensitive tests for physics beyond the Standard Model.

This thesis first documents the observation of two three-body *b*-baryon decays, and measurements of their phase-space integrated *CP*-asymmetries, which are some of the first to be performed on baryon decays. These measurements provide useful information on hadronisation in *b*-baryon decays, on the intermediate decay dynamics, and give a potential avenue to search for *CP*-violation in baryon decays.

An amplitude analysis of the $B^+ \to \pi^+\pi^+\pi^-$ decay is also performed, where sizable *CP*-violation was observed previously, and the *CP*-violating parameters that relate to the intermediate resonant structure extracted. This is achieved by formulating a model for the decay amplitude, which is dominated by the $\rho(770)^0$ resonance and various broad overlapping scalar resonances. The scalar contributions to this decay are modelled using the unitarity-conserving K-matrix model, which relies on historical scattering data for the relative couplings between the scalar resonances and between the possible final states. These results provide insight into the mechanism by which the *CP*-violation in the Standard Model manifests in practice, give information on SU(3)-flavour symmetry breaking phenomena in hadron decays, and are a valuable input into future measurements of the CKM unitarity triangle angles.

Acknowledgements

I would first and foremost like to thank Tim Gershon and Michal Kreps, for providing me with such incredible opportunities, wisdom and patient education. Particular thanks goes to Tom Latham, for his unwavering support in fielding questions that ran the gamut of topics a high energy physics research student might encounter, from the nuances of amplitude fits to 'What eats jellyfish?'.[1]

Thanks also goes to my officemates at Warwick, past and present, primarily for not *actively* sabotaging this work, but also for providing consistently high-quality opportunities for procrastination.

If it were not for Rafael Coutinho, I would probably still be trying to evaluate the trigger efficiency in the Λhh analysis, and without John Back's K-matrix implementation and assorted expertise, the model described in the latter part of this thesis would not have been possible. I have also benefited greatly from Tom Blake's fount of information regarding LHCb. I am also particularly grateful to Mark Whitehead for not punching me every time I mentioned transferring my consciousness into a robot body, and to Dan Craik for illuminating discussions regarding lemons.

I would also be remiss not to express my gratitude to the LHCb collaboration at-large, most notably to those from the $B \to 3\pi$ group and charmless working group, but also the numerous reviewers, readers, conveners, collaborators, authors of tools and respondents on mailing lists, that give their time and effort for the greater good.

Finally, I am indebted to my long-suffering parents, for everything else.

[1] Sea turtles, some species of large fish—and other jellyfish.

Contents

Chapter 1
Outline

The predictions of the Standard Model of fundamental interactions yield remarkable agreement with experimental measurements, with some consistent to one part in 10^9 [1], and as such the Standard Model currently represents humanity's best understanding of the behaviour of all known elementary particles. Nevertheless, there is mounting evidence for physical observations inconsistent with the predictions of the Standard Model: astrophysical observations of dark matter, dark energy, and the baryon asymmetry of the universe can only result from hitherto unknown fundamental interactions, and internal inconsistencies regarding the nature of neutrino masses challenge the completeness of the Standard Model.

The task for high-energy physics is to match these observations to properties of fundamental particles, either by directly detecting particles not compatible with the Standard Model, or by using high-precision measurements to identify discrepancies in parameters sensitive to effects with an origin beyond the Standard Model

This thesis documents exploration in the heavy-flavour sector of the Standard Model via precision studies of b-hadron decay properties, using data from the LHCb experiment at the Large Hadron Collider.

The existence of new physical processes, where an off-mass-shell, or 'virtual', beyond-the-Standard-Model particle mediates an interaction instead of an intermediate Standard Model gauge boson, can result in vastly suppressed or enhanced production rates for some processes, or cause discrepancies in otherwise precisely known angular or charge-parity-symmetry (CP) violating observables. As such, precision flavour physics measurements are complementary to direct searches for new particles, where the energy must be sufficient to produce the heavy new particle on-mass-shell, and as such often have much higher sensitivity. A description of the heavy-flavour sector of the Standard Model, phenomenological flavour observables, and how these can be used to search for 'new physics', can be found in Chap. 2.

For the last century [2], the best way to investigate the fundamental properties of nature has been to produce and study its fundamental particles in a controlled environment, probing conditions present within 10^{-12} s of the Big Bang. The measurements described in this thesis were performed on data from the LHCb experiment, located at Interaction Point 8 on the Large Hadron Collider (LHC). A brief description

© Springer Nature Switzerland AG 2018

D. O'Hanlon, *Studies of* CP-*Violation in Charmless Three-Body* b-*Hadron Decays*,
Springer Theses, https://doi.org/10.1007/978-3-030-02206-8_1

of the LHC machine can be found in Chap. 3, and a description of the LHCb detector, and the associated software and computing infrastructure, can be found in Chap. 4.

Violation of *CP*-symmetry in the Standard Model, a fundamental difference between particles and anti-particles, is associated with an additional free parameter, which must be determined experimentally. Over-constraint of this parameter via the unitarity of the Cabibbo-Kobayashi-Maskawa matrix is therefore an important test of the consistency of the Standard Model, which can be performed in a large variety of environments. In particular, constraints can come from 'tree'-level interactions, where only Standard Model contributions are expected, or 'loop'-level interactions, where additional new particles can contribute. As such, comparisons of these two scenarios are a powerful test for contributions from new physics.

Where, due to the existence of unknown hadronic effects, *CP*-violation observed in decays cannot be related to the global Standard Model parameters, interplay with increasingly precise theoretical work nevertheless permits deeper understanding of the nature of these contributions [3–5]. As such, measurements of branching fractions and phase-space integrated *CP*-asymmetries are essential to understanding the mechanisms of *b*-hadron decays more generally.

Measurements of *CP*-violation in *b*-baryon decays in particular are notably sparse: until the LHC era, *b*-baryons were not copiously produced by any of the accelerator experiments [6, 7]. Chapter 5 details a search for the suppressed decays of a Λ_b^0 or Ξ_b^0 baryon into a Λ baryon and two charged (π or K) hadrons, with a measurement of the branching fractions of the Λ_b^0 to the $\Lambda K^+\pi^-$ and ΛK^+K^- final states, along with one of the first *CP* violation measurements to be performed on decays of the Λ_b^0 with no charm quarks in the final-state.

Multi-body *b*-hadron decays proceed via many intermediate resonant states, many of which have very short ($\sim 10^{-22}$ s) lifetimes [7]. Resolving decay vertices experimentally to this level of precision is impossible, however these intermediate states can be identified via the enhancement present in the inclusive decay processes, at a characteristic invariant mass. Moreover, the decays of these intermediate states can quantum-mechanically interfere with each other, producing a rich structure which can be used as a tool to probe the Standard Model processes at the amplitude level.

Chapter 6 describes the techniques and formalism required to investigate the underlying physical processes that generate these structures in the so-called *Dalitz* plot. Presented in Chap. 7 is the detailed analysis of the amplitude for a B^+ meson decaying into three charged pions, where previously, significant *CP*-violation was observed in a model-independent analysis of the phase-space distribution. The charged pion, with mass[1] $m_{\pi^+} = 139.57\,\text{MeV}$, is the lightest bound state of a quark and an anti-quark, and therefore it, and the lightest of the resonances that decay into two pions, have a unique place in the theory of the strong interaction: quantum-chromodynamics. As such, a unitarity conserving model that uses input from scattering experiments, the K-matrix, is necessary to describe the numerous overlapping states and open decay channels at values of low $m(\pi^+\pi^-)$.

[1] Natural units are used throughout this thesis, where $\hbar = c = 1$, and inclusion of charge-conjugate processes is implied, unless otherwise specified.

This analysis results in the most precise measurements to-date of various quasi-two-body branching fractions; the origins of the observed *CP*-violation in the $B^+ \to \pi^+\pi^+\pi^-$ Dalitz plot; the evolution of the intermediate S-wave amplitude as a function of the di-pion invariant-mass; and provides information valuable to measurements of fundamental weak phases in the Standard Model.

A summary and conclusions to this work as a whole are given in Chap. 8.

References

1. D. Hanneke, S.F. Hoogerheide, G. Gabrielse, Cavity control of a single-electron quantum cyclotron: measuring the electron magnetic moment. Phys. Rev. A **83**, 052122 (2011). https://doi.org/10.1103/PhysRevA.83.052122. arXiv:1009.4831
2. J.D. Cockroft, E.T.S. Walton, Artificial production of fast protons. Nature **129** (1932)
3. H.-Y. Cheng, C.-K. Chua, Branching fractions and direct CP violation in charmless three-body decays of B mesons. Phys. Rev. D **88**, 114014 (2013). https://doi.org/10.1103/PhysRevD.88.114014. arXiv:1308.5139
4. S. Kränkl, T. Mannel, J. Virto, Three-body non-leptonic B decays and QCD factorization. Nucl. Phys. **B899**, 247 (2015). https://doi.org/10.1016/j.nuclphysb.2015.08.004, arXiv:1505.04111
5. S. Cheng, A. Khodjamirian, J. Virto, $B \to \pi\pi$ form factors from light-cone sum rules with B-meson distribution amplitudes. arXiv:1701.01633
6. J. Lewis, R. van Kooten, Review of physics results from the Tevatron: heavy flavor physics. Int. J. Mod. Phys. A **30**, 1541003 (2015). https://doi.org/10.1142/S0217751X15410031. arXiv:1412.5211
7. C. Patrignani et al., Review of particle physics. Chin. Phys. **C40**, 100001 (2016). https://doi.org/10.1088/1674-1137/40/10/100001. 2017 update

Chapter 2
Introduction to the Standard Model and Quark Flavour

In 1979, the Nobel Prize in physics was awarded to Sheldon Glashow, Abdus Salam, and Steven Weinberg for their 1961 work on the SU(2) × U(1) symmetry structure of the unified electroweak interaction, which catalysed the development of a consistent theory of all known fundamental particles. This theory, now known simply as the *Standard Model*, was vindicated in 2012 with the discovery of the scalar boson of the Brout–Englert–Higgs mechanism, and is regarded as the most predictive and robust in modern physics.

In the Standard Model, quarks are the only particle which can interact via all of the fundamental forces, which makes many of the phenomena they exhibit quite remarkable, and a unique probe of Standard Model physics. In particular, quarks are observed only as bound states of hadrons, and the challenge of quark-flavour physics is to extract information about the Standard Model from these hadrons.

This chapter introduces quarks within the Standard Model, the rich phenomenology of hadrons that can be studied at LHCb, and how these interactions can be used to investigate phenomena beyond the Standard Model.

2.1 Introduction

The Standard Model (SM) of particle physics is a quantum field theory encompassing all known particles and their fundamental interactions, and is both remarkably accurate and predictive. Quantum-electrodynamics, one of the constituent theories of the SM, predicts a value of the anomalous magnetic dipole moment of the electron that agrees with the experimental measurements to a precision of ten significant figures, making this the most accurately verified prediction in the history of physics [1].

The SM describes all fundamental particles thus far discovered in the universe (see Fig. 2.1). These particles are categorised by their spin – integer for bosons, half-integer for fermions – and how they couple to the fundamental forces. There are four

© Springer Nature Switzerland AG 2018

D. O'Hanlon, *Studies of* CP-*Violation in Charmless Three-Body* b-*Hadron Decays*,
Springer Theses, https://doi.org/10.1007/978-3-030-02206-8_2

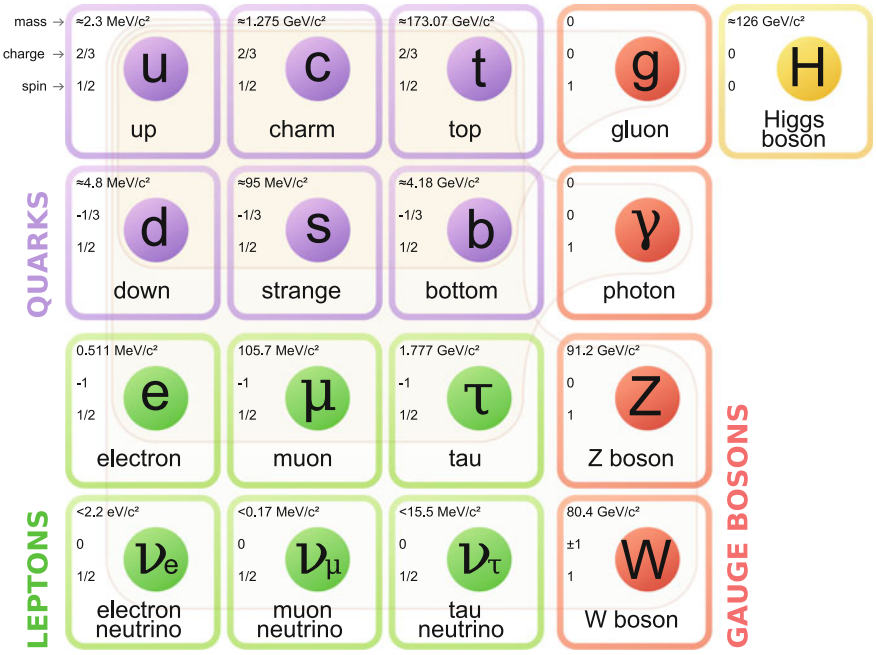

Fig. 2.1 The fundamental particles of the SM of particle physics [2]

kinds of spin-1 *vector* gauge boson, which arise from the symmetry structure of the SM and mediate the fundamental forces: the $W^{\pm}$, Z^0, and photon of the electroweak force, also described by quantum-electrodynamics (QED), as well as the gluon of the strong force, governed by quantum-chromodynamics (QCD). There is also the spin-0 *scalar* 'Higgs' boson, which arises out of a spontaneously broken symmetry by which mass terms are generated for most fundamental particles.

The 2012 discovery of the Higgs boson [3, 4], after being sought by various experiments since its theoretical conception in 1964 [5–7], completed the particle composition of the SM and confirmed its consistency. The latest combined measurement of the Higgs boson mass, 125.09 ± 0.24 GeV [8], is perfectly consistent with constraints imposed upon it from precision measurements of the other electroweak parameters of the SM, as can be seen in Fig. 2.2.

Of the 12 fermions in the SM, six are leptons, which are charged under the electroweak force but not under the strong force, and six are quarks, which are charged under both. The six quarks, also known as quark *flavours*, are the up quark (u), down quark (d), charm quark (c), strange quark (s), top quark (t), and bottom quark (b). The leptons are the electron (e), muon (μ), and tau (τ); and the three neutrinos, the electron-neutrino (ν_e), the muon-neutrino (ν_μ) and, the tau-neutrino (ν_τ). Historically neutrinos were assumed to be massless, however it has since been shown that these possess very small non-zero masses [10–12]. The magnitudes and origin of the neutrino masses are yet to be determined.

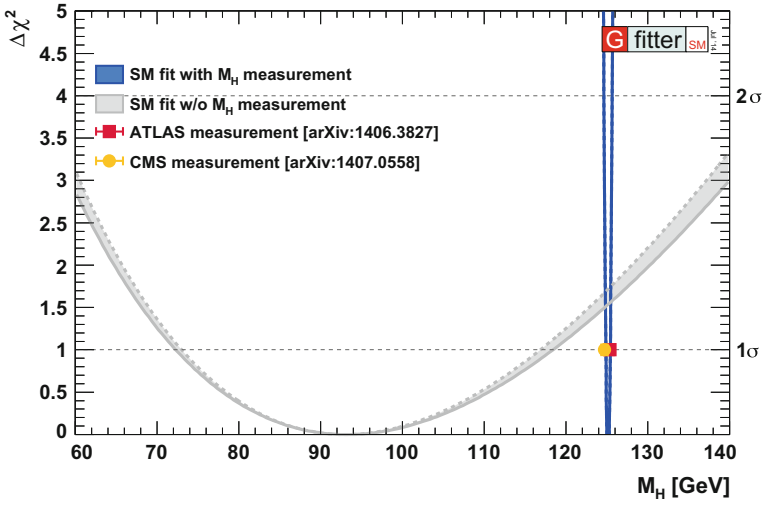

Fig. 2.2 The $\Delta\chi^2$ scan for the mass of the Higgs boson before (grey band), and after (blue band), the data from the individual ATLAS and CMS observations (red and yellow points, respectively) is included into the global electroweak fit [9]. The measured mass of the Higgs boson is around 1.2 Gaussian standard-deviations from the most likely value given the measured values of the other electroweak parameters

Both the quarks and the neutrinos are permitted to change flavour via the electroweak force, and both exhibit a generational structure: The up and down quarks, the charm and strange quarks, and the top and bottom quarks, can be approximately paired by mass, and the electron, muon, and tau can be paired to their associated neutrinos. Both of these structures exhibit conservation rules driven by symmetry relations in the SM, and flavours are permitted to *mix*, governed by the Pontecorvo–Maki–Nakagawa–Sakata (PMNS) and Cabibbo–Kobayashi–Maskawa (CKM) matrices for leptons and quarks, respectively.

As the quarks are also charged under the *colour* charge of QCD, they can also form composite colour-singlet objects of two, three, four [13, 14], five [15], and likely more, quarks or anti-quarks. Ordinary matter is comprised only of protons and neutrons, baryons containing uud or udd quarks, respectively. The studies presented in this thesis focus on the decays of bound states containing the heavier b-quarks, due to their increased decay phase-space, clear experimental signature, and the large degree of CP-violation in their decays predicted in the Standard Model.

Quark binding is due to the property of the gluon to couple to itself, which gives rise to two unique properties: at low energy (large distances), confinement dominates, where quarks are bound together by a force that does not diminish with distance, and results in the energy required to isolate a single quark rapidly tending to infinity (as it is more energetically favourable to create another colour singlet). At high energies (short distances) however, QCD exhibits asymptotic freedom, where quarks and gluons behave as free particles, detected as *jets* of hadrons. The running of the

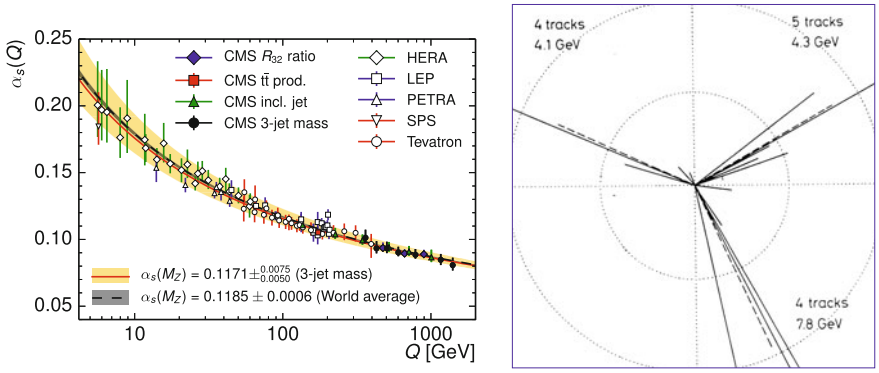

Fig. 2.3 The running of the strong coupling constant, α_s, versus energy [16] (left), where it can be seen that the coupling decreases as the energy scale increases, resulting in asymptotic freedom. A characteristic 'Mercedes' three jet event from the TASSO experiment [17] (right), where the presence of the third jet in the same plane indicates that this is a $e^+e^- \to q\bar{q}g$ event via gluon bremsstrahlung

coupling constant with energy can be seen in Fig. 2.3, along with an example of a three jet event used to claim evidence of the gluon.

Confinement, although not analytically proven to arise in QCD, is observed experimentally. The transition point between these two regimes, Λ_{QCD}, is around 200 MeV (in the $\overline{\text{MS}}$ renormalisation prescription, evaluated at the Z pole mass).

Gravity is notably absent from the SM: Being 10^{33} times weaker than electromagnetism it has a negligible effect on fundamental particles. However, where gravitational effects dominate, such as beyond the event horizon of black holes, the interface between the fundamental quantum field theories of the SM and the classical field theory of general relativity is of great importance to gain a full understanding of the physical phenomena. Nevertheless, there is still the limitation that in most proposed scenarios the hypothetical gravitational force carriers, spin-2 *gravitons*, are experimentally infeasible to detect [18]. The detection of gravitational waves in 2016 by the LIGO and Virgo experiments allows indirect model-independent limits to be placed on the graviton mass, a limit which currently stands at $m_{\text{G}} < 7.7 \times 10^{-23}$ eV [19].

2.2 Symmetries

The SM describes fundamental interactions governed by local gauge symmetries. These gauge symmetries themselves are described by the unitary product group,

$$\text{G}_{\text{SM}} = \text{SU(3)}_{\text{C}} \times \text{SU(2)}_{\text{L}} \times \text{U(1)}_{\text{Y}}, \tag{2.1}$$

which result in the conservation of colour charge (C), weak-isospin (acting only on left-handed fields, L), and weak hyper-charge (Y)

These fields are represented mathematically by the Lagrangian density of the SM, which is the most general renormalisable Lagrangian consistent with the gauge symmetries of Eq. 2.1 and the particle content listed in Fig. 2.1 (under the assumption of massless neutrinos).

This Lagrangian can be represented in three parts,

$$\mathcal{L}_{\text{SM}} = \mathcal{L}_{\text{gauge}} + \mathcal{L}_{\text{Higgs}} + \mathcal{L}_{\text{Yukawa}}, \tag{2.2}$$

where $\mathcal{L}_{\text{gauge}}$ contains the interaction terms of the electroweak force and QCD, $\mathcal{L}_{\text{Higgs}}$ contains the components whose symmetry is spontaneously broken to generate the Higgs interaction, and $\mathcal{L}_{\text{Yukawa}}$ contains the components required to couple the Higgs field to the massless quark and lepton fields.

In addition to these local gauge symmetries, there also exist various global symmetries under all or a particular subset of fundamental interactions in the SM. In the description of the strong force, QCD, flavour is an exact symmetry and no flavour changing interactions are permitted to exist. In the electroweak theory however, flavour changing currents are generated and mediate quark mixing.

Global symmetries are often approximate symmetries that become exact in the limit that a small parameter tends to zero. Isospin symmetry, which is exactly conserved under the assumption that the quark masses are identically zero, is a particularly useful quantity for hadrons containing only light quarks, where the associated SU(2) algebra can be used to relate various phenomena. There are also global symmetries present in the SM that are known as *accidental* symmetries, that generate lepton and baryon number conservation.

2.2.1 Discrete Symmetries

The SM also exhibits discrete symmetries, with an associated multiplicative conserved quantity, of charge conjugation (C), parity inversion (P), and time reversal (T). To enforce Lorentz invariance, the result of the combined CPT operation is always conserved, whereas C and P are individually maximally violated by the chiral weak interaction, as the left-handed and right-handed fields have different gauge representations. The operation that transforms between particles and anti-particles, CP, also happens to be violated in the SM, and the magnitude of this violation is one of the free parameters of the SM.

It was thought that the symmetry between particles and anti-particles, described by the combined charge and parity change operator CP, was conserved in nature, however, evidence from decays of K_{L}^0 mesons indicated that there was small violation of this symmetry [20], and hence a fundamental difference between matter and anti-matter. Since then, decays of various other particles have been observed to violate CP [21–25], and it is now possible to get a consistent picture of the degree of CP-

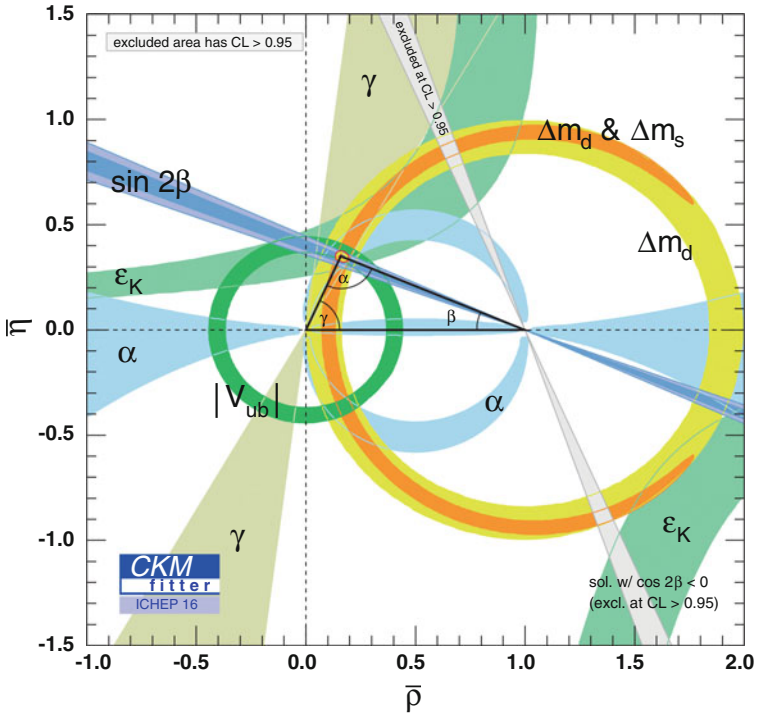

Fig. 2.4 The unitarity triangle visualisation [26] of the consistency of the quark flavour sector in the SM, over-constrained by experimental measurements, including the CKM phases α, β, and γ, that form the vertex angles, and products of CKM matrix elements that define the side lengths. Shaded areas indicate constraints on the global parameter fit from experimental measurements on the triangle side length or vertex angle. That these constraints form a triangle is a test of consistency of the CKM matrix

violation in the quark sector via the *unitarity* triangle, Fig. 2.4, and in addition probe the processes that demonstrate such phenomena.

It is very likely[1] that shortly after the Big Bang there were equal quantities of matter and anti-matter. As the universe cooled into what we observe today, an asymmetry between baryonic and anti-baryonic matter became apparent. The three requirements to generate this condition, the Sakharov conditions [27], are baryon number violation, C and CP symmetry violation, and interactions out of thermal equilibrium.

The quark flavour sector currently includes the only known CP symmetry (or simply, 'CP') violating phase in nature: the Kobayashi–Maskawa (KM) phase. However, it has been known for some time that the magnitude of the matter-anti-matter asymmetry generated via the KM phase is some 10^7 times too small [28] to explain the observed universal baryon asymmetry. The challenge then is to find another source

[1] Any initial asymmetry must have been very large to survive being washed out during the inflationary period, so a dynamical cause is more likely.

of *CP*-violation, either in the SM from the lepton flavour sector [29]; or from quark flavor contributions not taken into account by the KM phase; or from some other beyond the Standard Model process yet to be discovered.

The importance of gaining an understanding of *CP*-violation is underscored by its appearance as one of the three conditions proposed by Sakharov. However, there are various other motivations for studying the mechanisms by which *CP* is violated in the universe. Violation of *CP* symmetry is intrinsically related to several of the free parameters of the SM, in the quark sector and perhaps the neutrino sector, where powerful tests for generic new physics contributions can be performed [26].

2.2.2 The BEH Mechanism

Experimental results indicate that the masses of the photon and gluons are zero, however for all other fundamental particles this is not the case. Nevertheless, for the electroweak Lagrangian, inclusion of a mass term (i.e., a term quadratic in the field operators) for either the fermions or the vector bosons is not invariant under an SU(2) transformation.

A solution to this dilemma was proposed in the 1960s by Brout, Englert, and Higgs, drawing on related work in condensed-matter physics [5–7]. They proposed that a mass term could be included implicitly in a gauged quantum field theory by 'spontaneously' breaking the gauge symmetry. This is done by including scalar fields with a non-zero vacuum expectation value, which are then 'absorbed' by the vector bosons as mass degrees-of-freedom, and which have Yukawa couplings to fermions that generate mass terms. The crucial element of this is that, whilst the *Lagrangian* is invariant under the gauge transformation, the ground-state is not.

This has particular consequence for quarks in the SM. The couplings between quarks in the $\mathrm{SU(2)_L}$ group are described by

$$\mathcal{L}_W = \frac{g}{2\sqrt{2}} \overline{u}_L \gamma^\mu d_L W_\mu^+ + h.c, \tag{2.3}$$

where $\overline{u}_L$ are left-handed up-type quark fields, d_L are left-handed down-type quark fields, W_μ^+ is the charged-current W boson field, γ^μ are the Dirac matrices, and $h.c$ indicates the omitted Hermitian-conjugate expression (quark-flavour indices have been suppressed for brevity). The corresponding complex scalar Higgs doublet field is included as

$$\mathcal{L}_{\text{Higgs}} = \mu^2 \phi^\dagger \phi - \lambda (\phi^\dagger \phi)^2, \tag{2.4}$$

where μ is the Higgs-boson mass and λ is the Higgs self-coupling.

When the Higgs field acquires a vacuum expectation value,

$$\phi = \begin{pmatrix} 0 \\ \frac{v}{\sqrt{2}} \end{pmatrix}, \tag{2.5}$$

mass terms are generated for the quark fields in the above Lagrangian and the right-handed doublets are coupled with the left-handed singlets. After this spontaneous symmetry breaking, the Lagrangian can be written containing a Yukawa interaction term that couples the scalar Higgs field, ϕ, with two right handed Dirac fermion field singlets, u_R and d_R, and a left handed doublet, $Q_L = (u_L, d_L)$,

$$\mathcal{L}_Y = -Y^d_{ij} Q_{Li} \phi d_{Rj} - Y^u_{ij} Q_{Li} \epsilon \phi^* u_{Rj} + h.c. \tag{2.6}$$

The $Y^{u,d}$ are complex coupling constants, ϵ is the totally anti-symmetric tensor, and the quark generations are labelled by i, j. In addition to this, the previously massless excitations of the electroweak field, the W and Z bosons, gain mass. Finally, there is also an excitation associated with the Higgs field that represents a physical state, the Higgs boson, whose mass is one of the free parameters of the SM.

2.2.3 The CKM Matrix

In the flavour (W interaction) basis and quark mass basis, $Y^{u,d}$ is not equivalent. This results in flavour-changing interactions, or quark *mixing*, where quarks interacting via an intermediate W boson may change flavour. To obtain the quark mass states, $Y^{u,d}$ is diagonalised with four $V^{u,d}_{L,R}$ matrices, via the transformation $Y \to VYV^\dagger$. The quantity $V^u_L V^{d\dagger}_L$ describes the mixing between the various quark states, and is known as the Cabibbo–Kobayashi–Maskawa (CKM) matrix, $V_{\rm CKM}$.

The CKM matrix describes the couplings between the physical quark states and the charged current W interactions. The CKM matrix is a 3×3 unitary matrix that can be written in terms of the transition amplitudes between the i and j states, V_{ij},

$$V_{\rm CKM} = \begin{pmatrix} V_{ud} & V_{us} & V_{ub} \\ V_{cd} & V_{cs} & V_{cb} \\ V_{td} & V_{ts} & V_{tb} \end{pmatrix}. \tag{2.7}$$

In the 'standard' parameterisation, it is also parameterised by three mixing angles and a CP-violating Kobayashi–Maskawa (KM) phase, δ,

$$V_{\rm CKM} = \begin{pmatrix} c_{12}c_{13} & s_{12}c_{13} & s_{13}e^{-i\delta} \\ -s_{12}c_{23} - c_{12}s_{23}s_{13}e^{i\delta} & c_{12}c_{23} - s_{12}s_{23}s_{13}e^{i\delta} & s_{23}c_{13} \\ s_{12}s_{23} - c_{12}c_{23}s_{13}e^{i\delta} & -c_{12}s_{23} - s_{12}c_{23}s_{13}e^{i\delta} & c_{23}c_{13} \end{pmatrix} \tag{2.8}$$

where $s_{ij} \equiv \sin\theta_{ij}$ and $c_{ij} \equiv \cos\theta_{ij}$.

It is known that $\sin\theta_{13} \ll \sin\theta_{23} \ll \sin\theta_{12}$, so it is also sometimes convenient to use the Wolfenstein parameterisation, which highlights this hierarchy. Defining

$$s_{12} = \lambda, \tag{2.9}$$

$$s_{23} = A\lambda^2, \tag{2.10}$$

$$s_{13}e^{-i\delta} = A\lambda^3(\rho - i\eta), \tag{2.11}$$

then the CKM matrix can be expressed as

$$V_{\text{CKM}} = \begin{pmatrix} 1 - \lambda^2/2 & \lambda & A\lambda^3(\rho - i\eta) \\ -\lambda & 1 - \lambda^2/2 & A\lambda^2 \\ A\lambda^3(1 - \rho - i\eta) & -A\lambda^2 & 1 \end{pmatrix} + \mathcal{O}(\lambda^4), \tag{2.12}$$

where $\lambda \approx 0.23$. From this it can be seen that, for example, coupling between the t and b quarks is strong, $\mathcal{O}(1)$, however coupling between the u and b quarks is very weak, $\mathcal{O}(\lambda^3)$.

This is broadly reflected in the hadron decays. Decays of b-hadrons to a final state with a c-hadron are favoured over decays to a final state with purely light–quark hadrons (u- and d- hadrons), or s-hadrons (these are known as CKM-favoured or CKM-suppressed decays, respectively). Such charm-*less* decays are the subject of this thesis.

This reasoning is accurate for decays mediated purely by so-called 'tree' Feynman diagrams of the type in Fig. 2.5 (left), however there are also decays mediated by intermediate gluons that can carry additional suppression factors. Such a diagram with a single loop can be seen in Fig. 2.5 (right). Diagrams of this type are also known as *penguin* diagrams, and the degree to which these kinds of diagrams contribute to a decay process cannot, in general, be precisely calculated.

These penguin diagrams however have an advantage when searching for BSM physics, as heavy new particles can contribute off mass-shell in the loop and alter the decay quite considerably with respect to the SM predictions, and in particular can introduce new weak phases that result in additional sources of CP-violation. Such searches are often performed with electroweak penguins, where the final state particles include two leptons, as these are easy to reconstruct experimentally, and

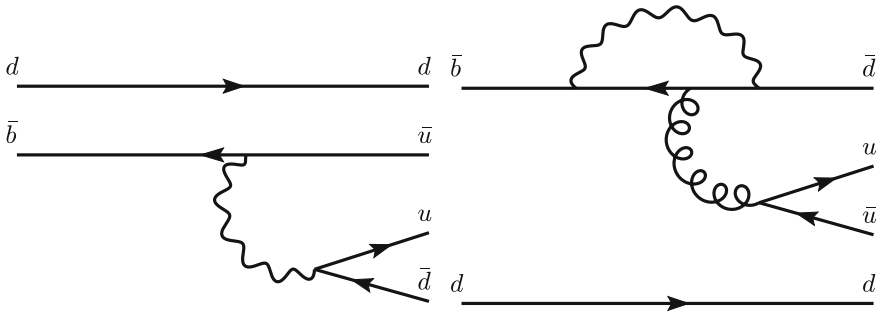

Fig. 2.5 Tree (left) and gluonic penguin loop (right) Feynman diagrams contributing to the $B^0 \to \pi^+\pi^-$ decay amplitude. Electroweak penguins also exist, where the gluon line is replaced with a Z boson or photon line, but this is yet further suppressed

Table 2.1 Global fit values for the three CKM unitarity triangle angles, obtained by the CKMFitter group [26]

Parameter	World average (°)
α	$90.4\ ^{+2.0}_{-1.0}$
β	$22.62\ ^{+0.44}_{-0.42}$
γ	$67.01\ ^{+0.88}_{-1.99}$

easier to make precise theoretical predictions about (as they often do not contain any contributions from tree diagrams or gluonic penguins) [30].

2.2.4 *Unitarity*

The unitarity constraint, $\sum_k V_{ik} V_{kj}^* = 0$, on the CKM matrix can be represented as one of three triangles. Conventionally this triangle is taken to be that where all terms are $\mathcal{O}(\lambda^3)$, formed from

$$V_{ud} V_{ub}^* + V_{cd} V_{cb}^* + V_{td} V_{tb}^* = 0. \tag{2.13}$$

The angles of the triangle, constructed by dividing Eq. 2.13 by the well-measured term $V_{cd} V_{cb}^*$, are defined such that

$$\alpha = \arg\left(-\frac{V_{td} V_{tb}^*}{V_{ud} V_{ub}^*}\right),\ \beta = \arg\left(-\frac{V_{cd} V_{cb}^*}{V_{td} V_{tb}^*}\right),\ \gamma = \arg\left(-\frac{V_{ud} V_{ub}^*}{V_{cd} V_{cb}^*}\right), \tag{2.14}$$

where the triangle has vertices at $(0, 0)$, $(1, 0)$, and $(\overline{\rho}, \overline{\eta})$. The global fit to this *unitarity* triangle in the $\overline{\rho} - \overline{\eta}$ plane, along with current constraints, can be seen in Fig. 2.4. Numerical results for world average values of the three angles are presented in Table 2.1. Of note is that in the absence of *CP*-violation in the SM the area of this triangle is zero. Over-constraining the parameters of this triangle is an important test of consistency of the quark-flavour sector of the SM, and therefore a sensitive probe for beyond the Standard Model contributions.

In general, the CKM angle γ can be thought of as the difference in phase acquired by the decay of a B and $\overline{B}$ to the same final state; β can be thought of as the difference in phase acquired in the decays of mixed and unmixed B-mesons to a *CP*-eigenstate; and α can be thought of as the difference in the phases acquired in the above two cases - between the decay of mixed and unmixed B-mesons.

2.3 Bound States

A curious property of the strong force is that the coupling, and hence the attraction between colour-charged particles, increases as distance decreases. This is caused

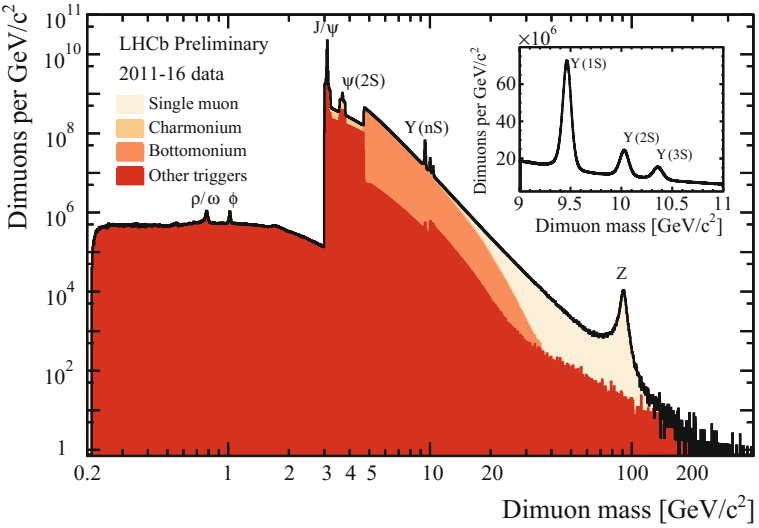

Fig. 2.6 Dimuon spectrum using data collected by the LHCb experiment during Run 1 and the beginning of Run 2, where the trigger line used is indicated by the shading. Clearly visible are various hadronic states, and the Z vector-boson resonance

by the non-zero gluon self-interaction, and is described by the non-Abelian theory of QCD. This results in what is known as confinement: the property of quarks to exist exclusively as bound states known as hadrons. Whilst this is clear experimentally, and has previously been observed in lattice QCD calculations [31], theoretical understanding of this phenomenon is limited by the non-perturbative nature of strong interactions.[2]

This presents somewhat of an issue, as to study quark-flavour physics one must study the hadrons that they form. Therefore, one of the most important tasks of modern quark-flavour physics is development of theoretical and experimental techniques to de-couple the hadronic strong-force contributions from the quark-level weak-force contributions.

It is useful to categorise hadrons into two types: particles and resonances. Particles are stable on the time-scale of the detector, and can be detected by the tracks that they leave in the trackers and the energy deposits they leave in the calorimeters. Resonances however exist only very briefly, and do not leave any detectable deposits. Their existence can only be inferred using the enhancement that results in the corresponding n-body invariant mass distribution of their decay products. The spectrum of resonances decaying into two muons can be seen in Fig. 2.6, using data collected by LHCb throughout Run 1 and the beginning of Run 2.

[2]Expansion in terms of the coupling is not possible, as at low energies ($E \ll \Lambda_{\text{QCD}}$), this is greater than unity. For high energies, quarks are asymptotically free and perturbation theory can be used.

The mean lifetime, τ, of a state is related to the total decay width, Γ,

$$\tau = \frac{1}{\Gamma} \propto \left[\sum_{i}^{\text{channels}} \Gamma_i \right]^{-1} . \tag{2.15}$$

A large width implies that the decay is via the strong force, as this dominates unless the decay violates conservation laws. One example where strong processes do not dominate is in decays that are suppressed via the Okubo–Zweig–Iizuka (OZI) rule, such as those of the J/ψ meson. This results in a significantly reduced cross-section to hadrons and a longer than expected lifetime, as the time-scale for the now more favourable weak decays is several orders of magnitude greater than for strong decays.

Interference between these strongly-decaying resonances in the weak-force mediated flavour-changing decays of the b-hadron gives direct access to the quantum-mechanical phases present in the SM, and permits measurements of CP-violation, but makes identifying individual resonant contributions a challenge. These issues are explored in further detail in the chapters that describe the amplitude analysis of $B^+ \to \pi^+\pi^+\pi^-$, Chaps. 6 and 7.

2.4 Heavy Flavour Phenomenology

In general there are two quantum-mechanical phases that appear in the decay amplitude for a b-hadron. In the SM, there are phases that arise from the complex couplings to the W boson (Y in Eq. 2.6), the CP-odd 'weak' phases that necessarily change sign under CP. The weak phase of any single contribution to the decay amplitude is arbitrary, however, the difference between two weak phases in a decay amplitude is related to the phases in the CKM matrix, and is therefore convention-independent. Extraction of these phases, and use of them to over-constrain CKM unitarity, is an important test of the SM and a sensitive probe for new physics.

There are also phases in the amplitude which do not change sign under CP. These CP-even phases are related to intermediate on-shell resonances in the decay, which are usually produced by strong interactions, and therefore this is known as the 'strong' phase. Similarly to the weak phase, only differences in the strong phase of the contributions to the amplitude are physically meaningful.

A strong phase difference is necessary for CP-violation to occur, however to determine the weak phase, one has to de-couple this from the strong phase contribution. As the strong phase is dominated by QCD effects in the non-perturbative regime, this is particularly difficult to calculate theoretically, and therefore the challenge is to make experimental measurements of the weak phase that are as insensitive as possible to the contribution from the strong phase.

2.4.1 Meson Oscillations

When the mass eigenstate is not equal to the flavour eigenstate, various neutral particles, for example, B^0, B_s^0, K^0, and D^0 mesons, exhibit a phenomenon known as oscillation. This is also similar for neutrinos, which are produced and detected in their flavour eigenstates, but propagate as mass eigenstates. An initial preparation of a quantum superposition of two flavour eigenstates, B and $\overline{B}$,

$$|\phi(0)\rangle = a(0)|B\rangle + b(0)|\overline{B}\rangle, \tag{2.16}$$

will evolve in time and also acquire final states f_0, f_1, ...,

$$|\psi(t)\rangle = a(t)|B\rangle + b(t)|\overline{B}\rangle + c_0(t)|f_0\rangle + c_1(t)|f_1\rangle + ... \tag{2.17}$$

As only the B and $\overline{B}$ states are of interest, and t can be assumed to be large compared to the characteristic strong interaction time-scale, an effective Hamiltonian, $\mathcal{H}$, can be introduced, with dynamics governed by the Schrödinger equation,

$$i\hbar\frac{\partial}{\partial t}\begin{pmatrix}B(t)\\ \overline{B}(t)\end{pmatrix} = \mathcal{H}\begin{pmatrix}B(t)\\ \overline{B}(t)\end{pmatrix} = \left(\mathbf{M} - \frac{i}{2}\mathbf{\Gamma}\right)\begin{pmatrix}B(t)\\ \overline{B}(t)\end{pmatrix}, \tag{2.18}$$

where $\mathbf{M}$ and $\mathbf{\Gamma}$ denote the Hermitian mass and decay width matrices, which are associated with off-shell (dispersive) and on-shell (absorptive) transitions, respectively. The addition of the $\frac{i}{2}\mathbf{\Gamma}$ term removes the hermiticity of the Hamiltonian and permits decay terms of the form $\exp(-\frac{i}{2}\mathbf{\Gamma}t)$.

Diagonal elements of $\mathcal{H}$ are associated with flavour conserving processes, $B \to B$, whereas the off-diagonal elements are associated with flavour-changing processes, $B \to \overline{B}$. Furthermore, if CPT is conserved, $\mathcal{H}_{11} = \mathcal{H}_{22}$. By diagonalising $\mathcal{H}$, the mass eigenstates can be written in terms of the flavour eigenstates,

$$|B_L\rangle = p|B\rangle + q|\overline{B}\rangle \tag{2.19}$$

$$|B_H\rangle = p|B\rangle - q|\overline{B}\rangle, \tag{2.20}$$

where the subscripts L and H represent heavy and light eigenstates, respectively, and q and p are complex parameters satisfying $|p|^2 + |q|^2 = 1$.

For the B_s^0 system, the dominant *box* diagram contributions to this process are shown on the left of Fig. 2.7, and the experimental measurement of B_s^0 mixing at LHCb can be seen in on the right [32]. This resulted in a value of the oscillation frequency of $\Delta m_s = 17.768 \pm 0.024\,\text{ps}^{-1}$, equivalent to the mass difference between the heavy and light B_s^0 eigenstates (for the B^0 system this is significantly smaller, $\Delta m_d = 0.5098 \pm 0.0035\,\text{ps}^{-1}$ [1]).

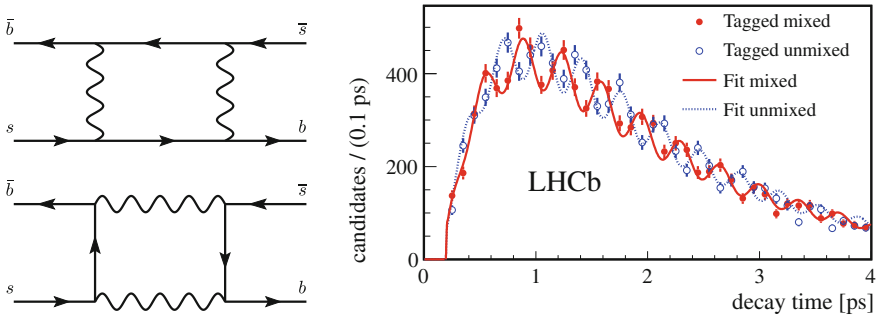

Fig. 2.7 Dominant box diagram contributions to B_s^0 mixing, via intermediate t quarks (top left) and intermediate W bosons (bottom left), and the experimental decay time measurement (left) of decays of mixed (red) and un-mixed (blue) B_s^0 mesons [32]

2.4.2 CP-Violation

In b-hadron decays, CP-violation can be classified into three types:

- CP-violation in decay: This occurs in decays of both charged and neutral b-hadrons, where the amplitude for the decay and its CP conjugate process have different magnitudes. This is the only type of CP-violation observable in charged b-hadron decays and b-baryon decays, where it is also possible to identify the CP conjugate decay without having to use flavour tagging or decays to a flavour-specific final state. Examples of decay modes where CP-violation in decay has been observed are $B^0 \to \pi^+\pi^-$, $\overline{B}^0 \to K^-\pi^+$, $\overline{B}_s^0 \to K^+\pi^-$, and $B^+ \to \pi^+\pi^+\pi^-$.
- CP-violation in mixing: This occurs when two neutral mass-eigenstates cannot be chosen to be CP eigenstates. To date, this has only been observed in K^0 mesons.
- CP-violation in the interference between decays with and without mixing: This occurs in decays which are common to both the b-hadron and its CP conjugate. It can often occur in combination with CP-violation in decay and CP-violation in mixing, and although it requires neutral b-meson mixing, it is in general distinct from these. Analyses of this type also in general require time-dependence and flavour-tagging to identify the flavour of the b-hadron at production and decay. Examples of decay modes which exhibit CP-violation in the interference between decays with and without mixing are $B^0 \to \phi K^0$, $B^0 \to K_S^0 K^+ K^-$, $B^0 \to \pi^+\pi^-$, and $B^0 \to J/\psi\, K_S^0$

CP-Violation in Decay

For CP-violation in decay, there must be at least two interfering amplitudes leading to the same final state, each with different weak and strong phases. The amplitude of a decay process A, and its CP conjugate, $\overline{A}$, can be written as

$$A = |A_1| \exp[i(\delta_1 + \phi_1)] + |A_2| \exp[i(\delta_2 + \phi_2)] \tag{2.21}$$

$$\overline{A} = |A_1| \exp[i(\delta_1 - \phi_1)] + |A_2| \exp[i(\delta_2 - \phi_2)], \tag{2.22}$$

where the subscripts indicate the individual interfering amplitudes, ϕ represents the CP-odd weak phase, and δ the CP-even strong phase. The CP violating rate asymmetry, $\mathcal{A}$, can then be written as

$$\mathcal{A}_{CP} = \frac{\Gamma(\overline{B} \to \overline{f}) - \Gamma(B \to f)}{\Gamma(\overline{B} \to \overline{f}) + \Gamma(B \to f)} \tag{2.23}$$

$$= \frac{2|A_1||A_2| \sin\delta \sin\phi}{|A_1|^2 + |A_2|^2 + 2|A_1||A_2| \cos\delta \cos\phi}, \tag{2.24}$$

where $\Gamma(B \to f)$ is the rate for a b-hadron decay to a final state f, $\delta = \delta_1 - \delta_2$, $\phi = \phi_1 - \phi_2$, and the convention for numerator is such that the rate for the decay of the particle containing the $\overline{b}$ is subtracted from that of the b. Here, ϕ is a function of the SM unitarity triangle angles, and it can be seen that for $\mathcal{A}_{CP}$ to be non-zero, both δ and ϕ must be non-zero.

This also exposes the downside of measuring a decay rate asymmetry of this form: with two observables ($|A_1|^2$, $|A_2|^2$) and four unknown parameters (A_1, A_2, ϕ, and δ), it is impossible to relate this to the fundamental parameters of the SM (or vice-versa), without some external input.

Decays that are favoured by the CKM structure, those that proceed via a $b \to c$ transition, have the same CKM phase in both the tree and loop diagrams contributions, and therefore this single phase dominates over all others. Decays involving other transitions, charmless decays, do not contain the same CKM factor in both the tree and loop contributions, and can have two different phases that are equal in magnitude. Therefore, this interference between the two possible amplitudes in charmless decays, in general, leads to a larger value of the weak phase difference, ϕ, in Eq. 2.24, and a larger amount of CP-violation in decay.

CP-Violation in Mixing

For CP-violation in mixing,

$$\left|\frac{q}{p}\right| \neq 1. \tag{2.25}$$

In charged-current semileptonic decays of neutral mesons this is the only source of CP-violation, as these decays are flavour-specific.

Mixing-Induced CP-Violation

Mixing-induced CP-violation occurs in the interference between a decay with mixing, $M^0 \to \overline{M}^0 \to f$, and a decay without mixing, $M^0 \to f$, which necessarily only occurs in decays to final states that are common to M^0 and $\overline{M}^0$.

This is the case if

$$\arg(\lambda_f) + \arg(\lambda_{\bar{f}}) \neq 0, \tag{2.26}$$

where

$$\lambda_f = \frac{q}{p}\frac{\overline{A}_f}{A_f}. \tag{2.27}$$

For eigenstates of CP this simplifies to $Im(\lambda_{f_{CP}}) \neq 0$.

2.5 Beyond the Standard Model

Despite the remarkable successes in explaining such varied phenomena with unparalleled precision, it is important to remember that the SM is still only an effective theory. For example, various astrophysical measurements, such as those of galactic rotation curves [33], cosmic microwave background radiation [34], and gravitational lensing in galaxy clusters [35], point to the existence of a form of matter that interacts very weakly with ordinary matter, and does not radiate electromagnetically. Despite the overwhelming evidence for this *dark* matter, no particle has been observed with characteristics consistent with this form of matter. If this phenomenon is particulate in nature, this necessarily indicates the existence of physics beyond the Standard Model, and there are numerous searches for potential dark matter candidates via either direct or indirect detection methods [36, 37].

Further indications of the incompleteness of the Standard Model come from the observed over-abundance of matter over anti-matter in the universe, inconsistent with precisely measured asymmetry generating mechanisms within the SM by a factor of around 10^7; the unknown nature and origin of neutrino masses; and the apparent 'fine-tuning' of the Higgs mass in the Standard Model.

There are also tensions with SM predictions in measurements made in various different sectors. In the quark-flavour sector for example, there are numerous discrepancies in the relative decay rates of $\overline{B}^0 \to D^{*+}\tau^-\overline{\nu}_\tau$ and $\overline{B}^0 \to D^{*+}\mu^-\overline{\nu}_\mu$ [38, 39]; $B^+ \to K^+\mu^+\mu^-$ and $B^+ \to K^+e^+e^-$ [40]; $B^0 \to K^{*0}\mu^+\mu^-$ and $B^0 \to K^{*0}e^+e^-$ [41] and in the angular observables of $B^0 \to K^{*0}\mu^+\mu^-$ [30]. It is difficult to form a consistent picture of the new physics contributions necessary to explain all of these [42]. However, many are in measurements that are sensitive to lepton universality violation, where the vector bosons couple differently to the various flavours of leptons, something which is forbidden in the SM.

Various so-called 'global' fits incorporate all $B \to s\ell\ell$ decay information to obtain values for Wilson coefficients, dimensionless complex coupling coefficients that enter in the operator-product expansion, which are zero in the SM [43, 44]. Two such coefficients are C_9^{NP} and C_{10}^{NP}, which parameterise anomalous vector and axial-vector couplings, respectively, and appear in the amplitude for the $B \to s\ell\ell$ electroweak penguin decays. The preferred values of these coefficients, given recent measurements of the angular variables and differential branching fractions of various $B \to s\ell\ell$ decays by the ATLAS, Belle, CMS, and LHCb experiments indicate significant deviation away from the SM value of zero. With the addition of the recent LHCb measurement of the double ratio of the $B^0 \to K^{*0}\mu^+\mu^-$ and $B^0 \to K^{*0}e^+e^-$

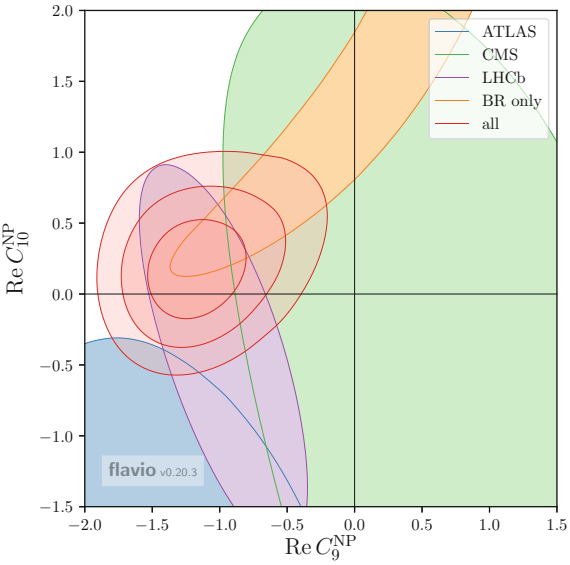

Fig. 2.8 The result of the Flavio [45] global fit for the C_9^{NP} and C_{10}^{NP} Wilson coefficients, incorporating results from $B \to s\ell\ell$ decay analyses from the ATLAS, Belle, CMS and LHCb experiments. The Standard Model value is at (0, 0), and the global fit best-fit-value is displayed with 68, 95, and 99.7% interval contours

branching fractions, to the ratio of $B^0 \to K^{*0} J/\psi\,(\mu^+\mu^-)$ to $B^0 \to K^{*0} J/\psi\,(e^+e^-)$ branching fractions [41], this tension has increased significantly. The result of such a global fit [45] for $\mathrm{Re}(C_9^{\mathrm{NP}})$ and $\mathrm{Re}(C_{10}^{\mathrm{NP}})$ can be seen in Fig. 2.8.

2.5.1 *The Hierarchy and New-Physics-Flavour Problems*

In the SM, the Higgs mass is a free parameter. However, in a hypothetical BSM model where the Higgs mass is a calculable quantity, the value will consist of a bare mass term plus a term containing higher order loop corrections, Δm_{H}. For an ultraviolet cut off at Λ_{UV}, the scale at which the model loses validity, the correction due to a fermion (e.g., the top quark) with coupling λ_f at one loop level goes like

$$\Delta m_H \sim -\frac{|\lambda_f|^2}{16\pi^2}\Lambda_{\mathrm{UV}}. \tag{2.28}$$

Assuming that Λ_{UV} is large, then the correction term must be comparable in magnitude to the bare term, such that these approximately cancel to given the measured Higgs mass of approximately 125 GeV. This large cancellation phenomenon is known as *fine tuning* [46].

This can be solved in two ways. The first is to have a Λ_{UV} that is not large compared to m_{H}, which implies that new particles should be apparent at around the TeV scale. Given the lack of evidence for new particles from the LHC experiments, this is becoming less likely. The second is to introduce bosonic degrees of freedom

that enter the calculation with a negative sign, and cancel the fermionic corrections almost exactly. This is known as supersymmetry, where each fermion has a boson counterpart, and vice versa, and is still under active investigation in measurements at the LHC.

This is further complicated as the SM flavour sector is remarkably successful at describing all phenomena so far observed - a property that would need to be preserved by any putative BSM model. A generic model of this type – where the only suppression of flavour changing neutral currents (FCNC) is due to the large masses of the mediators on the order of the new physics scale Λ – puts severe constraints on the value of this parameter. Assuming that an effective four–quark FCNC operator exists, the measured mixing and CP-violation parameters in B mesons put a bound on the new physics scale of $\Lambda \gtrsim 10^3$ TeV. Corresponding kaon measurements further constrain this to $\Lambda \gtrsim 10^4$ TeV. However, to solve the hierarchy problem, one requires the new physics scale to be $\Lambda \sim 1$ TeV, which implies that this new physics cannot replicate the flavour structure of the SM [47].

This is known as the *new-physics flavour problem*, and significantly constrains models that intend to replicate the generic flavour structure of the SM. One such model that satisfies these constraints is minimally flavour violating supersymmetry [48], where new physics is flavour blind. This, and other models, predict effects that are testable with the current generation of heavy-flavour experiments.

References

1. Particle Data Group, C. Patrignani et al., Rev. Part. Phys. Chin. Phys. **C40**, 100001 (2016) (2017 update). https://doi.org/10.1088/1674-1137/40/10/100001
2. Wikimedia commons, *Standard Model of Elementary Particles* (2014)
3. Atlas, G. Aad et al., Observation of a new particle in the search for the standard model Higgs Boson with the ATLAS detector at the LHC. Phys. Lett. **B716**, 1 (2012). https://doi.org/10.1016/j.physletb.2012.08.020, arXiv:1207.7214
4. CMS, S. Chatrchyan et al., Observation of a new Boson at a mass of 125 GeV with the CMS experiment at the LHC. Phys. Lett. **B716**, 30 (2012). https://doi.org/10.1016/j.physletb.2012.08.021, arXiv:1207.7235
5. F. Englert, R. Brout, Broken symmetry and the mass of Gauge vector mesons. Phys. Rev. Lett. **13**, 321 (1964). https://doi.org/10.1103/PhysRevLett.13.321
6. P.W. Higgs, Broken symmetries and the masses of Gauge Bosons. Phys. Rev. Lett. **13**, 508 (1964). https://doi.org/10.1103/PhysRevLett.13.508
7. G.S. Guralnik, C.R. Hagen, T.W.B. Kibble, Global conservation laws and massless particles. Phys. Rev. Lett. **13**, 585 (1964). https://doi.org/10.1103/PhysRevLett.13.585
8. ATLAS, CMS, G. Aad et al., Combined measurement of the Higgs Boson mass in pp collisions at $\sqrt{s} = 7$ and 8 TeV with the ATLAS and CMS experiments. Phys. Rev. Lett. **114**, 191803 (2015). https://doi.org/10.1103/PhysRevLett.114.191803, arXiv:1503.07589
9. Gfitter Group, M. Baak et al., The global electroweak fit at NNLO and prospects for the LHC and ILC. Eur. Phys. J. **C74**, 3046 (2014). https://doi.org/10.1140/epjc/s10052-014-3046-5, arXiv:1407.3792
10. Super-Kamiokande, Y. Fukuda et al., Evidence for oscillation of atmospheric neutrinos. Phys. Rev. Lett. **81**, 1562 (1998). https://doi.org/10.1103/PhysRevLett.81.1562, arXiv:hep-ex/9807003

11. S.N.O. Collaboration, Q.R. Ahmad et al., Measurement of the rate of $\nu_e + d \rightarrow p + p + e^-$ interactions produced by ^{8}B solar neutrinos at the sudbury neutrino observatory. Phys. Rev. Lett. **87**, 071301 (2001). https://doi.org/10.1103/PhysRevLett.87.071301
12. Daya Bay, F.P. An et al., Observation of electron-antineutrino disappearance at daya bay. Phys. Rev. Lett. **108**, 171803 (2012). https://doi.org/10.1103/PhysRevLett.108.171803, arXiv:1203.1669
13. LHCb, R. Aaij etal., Observation of the resonant character of the $Z(4430)^-$ state. Phys. Rev. Lett. **112** (2014). LHCB-PAPER-2014-014, CERN-PH-EP-2014-061 222002. https://doi.org/10.1103/PhysRevLett.112.222002, arXiv:1404.1903
14. Belle, R. Mizuk et al., Dalitz analysis of $B \rightarrow K^-\pi^+\psi'$ decays and the $Z(4430)^+$. Phys. Rev. D **80**, 031104 (2009). https://doi.org/10.1103/PhysRevD.80.031104, arXiv:0905.2869
15. LHCb, R. Aaij et al., Observation of $J/\psi p$ resonances consistent with pentaquark states in $\Lambda_b^0 \rightarrow J/\psi K^- p$ decays. Phys. Rev. Lett. **115**, 072001 (2015). https://doi.org/10.1103/PhysRevLett.115.072001, arXiv:1507.03414
16. CMS, V. Khachatryan et al., Measurement of the inclusive 3-jet production differential cross section in proton proton collisions at 7 TeV and determination of the strong coupling constant in the TeV range. Eur. Phys. J. **C75**(5), 186 (2015). https://doi.org/10.1140/epjc/s10052-015-3376-y, arXiv:1412.1633
17. Tasso, R. Brandelik et al., Evidence for planar events in e+ e- annihilation at high-energies. Phys. Lett. **B86**, 243 (1979). https://doi.org/10.1016/0370-2693(79)90830-X
18. T. Rothman, S. Boughn, Can gravitons be detected? Found. Phys. **36**, 1801 (2006). https://doi.org/10.1007/s10701-006-9081-9. arXiv:gr-qc/0601043
19. LIGO Scientific and Virgo Collaboration, B.P. Abbott et al., Gw170104: Observation of a 50-solar-mass binary black hole coalescence at redshift 0.2. Phys. Rev. Lett. **118**, 221101 (2017). https://doi.org/10.1103/PhysRevLett.118.221101
20. J.H. Christenson, J.W. Cronin, V.L. Fitch, R. Turlay, Evidence for the 2π decay of the k_2^0 meson. Phys. Rev. Lett. **13**, 138 (1964). https://doi.org/10.1103/PhysRevLett.13.138
21. NA48, V. Fanti et al., A new measurement of direct CP violation in two Pion decays of the neutral Kaon. Phys. Lett. **B465**, 335 (1999). https://doi.org/10.1016/S0370-2693(99)01030-8, arXiv:hep-ex/9909022
22. KTeV, A. Alavi-Harati et al., Observation of direct CP violation in $K_{S,L} \rightarrow \pi\pi$ decays. Phys. Rev. Lett. **83**, 22 (1999). https://doi.org/10.1103/PhysRevLett.83.22, arXiv:hep-ex/9905060
23. BaBar collaboration, B. Aubert et al., Observation of CP violation in the B^0 meson system. Phys. Rev. Lett. **87**, 091801 (2001). https://doi.org/10.1103/PhysRevLett.87.091801, arXiv:hep-ex/0107013
24. Belle, K. Abe et al., Observation of large CP violation in the neutral B meson system. Phys. Rev. Lett. **87**, 091802 (2001). https://doi.org/10.1103/PhysRevLett.87.091802, arXiv:hep-ex/0107061
25. LHCb, R. Aaij et al., First observation of CP violation in the decays of B_s^0 mesons. Phys. Rev. Lett. **110**(22), 221601 (2013). https://doi.org/10.1103/PhysRevLett.110.221601, arXiv:1304.6173
26. J. Charles et al., Current status of the standard model CKM fit and constraints on $\Delta F = 2$ new physics. Phys. Rev. **D91**(7), 073007 (2015). https://doi.org/10.1103/PhysRevD.91.073007, arXiv:1501.05013
27. A.D. Sakharov, Violation of CP invariance C asymmetry, and Baryon asymmetry of the universe. Sov. Phys. Uspekhi **34**, 392 (1967)
28. M.E. Shaposhnikov, Standard model solution of the baryogenesis problem. Phys. Lett. **B277**, 324 (1992) [Erratum: Phys. Lett. B282, 483 (1992)]. https://doi.org/10.1016/0370-2693(92)90753-Q
29. M. Fukugita, T. Yanagida, Barygenesis without grand unification. Phys. Lett. B **174**, 45 (1986). https://doi.org/10.1016/0370-2693(86)91126-3
30. LHCb Collaboration, R. Aaij et al., Search for hidden-sector Bosons in $B^0 \rightarrow K^{*0}\mu^+\mu^-$ decays. Phys. Rev. Lett. **115**, 161802 (2015). https://doi.org/10.1103/PhysRevLett.115.161802, arXiv:1508.04094

31. L. Susskind, Lattice models of quark confinement at high temperature. Phys. Rev. D **20**, 2610 (1979). https://doi.org/10.1103/PhysRevD.20.2610
32. LHCb Collaboration, R. Aaij et al., Precision measurement of the $B_s^0 - -\bar{B}_s^0$ oscillation frequency in the decay $B_s^0 \to D_s^- \pi^+$. New J. Phys. **15**, 053021 (2013). https://doi.org/10.1088/1367-2630/15/5/053021, arXiv:1304.4741
33. P. Salucci, A. Borriello, The intriguing distribution of dark matter in galaxies. Lect. Notes Phys. **616**, 66 (2003). arXiv:astro-ph/0203457
34. R. Massey, Dark matter maps reveal cosmic scaffolding. Nature **445**, 286 (2007). https://doi.org/10.1038/nature05497. arXiv:astro-ph/0701594
35. WMAP, G. Hinshaw et al., Five-year Wilkinson microwave anisotropy probe (WMAP) observations: data processing, sky maps, and basic results. Astrophys. J. Suppl. **180**, 225 (2009). https://doi.org/10.1088/0067-0049/180/2/225, arXiv:0803.0732
36. D.S. Akerib et al., Results from a search for dark matter in the complete LUX exposure, arXiv:1608.07648
37. ATLAS, CMS, A. de Cosa, LHC results for dark matter from ATLAS and CMS, in *Proceedings of the 12th Conference on the Intersections of Particle and Nuclear Physics (CIPANP 2015)* (Vail, Colorado, USA, 19–24 May 2015), arXiv:1510.01516
38. LHCb collaboration, R. Aaij et al., Measurement of the ratio of branching fractions $\mathcal{B}(\bar{B}^0 \to D^{*+}\tau^-\bar{\nu}_\tau)/\mathcal{B}(\bar{B}^0 \to D^{*+}\mu^-\bar{\nu}_\mu)$. Phys. Rev. Lett. **115**, 111803 (2015). https://doi.org/10.1103/PhysRevLett.115.111803, arXiv:1506.08614
39. BaBar collaboration, J.P. Lees et al., Evidence for an excess of $\bar{B} \to D^{(*)}\tau^-\bar{\nu}_\tau$ decays. Phys. Rev. Lett. **109**, 101802 (2012). https://doi.org/10.1103/PhysRevLett.109.101802, arXiv:1205.5442
40. LHCb collaboration, R. Aaij et al., Test of Lepton universality using $B^+ \to K^+\ell^+\ell^-$ decays. Phys. Rev. Lett. **113**, 151601 (2014). https://doi.org/10.1103/PhysRevLett.113.151601, arXiv:1406.6482
41. LHCb Collaboration, R. Aaij et al., Test of lepton universality with $B^0 \to K^{*0}\ell^+\ell^-$ decays (submitted to JHEP), arXiv:1705.05802
42. A. Crivellin, B-anomalies related to leptons and lepton flavour universality violation, in *16th International Conference on B-Physics at Frontier Machines* (Beauty 2016) Marseille, France, 2–6 May 2016. arXiv:1606.06861
43. T. Blake, G. Lanfranchi, D.M. Straub, Rare B decays as tests of the standard model. Prog. Part. Nucl. Phys. **92**, 50 (2017). https://doi.org/10.1016/j.ppnp.2016.10.001, arXiv:1606.00916
44. N. Serra, R. Silva Coutinho, D. van Dyk, Measuring the breaking of lepton flavor universality in $B \to K^*\ell^+\ell^-$. Phys. Rev. **D95**(3), 035029 (2017). https://doi.org/10.1103/PhysRevD.95.035029, arXiv:1610.08761
45. W. Altmannshofer, C. Niehoff, P. Stangl, D.M. Straub, Status of the $B \to K^*\mu^+\mu^-$ anomaly after Moriond (2017), arXiv:1703.09189
46. M. Farina, M. Perelstein, N. Rey-Le Lorier, Higgs couplings and naturalness. Phys. Rev. D **90**, 015014 (2014). https://doi.org/10.1103/PhysRevD.90.015014, arXiv:1305.6068
47. Y. Grossman, Beyond the standard model with B and K physics. Int. J. Mod. Phys. A **19**, 907 (2004). https://doi.org/10.1142/S0217751X04018865. arXiv:hep-ph/0310229
48. P. Paradisi, D.M. Straub, The SUSY CP problem and the MFV principle. Phys. Lett. B. **684**, 147 (2010). https://doi.org/10.1016/j.physletb.2009.12.054

Chapter 3
The Large Hadron Collider

The proton-proton (pp) Large Hadron Collider (LHC) is the final stage of the accelerator complex at the European Centre for Nuclear Research (CERN), located near Geneva, on the Franco-Swiss border. The LHC and its associated accelerator chain are the culmination of over 100 years of research into the production, acceleration, and focussing of charged particles, with the LHC being the world's largest and highest energy accelerator.

This chapter documents the necessary background material on the design and operating conditions of the accelerator which provides beams to the LHCb experiment.

3.1 Introduction

In 2015, the 26.6 km LHC accelerator reached an energy of 6.5×10^{12} eV (6.5 TeV) per beam (0.5 TeV short of the design energy) at a luminosity in excess of the design value of 1.0×10^{34} cm^{-2} s^{-1}, and is currently the world's the highest energy particle collider, surpassing the previous record of 1 TeV per-beam held by the Tevatron accelerator at Fermilab in 2009. A schematic of the CERN accelerator complex can be seen in Fig. 3.1.

The LHC is capable[1] of running in proton-proton, proton-ion, ion-proton,[2] or ion-ion configurations. For protons, the first stage in the LHC accelerator chain is a linear accelerator, Linac 2, which accelerates the protons to 50 mev. These are then injected into the Proton-Synchotron Booster (PSB), which is a set of four superimposed synchotron rings, designed to increase the energy such that the next accelerator

[1] Most operation is dedicated to proton-proton collisions, which is the only type relevant to the work presented in this thesis.

[2] This distinction is important, both due to the asymmetry of the LHCb and ALICE detectors with respect to the beam axis, and also to cancel systematic effects of the large boost caused by the difference in momenta.

© Springer Nature Switzerland AG 2018

D. O'Hanlon, *Studies of* CP-*Violation in Charmless Three-Body* b-*Hadron Decays*,
Springer Theses, https://doi.org/10.1007/978-3-030-02206-8_3

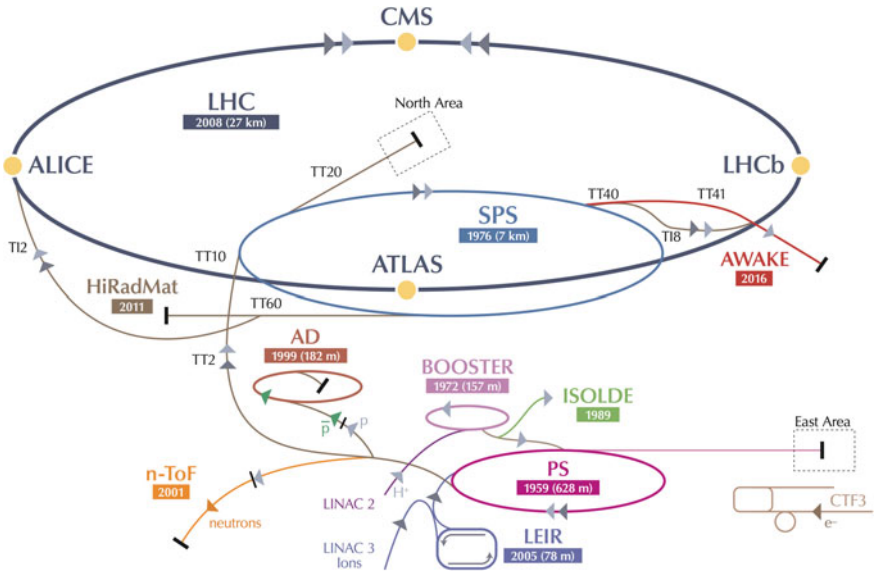

Fig. 3.1 The CERN accelerator complex. Adapted from Ref. [1]

in the chain can accept a much larger number of particles per-bunch, and which ultimately determines the bunch structure that finally enters the LHC. The PSB accelerates the protons to 1.4 GeV before injecting them into the oldest accelerator currently in operation at CERN, the Proton Synchotron (PS). The PS, which first entered operation in 1959 and was once itself the world's highest energy particle accelerator, is a synchotron with a circumference of 628 m, and accelerates protons to an energy of 25 GeV for injection into the Super Proton Synchotron (SPS). The SPS, housed in a tunnel 6.9 km in circumference, is the second largest accelerator at CERN, and in addition to providing protons for the LHC, also acts as a proton source for various fixed target and development beamlines. Several major scientific discoveries were made when the SPS was the flagship accelerator at CERN, most notably the discovery of the W and Z bosons by the UA1 and UA2 experiments. From the SPS, two injector lines connect it to the LHC, which at 2.6 km each are in total almost as long as the SPS itself.

The LHC consists of eight straight *insertion* sections, and eight *arc* sections where the beam is bent by 8.3 T superconducting dipole magnets [2]. Each of the four large LHC experiments, ATLAS, ALICE, CMS, and LHCb, are located on one of the straight sections, with the other four such sections being occupied by the radio-frequency accelerating cavities, beam dump areas, and beam cleaning and collimation apparatus. As the LHC is a $p\,p$ collider, the counter-circulating beams are guided in separate evacuated beam pipes with a pressure of 10^{-7} Pa, with separate superconducting dipole-magnet apertures. These beams are then focused by multipole magnets into collision at each interaction point (IP).

Due to the specialised designs of the LHCb and ALICE detectors, these detectors must operate with a lower pp collision luminosity than the LHC design. To achieve this, the beams at IP 5 and IP 8 are brought into collision at an offset that is adjusted such that the average number of interactions per bunch-crossing remains approximately constant during a fill, despite the total number of circulating protons decreasing due to collisions and beam losses. This, along with the broader beam profile at the interaction point, means that a precise instantaneous luminosity can be reached and maintained throughout a fill [3].

3.2 Magnets

The structure of the superconducting dipole magnets is dominated by the requirement that they provide a 8.3 T magnetic field, sufficient to bend the beams at the 7 TeV per-beam design energy. The cross-section of an LHC diopole magnet and cryostat can be seen in Fig. 3.2. To reach the required magnetic field in the superconducting regime, the type II Niobium–Titanium (Nb–Ti) superconductor must be cooled to 1.9 K, well below its superconducting critical temperature of 9.2 K, and below the superfluid transition point of the helium coolant [4]. This has other advantages: superfluid helium has the highest known thermal conductivity of any material, so can buffer

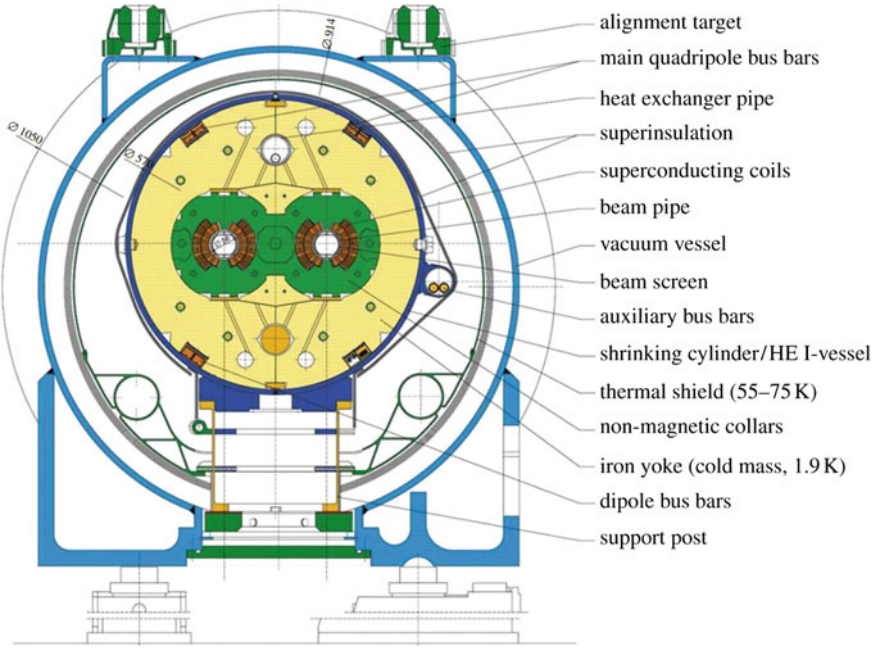

Fig. 3.2 Cross-section of an LHC dipole magnet [2]

heat generated in the superconductors without the need for fluid circulation pumps, and due to its low viscosity can permeate the porous insulation between the magnet windings. The disadvantage of this system is that it requires the entire 80 tonne He reservoir to be cooled to and maintained at 1.9 K.

Even a slight increase in temperature can cause a *quench*, when the Nb–Ti wires enter the resistive regime, resulting in large amounts of energy dissipated into the He coolant. The total energy stored in the magnet system is approximately 10 GJ, so uncontrolled dissipation of this energy can result in catastrophic failure of the magnet system [4]. Measures are put in place such that when a quench is detected the beam is automatically dumped, the magnets in the affected sector are heated to induce more even quenching along the magnet length, and the energy stored in the each of the magnets is diverted into an eight-tonne steel resistor – heating it to a temperature of 570 K.

In addition to the dipole magnets that steer the beam in the 27 km ring, there are also quadrupole and higher-order magnets which focus the beam. These prevent the beam from deviating from the circular orbit by applying sequential focusing and de-focussing in the plane normal to the plane of orbit [5], as well as bringing the beams into collision at the four interaction points.

3.3 Acceleration

Particles in the LHC are accelerated by resonant cavities which apply a difference in electric potential across the beam, known as radio-frequency (RF) cavities. These accelerate the particles from the injection energy (0.45 TeV) to the desired maximum energy, and ensure that the beam maintains the correct bunch structure to maximise the luminosity.

The frequency of the RF cavities must be an integer multiple of the revolution frequency, such that a particles always see a voltage in the same position. The frequency of the RF cavities is 400 MHz, and therefore there are 35, 640 such *buckets* in the LHC beam structure, with an inter-bucket spacing of one RF period. Due to this periodic nature of the acceleration, rather than the particles being uniformly distributed throughout the beam, they are located as *bunches* of particles within the buckets. These buckets can also be left free to perform adjustments to the bunch spacing, and multiple free buckets form the *abort gap* of 3 μs. This abort gap is neccessary such that when the beam is dumped the non-zero rise-time of the kicker magnets does not affect circulating protons and the beam is extracted cleanly.

Particles which are not in the centre of a bucket oscillate back and forth within the bunch due to the periodic RF field, a phenomenon known as synchotron oscillation, where the area of a bunch in position-momentum space is the *emittance*, ϵ [6].

3.4 Operating Conditions

During Run 1 of the LHC, protons were collided at a centre-of-mass energy of 7 TeV in 2011, and 8 TeV in 2012.[3] These beams were formed of 1380 bunches, consisting of 1.15×10^{11} protons, separated with a inter-bunch spacing of 50 ns. Hence, the beam crossing frequency under these conditions was 20 MHz.

In late 2012 the number of bunches was increased to the design value of 2808, and in 2016, with an inter-bunch spacing of 25 ns, the design instantaneous luminosity of 1×10^{34} cm^{-2}s^{-1} was achieved. The centre-of-mass energy was increased in 2015 to 13, 1 TeV short of the design energy, and increase to the maximum of 14 TeV is envisioned after the second long-shutdown.

The instantaneous luminosity at each interaction point is given by,

$$\mathcal{L} = \frac{f N_p^2 N_b}{4\pi\sigma^2} F = \frac{f N_p^2 N_b}{4\epsilon\beta^*}, \tag{3.1}$$

where f is the bunch revolution frequency, N_p is the number of protons per bunch, N_b is the number of bunches per beam, σ is the RMS radius of each beam, and F is a geometrical factor related to the beam-crossing angle. This can also be expressed in terms of the beam emittance, ϵ, which is a measure of the spread of the protons in position and momentum space, and the beta function (transverse size of the beams) at the interaction point, $\beta^* = \pi\sigma^2/\epsilon$.

During Run 1, the peak value of this instantaneous luminosity was 7.7×10^{33} cm^{-2}s^{-1} (4×10^{32} cm^{-2}s^{-1} at LHCb), corresponding to a nominal beam emittance of around 2.5 μm [7], and the total integrated luminosity recorded was around 28 fb^{-1} at each of ATLAS and CMS, and 3 fb^{-1} at LHCb. For LHCb, this corresponds to around 10^{11} b-hadrons produced within the detector acceptance [8].

3.5 Physics

At a hadron collider, it is useful to introduce the *pseudorapidity*, defined in terms of the angle, θ, between particle momentum and the positive direction of the beam axis, z,

$$\eta = -\ln\left[\tan\left(\frac{\theta}{2}\right)\right]. \tag{3.2}$$

This quantity is invariant under boosts in z, and therefore is meaningful regardless of the longitudinal momentum fraction, and hence the boost of the centre-of-mass frame, of the colliding partons.

[3] The LHC also operated for a short time in 2010 and 2013 with specialised conditions, however no analysis of data collected during these periods is presented in this thesis.

3.5.1 b-Hadron Production at the LHC

At the high centre-of-mass energies at which the LHC runs, the contribution to the proton parton-density-function from valence (uud) quarks is small, and the dominant contribution is from gluons (Fig. 3.3) [9]. As such, most heavy quarks are produced via gluon-initiated processes. The leading order ($\mathcal{O}(\alpha_s^2)$) contributions are the $2 \to 2$ quark annihilation (Fig. 3.4a) and gluon-gluon fusion processes (Fig. 3.4b), however, at LHC energies these are dominated by the next-to-leading-order ($\mathcal{O}(\alpha_s^3)$) contributions [10]. At 7 TeV centre-of-mass energy the dominant overall contribution is from flavour excitation (Fig. 3.4c), the second largest contribution comes from gluon splitting (Fig. 3.4d), and production via gluon-gluon fusion comes a distant third.

Unlike in the e^+e^- experiments, a production asymmetry of the b-hadrons can arise from contributions where an electroweak Wqq' vertex replaces a $gq\bar{q}$ vertex in Fig. 3.4, which necessitates the consideration of additional corrections in the measurements described in Chaps. 5 and 7.

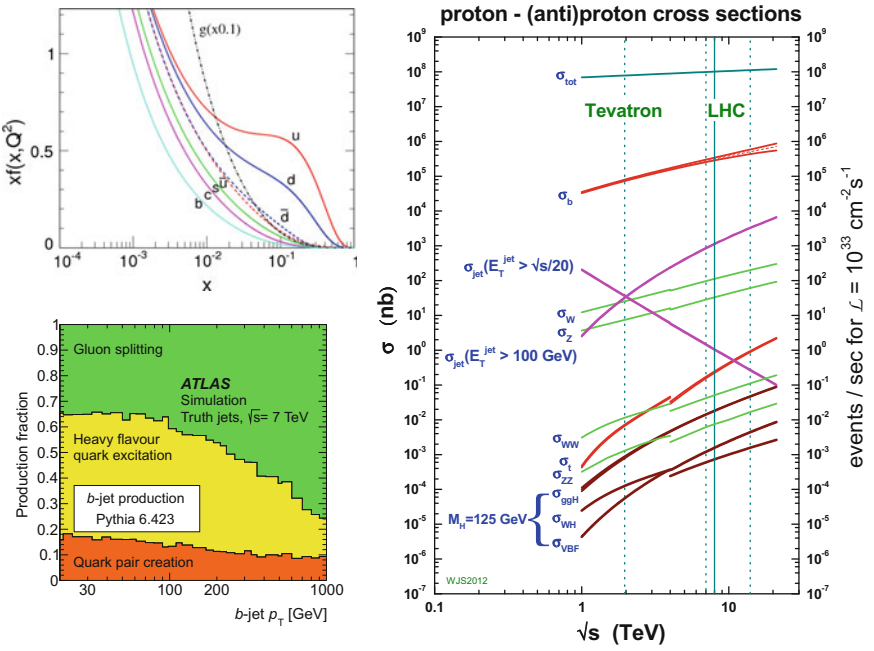

Fig. 3.3 Top left: Proton parton density function as a function of x, the fraction of the proton momentum carried by the struck parton [9], where the gluon contribution is scaled by a factor of 0.1 (typical values of x at LHCb are around 10^{-2}). Bottom left: Fraction of b-jets by production process as a function of b-jet p_{T}, in the ATLAS ($|\eta| < 2$) acceptance, where 'quark pair creation' refers to the leading order processes (Fig. 3.4a, b) [11]. Right: Total and process-level cross-sections for pp ($p\overline{p}$) scattering at the 7 TeV LHC (1.96 TeV Tevatron) centre-of-mass energy [12]. For comparison, the $e^+e^- \to b\bar{b}$ cross-section at $\Upsilon(4S)$ is approximately 1.1 nb [13]

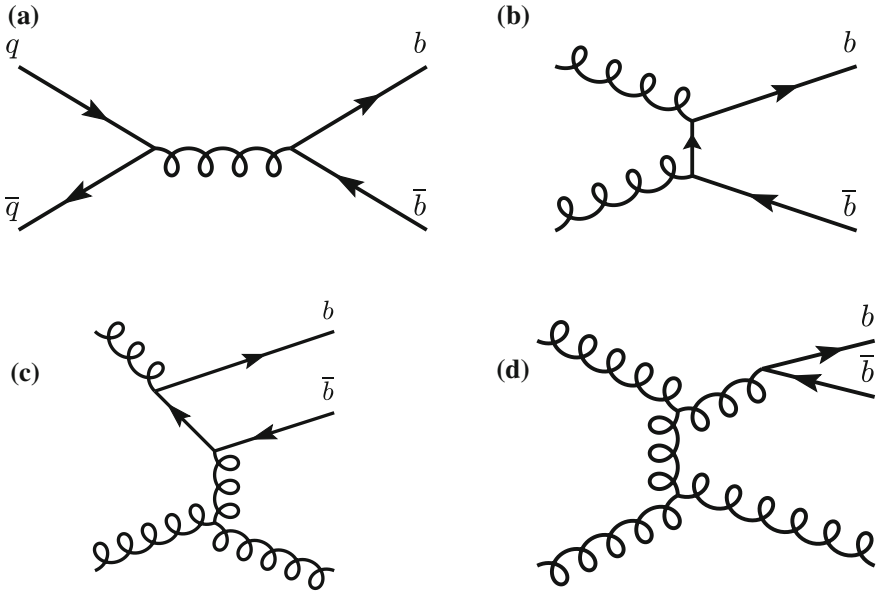

Fig. 3.4 Feynman diagrams for possible $b\bar{b}$ pair production mechanisms at the LHC: quark annihilation (Fig. 3.4a), gluon-gluon fusion (Fig. 3.4b), flavour excitation (Fig. 3.4c), and gluon splitting (Fig. 3.4d)

Whilst quarks preferentially hadronise into mesons, the production fraction of b-baryons relative to other b-hadrons was some 240% higher at the 2 TeV $p\bar{p}$ Tevatron collider than at the Z^0 mass at LEP [14], and at LHCb Λ_b^0-baryons are produced at 40% of the rate of B^+ and B^0-mesons. This gives the LHC experiments a unique opportunity to investigate the copiously produced, but relatively poorly studied, b-baryons.

3.5.2 LHC Experiments

The physics programme of the LHC is dominated by the four largest experiments: ALICE (A Large Ion Collider Experiment) [15], ATLAS (A Toroidal LHC ApparatuS) [16], CMS (Compact Muon Solenoid) [17], and LHCb [18].

The ATLAS and CMS experiments are designed primarily to study high-p_{T} physics in the central ($-2 < \eta < 2$) pseudorapidity region, and thereby detect decay products of high-mass Standard Model (SM) and beyond the Standard Model (BSM) particles. These detectors are optimised to study hadronic jets produced by quarks and gluons; photons and charged leptons; and perform measurements of 'missing' energy signatures, characteristic of neutrinos or other as-yet-undiscovered weakly interacting particles. In Run 1, ATLAS and CMS most notably announced the discovery

of the boson of the Brout–Englert–Higgs mechanism [19, 20], and have since made measurements of its spin and couplings [21–26]. In addition to this, various measurements have been made of W, Z, and t-quark cross-sections and couplings, large regions of the parameter space for supersymmetry (SUSY) and other models have been excluded, and searches for dark matter particles have been performed [27–30].

ATLAS and CMS have finely segmented hadronic and electromagnetic calorimeters with precise energy resolution, and close to a 4π solid-angle 'hermetic' acceptance, but lack high-precision tracking close to the interaction point; the ability to discriminate between pions, kaons and protons; and full instrumentation in the forward region: all of which are crucial for fully exploiting the quark-flavour physics potential of a hadron collider. Nevertheless, for studies where muons in the final state can be triggered on, several measurements of interesting quantities in b-hadron physics have been performed by both ATLAS and CMS, although the precision on the combination of these measurements from ATLAS, CMS, and LHCb, are, with a few exceptions, dominated by the LHCb measurements [31–34] (see, for example, the measurements of the weak phase ϕ_s and the B_s^0 decay width in Fig. 3.5). Various upgrades were performed on both detectors in the first Long Shutdown that will see them become more competitive in this regard, for Run 2 and beyond, particularly given that the integrated luminosity relative to LHCb will continue to increase [35, 36].

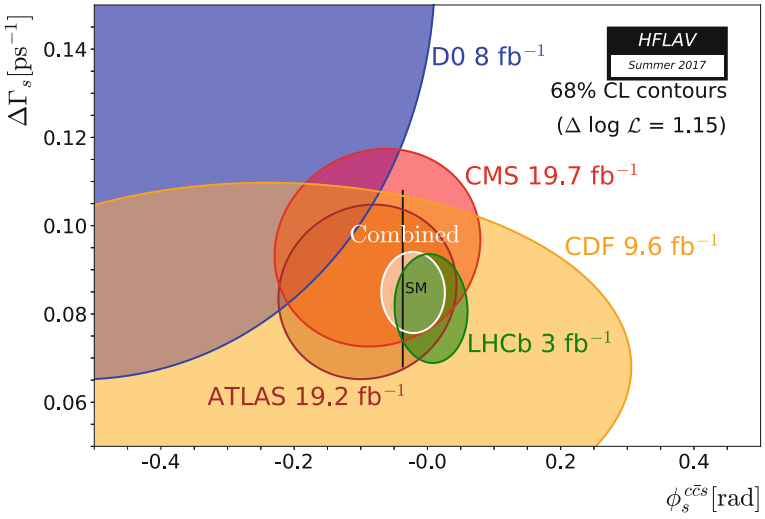

Fig. 3.5 Combination by the Heavy Flavour Averaging Group of measurements of ϕ_s, the *CP* violating weak phase difference between B_s^0 mixing and decay in $b \to c\bar{c}s$ decays (approximately equal to $2\beta_s$ in the Standard Model), versus the B_s^0 decay width, $\Delta\Gamma_s$ [14]. This is one of the few quantities where measurements have been made by all of ATLAS, CMS, LHCb, and the two Tevatron experiments, CDF and D0

The ALICE experiment is a specialised experiment that operates primarily when the LHC is in the proton-ion or ion-ion collision configuration, being optimised for studying the high multiplicity final states produced when these nuclei collide. Much of the ALICE physics programme is concentrated on the nature of the dense quark-gluon plasma of free partons that forms in the high matter-density created in these collisions, and more generally of the phenomenon of confinement in QCD [37].

The LHCb experiment was optimised to study decays of b- and c-hadrons, however thanks to the forward angular acceptance and flexible trigger programme, various other high-precision measurements can be made that are complementary to the regions probed by the ATLAS and CMS experiments [38, 39]. Most of the physics that LHCb studies involves searching for indirect signatures of BSM physics via precision measurements of quark-flavour physics observables, such as CP-asymmetries, angular observables, and CKM unitarity triangle parameters [40]. A more in-depth description of the LHCb detector and its physics programme can be found in Chap. 4.

References

1. F. Marcastel, CERN's Accelerator complex. La chaîne des accélérateurs du CERN
2. L. Evans, P. Bryant, L.H.C. Machine, J. Instrum. **3**, S08001 (2008)
3. F. Follin, D. Jacquet, Implementation and experience with luminosity levelling with offset beam, in *Proceedings of the ICFA Mini-Workshop on Beam-Beam Effects in Hadron Colliders (BB2013)*: (CERN, Switzerland, 2014), pp. 183–187. 18–22 March 2013. https://doi.org/10.5170/CERN-2014-004.183, arXiv:1410.3667. [183(2014)]
4. L. Rossi, Superconductivity: Its role, its success and its setbacks in the large hadron collider of CERN. Supercond. Sci. Technol. **23**, 034001 (2010)
5. E.D. Courant, M.S. Livingston, H.S. Snyder, The strong-focusing synchroton - a new high energy accelerator. Phys. Rev. **88**, 1190 (1952). https://doi.org/10.1103/PhysRev.88.1190
6. S. Baird, Accelerators for pedestrians; rev. version. https://cds.cern.ch/record/1017689, http://CERN-AB-Note-2007-014.PS-OP-Note-95-17-Rev-2, CERN-PS-OP-Note-95-17-Rev-2
7. M. Lamont, Status of the lhc. J. Phys.: Conf. Ser. **455**, 012001 (2013)
8. LHCb, R. Aaij et al., Measurement of $\sigma(pp \to b\bar{b}X)$ at $\sqrt{s} = 7$ TeV in the forward region. Phys. Lett. **B694**, 209 (2010). https://doi.org/10.1016/j.physletb.2010.10.010, arXiv:1009.2731
9. A.D. Martin, W.J. Stirling, R.S. Thorne, G. Watt, Parton distributions for the LHC. Eur. Phys. J. C **63**, 189 (2009). https://doi.org/10.1140/epjc/s10052-009-1072-5. arXiv:0901.0002
10. E. Norrbin, T. Sjostrand, Production and hadronization of heavy quarks. Eur. Phys. J. C **17**, 137 (2000). https://doi.org/10.1007/s100520000460. arXiv:hep-ph/0005110
11. ATLAS, G. Aad et al., Measurement of the flavour composition of dijet events in pp collisions at $\sqrt{s} = 7$ TeV with the ATLAS detector. Eur. Phys. J. **C73**(2), 2301 (2013). https://doi.org/10.1140/epjc/s10052-013-2301-5, arXiv:1210.0441
12. N. Cartiglia, Measurement of the proton-proton total, elastic, inelastic and diffractive cross sections at 2, 7, 8 and 57 TeV. arXiv:1305.6131
13. BABAR collaboration, B. Aubert et al., Measurement of the $e^+e^- \to b\bar{b}$ cross section between $\sqrt{s} = 10.54$ and 11.20 gev. Phys. Rev. Lett. **102**, 012001 (2009). https://doi.org/10.1103/PhysRevLett.102.012001
14. Y. Amhis et al., Averages of b-hadron c-hadron, and τ-lepton properties as of summer 2016. arXiv:1612.07233
15. The ALICE collaboration, T. A. collaboration,, The ALICE experiment at the CERN LHC. J. Instrum. **3**, S08002 (2008)

16. The ATLAS collaboration, G. Aad et al., The ATLAS collaboration, The ATLAS Experiment at the CERN Large Hadron Collider. J. Instrum. **3**, S08003 (2008)
17. The CMS collaboration, The CMS collaboration, The CMS experiment at the CERN LHC. JINST **3**, S08004 (2008). https://doi.org/10.1088/1748-0221/3/08/S08004
18. LHCb collaboration, A.A. Alves Jr. et al., The LHCb detector at the LHC. JINST **3**, S08005 (2008). https://doi.org/10.1088/1748-0221/3/08/S08005
19. ATLAS, G. Aad et al., Observation of a new particle in the search for the standard model higgs boson with the ATLAS detector at the LHC. Phys. Lett. **1**, B716 (2012). https://doi.org/10.1016/j.physletb.2012.08.020, arXiv:1207.7214
20. CMS, S. Chatrchyan et al., Observation of a new boson at a mass of 125 GeV with the CMS experiment at the LHC. Phys. Lett. **B716**, 30 (2012). https://doi.org/10.1016/j.physletb.2012.08.021, arXiv:1207.7235
21. ATLAS, CMS, G. Aad etal., Measurements of the Higgs boson production and decay rates and constraints on its couplings from a combined ATLAS and CMS analysis of the LHC pp collision data at $\sqrt{s} = 7$ and 8 TeV. arXiv:1606.02266
22. CMS, V. Khachatryan et al., Precise determination of the mass of the Higgs boson and tests of compatibility of its couplings with the standard model predictions using proton collisions at 7 and 8 TeV. Eur. Phys. J. **C75**(CMS–HIG–14–009, CERN–PH–EP–2014–288 212), 00 (2015). https://doi.org/10.1140/epjc/s10052-015-3351-7, arXiv:1412.8662
23. ATLAS, G. Aad et al., Study of the spin and parity of the Higgs boson in diboson decays with the ATLAS detector. Eur. Phys. J. **C75**(10), 476 (2015). https://doi.org/10.1140/epjc/s10052-015-3685-1, https://doi.org/10.1140/epjc/s10052-016-3934-y. arXiv:1506.05669. [Erratum: Eur. Phys. J.C76,no.3,152(2016)]
24. ATLAS, G. Aad et al., Determination of spin and parity of the Higgs boson in the $WW^* \to e\nu\mu\nu$ decay channel with the ATLAS detector. Eur. Phys. J. **C75**(5), 231 (2015). https://doi.org/10.1140/epjc/s10052-015-3436-3, arXiv:1503.03643
25. ATLAS, G. Aad et al., Measurements of Higgs boson production and couplings in the four-lepton channel in pp collisions at center-of-mass energies of 7 and 8 TeV with the ATLAS detector. Phys. Rev. **D91**(1), 012006 (2015). https://doi.org/10.1103/PhysRevD.91.012006, arXiv:1408.5191
26. CMS, V. Khachatryan et al., Observation of the diphoton decay of the Higgs boson and measurement of its properties. Eur. Phys. J. **C74**(10), 3076 (2014). https://doi.org/10.1140/epjc/s10052-014-3076-z, arXiv:1407.0558
27. ATLAS, CMS, A. Cakir, Searches for beyond standard model physics at the LHC: Run1 summary and Run2 Prospects. PoS **FPCP2015**, 024 (2015). arXiv:1507.08427
28. ATLAS, G. Aad et al., Summary of the ATLAS experiment's sensitivity to supersymmetry after LHC Run 1 – interpreted in the phenomenological MSSM. JHEP **10**, 134 (2015). https://doi.org/10.1007/JHEP10(2015)134, arXiv:1508.06608
29. ATLAS, CMS, K. Beernaert, Top-quark properties at the LHC, in *51st Rencontres de Moriond on QCD and high energy interactions* (La Thuile, Italy, 2016) 19–25 March 2016. arXiv:1605.05493
30. ATLAS, CMS, A. de Cosa, LHC results for dark matter from ATLAS and CMS, in *Proceedings of the 12th Conference on the Intersections of Particle and Nuclear Physics (CIPANP 2015)*, Vail, USA, 19–24 May 2015. arXiv:1510.01516
31. LHCb collaboration, R. Aaij et al., Measurement of B_s^0 violation and the $B_s^0 \to$ meson decay width difference with $B_s^0 \to J/\psi K^+K^-$ and $B_s^0 \to J/\psi\pi^+\pi^-$ decays. Phys. Rev. **D87**, 112010 (2013). https://doi.org/10.1103/PhysRevD.87.112010, arXiv:1304.2600
32. CMS, V. Khachatryan et al., Measurement of the CP-violating weak phase ϕ_s and the decay width difference $\Delta\Gamma_s$ using the B $_s^0 \to J/\psi\phi$ (1020) decay channel in pp collisions at $\sqrt{s} = 8$ TeV. Phys. Lett. **B757**, 97 (2016). https://doi.org/10.1016/j.physletb2016.03.046, arXiv:1507.07527
33. ATLAS, G. Aad et al., Time-dependent angular analysis of the decay $B_s^0 \to J/\psi\phi$ and extraction of $\Delta\Gamma_s$ and the CP-violating weak phase ϕ_s by ATLAS. JHEP **12**, 072 (2012). https://doi.org/10.1007/JHEP12(2012)072, arXiv:1208.0572

34. CMS and LHCb collaborations, V. Khachatryan et al., Observation of the rare $B_s^0 \to \mu^+\mu^-$ decay from the combined analysis of CMS and LHCb data. Nature **522**, 68 (2015). https://doi.org/10.1038/nature14474, arXiv:1411.4413
35. C. collaboration, Technical proposal for the upgrade of the CMS detector through 2020. http://cdsweb.cern.ch/search?p=CERN-LHCC-2011-006.LHCC-P-004&f=reportnumber&action_search=Search&c=LHCb+Reports. CERN-LHCC-2011-006. LHCC-P-004
36. Letter of Intent for the Phase-I Upgrade of the ATLAS Experiment. http://cdsweb.cern.ch/search?p=CERN-LHCC-2011-012.LHCC-I-020&f=reportnumber&action_search=Search&c=LHCb+Reports. CERN-LHCC-2011-012. LHCC-I-020
37. J. Schukraft, Heavy-ion physics with the ALICE experiment at the CERN Large Hadron Collider. Philos. Trans. R. Soc. Lond. A: Math. Phys. Eng. Sci. **370**, 917 (2012). https://doi.org/10.1098/rsta.2011.0469
38. W. Barter, A brief review of measurements of electroweak bosons at the LHCb experiment in LHC Run 1. Submitted to: Mod. Phys. Lett. (2016). arXiv:1607.08499
39. LHCb, D. Johnson, Electroweak physics and QCD at LHCb, in *Proceedings of the 50th Rencontres de Moriond, QCD and high energy interactions* (La Thuile, Italy, 2015), pp. 221–224. 21-28 March 2015. arXiv:1506.09106
40. T. Gershon, M. Needham, Heavy flavour physics at the LHC. Comptes Rendus Physique **16**, 435 (2015). https://doi.org/10.1016/j.crhy.2015.04.001. arXiv:1408.0403

Chapter 4
The LHCb Detector

The LHCb detector, located at Point 8 on the Large Hadron Collider, is a forward-arm spectrometer designed primarily for the investigation of b- and c-hadron decays, which, when produced in the $pp \to b\bar{b}X(c\bar{c}X)$ process, are predominantly distributed in the high pseudorapidity *forward* region. High-precision tracking close to the interaction point results in exceptional identification of b- and c-hadron decay vertices, and a ring-imaging Cherenkov detector allows excellent separation of different types of charged particles, enabling measurements of suppressed fully-hadronic final states. Nevertheless, the general purpose configuration of the sub-detectors and trigger system allows for a wide variety of physics measurements to be performed.

This chapter describes the LHCb detector and software configuration during Run 1 of the LHC, during which data corresponding to an integrated luminosity of $1.0\,\text{fb}^{-1}$ in 2011 and $2.0\,\text{fb}^{-1}$ in 2012 was collected. This comprises the data sample analysed in the latter part of this thesis.

4.1 Introduction

The LHCb detector is a single-arm spectrometer with a forward angular coverage from approximately 15–300 (250) mrad in the bending (non-bending) plane of the magnet, a schematic of which can be seen in Fig. 4.1. This angular coverage is motivated by the observation that at high energies, production of b- and $\bar{b}$-quarks are highly correlated, such that they are produced predominantly in the same forward or backward cone. The angular distribution of b-quarks can be seen in Fig. 4.2, with the LHCb acceptance indicated in red. This is advantageous with respect to the e^+e^- B-factories, as the significantly larger Lorentz boost results in an enhanced decay-time resolution.

Whilst the instantaneous luminosity of the LHC reached $1 \times 10^{34}\,\text{cm}^{-2}\,\text{s}^{-1}$ in Run 1, LHCb operated with collisions at a reduced instantaneous luminosity of

© Springer Nature Switzerland AG 2018

D. O'Hanlon, *Studies of* CP-*Violation in Charmless Three-Body* b-*Hadron Decays*,
Springer Theses, https://doi.org/10.1007/978-3-030-02206-8_4

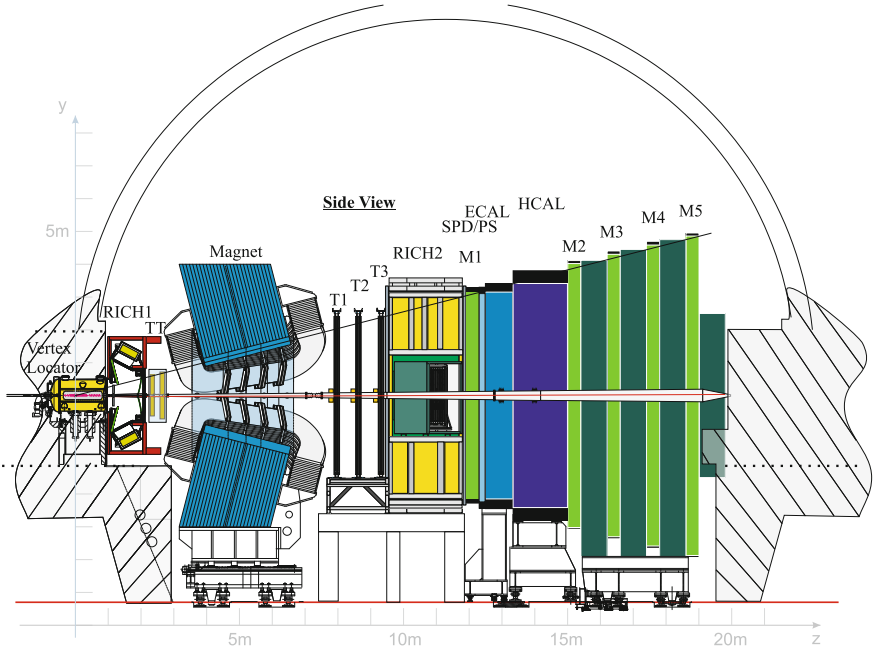

Fig. 4.1 The LHCb detector layout, with the positive z- (beam) axis going from left to right, the positive y-axis going from bottom to top, and the positive x-axis going into the page [1]

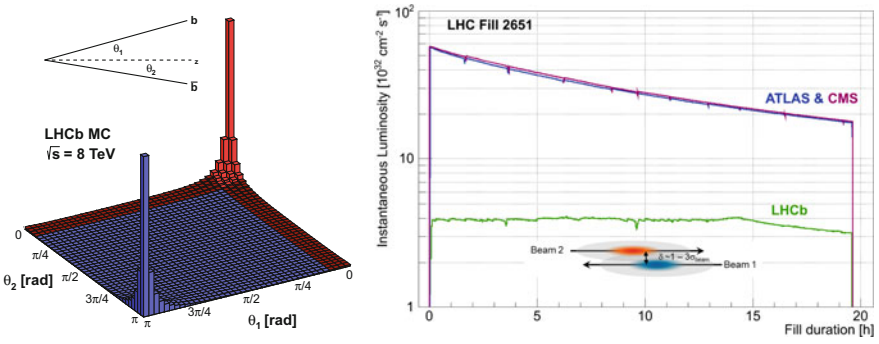

Fig. 4.2 Left: Distribution of b or $\overline{b}$ quarks produced using Pythia 8 [2] and the CTEQ6 NLO parton density functions [3], with a centre-of-mass energy of 8 TeV. The LHCb angular acceptance is indicated in red, corresponding to 27% of b or $\overline{b}$ quarks. Right: ATLAS, CMS, and LHCb integrated luminosity over fill 2651 of May 2012. The difference between the instantaneous luminosities of ATLAS and CMS, and LHCb past 15 h is due to the increased β^* at the LHCb interaction point [4]

a constant $4 \times 10^{32}\,\mathrm{cm}^{-2}\,\mathrm{s}^{-1}$ (about twice the LHCb design luminosity), using a luminosity levelling scheme. This involves colliding the beams off centre such that when protons circulating in the beams are lost due to collimation or collisions, the

offset of the beams can be decreased such that the instantaneous luminosity remains constant. The reduced value of this luminosity is a result of focussing the beams at the interaction point to a lesser degree than at ATLAS and CMS. The instantaneous luminosity over an example fill can be seen in Fig. 4.2. In Run 1 LHCb collected a total integrated luminosity of $3\,\text{fb}^{-1}$, and as of the end of 2016 operations, a total of $2\,\text{fb}^{-1}$ in Run 2.

The reason for the lower instantaneous luminosity compared to ATLAS and CMS is that LHCb is optimised for an average of one visible interaction per bunch-crossing. The trigger and reconstruction algorithms for heavy flavour decays rely on having a low number of *primary* vertices (PVs), the points at which the two protons interact to produce tracks of decay products visible in the detector. As *b*- and *c*-hadrons typically have a long flight-distance (at LHCb B^0 mesons typically fly for some 7 mm before decaying), a crucial signature of a heavy flavour decay is a *secondary* vertex, displaced some distance from the primary vertex. With many primary vertices, identification of primary and secondary vertices becomes time consuming, as all tracks in the region must be reconstructed.

The other reason a reduced luminosity is employed is to reduce the radiation damage to the high precision silicon strip vertex tracker surrounding the *pp* interaction region, the VELO, which during stable LHC beams comes within 7 mm of the beam to provide exceptional primary and secondary vertex resolution. Two ring imaging Cherenkov, RICH, radiation detectors, provide means to identify charged hadron species, and along with the electromagnetic and hadronic calorimeter, and muon system, comprise the particle identification system. This is complemented by the downstream tracking system, which provides high-precision tracking of heavy-flavour decay products.

This general-purpose configuration, along with the flexible trigger configuration, means that the LHCb detector can be utilised for various precision measurements in the forward region. In addition to work on heavy flavour physics, the LHCb collaboration has published analyses on, for example, vector boson production [5], the effective weak mixing angle [6], searches for long-lived exotic particles [7], and on the existence of near-side angular correlations in 5 TeV Pb-Pb collisions [8]. There also exists the possibility of injecting gas into the VELO region (otherwise used to perform luminosity measurements [9]), to measure cross-sections in a 'fixed target' configuration [10].

Information in this Chapter is derived from the LHCb detector paper (Ref. [1]), and other sources where indicated. From these only the salient points with respect to the rest of this thesis are included, and particular attention is given to the Vertex Locator and Ring Imaging Cherenkov detectors, which at the LHC are systems unique to LHCb, and enable the high-precision measurements documented in Chaps. 5 and 7.

4.2 The VELO

The VELO is comprised of two sets of 21 semi-circular modules, positioned on opposite sides of the beam, where the ∼3 cm irregular spacing between each of the modules is optimised to ensure that each track produced within the 300 mrad LHCb acceptance interacts with at least four VELO stations. The modules and the associated read-out electronics are located inside an evacuated cavity surrounding the beams at the interaction point, which replaces the conventional beryllium beam-pipe found upstream and downstream of the VELO, and are separated from the LHC machine vacuum by a 300 μm thick aluminium foil. This foil protects the primary LHC vacuum from possible outgassing from the detector elements, but also protects the detector from radio-frequency interference from the beam.

The modules are physically moved into the nominal data-taking position by a set of stepper motors when 'stable beams' are declared by the LHC control centre, but otherwise are stored 30 mm away from the beam axis to prevent damage whilst the beam profile is large during injection and ramping. During stable beams, the VELO modules are then moved to within 7 mm of the beam axis, where the beam position has to be determined each time this operation is performed, as the LHC machine does not guarantee the location of the beam axis to the precision required of the VELO module positioning. This procedure is carried out in a series of small steps, where at each step the beam condition monitors are checked to ensure that: the reported fluence is less than 5% of the dump threshold; the total silicon bias is less than 1000 μA above the dark current; and that the beam x and y position is consistent from the independent measurements using the each of the two VELO sides. This monitoring is continued once the VELO modules are completely closed.

Each sensor module (see Fig. 4.3) is composed of two sets of silicon strip detectors, known as R (radial) and Φ (azimuthal) sensors, which have silicon strips oriented orthogonal to each other, to resolve both the r and ϕ position of the track in the cylindrical VELO reference frame. The inter-strip pitch of these detectors varies from approximately 40–100 μm across the sensor. When brought together during stable beams, these modules are designed to overlap slightly, such that full coverage can be maintained. As the modules operate in a vacuum (and to mitigate radiation induced degradation), the VELO silicon and readout electronics are cooled using a bi-phase CO_2 system to around $-10\,^{\circ}C$.

These sensors are read out by analogue front-end application specific integrated circuits (ASICs), known as Beetle chips, located on the VELO modules. These sample events at the LHC bunch crossing frequency and store them in a 160 event pipeline waiting for the L0 trigger decision. When a positive trigger decision is received, these pipelines are read out to TELL1 field programmable gate array (FPGA) data acquisition (DAQ) boards located in the counting rooms outside the radiation zone.

The precise determination of primary and secondary vertices is essential to identify heavy quark decays and reduce background. For a typical event with 25 reconstructed tracks in the VELO associated with the primary vertex, the associated vertex resolution is 13.5 μm in the x position, 12.5 μm in the y position, 90 μm in the z position,

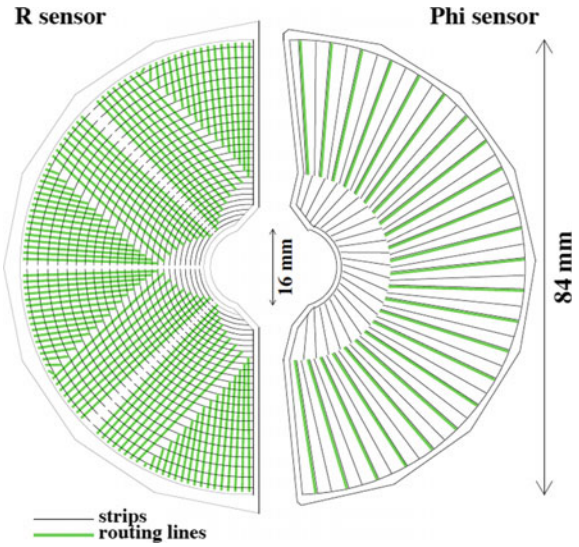

Fig. 4.3 Schematic of a VELO R and Φ sensor, looking along the beam axis

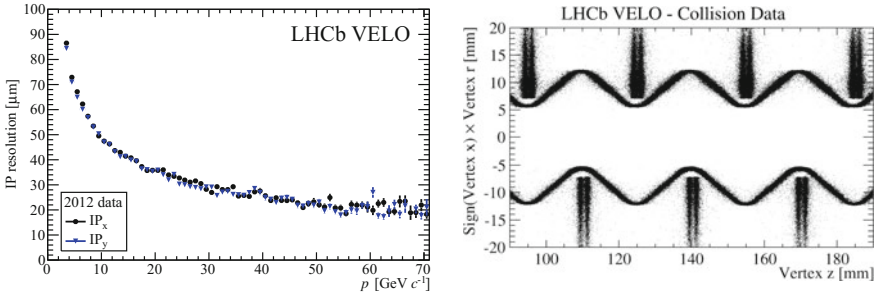

Fig. 4.4 Left: VELO impact parameter (IP) resolution versus track momentum. Right: Distribution of $r - z$ projected secondary vertices in collision data, as reconstructed by the VELO. In this figure, the RF foil (horizontal band) and VELO sensor modules (vertical bands) are clearly visible [11]

which gives the LHCb VELO world-leading resolution. The impact parameter (IP) resolution, the resolution on the distance-of-closest approach of a track produced at a secondary vertex extrapolated to a primary vertex, in the x and y axes versus the track momentum can be seen in Fig. 4.4 (left). The precision of the VELO is highlighted by imaging the VELO geometry and RF foil via reconstructed secondary vertices in collision data, produced using beam protons interacting with gas in the VELO, which can be seen in Fig. 4.4 (right).

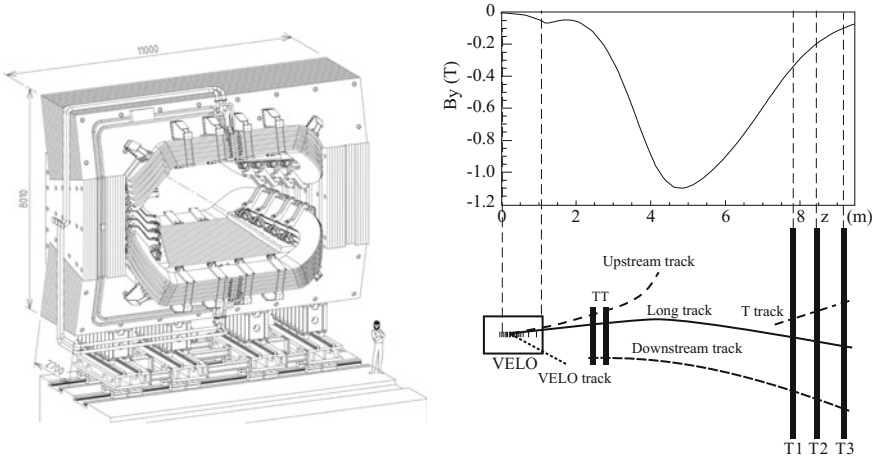

Fig. 4.5 Left: Schematic of the LHCb warm dipole magnet (looking upstream). Right: Magnetic field along the z-axis of the detector, with corresponding sub-detector z-positions indicated

4.3 The Magnet

The LHCb magnet (Fig. 4.5, left) is a warm dipole, capable of generating an inhomogeneous magnetic field corresponding to an integrated bending power of 4 Tm over a track length of 10 m, and is situated downstream of the VELO, RICH1, and TT, and upstream of the rest of the sub-detectors. In the presence of this magnetic field, charged particles experience a corresponding perpendicular force, the degree of which is determined by their momentum. The 4 Tm bending power allows a relative precision on the momentum of around 0.5% for tracks up to 200 GeV.

The magnet consists of two trapezoidal coils inside a 1.5 kT rectangular flux return yoke, mounted on the repurposed DELPHI[1] mounting apparatus. The magnet coils themselves were designed to fit within the relatively restrictive confines of the LHCb detector cavern, whilst minimising the stray magnetic field impinging on the photomultiplier tubes of the RICH1 and RICH2 sub-detectors. Another useful design feature is that the polarity of the magnet can be switched, such that when averaging over the entire data set charged tracks interact equally with each side of the detector, which is useful for minimising systematic effects in CP violation measurements [12].

To achieve the required momentum resolution, the total integrated magnetic field must be known to a few parts in 10^{-4}, and the position of the B field peak known to within a few millimetres. The mapping of the magnetic field has been performed in all dimensions, and the projection of the y-component of field as a function of z can be seen in Fig. 4.5 (right).

[1] The 'Detector with Lepton, Photon, and Hadron Identification' (DELPHI) experiment on the Large Electron Positron collider previously inhabited the cavern at Point 8.

The operation of the LHCb dipole magnet (and that of the ALICE experiment) has a significant effect on the LHC proton beams, and is corrected with compensator magnets such that no unwanted bunch interactions occur. In particular, by design the bunch-crossing at Interaction Point 8 is in the horizontal axis, the same as the LHCb dipole magnet. When the dipole polarity is switched, the crossing angle is modified, and all of the LHC collimator and beam condition monitors need to be re-validated, as well as altering the LHCb interaction region. This is particularly problematic at injection where there is higher beam emittance, and for 25 ns bunch-spacing where there are no gaps in the bunch structure to avoid parasitic collisions. For 2012 operations it was decided that the bunch crossing at Interaction Point 8 be rotated, to be more in the vertical axis, resulting in a diagonal luminosity levelling plane with respect to the beam orbits, which mitigates these issues without the need to power down the LHCb dipole at injection [13].

4.4 The Tracking Stations

The LHCb general purpose tracking system consists of four tracking stations in addition to the VELO: the Tracker Turicensis (TT) upstream of the magnet, and three stations downstream, each consisting of an inner (IT) and outer (OT) tracker.

4.4.1 Tracker Turicensis

The TT consists of four layers of silicon microstrip sensors with an inter-strip pitch of around 200 μm, with the interior two layers rotated $-5°$ and $+5°$ relative to the first and last layers. This strip pitch ensures a single hit resolution of 50 μm. All four layers are housed in a light-tight, thermally and electrically insulated volume, cooled to below 5 °C, which is continually flushed with nitrogen to prevent condensation.

The four detector layers are arranged in pairs, spaced approximately 27 cm apart in z, which aids reconstruction. The layout of one of the layers can be seen in Fig. 4.6 (left), and where each layer covers the full LHCb angular acceptance at this z location. Adjacent vertical modules within a layer are staggered by approximately 1 cm in z and a few millimetres in x to ensure coverage. The detector enclosure consists of two pieces, one each side of the beam-pipe, which are mounted on rails to facilitate easy access to the detector when not operational.

Similar to the VELO, the front-end readout is performed by Beetle ASICs at the LHC bunch-crossing frequency, the amplified signal is passed through digitiser cards, and then via optical fibre to TELL1 DAQ boards in the counting house.

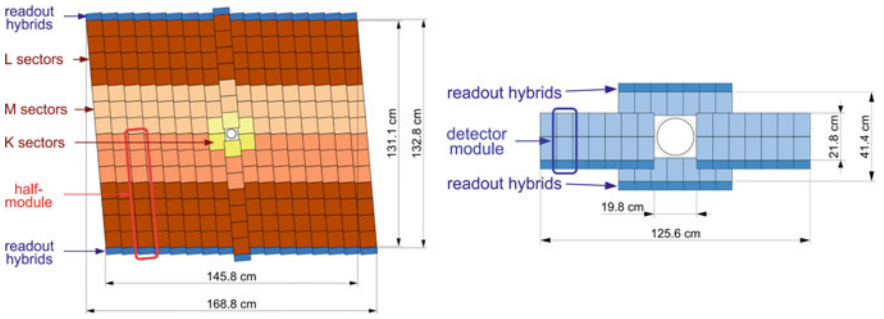

Fig. 4.6 Left: Schematic of Tracker Turicensis layer. Right: Schematic of the four modules comprising a Inner Tracker layer

4.4.2 Inner Tracker

The design of the IT is very similar to that of the TT, and occupies the central region of the downstream tracking stations (a layer of which can be seen in Fig. 4.6, right), where the track multiplicity is expected to be the highest. Each IT assembly consists of four light-tight boxes, consisting of four layers of silicon microstrip detectors, arranged as seven modules, which are staggered in z by 4 mm and overlap in x by 3 mm to ensure coverage and facilitate the relative alignment of the modules. Readout electronics and the readout pipeline are also similar to that of the TT.

4.4.3 Outer Tracker

The outer tracking volume in each tracker layer, which sees a lower proportion of the event activity than the inner tracker (designed for less than 10% occupancy at a luminosity of $2 \times 10^{32}\,\mathrm{cm}^{-2}\,\mathrm{s}^{-1}$), consists of two staggered layers of straw-tube drift chambers. The gas contained within these tubes is ionised by the passage of a charged particle, and the charge is collected by an anode in the centre of the tube. The time taken for the charge to reach the anode upon application of a current gives a measure of the relative position of the charged particle track within the tube. Each tube has an inner diameter of 4.9 mm, and contains a mixture of 70% Ar, 28.5% CO_2, and 1.5% O_2 in order to guarantee sub-50 ns drift time and a drift-coordinate resolution of 200 μm [14].

Each of the three stations consists of four modules, the first and last vertically oriented, and the inner modules oriented at $-5°$ and $+5°$ with respect to the vertical. The entire OT detector consists of 55 000 straw-tube channels, representing 12 sets of double-layered 2.4 m long tubes. Readout is performed with the ASDBLR amplifier chip, originally designed for use on the ATLAS transition radiation tracker, the output

of which is fed into an drift-time digitisation ASIC. The digitised signal is then transmitted by optical fibre to a set of TELL1 boards in the counting house.

During Run 1, a drift time resolution of less than 3 ns, and an average single-hit efficiency of well over 99% [14] per module was achieved.

4.5 The RICH Detectors

The Ring Imaging Cherenkov (RICH) detectors at LHCb enable differentiation of charged particle species. This permits the reduction of the more copiously produced pion backgrounds from kaon and proton final states, and also allows the separation of topologically similar final states produced in b-hadron decays.

The detectors themselves utilise the phenomenon of Cherenkov radiation: When a charged particle moves through a dielectric material it causes a momentary polarisation, which results in emission of photons as the medium immediately relaxes back to the ground state. If the velocity of the particle is less than the speed of the light in the medium the emission is isotropic and results in no far-field radiation. However, when a particle is travelling faster than the phase velocity of light in the medium, the medium is no longer polarised uniformly, and therefore a dipole is formed which releases electromagnetic radiation along the 'shock front' of the moving charge.

There is a simple relation between the angle, θ_c, of the Cherenkov light produced, relative to the axis of particle propagation,

$$\cos\theta_c = \frac{1}{n\beta}, \tag{4.1}$$

where n is the refractive index of the material, and $\beta = v/v_c$, the velocity of the particle, v, relative to the phase velocity of light in the medium, v_c. The momentum of the particle, as reconstructed by the tracking system, can be then used to allow particles of different masses to be discriminated by their Cherenkov angle.

Two such detectors are utilised within LHCb: RICH1 (Fig. 4.7, left) upstream of the magnet, between the VELO and TT, and RICH2 (Fig. 4.7, right) downstream of the magnet, between the tracking stations and the first muon station. In order to have sufficient Cherenkov photon production across the full 2–100 GeV track momentum range, multiple radiating materials, with different refractive indices for 400 nm photons, are used. In RICH1, both silica aerogel[2] (an ultra-low-density solid with a refractive index of 1.030), and gaseous C_4F_{10} (with a refractive index of 1.0014) are present, which cover the momentum range from 2 GeV to around 70 GeV. The second, RICH2, contains gaseous CF_4 (with a refractive index of 1.0005),[3] and

[2]The aerogel has been removed for Run 2 operations as it did not improve low-momentum performance as much as predicted. Its removal results in fewer uninformative Cherenkov photons, speeding up reconstruction, and a larger C_4F_{10} volume.

[3]A 5% by volume addition of CO_2 to quench scintillation was introduced during Run 1 operations [15].

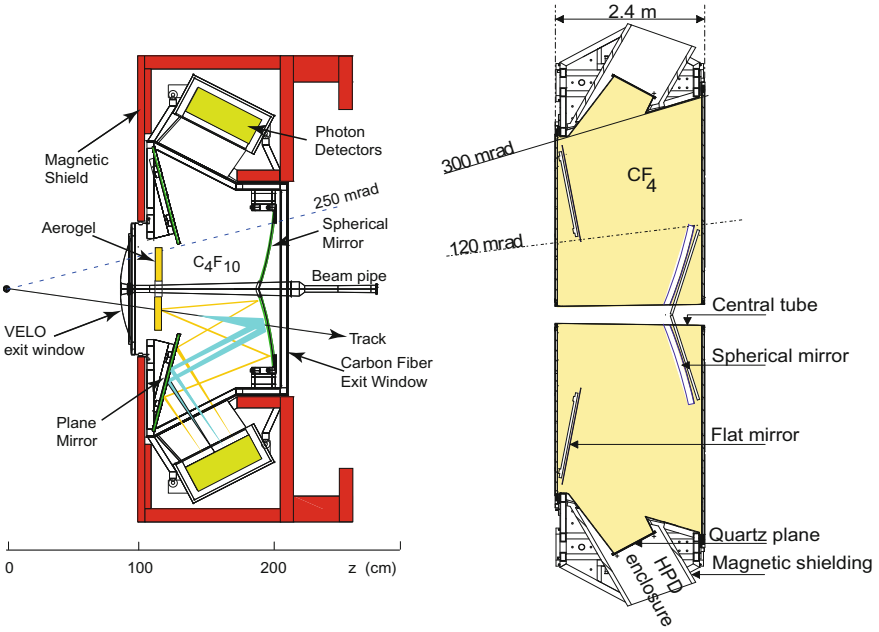

Fig. 4.7 Schematic of the RICH1 (left) and RICH2 (right) sub-detectors, indicating the presence of the spherical and plane mirrors

covers the momentum range from 16 to 100 GeV. For the C_4F_{10} radiator in RICH1, the distribution of Cherenkov angles for various particle species can be seen in Fig. 4.8 (left).

An ensemble of spherical and plane mirrors reflect the Cherenkov light on to arrays of hybrid photon detectors (HPDs) outside of the LHCb angular acceptance. These arrays of HPDs (196 in RICH1, 288 in RICH2) are separated from the detector gas volume by anti-reflection coated quartz windows. For $\beta \approx 1$, the expected photon yield from C_4F_{10} is around 16, for aerogel around 5, and for CF_4 around 14, and therefore single-photon sensitivity is required.

The mirror assembly results in the Cherenkov photons forming approximately circular rings on the HPDs. The likelihood for a particular configuration of HPD hits is calculated as a function of Cherenkov angle by solving a quartic equation for the angle between the Cherenkov photon emission and reflection points [17]. This likelihood can therefore be re-computed for each particle species for each track. However, to ensure that this can be calculated online, only likelihoods relative to the pion hypothesis are calculated. A greedy iterative procedure is performed, where the track with the greatest change in the likelihood has its hypothesis fixed at each iteration, and is continued until no significant increase in the likelihood is observed, and results in the RICH reconstruction time being quadratic rather than exponential in the number of tracks, with negligible efficiency loss.

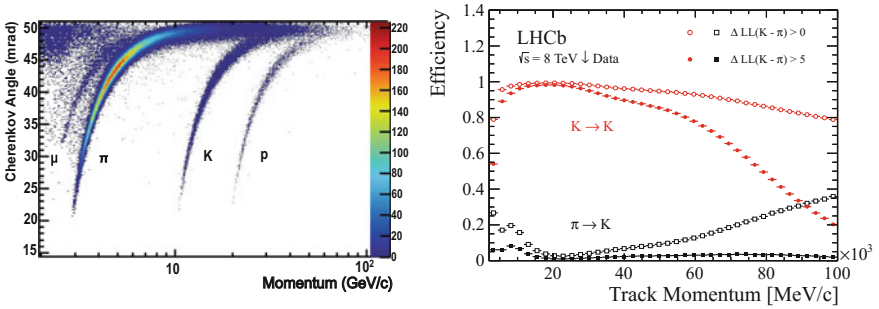

Fig. 4.8 Left: Cherenkov light angle versus track momentum in the RICH1 C_4F_{10} radiator for isolated tracks, where the various charged particle species are indicated [16]. Here it can be seen that at higher momentum (~ 20 GeV), separation by Cherenkov angle in this radiator alone becomes difficult. Right: Kaon identification and pion mis-identification efficiency as a function of track momentum for magnet down 2012 collision data, for two requirements on the difference in the particle hypothesis log-likelihoods. Below the aerogel Cherenkov threshold ($\sim$2 GeV), particles are assumed to be pions and the kaon efficiency is zero by construction

The relative likelihood can be used to quantify the relative confidence between two particle hypotheses. The kaon identification and $\pi \rightarrow K$ mis-identification efficiency can be seen in Fig. 4.8 (right), as a function of the track momentum [16]. In addition to these likelihood variables, there are also likelihood variables that include information from the calorimeters and muon stations, and variables that are derived from a neural network one-versus-all training that are more flexible.

4.6 The Calorimeters

The electromagnetic, ECAL (Fig. 4.9, left), and hadronic, HCAL (Fig. 4.9, right), calorimeters exist to identify and measure the energy of particles that primarily produce electromagnetic or hadronic showers, respectively, when impinging on a dense material. The calorimeters are arranged such that particles that initially shower electromagnetically have deposited the majority of their energy in the ECAL before reaching the HCAL. Calorimeters are essential to reconstruct decays with a photon or neutral pion in the final state, such as $B^0 \rightarrow K^{*0}\gamma$ or $B^0 \rightarrow \pi^+\pi^-\pi^0$ decays, and decays that feature high momentum electrons that radiate a copious number of photons via bremsstrahlung. Another important requirement of the calorimeters is to identify high transverse-energy (E_T) hadrons that are likely to originate from the decay of a b-hadron and communicate this information to the level-0 trigger decision unit.

Upstream of the ECAL and HCAL are the single-layer pre-shower (PS) and scintillating pad detectors (SPD), which are present to identify deposits from charged hadrons in the ECAL using ionisation energy loss, and whether the particle is neutral

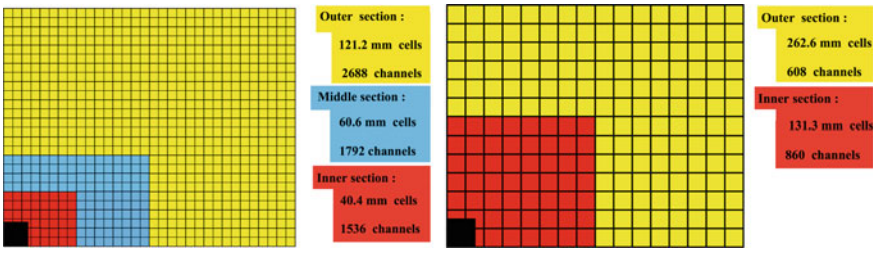

Fig. 4.9 Left: Schematic of SPD, PS and ECAL scintillating pads within a layer. Right: Schematic of HCAL scintillating pad regions

or charged (for example, to determine whether an ECAL deposit is due to an electron or photon), respectively, and are separated by a 15 mm layer of lead. This information used by the L0 trigger to efficiently determine which calorimeter cells to read-out, and, in the case of the PC, the energy measurement of which is combined with the measurement from the ECAL.

Each of these calorimeters operate on the sample principle: a hadronic or electromagnetic shower is initiated, and the resulting scintillation light within the calorimeter volume transmitted to photomultipliers via wavelength shifting fibres. The PS, SPD, and ECAL are separated into three regions (inner, middle, and outer), each with a different cell size, according to the expected occupancy of each region, governed by the expected the shower size. The HCAL is separated into just two regions, inner and outer.

4.6.1 Pre-shower and Scintillating Pad Detectors

The scintillating pads of the SPD and PS detectors are read out by wavelength shifting fibres to multi-anode photomultiplier tubes. Each channel is read out at the bunch crossing frequency and stored in a pipeline, awaiting the L0 decision. A ten bit ADC is required for the PS detector, whereas a single bit is all that is necessary for the SPD, as this simply indicates whether a charged particle traversed the cell. The SPD/PS consists of 12032 channels, with segmentation equal to those of the ECAL to ensure one-to-one correspondence. This segmentation results in 3072 inner cells, 3584 middle cells, and 5376 outer cells, with cell areas of approximately $4 \times 4\,\text{cm}$, $6 \times 6\,\text{cm}$, and $12 \times 12\,\text{cm}$, respectively (this can be seen in Fig. 4.9, left).

4.6.2 Electromagnetic Calorimeter

The ECAL consists of alternating tiles of 2 mm thick lead and 4 mm thick scintillator material, in the z and transverse axes (this is known as the 'shashlik' configuration). The 66 layers of this assembly results in a 42 cm deep stack corresponding to 25

radiation lengths, with a Molière radius (the radius of the cylinder containing 90% of the shower energy) of 3.5 cm. The ECAL is designed to give an energy resolution of $\sigma_E/E = 10\%/\sqrt{E[\text{GeV}]} \oplus 1\%$, and achieves an inclusive $\pi^0 \to \gamma\gamma$ resolution of 8 MeV after calibration [18].

4.6.3 Hadronic Calorimeter

The HCAL uses similar scintillating tiles to those of the ECAL, but orients them parallel to the beam axis. The longitudinal configuration consists of 3 scintillating tiles interspersed with 3 iron plates, each of 20 mm in the longitudinal direction. The detector contains 216 of these, alternating iron and scintillator in the transverse direction, with a scintillator thickness of 3 mm and an iron thickness of 7 mm, corresponding to a thickness of 2 cm per two modules. Hence this also follows the 'shashlik' configuration of interspersed absorber and active material.

The depth of the HCAL, whilst larger than the ECAL to accommodate the larger hadronic showers, is limited by the overall size of the LHCb detector to around 5.6 nuclear interaction lengths. Nevertheless, only high energy showers are lost, which does not impact the primary purpose of the HCAL in identifying high energy hadrons for the L0 trigger. This larger shower size is also reflected in the cell size of the HCAL, which can be seen in Fig. 4.9 (right), as less granularity is required. This configuration results in the HCAL having a design energy resolution of $\sigma_E/E = 69\%/\sqrt{E[\text{GeV}]} \oplus 0.9\%$.

4.7 The Muon Stations

Detection of muons is essential for much of the LHCb physics programme, as many leptonic and semi-leptonic b- and c-hadron decays are sensitive to beyond the Standard Model effects. Muons are also used to tag the decay flavour of b-hadrons for oscillation studies. As such, the muon system is required to perform excellent identification of muons offline, and provide online information to the L0 trigger.

The LHCb muon system is comprised of five stations, which can be seen in Fig. 4.10. One of these is located upstream of the calorimeters, and the rest are located downstream of the calorimeters, interspersed with 80 cm thick iron absorbers. The total absorber thickness from the first muon station, M1, to the last muon station, M5, is approximately 20 interaction lengths, which results in the minimum momentum of muon detected in M5 being around 6 GeV.

The location of M1, before the calorimeters, is in order to provide higher resolution muon p_{T} measurements. Stations M2 and M3 also have high spatial resolution in x, whereas M4 and M5 have limited spatial resolution and exist primarily to indicate penetrating particles. The segmentation of M1 can be seen in Fig. 4.10, where each region is separated into logical pads. For stations M2 and M3, the number of pad-

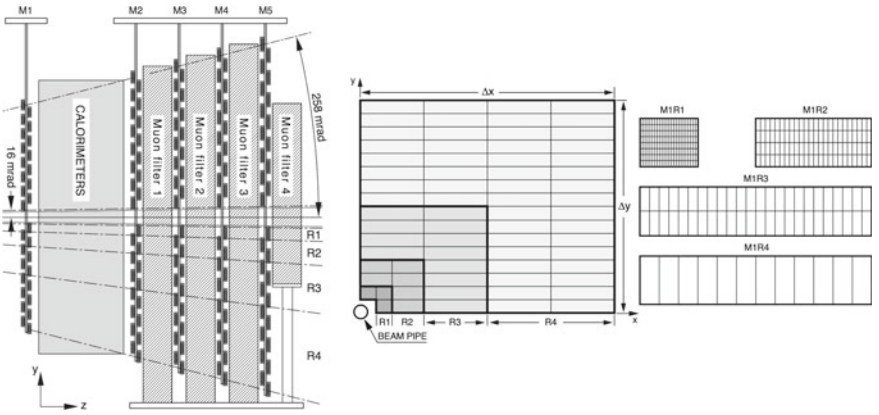

Fig. 4.10 Left: Schematic of the muon stations as viewed from above. Right: Schematic of the four regions comprising each muon station

columns per chamber is doubled, whereas for M4 and M5 this is halved. In each case, the number of pad-rows is the same, and the full system consists of 1380 chambers.

With the exception of the inner region of M1, the muon system is constructed from multiwire proportional chambers (MWPC). The inner region of M1, the region that has the highest occupancy, is constructed from triple gaseous-electron-multipliers (GEMs). To ensure a time resolution of 5 ns, the MWPCs use a wire plane spacing of 2 mm symmetrically placed in a gas-gap of 5 mm, and a gas mixture of Ar, CO_2, and CF_4, in a ratio of 40 : 55 : 5, respectively. The intersection of a horizontal and vertical strip defines a logical pad, where the regions with the highest resolution near the beam-pipe contain 8 horizontal and 6 vertical strips, which changes to 4 horizontal and 24 vertical strips for the regions furthest from the beam-pipe.

For the inner region of M1, M1R1, triple-GEM detectors with an active area of $20 \times 24\,\text{cm}^2$ are used. Each of the 12 chambers that comprise this region consist of two superimposed triple-GEM detectors, logically OR-ed. In these detectors, three foils are separated by a gas mixture. A charged particle passing through the gas creates ionisation electrons, which drift to the next foil, producing more electrons, which finally drift to an anode to produce an amplified signal. A time resolution of around 3 ns is achieved by a gas mixture of Ar, CO_2, and CF_4, in a ratio of 45 : 15 : 40, respectively.

The muon system is read out by front end CARDIAC boards, which perform amplification, shaping and discrimination of the chamber signals, as well as time alignment to correct for differing cable lengths, to remain synchronous with the bunch crossing rate. The data are read out to off-detector-electronics boards which tag the bunch crossing identifier, and route the data to trigger processors and TELL1 boards in the counting house via optical fibre.

In Run 1, performance corresponding to a muon identification efficiency of 93% at a hadron mis-identification efficiency of 0.6% was achieved [19].

4.8 The Trigger

The LHCb detector utilises a hardware level-0 (L0) trigger, which operates synchronously with the LHC bunch-crossing rate (a maximum of 40 MHz at design, although in practice this was lower in Run 1 with a 50 ns bunch-spacing), and two software high-level triggers (HLT1 and HLT2). As the production cross-section for b-hadrons is some 200 times lower than the total cross-section at LHC centre-of-mass energies, significant work has to be carried out in the trigger to identify decays of interest and reduce the rate of background with negligible impact on signal efficiency.

The L0 trigger requires an event with high E_{T} from one of the calorimeters or high p_{T} from the muon system in order to reduce the output rate to the 1 MHz at which the detector can be read out. High multiplicity events are rejected using the SPD system, to avoid swamping the HLT with large numbers of charged tracks. At 1 MHz, in HLT1, some reconstruction can be performed in the VELO and muon system, where tracks that have hits matched in both are fully reconstructed. VELO tracks are used to identify the PV and whether the tracks have a large impact parameter (IP) - the distance of closest approach to the PV - indicating that they are the product of a displaced secondary vertex. In HLT2, where the input rate is reduced to 40 kHz by HLT1, full event reconstruction is performed.

4.8.1 L0

The calorimeter L0 decision unit computes the transverse energy deposited in 2×2 cell clusters, using only cells in the same region. This transverse energy is defined as

$$E_{\mathrm{T}} = \sum_{i=1}^{4} E_i \sin\theta_i, \tag{4.2}$$

where E_i is the energy deposited in cell i, and θ_i is the angle between the z-axis and a line passing from the the mean position of the pp interaction envelope to the centre of the cell. From these clusters, `L0Hadron`, `L0Photon`, and `L0Electron` candidates are formed. The E_{T} of these clusters is compared to fixed thresholds, and events where at least one cluster passes these thresholds are retained by the L0 trigger. Typical E_{T} thresholds during Run 1 were $E_{\mathrm{T}} > 3.5$ GeV for `L0Hadron`, $E_{\mathrm{T}} > 2.5$ GeV for `L0Photon`, and $E_{\mathrm{T}} > 2.5$ GeV for `L0Electron`, along with a limit on the SPD multiplicity of 600 in each case.

The dedicated L0 muon trigger requires hits in all five muon stations. The p_{T} of the highest and second-highest p_{T} muons is passed to the L0 decision unit, where these are compared to a threshold for the highest p_{T} (`L0Muon`) or the product of the highest and the second highest p_{T} (`L0DiMuon`). During Run 1, typical thresholds for these were around $p_{\mathrm{T}} > 1.5$ GeV for `L0Muon`, and $\sqrt{p_{\mathrm{T}}^{\text{largest}} \times p_{\mathrm{T}}^{\text{2nd largest}}} > 1.3$ GeV for `L0DiMuon`, with a limit on the number of SPD hits of 600 and 900, respectively.

4.8.2 High Level Trigger

At 1 MHz, HLT1 can perform VELO reconstruction and impose requirements in order to reduce the data rate entering HLT2, where a full event reconstruction is performed. In HLT1, VELO tracks are matched to tracks in the downstream tracking stations and a Kalman fit is performed. Restrictions can then be placed on the track fit χ^2 such that the rate entering HLT2 is approximately 40 kHz.

All analyses described in this thesis make use of the `Hlt1TrackAllL0` HLT1 line, designed to select hadron decays that are significantly displaced from a primary vertex. This line puts loose requirements on the number of hits in the tracking stations for each track, the track impact parameter from the primary vertex, and the reconstructed secondary vertex quality, along with requirements on the track p and p_{T}. The exact values of these requirements can be seen in Ref. [20].

In HLT2, full reconstruction is performed on all candidates passing HLT1, and therefore the selections can be more flexible. Two types of trigger line are introduced at this stage: exclusive, which are optimised for specific final states or families thereof; and inclusive, where only generic topological requirements are imposed on the final state. The generic topological lines are primarily implemented via a novel *bonsai* boosted decision-tree (BBDT) algorithm [21], where the tree structure has been optimised to be efficient enough to run in real-time in the trigger and robust enough to be invariant under detector calibration conditions. Additional requirements are applied on reconstructed decays that feature certain particles, such as long lived Λ baryons or K^0_{S} mesons, and a full list of these can be found in Ref. [22].

4.8.3 Offline Reconstruction

Reconstruction is re-performed offline, with significantly looser requirements on the tracks and calorimeter clusters and their matching to the signal candidate (reconstructed tracks from an example event can be seen in Fig. 4.11). As such, discrepancies may arise between online and offline quantities and candidates, however this has little impact on the physics analyses presented in this thesis. For Run 2 operations this distinction has been removed, as online reconstruction is identical to that performed offline, and in some cases no additional offline reconstruction is performed (see Sect. 4.10).

'Long' tracks, tracks that traverse the full tracking system, are identified either by associating hits between a track extrapolated from the VELO and a single hit in the 'T' (IT or OT) tracking stations, or by matching VELO track segments with track segments formed in the T stations using a separate pattern matching algorithm. These tracks are then associated with tracks in the TT to improve the momentum determination. 'Downstream' tracks, tracks that are formed with hits only from the tracking stations downstream of the VELO, are identified by forming track segments in the T stations and matching these with hits in the TT.

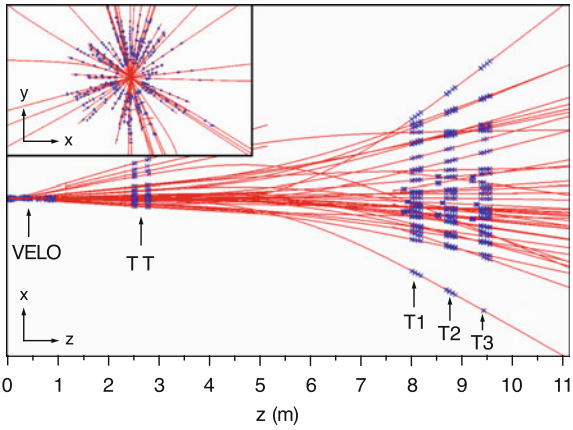

Fig. 4.11 Reconstructed tracks (red curves) and their corresponding hits in the VELO and downstream tracking stations (blue crosses) for an example event. The inset shows the VELO region for the same event, looking upstream [4]

Both types of tracks are then fitted with a Kalman filter, taking into account multiple scattering and ionisation energy losses, and resulting in a track state vector as a function of z position. In addition, the fit χ^2 is determined as a measure of track consistency. These tracks are post-processed with algorithms that determine whether two tracks have a sub-section in common, where only the track with the best χ^2 is kept, and whether a track is the result of spurious associations with 'ghost' track segments that do not correspond to a real particle traversing the trackers.

4.8.4 Efficiency Determination

Reconstructed decay candidates (and individual tracks, in the case of L0 and HLT1) can be associated with objects that result in trigger decisions. Those candidates that result in a particular trigger firing (i.e., the criteria are met for the event to pass a certain trigger requirement), are known as 'trigger on signal' (TOS) with respect to that trigger line. Candidate decays that are present in an event where one or more trigger lines fire independently of the candidate decay are known as 'trigger independent of signal' (TIS), with respect to the trigger lines in question. As it is possible for for an event to fire multiple triggers, it is not uncommon for a candidate to be TOS and TIS with respect to different trigger lines.[4]

To associate a signal track with a calorimeter object, the track is extrapolated to the z-plane of the calorimeter, and the cell intersected by the track and its eight neighbours are considered 'signal' cells. If any `L0Hadron/Photon/Electron` cluster arises from these cells, the cluster is associated with the track. If two out of the three hits recorded by M1-3 by the `L0Muon` candidate are shared with an offline

[4]There are also candidates that are 'trigger on both', where neither the presence of the candidate decay nor the rest of the event is sufficient individually to fire a trigger. Such candidates are rejected however, as the trigger efficiency is not measurable.

track, then this track is associated with the trigger object. For the HLT, at least 70% of the hits in a sub-detector (60% for the muon system) are required to be coincident with the track in question in order to be associated with that track.

Distributions of decays that fire the trigger (are TOS), are often highly biased by the trigger acceptance thresholds, and therefore it is of importance to understand the effect that the trigger has on these distributions. A data-driven efficiency method can be obtained via the TISTOS method [23]. This uses events which are TOS with respect to a trigger of interest and TIS with respect to any other trigger. Under the assumption that these TOS and TIS trigger decisions are uncorrelated, the unbiased TOS efficiency of a trigger line is given by

$$\epsilon_{\text{TOS}} = \frac{N_{\text{TIS \& TOS}}}{N_{\text{TIS}}}, \tag{4.3}$$

where $N_{\text{TIS \& TOS}}$ is the number of candidates that are TOS with respect to the trigger in question and TIS with respect to any other, and N_{TIS} is the number of candidates that are TIS with respect to the same TIS trigger in the numerator. The 'TIS' trigger can be, for example, the logical OR of all L0 physics lines, `L0Global`, or an individual trigger line.

4.9 Software, Simulation and Computing

In addition to the hardware and trigger system of the LHCb detector, there is also considerable software infrastructure that is necessary for the analysis of LHCb data.

4.9.1 Simulation

The use of simulated or *Monte-Carlo* (MC) data is an integral part of almost every analysis performed in particle physics. One can generate what signal would be observed in the detector given some physical process, a description of the detector and read-out chain, and some analysis procedure for identifying that signal. This information can then be used to determine efficiencies, set limits on speculative processes, study systematic uncertainties, constrain background yields and shapes, and investigate potential biases.

In the LHCb *Gauss* framework, simulated data is produced using a chain of specialised programs [24, 25]. The first step in the chain is the event generation, where the result of generic 7 and 8 TeV pp interactions are produced using *Pythia 8* [2]. This first simulates the result of the 'hard' process by using parton distribution functions that describe the relative composition of the protons as a function of the momentum of the incoming proton, and generates outgoing partons. These partons generate showers which eventually form colour neutral hadron 'strings', due to QCD

confinement. These strings then fragment into the primary hadrons. At LHCb the last part of this procedure is often repeated many times until a desired b- or c- hadron is produced. This hadron is then decayed using *EvtGen* [26] according to either a set of user specified intermediate states or via branching fractions according to the Particle Data Group (PDG) tables [27].

The result of this event generation process is then passed to the GEANT4 [28, 29] LHCb detector simulation, where the propagation of all generated particles and their interaction with the detector material is simulated. This simulated detector is read out using *Boole*, which simulates the various data acquisition electronics present in the real LHCb detector. Events are reconstructed using *Brunel*, and the L0 and high-level triggers are simulated by the *Moore* package. Both the reconstruction and trigger software are identical in simulation to those used in data-taking.

4.9.2 The Worldwide LHC Computing Grid

The *Worldwide LHC Computing Grid* was designed for the processing and storage requirements of the approximately 50 petabytes (PB) of data generated annually by the LHC experiments, and consists of thirteen 'tier-1' sites that provide several PB each of redundant data-storage capacity, connected to the central CERN 'tier-0' data-centre by 10 Gbps fibre-optic links. In addition to these storage nodes there are also around 100 smaller 'tier-2' sites connected via high-speed public network links, which along with the tier-1 sites provide compute nodes used for physics analysis and simulation. As of the end of 2016, these resources totalled 334 PB of storage and 620 000 logical CPU cores, around 10% of which are allocated for LHCb use.

At LHCb, the Grid is used for the storage of collision data and MC, centralised pre-selection (stripping) campaigns and MC productions, and the execution of user analysis jobs [30].

4.9.3 Stripping

To avoid the CPU-time consuming processes of each user analysis running over all raw collision data files, and the storage cost of saving multiple copies of the same event, LHCb implements a centralised pre-selection procedure known as *stripping*.

These analyst or physics working group specified selections, *stripping lines*, are run in bulk over the raw data, and the candidates that are flagged as passing one or more lines are duplicated into a user accessible area. Many of these selection algorithms save only information pertaining to the signal event to conserve storage space. Such pre-selections are also applied to centrally produced MC. In addition to this, it is possible to generate MC such that events not passing a specific stripping line are discarded, which helps to conserve storage space for large MC production

requests. This is known as *filtered* MC, which is utilised in the analysis of the $B^+ \to \pi^+\pi^+\pi^-$ decay in Chap. 7.

4.9.4 `PIDCalib`

Charged particle identification is essential to the LHCb physics programme, however the efficiency of the RICH detectors in particular is not well replicated by MC (this is mostly due to being highly correlated with the event multiplicity, which is not well replicated by the event generators). This necessitates a data-driven calibration method – `PIDCalib` [31]. This calibration is performed using high statistics control modes that can be reliably identified without the use of the PID system: $D^{*+} \to D^0(K^-\pi^+)\pi^+$, for pions and kaons, where the Cabbibo favoured decay of the D^0 or $\overline{D}^0$ is tagged by the charge of the slow pion from the flavour-specific D^{*+} decay; proton samples are derived from $\Lambda \to p\pi^-$ decays, where final states consistent with $K^0_S \to \pi^+\pi^-$ are vetoed, supplemented by a comparatively small sample of inclusive $\Lambda_c^+ \to pK^-\pi^+$ decays for high momentum tracks; and electron and muon samples are derived from inclusive $J/\psi \to \mu^+\mu^-$, e^+e^- decays, with the efficiency calculated using the tag-and-probe method (Fig. 4.12).

The invariant mass distribution of these data samples are fitted to extracts Weights [33], in order to perform background subtraction, and then binned into variables that are correlated with PID efficiency (usually p, p_T, and the number of reconstructed tracks in the event). The desired PID requirements are then applied to these data and the efficiency can be extracted on a per-bin basis.

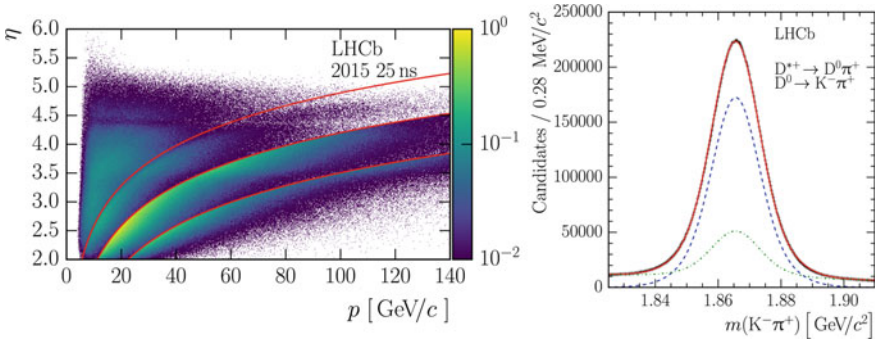

Fig. 4.12 Particle identification calibration samples for 2015 Run 2 data [32]. Left: Proton calibration sample distribution in momentum and pseudorapidity, where the red bands indicate the boundaries between different high-level trigger lines optimised for each region. Right: Invariant mass distribution of the $D^{*+} \to D^0(K^-\pi^+)\pi^+$ decay used for pion and kaon calibration samples, where the dashed lines indicate the components of the D^0 signal model

4.9.5 Decay Tree Re-fitting

In order to execute as fast as possible, the online reconstruction does not assume anything about the particle content of the decay being reconstructed. However, when applying the requirements from the trigger and some loose pre-selection, it is possible to re-fit the entire decay chain according to specific intermediate and final-state particle hypotheses. In doing so, improved resolution on the intermediate decay vertices and unconstrained invariant masses can be obtained.

In LHCb, this fit is performed with the 'Decay tree fitter' algorithm [34], which applies a Kalman filter to iteratively re-fit the entire decay chain. This makes use of internal constraints, such as the requirement that decay products originate from the same vertex, but also the exact external mass constraints, which are implemented into the Kalman filter by the method of Lagrange multipliers. This is of particular use in decays involving a photon or neutral pion, where conventional unconstrained fitting is not possible. Re-fitted decay chains with the incorrect mass hypothesis also result in a decrease in the vertex fit quality, which can be exploited to reject background of this kind.

In addition to improving the mass resolution for 'cascade' decays (such as the decays described in Chap. 5 that involve an intermediate $\Lambda \to p\pi^-$ decay), a b-hadron mass constraint ensures that in fits to quasi-two-body decay amplitudes in the Dalitz plot (such as those described in Chap. 7), all decays exist within the kinematic boundaries.

4.10 LHC Run 2

Several improvements to LHCb operations were made in preparation for Run 2, particularly with respect to the HLT. Although all of the analysis presented in this thesis is on Run 1 data, these are briefly summarised here. From the beginning of Run 2, the HLT2 operates completely asynchronously with respect to HLT1 (which still operates synchronously with the LHC bunch crossing frequency). This is to utilise the LHC machine availability more effectively: due to the depletion of protons in the beam, stable beam conditions for more than around 12 h at nominal operating luminosity becomes inefficient for the ATLAS and CMS detectors, and as such the beams are usually dumped before this.[5] The time taken to ramp down the magnets, re-inject protons from the SPS, ramp the magnets back up again, and optimise the bunch crossings, is around an hour at the fastest, assuming that no machine studies or repairs have to be performed. Further downtime is a result of 'technical stops' where experiment maintenance is performed. As such, in 2016 the LHC was only in 'stable beams' for around 40% of the total time (although this was close to 80% in July). If HLT2 was required to run synchronously, the rest of the time the 50 000 logical CPUs of the Event Filter Farm would be idle, and as such buffering a fraction

[5] Fill 5045 in June 2016 was the longest on record so far at over 37 h.

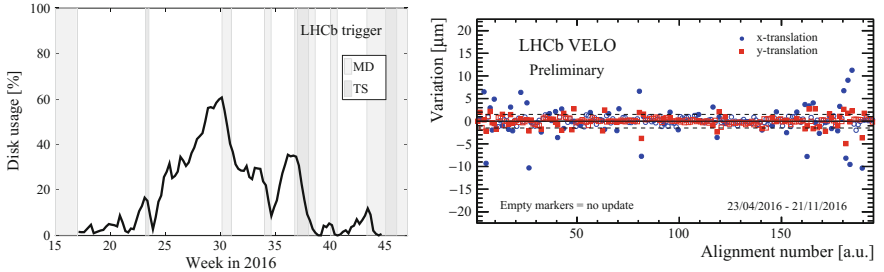

Fig. 4.13 Left: Asynchronous high-level trigger disk buffer utilisation as a percentage of the total capacity during 2016 operations. Right: VELO alignment status for fills in 2016, where markers indicate the difference between the VELO alignment constants of the current and previous fill

of the data to local disk results in a significantly higher effective throughput. The total occupancy of these buffers for 2016 operations can be seen in Fig. 4.13.

Another advantage of deferring HLT2 reconstruction is that calibration and alignment of the sub-detectors can be performed online at the beginning of a fill and immediately applied to the reconstructed data. This obviates the need to perform these operations offline after the fact, and allows accurate reconstruction in HLT2, which ultimately improves the quality of the trigger decisions. The fill-by-fill VELO alignment operation status for 2016 operations can be seen in Fig. 4.13 [35].

The quality of the HLT2 reconstruction is such that many physics analyses on high statistics modes, where the trigger ultimately limits the efficiency, can be performed within HLT2. Online reconstruction results in these high-rate channels being able to save only the signal candidates to disk, reducing storage requirements. This has resulted in publications in 2015 and 2016 where limited offline post-processing was required [36]. Furthermore, selections for calibration data samples, such as those for `PIDCalib`, are also applied in HLT2, which increases the retention rate of these data sets, but also allows correct particle ID efficiencies to be calculated for physics analysis modes present in HLT2.

References

1. LHCb collaboration, A.A. Alves Jr. et al., The LHCb detector at the LHC. JINST **3**, S08005 (2008). https://doi.org/10.1088/1748-0221/3/08/S08005
2. T. Sjöstrand, S. Mrenna, P. Skands, A brief introduction to PYTHIA 8.1. Comput. Phys. Commun. **178**, 852 (2008). https://doi.org/10.1016/j.cpc.2008.01.036, arXiv.org/abs/0710.3820
3. J. Pumplin et al., New generation of parton distributions with uncertainties from global QCD analysis. JHEP **07**, 012 (2002). https://doi.org/10.1088/1126-6708/2002/07/012. arXiv:hep-ph/0201195
4. LHCb collaboration, R. Aaij et al., LHCb detector performance. Int. J. Mod. Phys. A **30**, 1530022 (2015). https://doi.org/10.1142/S0217751X15300227, arXiv:1412.6352

5. LHCb collaboration, R. Aaij et al., Measurement of forward W and Z boson production in pp collisions at $\sqrt{s} = 8$ TeV. JHEP **01**, 155 (2016). https://doi.org/10.1007/JHEP01(2016)155, arXiv:1511.08039
6. LHCb collaboration, R. Aaij et al., Measurement of the forward-backward asymmetry in $Z/\gamma^* \to \mu^+\mu^-$ decays and determination of the effective weak mixing angle. JHEP **11**, 190 (2015). https://doi.org/10.1007/JHEP11(2015)190, arXiv:1509.07645
7. LHCb collaboration, R. Aaij et al., Search for long-lived heavy charged particles using a ring-imaging Cherenkov technique at LHCb. Eur. Phys. J. **C75**, 595 (2015). https://doi.org/10.1140/epjc/s10052-015-3809-7, arXiv:1506.09173
8. LHCb collaboration, R. Aaij et al., Measurement of two-particle correlations in proton-ion collisions at $\sqrt{s_{NN}} = 5$ TeV. Phys. Lett. **B762**, 473 (2016). https://doi.org/10.1016/j.physletb.2016.09.064, arXiv:1512.00439
9. LHCb collaboration, R. Aaij et al., Precision luminosity measurements at LHCb. JINST **9**, P12005 (2014). https://doi.org/10.1088/1748-0221/9/12/P12005, arXiv:1410.0149
10. LHCb collaboration, Measurement of j/ψ and D^0 production in pAr collisions at $\sqrt{s_{NN}} = 110$ GeV. LHCb-CONF-2017-001, http://cdsweb.cern.ch/search?p=LHCb-CONF-2017-001&f=reportnumber&action_search=Search&c=LHCb+Conference+Contributions
11. R. Aaij et al., Performance of the LHCb vertex locator. JINST **9**, P09007 (2014). https://doi.org/10.1088/1748-0221/9/09/P09007. arXiv:1405.7808
12. M. Vesterinen, Considerations on the LHCb dipole magnet polarity reversal. LHCb-PUB-2014-006. On behalf of the LHCb collaboration, http://cdsweb.cern.ch/search?p=LHCb-PUB-2014-006&f=reportnumber&action_search=Search&c=LHCb+Reports
13. B.J. Holzer, R. Versteegen, R. Alemany, Vertical crossing angle in IR8. CERN-ATS-Note-2013-024 PERF, http://cdsweb.cern.ch/search?p=CERN-ATS-Note-2013-024PERF&f=reportnumber&action_search=Search&c=LHCb+Reports
14. R. Arink et al., Performance of the LHCb outer tracker. JINST **9**, P01002 (2014). https://doi.org/10.1088/1748-0221/9/01/P01002. arXiv:1311.3893
15. T. Blake, Quenching the scintillation in CF_4 cherenkov gas radiator. Nucl. Instrum. Methods Phys. Res. Sect. A Accel. Spectrom. Detect. Assoc. Equip. **791**, 27 (2015). https://doi.org/10.1016/j.nima.2015.04.020
16. M. Adinolfi et al., Performance of the LHCb RICH detector at the LHC. Eur. Phys. J. C **73**, 2431 (2013). https://doi.org/10.1140/epjc/s10052-013-2431-9. arXiv:1211.6759
17. R.W. Forty, O. Schneider, RICH pattern recognition. LHCb-98-040, http://cdsweb.cern.ch/search?p=LHCb-98-040&f=reportnumber&action_search=Search&c=LHCb+Reports
18. R. Aaij et al., Performance of the LHCb calorimeters. LHCb-DP-2013-004, in preparation
19. F. Archilli et al., Performance of the muon identification at LHCb. JINST **8**, P10020 (2013). https://doi.org/10.1088/1748-0221/8/10/P10020. arXiv:1306.0249
20. R. Aaij et al., The LHCb trigger and its performance in 2011. JINST **8**, P04022 (2013). https://doi.org/10.1088/1748-0221/8/04/P04022. arXiv:1211.3055
21. V.V. Gligorov, M. Williams, Efficient, reliable and fast high-level triggering using a bonsai boosted decision tree. JINST **8**, P02013 (2013). https://doi.org/10.1088/1748-0221/8/02/P02013. arXiv:1210.6861
22. A. Puig, The LHCb trigger in 2011 and 2012, http://cdsweb.cern.ch/search?p=LHCb-PUB-2014-046&f=reportnumber&action_search=Search&c=LHCb+Reports
23. S. Tolk, J. Albrecht, F. Dettori, A. Pellegrino, Data driven trigger efficiency determination at LHCb. LHCb-PUB-2014-039. CERN-LHCb-PUB-2014-039, http://cdsweb.cern.ch/search?p=LHCb-PUB-2014-039.CERN-LHCb-PUB-2014-039&f=reportnumber&action_search=Search&c=LHCb+Reports
24. M. Clemencic, The LHCb simulation application, Gauss: design, evolution and experience. J. Phys. Conf. Ser. **331**, 032023 (2011). https://doi.org/10.1088/1742-6596/331/3/032023
25. G. Corti et al., How the Monte Carlo production of a wide variety of different samples is centrally handled in the LHCb experiment. J. Phys. Conf. Ser. **664**, 072014 (2015). https://doi.org/10.1088/1742-6596/664/7/072014

26. D.J. Lange, The EvtGen particle decay simulation package. Nucl. Instrum. Meth. **A462**, 152 (2001). https://doi.org/10.1016/S0168-9002(01)00089-4
27. Particle Data Group, C. Patrignani et al., Review of particle physics. Chin. Phys. **C40**, 100001 (2016) (2017 update). https://doi.org/10.1088/1674-1137/40/10/100001, http://pdg.lbl.gov/
28. Geant4 collaboration, S. Agostinelli et al., Geant4: a simulation toolkit, Nucl. Instrum. Meth. **A506**, 250 (2003). https://doi.org/10.1016/S0168-9002(03)01368-8
29. Geant4 collaboration, J. Allison et al., Geant4 developments and applications, IEEE Trans. Nucl. Sci. **53**, 270 (2006). https://doi.org/10.1109/TNS.2006.869826
30. A. Tsaregorodtsev, DIRAC3: the new generation of the LHCb grid software. J. Phys. Conf. Ser. **219**, 062029 (2010). https://doi.org/10.1088/1742-6596/219/6/062029
31. L. Anderlini et al., The PIDCalib package, LHCb-PUB-2016-021, http://cdsweb.cern.ch/search?p=LHCb-PUB-2016-021&f=reportnumber&action_search=Search&c=LHCb+Reports
32. O. Lupton, L. Anderlini, B. Sciascia, V. Gligorov, Calibration samples for particle identification at LHCb in Run 2. LHCb-PUB-2016-005. CERN-LHCb-PUB-2016-005, http://cdsweb.cern.ch/search?p=LHCb-PUB-2016-005.CERN-LHCb-PUB-2016-005&f=reportnumber&action_search=Search&c=LHCb+Reports
33. M. Pivk, F.R. Le Diberder, SPlot: a statistical tool to unfold data distributions. Nucl. Instrum. Meth. **A555**, 356 (2005). https://doi.org/10.1016/j.nima.2005.08.106, arXiv:physics/0402083
34. W.D. Hulsbergen, Decay chain fitting with a Kalman filter. Nucl. Instrum. Meth. **A552**, 566 (2005). https://doi.org/10.1016/j.nima.2005.06.078, arXiv:physics/0503191
35. G. Dujany, B. Storaci, Real-time alignment and calibration of the LHCb detector in Run II, http://cdsweb.cern.ch/search?p=LHCb-PROC-2015-011&f=reportnumber&action_search=Search&c=LHCb+Conference+ProceedingsLHCb-PROC-2015-011
36. R. Aaij et al., Tesla: an application for real-time data analysis in high energy physics, arXiv:1604.05596

Chapter 5
Search for Λ_b^0 and Ξ_b^0 Decays to $\Lambda h^+ h^-$

Charmless hadronic b-baryon decays are of particular interest as they proceed either by tree-level decays involving the CKM matrix element V_{ub} or by loop-induced amplitudes, and are therefore expected to have suppressed decay rates in the Standard Model. Consequently, such decays provide interesting possibilities to search for CP-violation effects, as have been seen in the corresponding b-meson decays [1–5]. Moreover, they may also provide insights into the mechanisms of hadronisation in b-baryon decays.

This chapter details a search for the suppressed decays of a Λ_b^0 or Ξ_b^0 baryon into a Λ baryon and two charged π or K hadrons, with a measurement of the branching fractions of the Λ_b^0 to the $\Lambda K^+\pi^-$ and $\Lambda K^+ K^-$ final states, along with two of the first searches for CP-violation to be performed in decays of the Λ_b^0 baryon. The work described in this chapter is the subject of a 2016 publication by the LHCb Collaboration [6].

5.1 Introduction

The study and exploitation of b-baryon decays is still in its infancy: Until recently, the main contributions to the knowledge of b-baryon decays came from the Tevatron experiments [7], however small samples sizes have hindered precision measurements. The e^+e^- B-factories operated at centre-of-mass energies below the threshold required to produce b-baryons, and therefore the BaBar and Belle experiments have made no contributions to this area.

Within the LHCb detector acceptance, Λ_b^0 baryons in particular are produced at a rate of around twice that of B_s^0 mesons [8]. With a high pp collision centre-of-mass energy and a large number of b-baryon decays recorded to disk, LHCb is in a prime position to make a significant contribution to this sector, and several important results have recently been published [9–12]. In particular, the first observation of a charmless hadronic three–body decay of a b-baryon, $\Lambda_b^0 \to K_s^0 p\pi^-$, has recently been made [13]. At the time this analysis was published no evidence had previously

© Springer Nature Switzerland AG 2018

D. O'Hanlon, *Studies of* CP-*Violation in Charmless Three-Body* b-*Hadron Decays*,
Springer Theses, https://doi.org/10.1007/978-3-030-02206-8_5

been observed for any Ξ_b decays to a charmless final state, however in late 2016 the LHCb collaboration announced the observation of the decay $\Xi_b^- \to p K^- K^-$ [14].

Here a search is presented for the previously unobserved charmless hadronic three–body decay modes $\Lambda_b^0(\Xi_b^0) \to \Lambda h^+ h'^-$ ($h^{(\prime)} = \pi, K$), the branching fractions of which are determined relative to the precisely measured $\Lambda_b^0 \to \Lambda_c^+(\Lambda \pi^+)\pi^-$ channel, with similar topology to the signal mode. The nominal signal regions, where the reconstructed masses of the b-baryons are within ± 50 MeV of the world-average mass of the Λ_b^0, $m(\Lambda_b^0) = 5619.58 \pm 0.17$ MeV, and Ξ_b^0, $m(\Xi_b^0) = 5791.9 \pm 0.5$ MeV, were not inspected until the selection was finalised, to avoid potentially biasing the measurement of the branching fractions.

Decays throughout this chapter are listed for particles only, with the conjugate mode implied, unless otherwise stated. In the case of the $K^\pm \pi^\mp$ final states, $\Lambda_b^0 \to \Lambda K^- \pi^+$ decays are suppressed with respect to $\Lambda_b^0 \to \Lambda K^+ \pi^-$ decays by at least a factor of $|V_{tb}^* V_{td}|^2$, whereas $\Xi_b^0 \to \Lambda K^+ \pi^-$ decays are suppressed with respect to $\Xi_b^0 \to \Lambda K^- \pi^+$ decays by a similar factor. These suppressed modes are considered negligible in this analysis, and therefore the $\Lambda K^+ \pi^-$ and $\Lambda \pi^+ K^-$ data samples are merged, to allow for a simultaneous fit to the corresponding final states.

This analysis is performed on the LHCb Run 1 collision data sample corresponding to an integrated luminosity of 1 fb^{-1} collected during 2011 with a pp collision energy $\sqrt{s} = 7$ TeV, and 2 fb^{-1} collected during 2012 with $\sqrt{s} = 8$ TeV. Throughout the analysis, much of the optimisation and efficiency calculations are performed using simulated data that has been through the full LHCb detector simulation (MC). Throughout this chapter, the terms 'collision data' and 'simulated data', are used to refer specifically to these data types, while 'data' is used as a collective term. All of the MC used throughout this chapter is of a true b-hadron decay, which is then reconstructed and selected under the assumption that it is one of the signal final states, to replicate the corresponding effect in the collision data.

5.1.1 Motivation

All baryon decays observable at LHCb have a proton in the final state, which tags the flavour of the parent b-baryon. Furthermore, the presence of intermediate charm decays that proceed purely by a $b \to c$ tree transition (therefore having negligible CP-violation), can be used to measure the absolute CP-asymmetry in these decays. Due to conservation of baryon number there can be no b-baryon mixing, and therefore no mixing-induced CP-violation in baryon decays. Hence all CP-violation measurements using baryon decays are of CP-violation in decay.

Charmless modes such as those being searched for in this chapter are good candidates in the search for CP-violation, as the amplitudes of the tree and penguin diagram transitions are expected to be of approximately the same magnitude. It has been noted that $\Lambda_b^0 \to \Lambda \pi^+ \pi^-$ is a potentially interesting channel for a measurement of CP-violation, possibly enhanced by $\rho - \omega$ mixing [15]. It has also been suggested that the $\Lambda_b^0 \to \Lambda h^+ h'^-$ modes (specifically, $\Lambda_b^0 \to \Lambda \pi^+ \pi^-$) are a promising

target for the measurement of triple-product asymmetries [16], which supplements the sensitivity of the integrated *CP* violating rate asymmetries. However, given that these are three-body modes the extra degree-of-freedom obtained from a polarised Λ_b^0 or Λ baryon is required, which is unlikely in practice as the transverse production polarisation of Λ_b^0 baryons in pp collisions has been measured to be negligible [17].

The branching fraction of $\Lambda_b^0 \to \Lambda\,\pi^+\pi^-$ has been predicted using heavy quark effective theory [16], and is expected to be approximately 4×10^{-8}. This is in contrast with the recent studies of the analogous $B^0_{d,s} \to K^0_S h^+ h'^-$ decays [18] where the branching fractions were found to be on the order of 10^{-6}, despite the only difference being the addition of a spectator quark.

In addition to charmless final states, the decay $\Lambda_b^0 \to \Lambda D(K^+\pi^-)$ can be used in a measurement of the weak phase γ [19] (where D represents an admixture of D^0 and $\overline{D}^0$ states) [20, 21]. Therefore, whilst any intermediate D decay is vetoed in the analysis of the charmless modes, the observation of such a decay would be of great interest to a future measurement of γ in baryon decays.

5.1.2 Analysis Strategy

The branching fractions of these modes are measured relative to the $\Lambda_b^0 \to \Lambda_c^+(\Lambda\,\pi^+)\,\pi^-$ decay, where the Λ_c^+ is selected from the inclusive $\Lambda_b^0 \to \Lambda\,\pi^+\pi^-$ dataset. There are several reasons for this:

- Absolute branching fractions cannot be measured precisely at LHCb, as at a hadron collider the integrated luminosity and production mechanism, and therefore the total number of b-hadrons produced, are not sufficiently well known. This is in contrast with the B-factories, where the number and the type of B-mesons, coming from $\Upsilon(4S)$ decays produced by a e^+e^- interaction, can be precisely known.
- With the use of a normalisation mode with the same topology, and moreover, data selected with the same criteria, various systematic uncertainties related to the selection efficiency can be expected to cancel to first order.
- The existence of an intermediate state produced purely by a $b \to c$ tree process, and therefore with negligible *CP*-violation, can be used to cancel asymmetries introduced by the b-baryon production mechanism and the detector reconstruction. Therefore, a measurement of the *CP*-asymmetry of the charmless mode can be made, as documented in Sect. 5.7.

In this analysis, the branching fraction of $\Lambda_b^0(\Xi_b^0) \to \Lambda\,h^+h'^-$ relative to $\Lambda_b^0 \to \Lambda_c^+(\Lambda\,\pi^+)\,\pi^-$ is given by

$$\frac{\mathcal{B}(\Lambda_b^0(\Xi_b^0) \to \Lambda\,h^+h'^-)}{\mathcal{B}(\Lambda_b^0 \to \Lambda_c^+(\Lambda\,\pi^+)\,\pi^-)} = \frac{N_{\Lambda_b^0(\Xi_b^0)\to\Lambda\,h^+h'^-}}{N_{\Lambda_b^0\to\Lambda_c^+(\Lambda\,\pi^+)\,\pi^-}} \times \frac{\epsilon_{\Lambda_b^0\to\Lambda_c^+(\Lambda\,\pi^+)\,\pi^-}}{\epsilon_{\Lambda_b^0(\Xi_b^0)\to\Lambda\,h^+h'^-}}, \tag{5.1}$$

where, for each mode, $\mathcal{B}$ denotes the branching fraction, ϵ denotes the detection efficiency, and N is the raw event yield. In the case of the Ξ_b^0 decays, this quantity is implicitly multiplied by the currently undetermined ratio of production fractions for the Ξ_b^0 and Λ_b^0 baryons, $f_{\Xi_b^0}/f_{\Lambda_b^0}$, the relative probability that a b-quark hadronises into a Ξ_b^0 or Λ_b^0.

There are several complications in this analysis related to the evaluation of the efficiencies. The signal modes are three–body decays, of which the decay dynamics cannot be determined *a priori* as the decays are unobserved. The efficiencies will depend on intermediate resonances that decay to Λh and h^+h^-, however the MC generated assumes that events are distributed flat in the square Dalitz-plot definition of the phase-space (a description of this can be found in Sect. 6.6.2). Therefore, for decays where a signal is observed, the efficiencies need to be determined on an event-by-event basis, depending on the observed phase-space distribution.

Both the signal and normalisation decays contain a long-lived Λ baryon, which often does not decay within the volume of the vertex locator surrounding the interaction point. As such, the data has to be separated by whether the p and π^- tracks are reconstructed including VELO hits (long tracks), or whether they are reconstructed only with detector hits downstream of the VELO (downstream tracks). These downstream-downstream (DD) or long-long (LL) reconstructed Λ particles have different efficiencies – DD tracks tend to have higher momentum, but lower reconstruction efficiency, higher background, and worse mass resolution[1] due to the lack of precise knowledge of the decay vertex from the VELO. As such, candidates in the DD and LL reconstruction categories are treated separately throughout the analysis until the final combination.

Another complication from the presence of a Λ in the decay is that the topological HLT trigger line that is used in the analysis was not initially able to trigger on the daughters of a downstream Λ baryon (or K_s^0 meson) decay. This was updated in the middle of 2012 operations, and resulted in an increase in efficiency as subsequently all four tracks can fire the HLT, although this does not equally affect the signal and normalisation mode due to the differing kinematics. Therefore the 2012 data is split between the early 2012 running period, prior to the update to the HLT during the June technical stop, which is denoted 2012a, and the later 2012 running period, which is denoted 2012b. Efficiencies and yields are determined separately for these, as they are for the DD and LL categories, and the final measurements combined.

To measure the parameter corresponding to the underlying CP-violation, the raw asymmetry of the efficiency-corrected yields has to be corrected for possible detection, $\mathcal{A}_\mathrm{D}$, and production, $\mathcal{A}_\mathrm{P}$, asymmetries, $\mathcal{A}_{CP} = \mathcal{A}_{CP}^\mathrm{raw} - \mathcal{A}_\mathrm{P} - \mathcal{A}_\mathrm{D}$. This can be conveniently achieved with the $\Lambda_b^0 \to \Lambda_c^+(\Lambda\pi^+)\pi^-$ control mode, which is expected to have negligible CP-violation. Since this mode shares the same initial state as the mode of interest, it has the same production asymmetry, and moreover, its final state differs only in the PID requirements. Therefore, most detection asymmetry effects

[1] This is true in general, however due to the low Q-value of the Λ decay this is mitigated by the use of a progressive decay-tree fit using the `DecayTreeFitter` package (see Chap. 4).

also cancel (apart from small differences arising from the differing decay kinematics which can be ignored at this level of precision). Thus,

$$\mathcal{A}_{CP}(\Lambda_b^0 \to \Lambda h^+ h'^-) = \mathcal{A}_{CP}^{\text{raw}}(\Lambda_b^0 \to \Lambda h^+ h'^-) - \mathcal{A}_{CP}^{\text{raw}}(\Lambda_b^0 \to \Lambda_c^+(\Lambda\pi^+)\pi^-)\,. \tag{5.2}$$

5.2 Selection

Data events are pre-processed by the `Lb2V0hh` stripping line, which for collision data was part of the `Bhadron` micro-DST stream.[2] These stripping lines initially assume that the signal decay is $\Lambda_b^0 \to \Lambda\,\pi^+\pi^-$, but are implemented using wide enough mass windows that the final states that arise from a $\pi \to K$ swap can be selected, along with decays to these final states from a Ξ_b^0 baryon. Hence these cuts are formulated in terms of Λ_b^0 baryons and pions, but this does not result in a loss of generality.

It is required that either the `L0Hadron` trigger has been fired by any of the tracks in the signal decay (trigger on signal, TOS) or that any L0 physics trigger line has fired on any other tracks in the event (trigger independent of signal, TIS); that the tracks of candidate b-baryon passes the `Hlt1TrackAllL0` requirements; and that the candidate is selected by either the 'simple' or the boosted decision-tree topological requirements for two, three, or four body decays in HLT2. The 'simple' topological line was removed during 2012, so is only included in the 2011 selection. Events are selected that pass the two or four body topological trigger, despite the signal decays being three body at the reconstruction level. Candidates pass the two-body line, as often true decays have tracks which are too low in momentum to meet the track-level requirements. Long-lived Λ baryons and K_S^0 mesons projected back to the b-hadron production (primary) vertex, PV, are also counted as 'tracks' in HLT2, so these can contribute to a two- or three-body decision. A small efficiency is observed for the four-body line, either from short-lived Λ baryons that do not fly far from the Λ_b^0 vertex, or due to the difference between the online HLT and offline reconstruction, where a different Λ candidate is selected to form the Λ_b^0 signal candidate.

The decay of each candidate b-baryon is reconstructed by combining a Λ candidate with two oppositely charged tracks, and the Λ baryon is reconstructed in the $p\pi^-$ final state, where these tracks must be inconsistent with originating from any PV. The Λ candidate is associated to the PV which gives the smallest χ^2_{IP}. The impact parameter, IP, is defined as the distance between the fitted track and a particular vertex, without the constraint that the track comes from that vertex, and χ^2_{IP} is the difference in fit χ^2 between a vertex reconstructed with and without that track. Significant separation is required between the PV and the b-baryon decay vertex,

[2] To minimise storage space this stream includes only detector hits identified as coming from the signal b-hadron after the full reconstruction, along with specific associated variables such as the vertex isolation information.

Table 5.1 Stripping selection requirements for Λ candidates

Variable definition	Selection requirement
StdLooseLambdaLL	
Mass difference with respect to (w.r.t) nominal Λ mass	$\lvert m_{p\pi} - m_\Lambda \rvert < 35\,\text{MeV}$
χ^2 of Λ vertex fit	$\chi^2_{\Lambda\,\text{vtx}} < 30$
Λ daughter track momentum	$p_{\Lambda\,\text{daug}} > 2\,\text{GeV/c}$
Λ daughter minimum IP χ^2 w.r.t PVs	$\chi^2(\text{IP})_{\text{min}} > 9$
Requirements from Lb2V0hh line on LL Λ candidates	
Mass difference w.r.t nominal Λ mass	$\lvert m_{p\pi} - m_\Lambda \rvert < 15\,\text{MeV}$
χ^2 of Λ vertex fit	$\chi^2_{\Lambda\,\text{vtx}} < 12$
χ^2 separation of Λ vertex and associated PV	$\chi^2_{\Lambda-\text{PV VD}} > 50$
Λ daughter track fit χ^2/ndof	$\chi^2_{\pi\text{trk}}/\text{ndof} < 4$
StdLooseLambdaDD	
Mass difference w.r.t. nominal Λ mass	$\lvert m_{p\pi} - m_\Lambda \rvert < 64\,\text{MeV}$
χ^2 of Λ vertex fit	$\chi^2_{\Lambda\,\text{vtx}} < 25$
Λ daughter track momentum	$p_{\Lambda\,\text{daug}} > 2\,\text{GeV/c}$
Λ daughter minimum IP χ^2 w.r.t PVs	$\chi^2(\text{IP})_{\text{min}} > 4$
Requirements from Lb2V0hh line on DD Λ candidates	
Mass difference w.r.t. nominal Λ mass	$\lvert m_{p\pi} - m_\Lambda \rvert < 20\,\text{MeV}$
χ^2 of Λ vertex fit	$\chi^2_{\Lambda\text{vtx}} < 12$
χ^2 separation of Λ vertex and associated PV	$\chi^2_{\Lambda-\text{PV VD}} > 50$
Λ flight distance from PV	$\Lambda_{FD} > 300\,\text{mm}$
Λ momentum	$p_\Lambda > 8\,\text{GeV/c}$

which is enforced by a requirement on the square of this distance divided by the uncertainty on the distance, χ^2_{VS}.

For each event, the `Lb2V0hh` stripping line first applies a global cut on the number of long tracks, $N_{\text{long}} < 250$, to improve computational performance with a negligible loss in efficiency. Initially, the Λ_b^0 candidates are formed by simple four–momentum addition. These then undergo loose 'combination cuts' (replicated in Table 5.1) to further reduce the number of events that undergo the full vertex fit. Following the vertex fit, further quality cuts ('mother cuts') are made on the Λ_b^0 candidate, which are given in Table 5.2.

Decay Tree Fits

Candidates are subsequently re-fit after the stripping selection using the Decay Tree Fitter (DTF) package (see Chap. 4). The two charged hadrons that were initially assigned the pion particle hypothesis at the stripping level are re-fit under the $K^+\pi^-$, $K^-\pi^+$ and K^+K^- hypotheses, and in each case the Λ decay products are constrained to the p and π mass hypotheses. Vertex coordinates, vertex fit quality, and particle lifetimes, are also re-calculated, and the Λ_b^0 is constrained to originate from the primary vertex with the best vertex fit quality. To calculate the square and conventional Dalitz-plot variables, and angular variables, the Λ_b^0 mass is additionally constrained

Table 5.2 Stripping selection requirements Λ_b^0 candidates

Variable definition	Selection requirement
Combination cuts	
Sum of the daughters' transverse momenta (DD)	$\sum_{\text{daug}} p_{\text{T}} > 4200\,\text{MeV}$
Sum of the daughters' transverse momenta (LL)	$\sum_{\text{daug}} p_{\text{T}} > 3000\,\text{MeV}$
p_{T} of at least two Λ_b^0 daughters	$p_{\text{T}} > 1000\,\text{MeV}$
Mass of the Λ_b^0 candidate	$4301 < m_{\Lambda hh} < 6120$ MeV
IP w.r.t PV of highest p_{T} of Λ_b^0 daughter	IP > 0.05 mm
Maximum DOCA χ^2 of any 2 daughters	$\chi^2(\text{DOCA})_{\text{max}} < 5$
'Mother' cuts	
Transverse momentum of the Λ_b^0 candidate	$p_{\text{T}} > 1500$ MeV
χ^2 of Λ_b^0 vertex fit	$\chi^2_{\Lambda_b^0\,\text{vtx}} < 12$
Minimum Λ_b^0 IP χ^2 w.r.t PVs	$\chi^2(\text{IP})_{\text{min}} < 8$
Minimum vertex distance w.r.t PVs	$\left\lvert \Lambda^0_{b\,\text{vtx}} - PV \right\rvert_{\text{min}} > 1$ mm
χ^2 separation of Λ_b^0 vertex and associated PV	$\chi^2_{\Lambda_b^0-\text{PV VD}} > 50$

to its world-average value to ensure that all events exist within the kinematic limits. These mass constraints mean that, except implicitly in the level-0 trigger decisions, no calorimetric energy measurements are use in this analysis.

5.2.1 Backgrounds

The purpose of the selection criteria is to minimise the background contamination in the signal region whilst maximising the number of signal decays selected, in order to maximise the sensitivity to the suppressed b-baryon decay modes. These backgrounds can be separated into various categories depending on their source and how they are mitigated.

Combinatorial Background

Combinatorial background is a result of mis-association of charged tracks in an event to a signal candidate decay, which happen to have the properties required by the selection criteria. As these do not come from a signal b-hadron decay, they are, in general, uncorrelated with the reconstructed b-hadron mass. This results in a background that forms a smooth distribution in the reconstructed b-hadron invariant mass. This background can also contain real $\Lambda \to p\pi^-$ decays and resonance decays to h^+h^- that do not come from the signal b-hadron.

As a result, combinatorial background is comparatively easily removed compared to other background categories. For example, decay products of b-hadrons come from the same reconstructed vertex, which is displaced from the pp interaction point, so the variables that describe the consistency of this hypothesis are powerful discriminators

between the signal and combinatorial background. Requirements on these variables are optimised using a boosted decision-tree (BDT) [22] algorithm to separate signal and background events.

Boosted Decision-Tree Classifiers

Boosted decision-trees consist of a weighted set of decision criteria on subsets of the input variables (decision trees) to separate the dataset into two categories according to the characteristics of the training data, which provide ground-truth assignments for the signal and background categories. In this analysis, as the signal decays are yet to be observed, the training data used for the signal category is a sample of 'full' MC (including the full detector simulation, reconstruction, and trigger) that has been truth-matched and undergoes the same selection criteria as the collision data. As there is potential for the distribution of variables in the MC to not faithfully represent those that would be found in collision data, only variables that are well replicated by the MC are included. In particular, variables that are highly correlated with the rest of the event (such as charged track multiplicity, isolation criteria, or any of the particle ID information) are not considered.

To obtain a reliable estimate for the distributions of the corresponding variables in the combinatorial background, it is necessary to isolate such a background sample from collision data. In particular, in this analysis a region from the b-baryon invariant mass distribution is used, corresponding to $5838 < m(\Lambda\pi^+\pi^-) < 6100\,\text{MeV}$. This region is chosen as it avoids potential partially reconstructed backgrounds (see Sect. 5.2.3) below the nominal b-baryon signal regions, and is sufficiently far away from any Ξ_b^0 signal distribution such that contamination from true b-baryon signal decays is negligible. These data are used with all of the previous trigger and stripping selection criteria applied.

As noted in Sect. 5.1.2, the DD and LL subsamples, along with the 2011, 2012a, and 2012b subsamples, have different kinematic properties and are treated differently by the reconstruction and trigger, so separate BDTs are trained for each. As the data for each of the final state hypotheses arises from a particle ID swap of the stripped data (originally reconstructed as $\Lambda\pi^+\pi^-$), there is significant overlap in the sets of candidates that appear in the background regions for each final state. As such, only data reconstructed as $\Lambda\pi^+\pi^-$ is used to train the BDT, along with the corresponding signal MC sample. The same BDT is applied to each final state, but the selection requirement on the output is optimised independently in each case.

The variables of the above signal and background data that enter the BDT can be seen in Table 5.3.

Definitions of the parameters in Table 5.3 can be found in Sect. 5.2, except `DIRA_OWNPV`, which is defined as the cosine of the angle between the momentum of the particle and a vector projected from its primary vertex to its decay vertex.

When training, it is possible for the BDT to be optimised such that near-perfect classification can be achieved on the training dataset, but such performance is necessarily not replicated when the classifier is applied to an independent dataset (such as those in the signal region of the collision data). To control for this *over*fitting effect,

Table 5.3 Variables used to build the BDT classifiers. Some variables are not applicable for use in both LL and DD classifiers, and this applicability is indicated by the 'Track type' column

Variable name	Description	Track type
Lb_PT	Λ_b^0 (Ξ_b^0) transverse momentum	DD LL
Lb_ETA	Λ_b^0 (Ξ_b^0) pseudorapidity	DD LL
Lb_IPCHI2_OWNPV	Λ_b^0 (Ξ_b^0) IP χ^2 w.r.t PV	DD LL
Lb_VDCHI2_OWNPV	Λ_b^0 (Ξ_b^0) flight distance χ^2 w.r.t PV	DD LL
Lb_DIRA_OWNPV	Λ_b^0 (Ξ_b^0) pointing angle	DD LL
Lb_ENDVERTEX_CHI2	Λ_b^0 (Ξ_b^0) vertex fit χ^2	DD LL
SUM_h_IPCHI2_OWNPV	Sum of hadron IP χ^2 w.r.t PV	DD LL
Lz_ENDVERTEX_CHI2	Λ vertex fit χ^2	DD
Lz_VDCHI2_OWNPV	Λ flight distance χ^2 w.r.t PV	LL
Lz_IPCHI2_OWNPV	Λ IP χ^2 w.r.t PV	LL

the hyperparameters that control the training of the BDT are chosen by evaluating the performance on a second independent dataset. This is known as *cross-validation*.

Furthermore, by using the background distributions from true collision data which then enter the final fit to extract the signal yields, and signal distributions from the signal MC which are then used to calculate the efficiencies, a subsequent bias in the estimated signal yields and the signal efficiency arises, which is difficult to quantify without an independent validation sample.

Both of these effects are reduced when training the classifier on a proportion of the full dataset, which is subsequently discarded, and using the rest to validate the classifier. However, instead of discarding a portion of the data in this way, k classifiers are trained on $1 - (1/k)$ of the data, and are then applied on the remaining $1/k$ to calculate the classifier performance and calculate efficiencies in an unbiased way. This is known as *k-folding*, and the evaluation of classifier performance in this way known as k-fold cross-validation.

In this analysis, two classifiers are trained for each category, each trained on the signal and background subsamples with either even or odd event numbers, and then applied for the rest of the analysis on the other set. It is important that this split is uncorrelated with the probability of the collision data being signal or background. These are individually denoted as `BDT0`, trained on data with even event number, and `BDT1`, trained on data with an odd event number. The even and odd event numbered data, along with the corresponding classifier output, are then merged, and henceforth only a single `BDT` will be referred to. A comparison between the 2012b DD BDT output for these two datasets can be seen in Fig. 5.1 (left).

Optimisation of the Boosted Decision-Tree Requirements

The BDTs are trained with the TMVA package [23], and output a continuous variable in $[-1, 1]$. To find the value of this parameter that optimises the approximate significance of the unobserved modes, there are several proposed figures-of-merit. The most robust when the expected number of signal events is unknown is given in

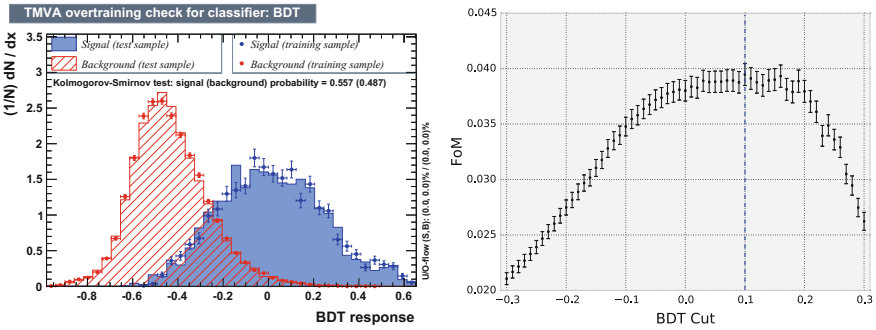

Fig. 5.1 Comparison between signal and background data for the 2012b DD BDT training and test samples (left), and figure-of-merit scan for $\Lambda_b^0 \to \Lambda K^+ K^-$ 2012b DD data (right), with the optimal cut value indicated by the vertical dashed line

terms of the signal efficiency, ϵ, and the number of background events in the signal region, N_{bkg}, under the proposed cut, by [24]

$$\text{FoM} = \frac{\epsilon}{a/2 + \sqrt{N_{\text{bkg}}}}, \tag{5.3}$$

where a is the desired significance in units of Gaussian standard deviations, which is set to 5. In this case, ϵ is estimated using the signal MC, and the number of background events in the signal region is estimated by fitting a second-order Chebychev polynomial to the upper sideband ($5838 < m(\Lambda h^+ h^-) < 6100\,\text{MeV}$), and extrapolating to the corresponding signal region. As each signal mode has a separate signal MC sample, with slightly different distributions of the variables that enter the BDT, and a different distribution and fraction of the background events in the b-baryon invariant mass,[3] these, and the different reconstruction categories (DD, LL) and running periods (2011, 2012a, and 2012b) are optimised separately. This figure-of-merit for various cut values for the 2012b DD data sample and BDT can be seen in Fig. 5.1 (right), with the chosen cut value in this case indicated. The optimised cuts on the BDT output are around 0.1 for all signal modes.

5.2.2 *Cross-Feed Background*

Another source of background arises when the final state hadrons are mis-identified. Without any use of the particle identification system the three final states ($\Lambda\pi^+\pi^-$, $\Lambda K^+\pi^-$, and $\Lambda K^+ K^-$) would overlap in the reconstructed b-baryon invariant mass.

[3] For the different final states these are often the same events in each case, but shifted due to the different mass of the decay products.

Fortunately, with the use of the PID variables, these can be separated with a high efficiency, but there still exists some residual background that appears shifted from the signal mass peak in the Λh^+h^- invariant-mass distribution, which is known as *cross-feed*.

The particle ID variables used here, `PROBNN`, are the output of a neural network whose inputs include the combined RICH1 and RICH2 hypotheses, information from the muon and calorimetry systems, and the probability of being a 'ghost' track (a result of a random combination of hits, or a mismatch between extrapolated sub-tracks, rather than a real charged particle). These represent posterior probabilities, so can be combined to simultaneously favour and reject two particular hypotheses (for example, `PROBNNK × (1 - PROBNNpi)`).

The particle ID information can also be useful to reject combinatorial background in addition to cross-feed background, as often the random track incorrectly associated with the decay is of a different type to the signal track. This is most effective for the final state with one or more kaons, as most combinatorial tracks are pions from the primary vertex.

Optimisation of the Particle ID Requirements

The PID requirements are optimised by scanning through possible PID cut values for each of the tracks, resulting in a two-dimensional figure-of-merit surface. For the optimisation to reject combinatorial background, this is calculated similarly to the method described in Sect. 5.2.1, but where the cut efficiency is calculated using the `PIDCalib` package (see Sect. 4.9.4). To optimise with respect to the cross-feed background the efficiency is again taken from `PIDCalib`, and the number of background events taken to be the number of $\Lambda_b^0 \to \Lambda_c^+(\Lambda K^+)\pi^-$ and $\Lambda_b^0 \to \Lambda_c^+(\Lambda \pi^+)K^-$ cross-feed events in the $\Lambda_b^0 \to \Lambda_c^+(\Lambda \pi^+)\pi^-$ mass spectrum in collision data, selected by taking a ± 30 MeV window around the world-average Λ_c^+ mass.

The results of this procedure can be seen in Fig. 5.2, for 2012b DD $\Lambda_b^0 \to \Lambda K^+\pi^-$ data, optimising for combinatorial background rejection (left), and for cross-feed background rejection (right). The optimised cuts on the PID requirements are around 0.35 for each pion track, and around 0.45 for each kaon track, where cuts for the LL data category are slightly looser than for the DD category. An example of the cross-feed distribution of $\Lambda_b^0 \to \Lambda \pi^+\pi^-$ mis-identified as $\Lambda_b^0 \to \Lambda K^+\pi^-$ for 2012b LL Λ signal MC can be seen in Fig. 5.3 (left).

5.2.3 *Partially Reconstructed Background*

The signal final state is reconstructed as Λh^+h^-, and therefore true decays of the parent b-baryon to this final state plus one or more extra particles are known as partially reconstructed decays. Decays of the b-baryons that involve two additional charged tracks have a distribution in invariant mass far from the signal region, so

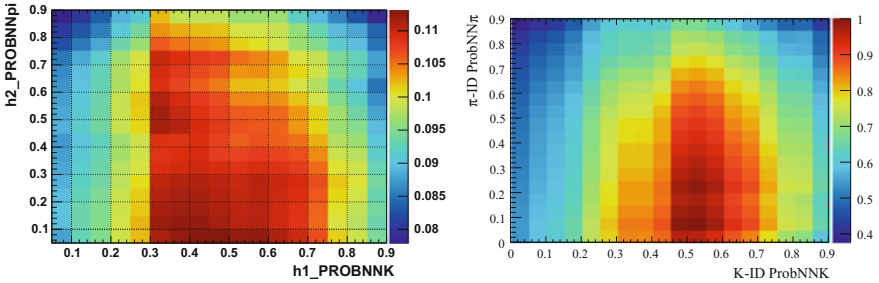

Fig. 5.2 Particle ID criteria optimisation for 2012b DD $\Lambda_b^0 \to \Lambda K^+\pi^-$ data, optimising for combinatorial background rejection (left), and cross-feed background rejection (right). Here h_1 corresponds to the kaon track, and h_2 corresponds to the pion track, and the z-axis corresponds to the figure-of-merit

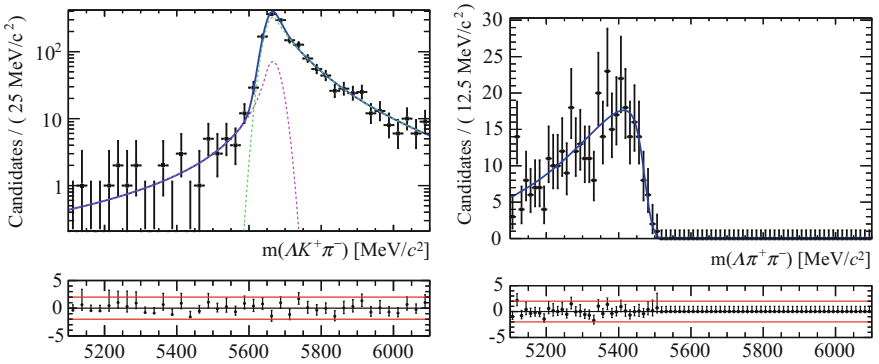

Fig. 5.3 Cross-feed to $\Lambda_b^0 \to \Lambda K^+\pi^-$ from 2012b MC for LL Λ category, of $\Lambda_b^0 \to \Lambda \pi^+\pi^-$ signal MC (left), and partially reconstructed $\Lambda_b^0 \to \Lambda\rho^+(\pi^+\pi^0)\pi^-$ MC, DD Λ category, reconstructed as $\Lambda_b^0 \to \Lambda \pi^+\pi^-$ (right). The overlaid blue curves are fit projections, the parameters of which enter the final fit to data (see Sect. 5.4)

these are not considered further. Extra neutral particles however form a plausible background to the signal, and are considered in this section.

Decays with final states corresponding to $X_b \to \Lambda h^+h^-\pi^0$ and $X_b \to \Lambda h^+h^-\gamma$ will form partially reconstructed backgrounds where the soft neutral particle is produced via a the two body decay of a charged intermediate resonance. In the case of neutral pions, these are shifted in the Λh^+h^- invariant-mass spectrum by an amount characteristic of the energy of the unreconstructed particle, and hence in this analysis certain characteristic 'canonical' decays, via a $K^{*+} \to K^+\pi^0$ or $\rho^+ \to \pi^+\pi^0$ decay, are considered. These are then included as components in the fit, and example of $\Lambda_b^0 \to \Lambda\rho^+(\pi^+\pi^0)\pi^-$ MC reconstructed as $\Lambda_b^0 \to \Lambda \pi^+\pi^-$ can be seen in Fig. 5.3 (right).

There may also be b-baryon decays via a $\Sigma \to \Lambda\gamma$ transition. These are particularly dangerous, as the photon has low energy, and therefore the distribution peaks

close to the signal distribution, due to the difference between the Σ and Λ masses being only around 80 MeV. Models for decays of this type involving all of the signal final states are included in the final fit.

Decays of $\Lambda_b^0 \to \Lambda\,\eta'(\pi^+\pi^-\gamma)$ would in principle be present in the signal region, with the momentum distribution of the photon being slightly harder than that of the above Σ decays. A limit was placed on $\mathcal{B}(\Lambda_b^0 \to \Lambda\,\eta') < 6.3 \times 10^{-6}$ at 95% confidence level [25], and therefore the limit on $\Lambda_b^0 \to \Lambda\,\eta'(\pi^+\pi^-\gamma)$ is approximately 1.8×10^{-6}. As such, decays of this kind are not included in the fit model, as the efficiency is expected to be significantly lower than that of the signal mode.

In addition, for the normalisation mode, a tight cut around the Λ_c^+ mass in the $\Lambda\pi^+$ spectrum should remove partially reconstructed decays of the form $\Lambda_b^0 \to \Lambda_c^+(\Lambda\pi^+X)\pi^-$, where X is not reconstructed, as these occupy the spectrum below the Λ_c^+ mass. Therefore the only relevant partially reconstructed backgrounds are those with a π^0/γ not directly from the Λ_c^+ decay, of which $\Lambda_b^0 \to \Sigma_c^+(\Lambda_c^+(\Lambda\,\pi^+)\,\pi^0)\,\pi^-$ is included in the fit.

5.2.4 Intermediate Charm Decays

The main source of background from intermediate charm resonances is the decay $\Lambda_b^0 \to \Lambda_c^+(\Lambda h^+)h^-$. The product branching fraction of $\Lambda_b^0 \to \Lambda_c^+(\Lambda\pi^+)\pi^-$ is $(6.29 \pm 0.78) \times 10^{-5}$ [26], and is also used for the normalisation of the branching fraction measurements. The decays $\Lambda_b^0 \to \Lambda_c^+(\Lambda K^+)\pi^-$ and $\Lambda_b^0 \to \Lambda_c^+(\Lambda\pi^+)K^-$, which have branching fractions of $(3.0 \pm 0.6) \times 10^{-6}$ and $(4.7 \pm 0.5) \times 10^{-6}$, respectively, are used as a control mode for cross-checks of the branching fraction measurement procedure and for the optimisation of the cross-feed background rejection in Sect. 5.2.2. The branching fraction of $\Lambda_b^0 \to \Lambda_c^+(\Lambda K^+)K^-$ is $(0.22 \pm 0.05) \times 10^{-6}$. The region in the Λh^+ reconstructed invariant mass distribution corresponding to ± 30 MeV of the Λ_c^+ world-average mass is vetoed in the analysis of the signal decays, and decays via the intermediate Ξ_c^+ baryon are similarly vetoed (although these branching fractions are unknown).

Decays via a J/ψ or $\psi(2S)$ that decays into two hadrons are considered negligible due to the suppressed decay rate, and the small branching fraction of the $\Lambda_b^0 \to J/\psi\,\Lambda$ decay, corresponding to a total branching fraction of $\mathcal{O}(10^{-9})$. Other sources of background are decays via intermediate D^0 mesons, $\Lambda_b^0 \to \Lambda D^0(h^+h^-)$, which are vetoed by removing the h^+h^- invariant mass region within ± 30 MeV of the world-average D^0 mass, for each h^+h^- combination.

5.2.5 Other Peaking Backgrounds

Decays where two muons are mis-identified as the two charged hadrons in the signal final state can also occur. These arise primarily from decays involving charmonia,

such as $\Lambda_b^0 \to J/\psi(\mu^+\mu^-)\Lambda$ or $\Lambda_b^0 \to \psi(2S)(\mu^+\mu^-)\Lambda$, where the two muons are mis-identified as h^+h^-. Muon tracks are cleanly identified by their presence in the muon stations, so requiring that a track cannot be associated with a hit in the muon system can be used to remove these backgrounds with high efficacy (see Sect. 5.3). The $\Lambda_b^0 \to \Lambda\mu^+\mu^-$ decays are also removed by this requirement.

Decays Without an Intermediate Λ Baryon

Decays to the same final state as the signal modes, but without a true Λ decay, such as the recently observed $\Lambda_b^0 \to p\,\pi^-h^+h'^-$ decays [27], will peak in the same region as the true signal peak. However, the lack of a displaced Λ vertex means that, where present, they will peak only in the LL reconstruction category, where they will be largely removed by the 30 mm Λ–Λ_b^0 z-vertex difference cut in the initial selection. As a result, no events in the corresponding $\Lambda_b^0 \to p\,\pi^-h^+h'^-$ MC sample pass the nominal selection criteria.

Decays Where a K_S^0 Meson is Mis-Identified as a Λ Baryon

The main background in this category is the case where the K_S^0 is mis-reconstructed as a Λ in $B_{d,s}^0 \to K_S^0h^+h'^-$ decays. The dominant such decay is the $B^0 \to K_S^0\pi^+\pi^-$ mode, which has a branching fraction of $(2.60 \pm 0.12) \times 10^{-5}$.

These backgrounds can be vetoed by recalculating the invariant mass of the $\Lambda \to p\pi^-$ candidates under the $\pi^+\pi^-$ hypothesis and removing the region around the K_S^0 mass. In MC however this has low efficiency for the signal mode, so instead these backgrounds are handled by applying loose proton PID requirements on the positive (negative) Λ ($\overline{\Lambda}$) daughter track, corresponding to a cut of `Lzp_PROBNNp × (1 - Lzp_PROBNNpi) > 0.05` (this choice has been informed by the PID variable distribution in collision data corresponding to $B^0 \to K_S^0\pi^+\pi^-$). Similar modes with one or more kaons ($B_s^0 \to K_S^0K^\pm\pi^\mp$, $B^0 \to K_S^0K^+K^-$) will also be handled by this requirement.

Using the relative efficiencies, the measured branching fractions of the $B_{d,s}^0 \to K_S^0h^+h'^-$ decays, and the fragmentation fractions relative to Λ_b^0, the expected proportion of $B_{d,s}^0 \to K_S^0h^+h'^-$ candidates relative to the $\Lambda_b^0 \to \Lambda_c^+(\Lambda\,\pi^+)\,\pi^-$ normalisation mode yield can be calculated. The PID efficiency is calculated using the `PIDCalib` calibration in the same way as the signal MC.

This results in a relative yield in most data categories of less than 1% that of the normalisation mode. Therefore as the expected branching fractions of the signal modes are $\mathcal{O}(10^{-6})$, and the distribution of $B_{d,s}^0 \to K_S^0h^+h'^-$ events results in a falling tail in the signal regions, these backgrounds are considered negligible enough to be included in the combinatorial component with little bias. Furthermore, this calculation does not take into account the efficiency of the various background vetoes, nor where the events lie in the Λh^+h^- invariant mass, so is likely to be an overestimate.

Table 5.4 The backgrounds under consideration in this section, along with the method of accounting for them and whether they have been observed previously

Background	Observed	Method
$B^0_{d,s} \to K^0_S h^+ h'^-$	Yes	PID cut on p from Λ
$\Lambda^0_b \to \Lambda^+_c(\Lambda h^+) h'^-$	Yes	Vetoed (see Table 5.5)
$\Lambda^0_b \to \Xi^+_c(\Lambda h^+) h'^-$	No	Vetoed (see Table 5.5)
$\Lambda^0_b \to \Lambda D^0(h^+ h'^-)$	No	Vetoed (see Table 5.5)
$\Lambda^0_b \to \Lambda \mu^+ \mu^-$	Yes	Vetoed (via `isMuon` PID cut)
$\Lambda^0_b \to p \pi^- h^+ h'^-$	Yes	Λ flight-distance cut (LL)
$\Lambda^0_b \to \Lambda \rho^+(\pi^+\pi^0) h^-$	No	Included in fit model
$\Lambda^0_b \to \Lambda K^{*+}(K^+\pi^0) h^-$	No	Included in fit model
$\Lambda^0_b \to \Sigma(\Lambda\gamma) h^+ h'^-$	No	Included in fit model
$\Lambda^0_b \to \Sigma^+_c(\Lambda^+_c(\Lambda \pi^+)\pi^0)\pi^-$	No	Included in fit model
Cross-feeds	No	Included in fit model
Combinatorial	—	Included in fit model

Table 5.5 Vetoes for peaking backgrounds and the corresponding veto window, based on the PDG value for the mass of the intermediate particle

Background	Veto window
$\Lambda^0_b \to \Lambda^+_c(\Lambda h^+) h'^-$	$\lvert m(\Lambda h^+) - m(\Lambda^+_c)_{\rm PDG}\rvert < 30\,\text{MeV}$
$\Lambda^0_b \to \Xi^+_c(\Lambda h^+) h'^-$	$\lvert m(\Lambda h^+) - m(\Xi^+_c)_{\rm PDG}\rvert < 30\,\text{MeV}$
$\Lambda^0_b \to \Lambda D^0(h^+ h'^-)$	$\lvert m(h^+h^-) - m(D^0)_{\rm PDG}\rvert < 30\,\text{MeV}$

5.2.6 Summary of Backgrounds

Table 5.4 summarises the backgrounds under consideration in this section, along with the method of accounting for them. Modes that have not yet been observed are indicated, and background decays that are vetoed are listed in Table 5.5.

5.2.7 Multiple Candidates

After the above selection criteria, there are still sometimes multiple signal candidates per-event, at a rate of around 0.1%. To avoid biasing the signal yield or background distributions, all but one of the signal candidates in these cases are randomly removed.

5.3 Efficiencies

The detection efficiency expresses the probability for a signal event to be reconstructed and accepted by the selection criteria. This is dependent on the properties of the specific decay under study and is therefore primarily evaluated with fully reconstructed Monte-Carlo, and factorised into several contributions,

$$\epsilon = \epsilon^{\text{gen.}} \times \epsilon^{\text{reco.+strip.}} \times \epsilon^{\text{trigger}} \times \epsilon^{\text{offline}} \times \epsilon^{\text{PID}}. \tag{5.4}$$

- $\epsilon^{\text{gen.}}$ – Generator level efficiency: This is not *per se* a separate physical contribution, but rather an artifact of the MC generation process. It is more efficient computationally to only run the detector simulation for final state particles in the LHCb acceptance, and therefore this factor corrects for the LHCb angular acceptance and is calculated during the MC generation process.
- $\epsilon^{\text{reco.+strip}}$ – Reconstruction and stripping efficiency: This includes the efficiency of the LHCb event reconstruction algorithms to identify and reconstruct the signal process from the individual sub-detector hits, and the effect of the loose analysis pre-selection. These are evaluated on the fully simulated MC, with the same algorithms that are run on the collision data.
- $\epsilon^{\text{trigger}}$ – Trigger efficiency: Efficiency of the hardware and high-level trigger algorithms to select the signal decay. This is evaluated on fully simulated MC, and for the HLT, with the same algorithms that are run online to ensure accuracy of the efficiency. For the hardware L0 trigger, the most efficient trigger for these decays is the `L0Hadron` line, however this makes use of the hadronic calorimeter for transverse energy measurements, and needs to be corrected using a data-driven method.
- $\epsilon^{\text{offline}}$ – Offline selection efficiency: Efficiency of the tighter optimised selection applied offline. This includes all required fiducial cuts, as well as cuts on the flight distance of the Λ to explicitly remove backgrounds without a true Λ decay. This is dominated by the efficiency of the boosted decision-tree classifier used to reject combinatorial background.
- ϵ^{PID} – Particle ID efficiency: This analysis makes extensive use of the LHCb particle ID system, with requirements on all four tracks, and the efficiency of which is not well reproduced in the MC as it depends strongly on the event track multiplicity (which itself is not well reproduced by the event generators). This is evaluated with a data driven method using decays of high-statistics control modes, of which the particle content can be identified without using the PID system [28].

A multi-body decay is, in general, composed of several quasi-two-body decays plus a non-resonant contribution, and the distribution of the events in the phase-space is driven by the dynamics of these processes. This distribution is not known a priori, and therefore must be determined by the distributions found in data. In this section only phase-space integrated efficiencies are reported, with the implication that the efficiencies used in the analysis are phase-space dependent, where appropriate.

5.3.1 Generator Level Efficiency

The generator level efficiency corresponds to the requirement that each of the charged tracks of a given decay must fall within the $10 < \theta < 400$ mrad acceptance of the LHCb detector. These are typically around 19% for the signal and normalisation modes.

5.3.2 Reconstruction and Stripping Efficiencies

The reconstruction efficiency calculation is performed by requiring that the h^+h^- pair satisfy the criteria to be reconstructed as long tracks, and the Λ daughters satisfy the criteria to be reconstructed as either downstream (DD) or long (LL) tracks, and is only calculated for b-baryon candidates in the detector acceptance. This includes the requirement that, in simulated data, the reconstructed b-baryon candidate matches the true generated candidate, and the requirement that the constrained DTF fit be successful for the true daughter candidates. Typical values for this efficiency are around 1.5% for the $\Lambda_b^0 \to \Lambda\,\pi^+\pi^-$ decay, increasing to approximately 1.7% for $\Lambda_b^0 \to \Lambda\,K^+K^-$ due to the higher momentum tracks. For decays with an additional (charm) decay vertex, such as $\Lambda_b^0 \to \Lambda_c^+(\Lambda\,\pi^+)\,\pi^-$, these are around 1.1%.

5.3.3 Trigger Efficiency

The separation of the full 2012 dataset into the 2012a (2012 pre-June technical-stop) and 2012b (2012 post June technical-stop) subsets is motivated by the difference in the HLT2 response for long-lived particles for each period. This can be seen in the relative trigger efficiencies for each period (Table 5.6), where the DD category sees a significant increase in efficiency in 2012b compared to 2012a. The LL reconstruction category however experiences a slight drop in efficiency due to the tightened flight-distance cut [29].

5.3.4 Offline Selection Efficiency

This category is comprised of the efficiencies related to the cut on the BDT output, given in Sect. 5.2.1, along with the cuts that have been implemented to reduce combinatorial and other backgrounds. Amongst these cuts are the background vetoes given in Table 5.5.

Table 5.6 Phase-space integrated trigger efficiencies for 2011, 2012a, and 2012b Monte-Carlo

Mode	2011 $\epsilon^{\text{trig.}}$ (%)	2012a $\epsilon^{\text{trig.}}$ (%)	2012b $\epsilon^{\text{trig.}}$(%)
$\Lambda_b^0 \to \Lambda\,\pi^+\pi^-$ (DD)	17.09 ± 0.22	17.92 ± 0.27	21.62 ± 0.18
$\Lambda_b^0 \to \Lambda\,\pi^+\pi^-$ (LL)	24.10 ± 0.53	29.57 ± 0.74	27.93 ± 0.42
$\Lambda_b^0 \to \Lambda\,K^+\pi^-$ (DD)	17.58 ± 0.26	18.67 ± 0.28	22.21 ± 0.22
$\Lambda_b^0 \to \Lambda\,K^+\pi^-$ (LL)	24.23 ± 0.61	30.60 ± 0.76	28.41 ± 0.51
$\Lambda_b^0 \to \Lambda\,K^+K^-$ (DD)	17.74 ± 0.26	19.46 ± 0.29	22.80 ± 0.22
$\Lambda_b^0 \to \Lambda\,K^+K^-$ (LL)	24.60 ± 0.60	30.62 ± 0.76	27.54 ± 0.51
$\Lambda_b^0 \to \Lambda_c^+(\Lambda\,\pi^+)\,\pi^-$ (DD)	22.27 ± 0.35	22.29 ± 0.36	24.72 ± 0.28
$\Lambda_b^0 \to \Lambda_c^+(\Lambda\,\pi^+)\,\pi^-$ (LL)	26.72 ± 0.77	31.09 ± 0.93	29.18 ± 0.64

The BDT efficiency on signal MC is around 40% for DD candidates, and around 50% for LL candidates, whilst rejecting approximately 90% of combinatorial background across the invariant mass region of the analysis. The efficiency of the other selection cuts is around 70% for DD candidates, and around 75% for LL candidates.

5.3.5 PID Efficiency

The PID efficiency is calculated using calibration samples from the `PIDCalib` package, as described in Chap. 4. The efficiency of the optimised PID criteria in Sect. 5.2.2, including the requirement for the track not to be associated with a hit in the muon system and the loose requirements on the final state proton, is around 60% on signal MC, for both DD and LL categories. The $K \to \pi$ mis-ID probability (*i.e.* the probability of incorrectly identifying a true kaon as a pion) is around 18%, whereas the $\pi \to K$ mis-ID rate is around 3%. These values are used to constrain the cross-feed contamination in the fit to data (Sect. 5.4).

The uncertainties on these efficiencies are a combination of the statistical uncertainty on the efficiency from the `PIDCalib` dataset and the statistical uncertainty on the p, p_{T} and η distributions in signal MC data. The former of these is taken from `PIDCalib`, where it is estimated from the yield of the fit to the calibration data set. The latter is estimated using the bootstrap resampling method, where the `PIDCalib` efficiency is evaluated on an ensemble of data sets with kinematic distributions that are sampled with replacement from the original signal MC dataset, and have the same number of entries.

5.3.6 Phase-Space Dependent Efficiency Correction

In general [30], the differential decay rate for the decay of an unstable particle of mass M into three decay products with known energies, can be expressed in terms

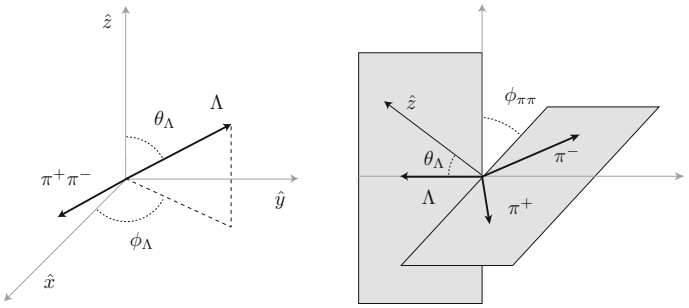

Fig. 5.4 Schematic of the angular variables used in this analysis, $(\theta_\Lambda, \phi_\Lambda)$ left and θ_{hh} right, for the $\Lambda_b^0 \to \Lambda\pi^+\pi^-$ decay

of the matrix element for the decay, $\mathcal{M}$, the energies of any two decay products, E_1 and E_2, and the three Euler angles that give the relative orientation in space of the decay products with respect to the initial particle, (α, β, γ),

$$d\Gamma = \frac{1}{(2\pi)^5}\frac{1}{16M}|\mathcal{M}(E_1, E_2, \alpha, \cos\beta, \gamma)|^2\, dE_1\, dE_2\, d\alpha\, d(\cos\beta)\, d\gamma. \tag{5.5}$$

In the decays of a B-meson to three pseudoscalars, there is no dependence of the decay dynamics on the Euler angles, as no additional degrees-of-freedom are held by the B-meson or the decay products. These additional angles can be integrated out, such that the only dependence is on the Dalitz-plot variables, m_{12}^2 and m_{23}^2,

$$d\Gamma = \frac{1}{(2\pi)^3}\frac{1}{32M^3}\overline{|\mathcal{M}|^2}\, dm_{12}^2\, dm_{23}^2. \tag{5.6}$$

However, in the case of a spin-$\frac{1}{2}$ particle decay, the additional degrees-of-freedom can result in non-trivial distributions of the Euler angles for the decay products.[4] Here, the following angles are chosen, such that they are independent of each other and the Dalitz-plot variables, and uniform for phase-space decays (i.e., without intermediate resonance dynamics). The angles (see Fig. 5.4) are described in the Λ_b^0 rest frame, and defined by the axes:

- $\hat{\mathbf{x}}$: direction of Λ_b^0 ($p_{\Lambda_b^0}$) in the lab frame,
- $\hat{\mathbf{z}}$: cross product of the beam axis and $\hat{x}$,
- $\hat{\mathbf{y}}$: cross product of $\hat{z}$ and $\hat{x}$,

where the beam axis is taken to be in the positive z_{lab} direction in the lab frame.

[4] When these are expressed in terms of the helicity angles, and assuming no longitudinal Λ_b^0 polarisation, it subsequently has been shown that the the decay depends only on the angular variables when the Λ_b^0 transverse polarisation is non-zero [31].

The angles are then:

- $\cos(\theta_\Lambda)$: cosine of the polar angle of the Λ momentum in the above reference frame,
- ϕ_Λ: azimuthal angle of the Λ momentum in the above reference frame,
- ϕ_{hh}: the angle between the plane formed by the h^+ and h^- momenta, and the plane formed by the Λ momentum and $\hat{z}$.

Factorisation of the Phase-Space Variables

The assumption that the efficiency description is independent between the three angles and the Dalitz-plot variables, such that these can be factorised, is verified by calculating the linear correlation between the five variables for fully selected signal MC. This is consistent with zero between the angular variables, and no higher-order correlations are observed in the corresponding two-dimensional distributions.

Obtaining the Correction Factor

For those modes where a significant signal yield is obtained, the event-by-event signal $sWeights$, w_i, for an event, i, from the fit of each signal channel are extracted. The efficiency-corrected yield is then given by

$$N_{\text{sig}}^{\text{corr}} = \sum_{\text{events}} \frac{w_i}{\epsilon_i}, \tag{5.7}$$

where ϵ_i is the efficiency in a bin of the $(2+3)$D phase-space described by the square Dalitz-plot and the above angular variables. The average efficiency is then

$$\bar{\epsilon} = \frac{N_{\text{sig}}}{N_{\text{sig}}^{\text{corr}}}, \tag{5.8}$$

where $N_{\text{sig}} = \sum_{\text{events}} w_i$.

In the cases where no significant signal is obtained, the binned distributions of the efficiencies as a function of the above phase-space variables are used to construct 1D histograms of the variation in efficiency. The mean value over this histogram is taken as the central value used in the calculation of the branching fraction, and the standard deviation is used to determine the systematic uncertainty due to the efficiency variation across the phase-space.

5.3.7 `L0Hadron` Trigger Correction

There is a possibility of a mismatch between the MC and data `L0Hadron` trigger efficiency, caused by mis-calibration of the calorimetric transverse energy, E_{T}, measurements, and ageing effects within the HCAL. Using the TISTOS method (see Chap. 4) on tracks from inclusive $D^{*+} \to D^0(K^-\pi^+)\pi^+$ decays, the `L0Hadron`

efficiency is obtained for pions, kaons, and protons; for both magnet configurations; and for inner and outer calorimeter regions. Where there is a significant signal yield, these calibrated efficiencies are used to correct the `L0Hadron` efficiency, and a systematic assigned according to the E_{T} binning. Otherwise, the average deviation over the phase-space is taken as a systematic.

An additional related correction is required due to overlaps of the track energy deposits within the HCAL, which result in a slight under-estimate of the true `L0Hadron` efficiency, due to the effective increase in E_{T} measured by the HCAL. The strategy to correct for this effect is similar to that used in the amplitude analysis of $B_s^0 \to \overline{D}^0 K^- \pi^+$ [32, 33].

5.3.8 Summary of Efficiencies

The average efficiency over the phase space for the Λ_b^0 signal modes is around 1.0×10^{-4} for the DD Λ reconstruction category, around 0.4×10^{-4} for the LL Λ reconstruction category, and is similar for each final state. For the Ξ_b^0 decays, this efficiency is approximately 20% greater in each case due to the increased reconstruction efficiency of the higher momentum tracks from the Ξ_b^0 decay. The $\Lambda_b^0 \to \Lambda_c^+ (\Lambda \pi^+) \pi^-$ control mode efficiency is around 30% lower than that of the Λ_b^0 signal modes, due to the selection requirements on the impact parameter of the charged tracks and Λ_b^0 vertex quality rejecting decays decays where the Λ_c^+ has a long lifetime.

The phase-space dependent efficiency distribution (not including the approximately flat generator-level efficiency of 19%), in the square Dalitz plot, for 2012b $\Lambda_b^0 \to \Lambda \pi^+ \pi^-$ (left) and $\Xi_b^0 \to \Lambda \pi^+ \pi^-$ (right) signal MC, where the Λ is reconstructed as DD, can be seen in Fig. 5.5. The regions of low efficiency around $m' = 0.8, \theta' = 0.1, 0.9$ correspond to the two corners of the conventional Dalitz plot where one of the two charged $h^+ h^-$ hadrons is at rest. The values of θ' where $m' = 0$ corresponds to the third corner of the conventional Dalitz plot, where the Λ baryon is at rest. The drop in efficiency around $m' = 0.5$ is primarily a result of the momentum requirement on the final state tracks from the trigger, which is more efficient for the $h^+ h^-$ tracks than for the Λ. This distribution is qualitatively similar for all other final states and the LL Λ reconstruction category.

5.4 Fit Model

To extract the yields for the six signal modes and the normalisation mode, an unbinned extended-maximum-likelihood fit to the $\Lambda h^+ h'^-$ spectra is performed. This fit is performed simultaneously for DD and LL Λ reconstruction categories, for all modes and running periods, including the $\Lambda_b^0 \to \Lambda_c^+ \pi^-$ normalisation mode and its cross-feeds.

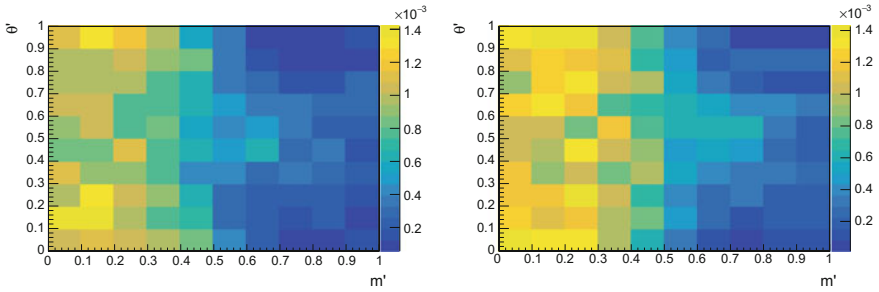

Fig. 5.5 Phase-space dependent efficiency distribution (not including the approximately 19% flat generator-level efficiency), in the square Dalitz plot, for 2012b $\Lambda_b^0 \to \Lambda\,\pi^+\pi^-$ (left) and $\Xi_b^0 \to \Lambda\,\pi^+\pi^-$ (right) signal MC, where the Λ is reconstructed as DD

To constrain the various nuisance parameters of the fit model, the parameters for the various models are extracted from MC.

5.4.1 Signal Parameterisation

The $\Lambda_b^0(\Xi_b^0) \to \Lambda\, h^+ h'^-$ signal mass distributions are modelled as the sum of two Crystal-Ball functions with a common mean and width. The Crystal-Ball function is defined as a central Gaussian function with a power-law tail,

$$CB(t; n, \alpha, \sigma) = \mathcal{N} \cdot \begin{cases} \exp\left(-t^2/2\sigma^2\right) & \text{if } t/\sigma > -|\alpha| \\ \left(\frac{n}{|\alpha|}\right)^n \left(\frac{n-\alpha^2}{|\alpha|} - \frac{t}{\sigma}\right)^{-n} \exp\left(-\alpha^2/2\right) & \text{if } t/\sigma \leq -|\alpha|, \end{cases} \tag{5.9}$$

where t is related to the reconstructed mass m, $t = \text{sign}(\alpha)(m - \mu)$, μ and σ are the mean and resolution of the Gaussian function, respectively, and $\mathcal{N}$ is a normalisation factor. The power law in the tail is controlled by n and the sign of α determines its side relative to the mean of the central Gaussian. Instead of having independent normalisation factors, in the double Crystal-Ball PDF a parameter, $f = \mathcal{N}_1/\mathcal{N}_2$, is introduced which governs the ratio of the normalisation parameters and thus the relative sizes of the two Crystal-Ball functions.

The left tail of the double Crystal-Ball primarily describes the radiative tail of the mass distribution, which has been shifted to lower values by the radiation of one or more photons by the final state particles, in addition to tracking imperfections and other related stochastic detector effects. The final state radiation is expected to be a smaller effect in the modes containing one or more kaons, owing to their higher mass. The right tail accounts for only the effect of the non-Gaussian detector resolution.

The shape parameters (all parameters except the mean and width of the central Gaussian) of the double Crystal-Ball function are determined by fits to the signal MC, and these are then fixed in the fit to data.

5.4.2 Signal Cross-Feeds

After the particle identification criteria have been applied, final states with a $\pi \leftrightarrow K$ mis-identification form a peak in the invariant mass distribution of the signal mode. These contributions are also modelled by a double Crystal-Ball PDF, as described above, and the shape parameters similarly fixed in the final fit to data. The events are weighted according to their `PIDCalib` efficiency, in an effort to maintain the modification that the PID requirements have on the invariant mass distribution, but retain sufficient statistics for an accurate determination of the parameters.

5.4.3 Combinatorial Background

The combinatorial background is described by a single exponential function, with a single floating parameter that is shared between the running periods for each final state and reconstruction category.

5.4.4 Partially Reconstructed Background

Partially reconstructed backgrounds are modelled by an ARGUS threshold function convoluted with a Gaussian to account for detector resolution, where the parameters are obtained and constrained to those found in MC, as above.

The generalised ARGUS function is defined via three parameters, m_t, c, and p,

$$A(m; m_t, c, p) = \frac{2^{-p} c^{2(p+1)}}{\Gamma(p+1) - \Gamma(p+1, c^2/2)} \frac{m}{m_t^2} \left(1 - \frac{m^2}{m_t^2}\right)^p \exp\left\{-\frac{1}{2} c^2 \left(1 - \frac{m^2}{m_t^2}\right)\right\}, \quad (5.10)$$

when $m < m_t$, and zero elsewhere. $\Gamma(x)$ and $\Gamma(s, x)$ are the gamma and upper incomplete gamma functions, respectively, m_t is a threshold mass value, c governs the curvature of the function, and p controls the falling of the slope.

For the nominal fit, the resolution parameter in the Gaussian, σ, is taken to be 17 MeV, and the threshold masses are determined by the nominal Λ_b^0 mass minus the mass of the unreconstructed particle. Due to the small sample sizes, the model parameters are extracted from the pooled 2011 and 2012 MC samples.

A non-parametric `RooKeysPdf` kernel density estimate is used for the $\Lambda_b^0 \to \Sigma_c^+ (\Lambda_c^+ (\Lambda\, \pi^+)\, \pi^0)\, \pi^-$ background to the normalisation mode.

5.4.5 Constrained Parameters

The advantage of performing a simultaneous fit to all invariant mass spectra is that, in addition to being able to constrain parameters to those found in the MC samples, the

relative yields of particular components can also be constrained, where appropriate, to reduce the number of free parameters in the fit and improve stability. Specifically, in addition to the above constraints on the shape parameters from MC, the parameters that are constrained in the fit to collision data are:

- The parameter in the exponential describing combinatorial background is constrained to be the same in each spectrum, across the running periods, for DD and LL separately.
- The cross-feed yields for each mode are constrained to the corresponding yield in their signal spectrum, multiplied by the mis-identification rate obtained by the calibrated PID information (see Sect. 5.3).
- The mean of the core Gaussian function in all Λ_b^0 signal PDFs are common.
- The signal PDF widths for all modes are common within the DD and LL categories. A small correction factor (taken from MC) is included to correct for the difference in width between the charmless signal and Λ_c^+ normalisation mode due to the additional charm vertex.
- The difference between the Λ_b^0 and Ξ_b^0 masses is fixed to the latest LHCb value of $m_{\Xi_b^0} - m_{\Lambda_b^0} = 174.8 \pm 2.5\,\text{MeV}$ [34].

5.4.6 *Results of the Fit to Collision Data*

The results of the fit to collision data can be seen in Figs. 5.6 and 5.7, where a significant signal is observed in the $\Lambda_b^0 \to \Lambda K^+\pi^-$ and $\Lambda_b^0 \to \Lambda K^+K^-$ modes, a reasonable signal in the $\Lambda_b^0 \to \Lambda \pi^+\pi^-$ mode, and small to negligible signals for the Ξ_b^0 decays. The yields from this fit, for each category and signal mode, can be seen in Table 5.7. Efficiency-corrected and background-subtracted Dalitz-plot distributions, using the sWeights extracted from the fit, for $\Lambda_b^0 \to \Lambda K^+\pi^-$ and $\Lambda_b^0 \to \Lambda K^+K^-$ decays, can be seen in Fig. 5.8.

After unblinding a lack of events was observed in the $\Xi_b^0 \to \Lambda K^+K^-$ signal regions in the LL reconstruction category. The lack of any data causes problems for maximum likelihood fits, as the maximum of the total likelihood in this instance can be achieved by one of the model parameters tending to infinity. When the method used is *extended* maximum likelihood, with an additional Poisson term for the overall yield, this can result in the fitted yield tending to extreme negative values. This phenomenon is documented in more detail in Ref. [35], which proposes that the most reasonable solution to this is to constrain the fit such that configurations that would result in a negative total PDF are prohibited. Therefore a lower bound of zero is set on the $\Xi_b^0 \to \Lambda K^+K^-$ yields for the LL reconstruction category, and henceforth this is referred to as the nominal fit model.

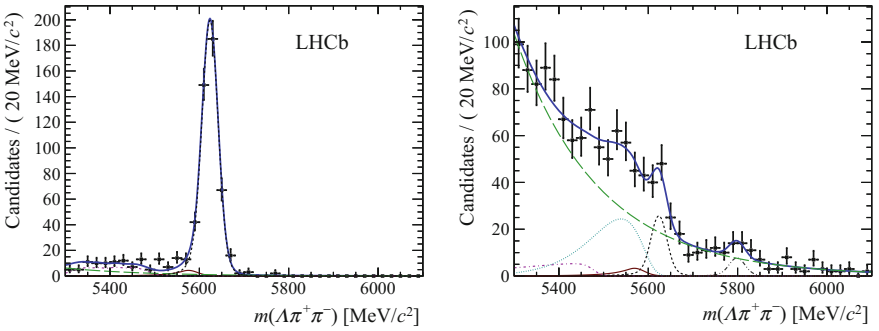

Fig. 5.6 Results of the fit for the (left) $\Lambda_b^0 \to \Lambda_c^+(\Lambda\pi^+)\pi^-$ control mode and (right) $\Lambda\pi^+\pi^-$ signal final states, for all subsamples combined. Superimposed on the data are the total result of the fit as a solid blue line, the Λ_b^0 (Ξ_b^0) decay as a short-dashed black (double dot-dashed grey) line, cross-feed as triple dot-dashed brown lines, the combinatorial background as a long-dashed green line, and partially reconstructed background components with either a missing neutral pion as a dot-dashed purple line or a missing soft photon as a dotted cyan line

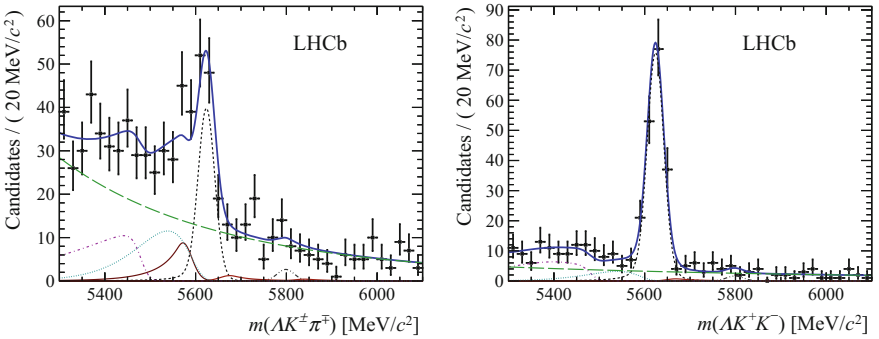

Fig. 5.7 Results of the fit for the (left) $\Lambda K^\pm\pi^\mp$ and (right) ΛK^+K^- final states, for all subsamples combined. Superimposed on the data are the total result of the fit as a solid blue line, the Λ_b^0 (Ξ_b^0) decay as a short-dashed black (double dot-dashed grey) line, cross-feed as triple dot-dashed brown lines, the combinatorial background as a long-dashed green line, and partially reconstructed background components with either a missing neutral pion as a dot-dashed purple line or a missing soft photon as a dotted cyan line

5.5 Systematic Uncertainties

By a judicious choice of the normalisation mode, $\Lambda_b^0 \to \Lambda_c^+(\Lambda\,\pi^+)\,\pi^-$, with a similar topology and final state to the charmless signal modes, most systematic uncertainties can be assumed to cancel, at least to first order, in the branching fraction ratio. The systematics that are explicitly considered and documented in this section are those related to the selection efficiency and its variation over the phase-space, the PID calibration, the fit model and fit biases, and the normalisation channel branching fraction. These are combined with the statistical uncertainty on the normalisation

Table 5.7 Signal yields for the Λ_b^0 and Ξ_b^0 decay modes under investigation. The totals are simple sums and are not used in the analysis. Uncertainties are statistical only

Mode	Run period	Λ_b^0 Yield		Ξ_b^0 Yield	
		Downstream	Long	Downstream	Long
$\Lambda\pi^+\pi^-$	2011	10.2 ± 5.5	8.7 ± 4.7	-0.6 ± 2.4	4.9 ± 3.2
	2012a	9.1 ± 5.2	13.6 ± 5.7	5.3 ± 3.6	1.0 ± 2.6
	2012b	17.2 ± 7.1	6.2 ± 4.6	3.9 ± 4.0	4.1 ± 2.7
	Total	65 ± 14		19 ± 8	
$\Lambda K^\pm\pi^\mp$	2011	20.9 ± 6.4	8.2 ± 3.5	3.5 ± 3.7	-0.7 ± 2.4
	2012a	9.3 ± 3.7	1.7 ± 3.6	-0.1 ± 1.7	0.3 ± 1.5
	2012b	39.7 ± 8.9	16.9 ± 5.1	2.9 ± 4.5	-1.8 ± 1.5
	Total	97 ± 14		4 ± 7	
ΛK^+K^-	2011	32.3 ± 6.4	20.1 ± 4.6	0.6 ± 2.3	0.0 ± 0.6
	2012a	22.2 ± 5.3	15.9 ± 4.2	0.5 ± 2.4	0.0 ± 0.5
	2012b	60.5 ± 8.5	34.4 ± 6.1	3.0 ± 2.7	0.0 ± 0.6
	Total	185 ± 15		4 ± 4	
$\Lambda_c^+(\Lambda\pi^+)\pi^-$	2011	78.1 ± 9.1	78.9 ± 9.2		
	2012a	45.0 ± 7.0	63.0 ± 8.3		
	2012b	115.3 ± 11.1	90.7 ± 9.8		
	Total	471 ± 22			

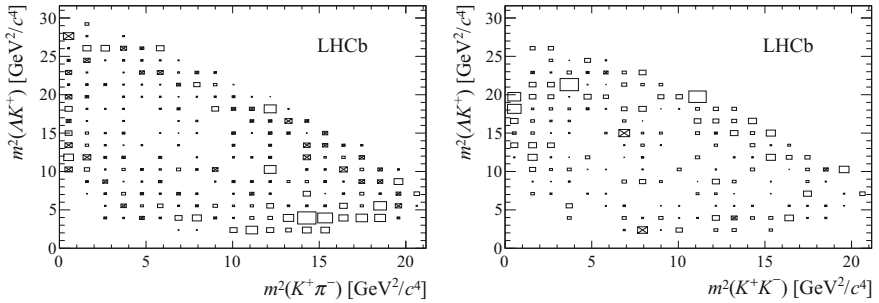

Fig. 5.8 Background-subtracted and efficiency-corrected Dalitz-plot distributions for (left) $\Lambda_b^0 \to \Lambda K^+\pi^-$ and (right) $\Lambda_b^0 \to \Lambda K^+K^-$ with data from all subsamples combined. Boxes with a cross indicate negative central values

mode yield and the statistical uncertainties on the signal and normalisation mode efficiencies to form the total systematic uncertainty. In the following, the values are obtained as the individual systematic components on the ratio of the efficiency-corrected yields for the signal and normalisation modes for each data category.

A summary of the various contributions to the absolute total systematic uncertainty for each mode, can be found in Table 5.8.

Table 5.8 Summary of the absolute systematic uncertainties on the branching fraction ratios assigned in this section. 'PhSp' corresponds to the uncertainty due to the phase-space distribution of the signal decay (if no significant signal is seen); 'Fit' corresponds to the combined uncertainties due to the choice of fit model and the fixed parameters in the fit model; 'Vetoes' corresponds to the systematic uncertainty due to the veto width; 'PID' corresponds to the systematic due to the particle identification criteria imposed on the data; 'Norm. yield' corresponds to the statistical uncertainty on the normalisation channel yield; 'ϵ' corresponds to the uncertainty on the efficiency, including the L0 HCAL correction, and where appropriate the uncertainty due to the phase-space efficiency correction. 'Total' corresponds the sum in quadrature of all other entries

	PhSp (10^{-3})	Fit (10^{-3})	Vetoes (10^{-3})	PID (10^{-3})	Norm. yield (10^{-3})	ϵ (10^{-3})	Total (10^{-3})
$\Lambda_b^0 \to \Lambda\,\pi^+\pi^-$	19.7	8.4	2.2	0.4	3.5	2.0	21.9
$\Lambda_b^0 \to \Lambda\,K^+\pi^-$	–	1.7	1.3	2.9	4.6	11.7	13.1
$\Lambda_b^0 \to \Lambda\,K^+K^-$	–	6.7	2.2	4.2	15.9	5.4	18.7
$\Xi_b^0 \to \Lambda\,\pi^+\pi^-$	7.0	4.1	–	0.1	1.2	0.7	8.2
$\Xi_b^0 \to \Lambda\,\pi^+K^-$	3.5	1.5	–	0.1	0.7	0.4	4.0
$\Xi_b^0 \to \Lambda\,K^+K^-$	0.8	0.1	–	0.0	0.2	0.1	0.8

5.5.1 Selection Efficiency

The same selection (excluding vetoes) is applied to the $\Lambda_b^0 \to \Lambda_c^+(\Lambda\,\pi^+)\,\pi^-$ mode, and therefore most contributions in this area are expected to cancel in the ratio. Those that do not are those uncertainties related to the vetoes and the phase-space variation of the selection efficiency.

Vetoes

The absolute systematic uncertainty due to the choice of the veto window is evaluated by varying the window sizes by $\pm 10\%$ and repeating the analysis. The systematic uncertainties associated with the veto window choice are generally much less than 1% per data category.

Phase-Space Variation

As mentioned in Sect. 5.3.6, for channels where a significant signal is observed, the average efficiency is determined using the information on where the events lie in the phase-space. If no signal is observed however, a value for the average efficiency must be assumed and a corresponding systematic uncertainty needs to be assigned based on the scale of the variation of the efficiency across the phase-space. Specifically, the standard-deviation of the variation of the efficiency across the binned histogram

for each phase-space variable is used. The absolute systematic uncertainty on the efficiency from this is on the order of 1×10^{-4} for each data category.

5.5.2 PID Calibration

A possible bias is introduced in the calculation of the PID efficiencies, as the `PIDCalib` calibration data differs from the real signal data. The assumptions are that the RICH response can be completely parameterised by p, p_{T}, and `nTracks`, and that the efficiency is slowly varying within the chosen bins in these variables. In addition, the kinematics of the signal MC samples are assumed to match those of the data.

To evaluate the uncertainty introduced by any deviations from these assumptions, different binning schemes are considered for the `PIDCalib` calibration data and the calculation of the efficiencies repeated. Specifically, the number of bins in each dimension is reduced by 1/3. Only the relative differences in the phase-space integrated efficiencies are considered, rather than those that depend on the phase-space location via the extracted sWeights. This is in an attempt to isolate only those effects due to to the `PIDCalib` procedure rather than statistical fluctuations from the relatively low signal yields. The absolute systematic uncertainty estimated from this procedure is on the order of 1% per data category.

In addition, an absolute systematic uncertainty of 0.1% is assigned due the uncertainty on the sWeights in `PIDCalib`. This accounts for small correlations in the control mode between the distributions of the variables used to parameterise the efficiency and those used to obtain the sWeights, which violates one of the assumptions of the sWeight procedure.

5.5.3 Trigger

In the case of a significant signal yield, the `L0Hadron` efficiency is calibrated using a high statistics calibration sample (see Sect. 5.3), rather than assigning a systematic uncertainty related to this mis-match. If no significant signal is observed, a systematic is assigned equal to the standard deviation of this correction across the MC phase-space (along with a correction corresponding to the average of this value). This results in a relative systematic uncertainty of around 2×10^{-5} per data category.

5.5.4 Fit

The fitting procedure introduces three major systematic uncertainties. The first is the choice of fit model, which is estimated by repeating the fit with alternative fit

models for each component. The second is introduced by fixing certain model shape parameters to MC data to stabilise the final simultaneous fit, and the uncertainty introduced by this is evaluated by toy pseudoexperiments where the parameters in question are varied within their uncertainties when generating the various datasets. The third source is from bias in the fitting procedure, and likewise is estimated by using toy pseudo-experiments, where the systematic deviation from the true signal yield is evaluated.

Fit Model Choice

The nominal fit consists of double Crystal-Ball PDFs for the signal and cross-feed distributions, an ARGUS function convoluted with a Gaussian resolution function to model the partially-reconstructed background, and an exponential function to account for the combinatorial background. To estimate the systematic uncertainty introduced by the choice of these models they are replaced with equivalent alternative models, the fit repeated, and the systematic uncertainty taken to be the deviation of the result with respect to that of the nominal fit.

In particular, the signal and cross-feed models are replaced with double Gaussian functions with a common mean, the partially reconstructed background PDFs are replaced with `RooKeysPdf` kernel density estimates, and the combinatorial background model is replaced with a second order Chebychev polynomial.

The absolute systematic uncertainty on the ratio of the signal and normalisation yields, when averaging over all data categories, is less than 1% when the signal models are substituted, less than 1% when the partially-reconstructed background models are substituted, and around 2% when the combinatorial background model is substituted.

Fixed Parameters

To increase the simultaneous fit stability certain shape parameters are determined by fits to MC and then fixed in the final fit. To estimate the systematic uncertainty introduced by these fixed parameters, an ensemble of toy pseudoexperiments is generated based on the nominal fit results. Using the covariance matrix from the fits to simulation, new sets of values for the fixed PDF parameters are also generated. Every toy experiment is fitted using each of these new sets of values as well as the nominal values. The difference between the yield returned by the fit using the nominal parameter values and the yields from each of the fits using the modified parameter values is determined, and the systematic uncertainty is assigned to be the average value of the standard deviation over the ensemble of toy experiments. To reduce statistical fluctuations due to the small yields extracted in the fit to data, these toys are generated with yields that are several times those observed in data.

The absolute systematic uncertainty on the ratio of signal and normalisation yields estimated from this procedure is, when averaging over all data categories, less than 1% for all modes except $\Lambda_b^0 \to \Lambda K^+ K^-$, where it is around 2%.

5.5.5 Normalisation Channel Branching Fraction

The product branching fraction of the $\Lambda_b^0 \to \Lambda_c^+(\Lambda\pi^+)\pi^-$ normalisation mode is $(6.29 \pm 0.78) \times 10^{-5}$ [11, 36, 37]. This uncertainty is included as a systematic on the absolute branching fraction. Also included in the systematic uncertainties is the statistical uncertainty on the normalisation yield extracted from the fit.

5.6 Branching Fractions

For each mode under investigation, there are six data categories and therefore six separate yields extracted in the fit (for DD and LL, and for 2011, 2012a, and 2012b). For each of these, the individual branching fraction ratio, Eq. 5.1, is calculated via profile likelihood scans for the yields converted into the ratio of efficiency-corrected yields. These consist of the maximum likelihood value of a fit performed when the yields are fixed to a particular value of the yield. These are then convoluted with Gaussian distributions with mean zero and width equal to the corresponding total systematic uncertainty for the category.

These results are then combined into the likelihood scan for the total branching fraction ratio for each mode by summing the log-likelihoods. To calculate the contribution of the individual sources of systematic uncertainty to the total systematic uncertainty on the final branching fraction ratio, as in Table 5.8, a weight is calculated that corresponds to the relative contribution of each of the data categories at the maximal likelihood value. As each data category necessarily has a different value for a particular source of uncertainty, this weight is applied to each data category for each systematic type to obtain the total contribution of that systematic uncertainty.

The absolute branching fraction ratio is also calculated, using the LHCb results for $\mathcal{B}(\Lambda_b^0 \to \Lambda_c^+\pi^-)$ [11], the FOCUS results for $\mathcal{B}(\Lambda_c^+ \to \Lambda\pi^+)/\mathcal{B}(\Lambda_c^+ \to pK^-\pi^+)$ [36], and the Belle results for $\mathcal{B}(\Lambda_c^+ \to pK^-\pi^+)$ [37]. Upper limits are reported only in terms of these absolute branching fractions.

Assuming gaussianity of the likelihoods around the maxima, the 68% confidence interval around the central value is calculated as the values at which twice the log-likelihood with respect to the minimum changes by one unit. The combined branching fractions, relative to the $\Lambda_b^0 \to \Lambda_c^+(\Lambda\pi^+)\pi^-$ normalisation mode, are therefore found to be

$$\frac{\mathcal{B}(\Lambda_b^0 \to \Lambda\pi^+\pi^-)}{\mathcal{B}(\Lambda_b^0 \to \Lambda_c^+(\Lambda\pi^+)\pi^-)} = (7.3 \pm 1.9\,(\text{stat}) \pm 2.2\,(\text{syst})) \times 10^{-2},$$

$$\frac{\mathcal{B}(\Lambda_b^0 \to \Lambda K^+\pi^-)}{\mathcal{B}(\Lambda_b^0 \to \Lambda_c^+(\Lambda\pi^+)\pi^-)} = (8.9 \pm 1.2\,(\text{stat}) \pm 1.3\,(\text{syst})) \times 10^{-2},$$

$$\frac{\mathcal{B}(\Lambda_b^0 \to \Lambda K^+K^-)}{\mathcal{B}(\Lambda_b^0 \to \Lambda_c^+(\Lambda\pi^+)\pi^-)} = (25.3 \pm 1.9\,(\text{stat}) \pm 1.9\,(\text{syst})) \times 10^{-2},$$

$$\frac{\mathcal{B}(\Xi_b^0 \to \Lambda\,\pi^+\pi^-)}{\mathcal{B}(\Lambda_b^0 \to \Lambda_c^+(\Lambda\,\pi^+)\,\pi^-)} \times f_{\Xi_b^0}/f_{\Lambda_b^0} = (2.0 \pm 1.0\,(\text{stat}) \pm 0.8\,(\text{syst})) \times 10^{-2}\,,$$
$$\frac{\mathcal{B}(\Xi_b^0 \to \Lambda\,K^+\pi^-)}{\mathcal{B}(\Lambda_b^0 \to \Lambda_c^+(\Lambda\,\pi^+)\,\pi^-)} \times f_{\Xi_b^0}/f_{\Lambda_b^0} = (0.1 \pm 0.8\,(\text{stat}) \pm 0.4\,(\text{syst})) \times 10^{-2}\,.$$

These correspond to absolute branching fractions of

$$\begin{aligned}
\mathcal{B}(\Lambda_b^0 \to \Lambda\,\pi^+\pi^-) &= (4.6 \pm 1.2\,(\text{stat}) \pm 1.4\,(\text{syst}) \pm 0.6\,(\text{norm})) \times 10^{-6}\,,\\
\mathcal{B}(\Lambda_b^0 \to \Lambda\,K^+\pi^-) &= (5.6 \pm 0.8\,(\text{stat}) \pm 0.8\,(\text{syst}) \pm 0.7\,(\text{norm})) \times 10^{-6}\,,\\
\mathcal{B}(\Lambda_b^0 \to \Lambda\,K^+K^-) &= (15.9 \pm 1.2\,(\text{stat}) \pm 1.2\,(\text{syst}) \pm 2.0\,(\text{norm})) \times 10^{-6}\,,\\
\mathcal{B}(\Xi_b^0 \to \Lambda\,\pi^+\pi^-) \times f_{\Xi_b^0}/f_{\Lambda_b^0} &= (1.3 \pm 0.6\,(\text{stat}) \pm 0.5\,(\text{syst}) \pm 0.2\,(\text{norm})) \times 10^{-6}\,,\\
\mathcal{B}(\Xi_b^0 \to \Lambda\,K^+\pi^-) \times f_{\Xi_b^0}/f_{\Lambda_b^0} &= (0.6 \pm 0.5\,(\text{stat}) \pm 0.3\,(\text{syst}) \pm 0.1\,(\text{norm})) \times 10^{-6}\,.
\end{aligned}$$

Where, in the case of the Ξ_b^0 modes, the ratio of fragmentation fractions $f_{\Xi_b^0}/f_{\Lambda_b^0}$ is yet to be measured, so the product of the final branching fractions and this ratio are reported.

An example of the individual $\Delta \log \mathcal{L}$ curves for each data category and the combined $\Delta \log \mathcal{L}$, including all systematics, for the $\Lambda_b^0 \to \Lambda\,\pi^+\pi^-$ branching fraction ratio, can be seen in Fig. 5.9.

5.6.1 Significances

Significances are calculated using the above-mentioned log-likelihood scans, where the significance in Gaussian standard deviations is given by $\sqrt{2\Delta \ln \mathcal{L}}$, where $\Delta \ln \mathcal{L}$ is the difference in log-likelihood between the zero signal yield (null) model and the nominal fit model. The results of this can be seen in Table 5.9, which includes significances where only the statistical uncertainty on the total yield is taken into account, and where both the statistical and systematic uncertainties are included in the log-likelihood scan.

5.6.2 Upper Limits

The likelihood fit is well behaved only when the yield parameter for the $\Xi_b^0 \to \Lambda\,K^+K^-$ mode is constrained to be positive. However, as it is still possible to use the information on the background yields obtained from this fit, the problem lends itself naturally to a *hierarchical* Bayesian model, HBM, where the parameters of the prior distribution for the background contributions are taken from the likelihood fit. This HBM is then evaluated using Markov chain Monte-Carlo, MCMC.

Table 5.9 Significances for signal modes where the only statistical uncertainty is taken into account, and corresponding values where the systematic uncertainty is also included. Modes where the significance is negligible are not included

Mode	Stat. (σ)	Stat. + Syst. (σ)
$\Lambda_b^0 \to \Lambda\,\pi^+\pi^-$	5.2	4.7
$\Lambda_b^0 \to \Lambda\,K^+\pi^-$	8.5	8.1
$\Lambda_b^0 \to \Lambda\,K^+K^-$	20.5	15.8
$\Xi_b^0 \to \Lambda\,\pi^+\pi^-$	2.8	2.5

The Ξ_b^0 signal region is defined to be the range $5763 < m(\Lambda K^+K^-) < 5823$ MeV (approximately twice the width of the signal distribution from simulated data), and it is assumed that the total observed yield in this region is the Poisson distributed sum of a background and signal component. The yield of the combinatorial background component is obtained from the nominal fit and is introduced as a truncated Gaussian prior on the Poisson rate parameter of the background distribution. The prior on the branching fraction ratio is taken to be uniform in [0, 100].

The normalisation mode yield, and efficiencies for the signal and normalisation modes, are introduced directly into this calculation, along with their uncertainties, as 1-dimensional log-normal distributions. In this way, the 'partial' branching fractions – branching fractions calculated for a single category only – can be combined by maximising the total posterior probability (much like the combination of likelihoods above). This can be implemented as a simple deterministic transformation of the signal yield via the samples drawn from the log-normal and Gaussian distributions corresponding to the efficiencies and normalisation yield. However, an uncertainty can be introduced, for example, in the ratio of the signal and normalisation efficiencies by assuming that this ratio is itself drawn from a Gaussian distribution with mean equal to the ratio of signal and normalisation values, and width equal to the systematic uncertainty on this ratio. In this way, external systematic uncertainties that depend on the data category, such as those from the PID calibration procedure, are introduced to the total combined branching fraction.

To perform the numerical marginalisation over the nuisance parameters, the Metropolis-Hastings MCMC implementation in the PyMC package [38] is used, and the combination is performed in practice by requiring a common branching fraction for all categories. The limit in this case is calculated integrating the posterior probability of the branching fraction value to the 90 (95)th percentile.

These upper limits on the Ξ_b^0 branching fractions correspond to

$$\mathcal{B}(\Xi_b^0 \to \Lambda\,\pi^+\pi^-) \times f_{\Xi_b^0}/f_{\Lambda_b^0} < 1.7\ (2.1) \times 10^{-6} \text{ at } 90\ (95)\,\% \text{ confidence level},$$
$$\mathcal{B}(\Xi_b^0 \to \Lambda\,K^+\pi^-) \times f_{\Xi_b^0}/f_{\Lambda_b^0} < 0.8\ (1.0) \times 10^{-6} \text{ at } 90\ (95)\,\% \text{ confidence level},$$
$$\mathcal{B}(\Xi_b^0 \to \Lambda\,K^+K^-) \times f_{\Xi_b^0}/f_{\Lambda_b^0} < 0.3\ (0.4) \times 10^{-6} \text{ at } 90\ (95)\,\% \text{ confidence level},$$

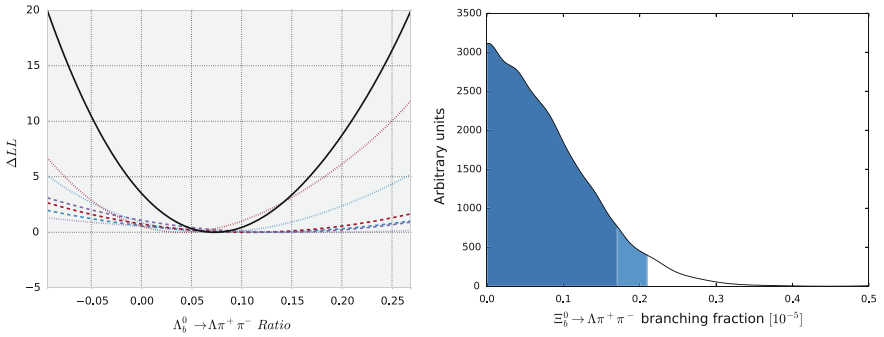

Fig. 5.9 Individual $\Delta \log \mathcal{L}$ curves for each data category (dashed and dotted-lines) and the combined (solid-black line) $\Delta \log \mathcal{L}$ curve, including all systematics, for the $\Lambda_b^0 \to \Lambda\,\pi^+\pi^-$ branching fraction ratio (left), and posterior probability of the absolute $\Xi_b^0 \to \Lambda\,\pi^+\pi^-$ branching fraction, multiplied by $f_{\Xi_b^0}/f_{\Lambda_b^0}$, as calculated from the HBM (right). The region shaded in dark-blue is 90% of the integral of the distribution in the range $[0, \infty]$, and the dark-blue plus light-blue regions comprise 95% of this distribution

which are consistent with the conventional profile likelihood integration procedure (except where, in the case of the $\Xi_b^0 \to \Lambda\,K^+K^-$ limit, this comparison is not possible). As a cross-check, various other parametric forms of the priors listed in Sect. 5.6.2 were tried, with corresponding parameters, all giving consistent results. The Markov chains used to obtain these results were verified to have converged successfully, and give negligible contribution to the resulting total uncertainty on the parameters.

These Bayesian limits are often more correctly known as *credible* regions, which emphasises that these are the result of marginalisation over the nuisance parameters and integration of the resulting posterior probability, and therefore do not guarantee frequentist coverage. In this case however, the coverage of these limits is verified using random pseudoexperiments generated assuming a range of true branching fractions up to a value of 3×10^{-6}.

The posterior probability distribution for the absolute branching fraction of $\Xi_b^0 \to \Lambda\,\pi^+\pi^-$, multiplied by $f_{\Xi_b^0}/f_{\Lambda_b^0}$, can be seen in Fig. 5.9, where the 90–95% regions are indicated.

5.7 *CP* Asymmetry Measurements

The significant yields observed for the $\Lambda_b^0 \to \Lambda K^+\pi^-$ and ΛK^+K^- decays allow measurements of their phase-space integrated *CP* asymmetries, using the $\Lambda_b^0 \to \Lambda_c^+(\Lambda\pi^+)\pi^-$ decay as a control mode, to account for production, $\mathcal{A}_{\rm P}$, and detection, $\mathcal{A}_{\rm D}$, asymmetries. The simultaneous extended maximum likelihood fit is modified to allow the determination of the raw asymmetry, defined as

Table 5.10 Systematic uncertainties on $\mathcal{A}_{CP}$ (10^{-3})

Systematic	$\mathcal{A}_{CP}(\Lambda_b^0 \to \Lambda K^+\pi^-)$	$\mathcal{A}_{CP}(\Lambda_b^0 \to \Lambda K^+K^-)$
Control mode	66	57
PID asymmetry	20	–
Fit model	27	32
Fit bias	14	4
Efficiency uncertainty	80	28
Total	110	71

$$\mathcal{A}_{CP}^{\text{raw}} = \frac{N_f^{\text{corr}} - N_{\bar{f}}^{\text{corr}}}{N_f^{\text{corr}} + N_{\bar{f}}^{\text{corr}}}\,, \tag{5.11}$$

where N_f^{corr} ($N_{\bar{f}}^{\text{corr}}$) is the efficiency-corrected yield for Λ_b^0 ($\overline{\Lambda}_b^0$) decays. These efficiencies are calculated identically to those for the branching fraction analysis (see Sect. 5.3), but separately for Λ_b^0 and $\overline{\Lambda}_b^0$. The use of the efficiency-corrected yields accounts for the possibility that there may be larger *CP*-violation effects in certain regions of phase-space, as seen in other charmless three-body b-hadron decays [5], and ensures that the reported values do not encode information related to the selection efficiency.

The measured raw asymmetries, including the efficiency correction for the signal modes, for $\Lambda_b^0 \to \Lambda K^+\pi^-$, $\Lambda_b^0 \to \Lambda K^+K^-$, and $\Lambda_b^0 \to \Lambda_c^+(\Lambda\pi^+)\pi^-$ are determined by a performing simultaneous fit to the samples of Λ_b^0 and $\overline{\Lambda}_b^0$ candidates. They are found to be $\mathcal{A}_{CP}^{\text{raw}}(\Lambda_b^0 \to \Lambda K^+\pi^-) = -0.46 \pm 0.23$, $\mathcal{A}_{CP}^{\text{raw}}(\Lambda_b^0 \to \Lambda K^+K^-) = -0.21 \pm 0.10$ and $\mathcal{A}_{CP}^{\text{raw}}(\Lambda_b^0 \to \Lambda_c^+(\Lambda\pi^+)\pi^-) = 0.07 \pm 0.07$, where the uncertainties are statistical only, and correlations between the signal yields are taken into account. The asymmetries for the background components are found to be consistent with zero, as expected.

Several sources of systematic uncertainty are considered, as summarised in Table 5.10. The uncertainty on $\mathcal{A}_{\text{P}} + \mathcal{A}_{\text{D}}$ comes directly from the result of the fit to $\Lambda_b^0 \to \Lambda_c^+(\Lambda\pi^+)\pi^-$ decays. The effect of variations of the detection asymmetry with the decay kinematics, which can be slightly different for reconstructed signal and control modes, is negligible. However, for the $\Lambda_b^0 \to \Lambda K^+\pi^-$ channel, a possible asymmetry in kaon detection, which is conservatively taken to be 2% [39], has to be accounted for. Effects related to the choices of signal and background models, possible intrinsic fit biases, and uncertainties in the efficiencies are evaluated in a similar way as for the branching fraction measurements. The total systematic uncertainty is obtained by summing all contributions in quadrature.

The results for the phase-space integrated *CP* asymmetries are

$$\begin{aligned}\mathcal{A}_{CP}(\Lambda_b^0 \to \Lambda K^+\pi^-) &= -0.53 \pm 0.23\,(\text{stat}) \pm 0.11\,(\text{syst})\,,\\ \mathcal{A}_{CP}(\Lambda_b^0 \to \Lambda K^+K^-) &= -0.28 \pm 0.10\,(\text{stat}) \pm 0.07\,(\text{syst})\,,\end{aligned}$$

which are both within 3σ of zero.

5.8 Summary and Subsequent Work

Using a data sample collected by the LHCb experiment corresponding to an integrated luminosity of 3 fb^{-1} of high-energy pp collisions, a search for the charmless three-body decays of b baryons to the $\Lambda\pi^+\pi^-$, $\Lambda K^\pm\pi^\mp$ and ΛK^+K^- final states is performed. The $\Lambda_b^0 \to \Lambda K^+\pi^-$ and $\Lambda_b^0 \to \Lambda K^+K^-$ decay modes are observed for the first time, and their branching fractions and CP asymmetry parameters are measured. Evidence is seen for the $\Lambda_b^0 \to \Lambda\pi^+\pi^-$ decay and limits are set on the branching fractions of the other decay modes studied.

An analysis of the $\Lambda_b^0 \to \Lambda K^+K^-$ decay in the $\phi(1020)$ mass region was published shortly after this work [40], and measured a branching fraction of the $\Lambda_b^0 \to \Lambda\phi$ decay to be $(5.18 \pm 1.04 \pm 0.35^{+0.67}_{-0.62}) \times 10^{-6}$, which is consistent with the branching fraction measured in this analysis and with the enhancement observed at low $m_{K^+K^-}$ in the $\Lambda_b^0 \to \Lambda K^+K^-$ Dalitz plot.

Subsequent phenomenological work [41, 42] indicates that these branching fractions are consistent with predictions from a next-to-leading-order QCD factorisation scheme in the operator-product expansion, and in particular are a useful probe of non-factorisable contributions to quasi-two-body Λ_b^0 decays. Furthermore, comparison with numerical calculations indicates that under this approach, the $\Lambda_b^0 \to \Lambda\pi^+\pi^-$ branching fraction measured in this work is consistent with that expected from dominant $\Lambda_b^0 \to \Lambda f_0(980)$ and $\Lambda_b^0 \to \Lambda f_0(1500)$ contributions.

References

1. BaBar collaboration, J.P. Lees et al., Measurement of CP asymmetries and branching fractions in charmless two-body B-meson decays to pions and kaons. Phys. Rev. **D87**, 052009 (2013). https://doi.org/10.1103/PhysRevD.87.052009, hyperimage-http://arxiv.org/abs/1206.3525arXiv:1206.3525
2. Belle collaboration, Y.-T. Duh et al., Measurements of branching fractions and direct CP asymmetries for $B \to K\pi$, $B \to \pi\pi$ and $B \to KK$ decays. Phys. Rev. **D87**, 031103 (2013). https://doi.org/10.1103/PhysRevD.87.031103, arXiv:1210.1348
3. CDF collaboration, T. Aaltonen et al., Measurements of direct CP violating asymmetries in charmless decays of strange bottom mesons and bottom baryons. Phys. Rev. Lett. **106**, 181802 (2011). https://doi.org/10.1103/PhysRevLett.106.181802, arXiv:1103.5762
4. LHCb collaboration, R. Aaij et al., First observation of CP violation in the decays of B_s^0 mesons. Phys. Rev. Lett. **110**, 221601 (2013). https://doi.org/10.1103/PhysRevLett.110.221601, arXiv:1304.6173
5. LHCb collaboration, R. Aaij et al., Measurement of CP violation in the three-body phase space of charmless B^+ decays. Phys. Rev. **D90**, 112004 (2014). https://doi.org/10.1103/PhysRevD.90.112004, arXiv:1408.5373
6. LHCb collaboration, R. Aaij et al., Observations of $\Lambda_b^0 \to \Lambda K^+\pi^-$ and $\Lambda_b^0 \to \Lambda K^+K^-$ decays and searches for other Λ_b^0 and Ξ_b^0 decays to Λh^+h^- final states. JHEP **05**, 081 (2016). https://doi.org/10.1007/JHEP05(2016)081, arXiv:1603.00413
7. CDF Collaboration, T.A. Aaltonen et al., Measurements of Direct CP-Violating Asymmetries in Charmless Decays of Bottom Baryons. arXiv:1403.5586

8. LHCb collaboration, R. Aaij et al., Measurement of b hadron production fractions in 7 TeV pp collisions. Phys. Rev. **D85**, 032008 (2012). https://doi.org/10.1103/PhysRevD.85.032008, arXiv:1111.2357
9. LHCb collaboration, R. Aaij et al., Study of beauty baryon decays to $D^0 ph^-$ and $\Lambda_c^+ h^-$ final states. Phys. Rev. **D89**, 032001 (2014). https://doi.org/10.1103/PhysRevD.89.032001, arXiv:1311.4823
10. LHCb collaboration, R. Aaij et al., Study of beauty hadron decays into pairs of charm hadrons. Phys. Rev. Lett. **112**, 202001 (2014). https://doi.org/10.1103/PhysRevLett.112.202001, arXiv:1403.3606
11. LHCb collaboration, R. Aaij et al., Study of the kinematic dependences of Λ_b^0 production in pp collisions and a measurement of the $\Lambda_b^0 \to \Lambda_c^+ \pi^-$ branching fraction. JHEP **08**, 143 (2014). https://doi.org/10.1007/JHEP08(2014)143, arXiv:1405.6842
12. LHCb collaboration, R. Aaij et al., Observation of the $\Lambda_b^0 \to J\psi p\pi^-$ decay. JHEP **07**, 103 (2014). https://doi.org/10.1007/JHEP07(2014)103, arXiv:1406.0755
13. LHCb collaboration, R. Aaij et al., Searches for Λ_b^0 and Ξ_b^0 decays to $K_S^0 p\pi^-$ and $K_S^0 pK^-$ final states with first observation of the $\Lambda_b^0 \to K_S^0 p\pi^-$ decay. JHEP **04**, 087 (2014). https://doi.org/10.1007/JHEP04(2014)087, arXiv:1402.0770
14. LHCb collaboration, R. Aaij et al., Observation of the decay $\Xi_b^0 - \to pK^-K^-$. Phys. Rev. Lett. **118**, 071801 (2017). https://doi.org/10.1103/PhysRevLett.118.071801, arXiv:1612.02244
15. X.-H. Guo, A.W. Thomas, Direct CP violation in $\Lambda_b^0 \to n(\Lambda_b^0)\pi^+\pi^-$ decays via $\rho\omega$ mixing. Phys. Rev. D **58**, 096013 (1998). https://doi.org/10.1103/PhysRevD.58.096013, arXiv:hep-ph/9805332
16. S. Arunagiri, C.Q. Geng, T violating triple product asymmetries in $\Lambda_b^0 \to \Lambda\pi^+\pi^-$ decay. Phys. Rev. D **69**, 017901 (2004). https://doi.org/10.1103/PhysRevD.69.017901, arXiv:hep-ph/0307307
17. LHCb collaboration, R. Aaij et al., Measurements of the $\Lambda_b^0 \to J/\psi\Lambda$ decay amplitudes and the Λ_b^0 polarisation in pp collisions at $\sqrt{s} = 7$TeV. Phys. Lett. **B724**, 27 (2013). https://doi.org/10.1016/j.physletb.2013.05.041, arXiv:1302.5578
18. LHCb collaboration, R. Aaij et al., Study of $B_{(s)}^0 \to K_S^0 h^+ h'^-$ decays with first observation of $B_s^0 \to K_S^0 K^\pm \pi^\mp$ and $B_s^0 \to K_S^0 \pi^+\pi^-$. JHEP **10**, 143 (2013). https://doi.org/10.1007/JHEP10(2013)143, arXiv:1307.7648
19. A.K. Giri, R. Mohanta, M.P. Khanna, Possibility of extracting the weak phase gamma from $\Lambda_b^0 \to \Lambda D^0$ decays. Phys. Rev. D **65**, 073029 (2002). https://doi.org/10.1103/PhysRevD.65.073029, arXiv:hep-ph/0112220
20. D. Atwood, I. Dunietz, A. Soni, Enhanced CP violation with $B \to K D^0(\bar{D}^0)$ modes and extraction of the CKM angle γ. Phys. Rev. Lett. **78**, 3257 (1997). https://doi.org/10.1103/PhysRevLett.78.3257, arXiv:hep-ph/9612433
21. D. Atwood, I. Dunietz, A. Soni, Improved methods for observing CP violation in $B^\pm \to K^\pm D$ and measuring the CKM phase γ. Phys. Rev. D **63**, 036005 (2001). https://doi.org/10.1103/PhysRevD.63.036005, arXiv:hep-ph/0008090
22. L. Breiman, J.H. Friedman, R.A. Olshen, C.J. Stone, *Classification and Regression Trees* (Wadsworth international group, USA, 1984)
23. A. Hoecker et al., *TMVA - Toolkit for Multivariate Data Analysis* (2007). arXiv:physics/0703039. ArXiv Physics e-prints
24. G. Punzi, Sensitivity of searches for new signals and its optimization, in *Astrophysics, and Cosmology*, ed. by L. Lyons, R. Mount, R. Reitmeyer (2003), p. 79. arXiv:physics/0308063
25. LHCb collaboration, R. Aaij et al., Search for the $\Lambda_b^0 \to \Lambda\eta$ and $\Lambda_b^0 \to \Lambda\eta'$ decays with the LHCb detector. JHEP **09**, 006 (2015). https://doi.org/10.1007/JHEP09(2015)006, arXiv:1505.03295
26. Particle Data Group, C. Patrignani et al., Review of particle physics. Chin. Phys. **C40**, 100001 (2016). https://doi.org/10.1088/1674-1137/40/10/100001, http://pdg.lbl.gov/. 2017 update

27. LHCb collaboration, R. Aaij et al., Measurement of matter-antimatter differences in beauty baryon decays. Nat. Phys. **13**, 391 (2017). https://doi.org/10.1038/nphys4021, arXiv:1609.05216
28. L. Anderlini et al., The PIDCalib package. http://cdsweb.cern.ch/search?p=LHCb-PUB-2016-021&f=reportnumber&action_search=Search&c=LHCb+Reports
29. A. Puig, The LHCb trigger in 2011 and 2012, LHCb-PUB-2014-046. http://cdsweb.cern.ch/search?p=LHCb-PUB-2014-046&f=reportnumber&action_search=Search&c=LHCb+Reports
30. Particle Data Group, K.A. Olive et al., Review of particle physics. Chin. Phys. **C38**, 090001 (2014). https://doi.org/10.1088/1674-1137/38/9/090001, http://pdg.lbl.gov/. 2015 update
31. LHCb collaboration, R. Aaij et al., Study of the $D^0 p$ amplitude in $\Lambda_b^0 \to D^0 p\pi^-$ decays. JHEP **05**, 03 (2017). https://doi.org/10.1007/JHEP05(2017)030, arXiv:1701.07873
32. LHCb collaboration, R. Aaij et al., Observation of overlapping spin-1 and spin-3 $\bar{D}^0 K^-$ resonances at mass 2.86GeV/c^2. Phys. Rev. Lett. **113**, 162001 (2014). https://doi.org/10.1103/PhysRevLett.113.162001, arXiv:1407.7574
33. LHCb collaboration, R. Aaij et al., Dalitz plot analysis of $B_s^0 \to \bar{D}^0 K^-\pi^+$ decays. Phys. Rev. **D90**, 072003 (2014). arXiv:1407.7712
34. LHCb collaboration, R. Aaij et al., Precision measurement of the mass and lifetime of the Ξ_b^0 baryon. Phys. Rev. Lett. **113**, 032001 (2014). https://doi.org/10.1103/PhysRevLett.113.032001, arXiv:1405.7223
35. F. Porter, Low statistics likelihood fits are tricky. http://www.hep.caltech.edu/~fcp/statistics/maxlikfitnote.ps
36. FOCUS collaboration, J.M. Link et al., Study of Λ_c^+ Cabibbo-favored decays containing a Λ baryon in the final state. Phys. Lett. **B624**, 22 (2005). https://doi.org/10.1016/j.physletb.2005.08.014, arXiv:hep-ex/0505077
37. Belle collaboration, A. Zupanc et al., Measurement of the branching fraction $\mathcal{B}(\Lambda_c^+ \to pK^-\pi^+)$. Phys. Rev. Lett. **113**, 042002 (2014). https://doi.org/10.1103/PhysRevLett.113.042002, arXiv:1312.7826
38. A. Patil, D. Huard, C. Fonnesbeck, PyMC: Bayesian stochastic modelling in Python. J.Stat. Softw. **35** (2010). https://doi.org/10.18637/jss.v035.i04
39. LHCb collaboration, R. Aaij et al., Measurement of CP asymmetry in $D^0 \to K^-K^+$ and $D^0 \to \pi^-\pi^+$ decays. JHEP **07**, 041 (2014). https://doi.org/10.1007/JHEP07(2014)041, arXiv:1405.2797
40. LHCb collaboration, R. Aaij et al., Observation of the $\Lambda_b \to \Lambda_\phi$ decay. Phys. Lett. **B759**, 282 (2016). https://doi.org/10.1016/j.physletb.2016.05.077, arXiv:1603.02870
41. C.Q. Geng, Y.K. Hsiao, Y.-H. Lin, Y. Yu, Study of $\Lambda_b \to \Lambda(\phi, \eta^{(\prime)})$ and$\Lambda_b \to \Lambda K^+K^-$ decays. Eur. Phys. J. C **76**, 399 (2016). https://doi.org/10.1140/epjc/s10052-016-4255-x, arXiv:1603.06682
42. Y.K. Hsiao, Y.-H. Lin, Y. Yu, C.Q. Geng, Roles of scalar mesons in charmless Λ_b decays. Phys. Rev. D **93**, 114008 (2016). https://doi.org/10.1103/PhysRevD.93.114008, arXiv:1604.04043

Chapter 6
Amplitude Analysis

Multi-body decays of unstable particles proceed, where permitted, via various short-lived intermediate resonant states. To probe the interactions that govern these decays, an understanding of the quantum-mechanical amplitude that describes these process is required.

The distributions of the angular components of this amplitude are well known and constrained by angular momentum conservation, which permits the separation of various interfering resonant components of differing spin. Interfering components of the same spin result in complicated distributions in the invariant-mass projections that are not as well understood, and are further complicated by the numerous decay channels opening with increasing invariant-mass. In addition to the construction of the amplitude, there are also various issues related to the implementation and inference of the parameters of the amplitude model that are peculiar to amplitude analyses.

6.1 Introduction

Amplitude analyses are used to decouple the various resonant and non-resonant intermediate states in the decay of a heavy hadron in order to better understand the decay dynamics: e.g., investigations into the relative rates of the intermediate quasi-two-body decays; studying how CP violation arises in the production of the intermediate resonances; or to understand the nature of the intermediate resonances themselves. This study of the characteristic enhancement in the inclusive decay rate is the only way to investigate bound states of quarks that decay rapidly via the strong force. As the strong force conserves CP, only their production in the weak-mediated b-hadron decay can violate CP. These resonance states interfere quantum-mechanically with each other, giving sensitivity to potential CP violation manifesting in the relative phases between the resonant contributions, additionally permitting inference of the strong and weak phase variations across the phase-space. In general, resonances that do not decay promptly are removed from the phase-space

© Springer Nature Switzerland AG 2018

D. O'Hanlon, *Studies of* CP-*Violation in Charmless Three-Body* b-*Hadron Decays*,
Springer Theses, https://doi.org/10.1007/978-3-030-02206-8_6

distribution, as their long lifetime implies a very narrow width, resulting in negligible interference with the rest of the resonant contributions.

This Chapter is presented in the context of the amplitude analysis of $B^+ \to \pi^+\pi^+\pi^-$, the decay of a scalar B^+ meson into three pseudoscalar charged pions, where the results of the analysis of this decay mode with Run 1 LHCb data is presented in Chap. 7.

6.2 Three-Body Kinematics

For a generic three-body decay, there are twelve possible degrees-of-freedom, from the three 4-vectors of the final state particles. Knowledge of the final-state particle masses removes three of these, and energy-momentum conservation removes another four. For a (pseudo)scalar decaying into three (pseudo)scalars, there is no angular dependence to the decay (and therefore no preferred orientation in space) and these can be integrated out, leaving two remaining degrees of freedom. These are commonly taken to be two of the three invariant-mass-pairs squared, $m^2_{ij} = (p^\mu_i + p^\mu_j)^2$.

Further useful variables are the momentum of one of the resonance daughters in the resonance rest frame, q, the momentum of the 'bachelor' b-hadron daughter (the decay product that does not arise from an intermediate resonance) in the resonance rest frame, p, and the momentum of the bachelor in the b-hadron rest frame, p^*. The *helicity* angle, θ_{hel}, is the angle between one of the resonance daughters and the bachelor meson in the resonance rest frame. These can be related back to the invariant-mass-pairs squared, for example,

$$\begin{aligned} m^2_{13} &= (p^\mu_1 + p^\mu_3)^2 = (-2pq\cos\theta_{13}) + m^2_1 + m^2_2 + 2E_1E_3, \\ &= (-2pq\cos\theta_{13}) + m^2_1 + m^2_3 + 2\sqrt{p + m^2_1}\sqrt{q + m^2_3}, \end{aligned} \tag{6.1}$$

where here the helicity angle is denoted θ_{13}, and the invariant-masses and energies of the daughter particles are m_i and E_i, respectively.

6.3 The Dalitz Plot

The two-dimensional distribution of two invariant-mass pairs squared is known as the *Dalitz* plot [1]. For the decay of a scalar into three pseudoscalars, where there are only two degrees of freedom, it provides a visualisation of all of the intermediate decay dynamics. A schematic of the Dalitz plot and its kinematical boundaries can be seen in Fig. 6.1.

If there are no intermediate structures, the distribution in this space will be uniform. However, a resonant contribution in, for example, $B \to R(P_1P_3)P_2$ will produce a band at the invariant-mass-squared of the resonance, R, at $m^2_{13} = m^2_R$, across the full

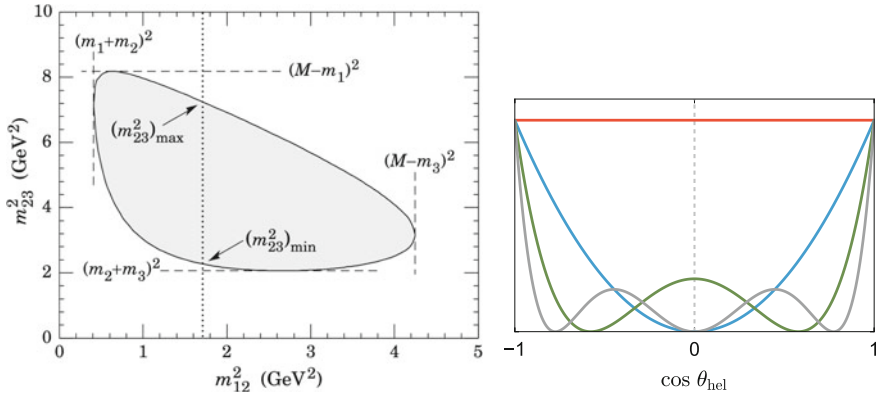

Fig. 6.1 Left: Schematic of the (unsymmetrised) conventional Dalitz-plot, with values corresponding to the boundaries and corners indicated. Right: Distributions of the decay intensities projected on the cosine of the helicity angle, (corresponding to the squares of unnormalised Legendre polynomial angular momentum eigenfunctions), for intermediate resonances exclusively of spin-0 (orange), spin-1 (blue), spin-2 (green), and spin-3 (grey)

extent of m^2_{23} (and vice-versa for a decay $B \to R(P_2P_3)P_1$, however a decay $B \to R(P_1P_2)P_3$ in this configuration will result in a diagonal band). This band in general is not uniform in m^2_{23}, as conservation of total angular momentum enforces a structure in the cosine of the helicity angle, $\cos\theta_{13}$, as described in Sect. 6.4.2. The angular distribution is reflected in m^2_{23}, as m^2_{23} can be expressed in terms of the cosine of the helicity angle, per Eq. 6.1. Hence, an isolated resonance's spin, or more correctly, the relative orbital angular momentum between the resonance and the bachelor meson (where in the case of a scalar meson decaying into three pseuduoscalar mesons, these are equivalent), is uniquely determined by the distribution in the Dalitz plot.

6.4 The Isobar Formalism

The main simplifying assumption made in amplitude analyses is that the total three-body amplitude can be expressed as a sum of successive amplitudes of two-body decays. This is known as the isobar formalism, and is in general a good approximation for the decays of B and D mesons.

In this case, the total amplitude is

$$\mathcal{A}(m^2_{13}, m^2_{23}) = \sum_j c_j F_j(m^2_{13}, m^2_{23}), \tag{6.2}$$

where c_j are the complex isobar coefficients that govern the relative magnitudes and interferences between the contributions, and are in general extracted in a fit to the data, and F_j are the normalised dynamical components that describe the properties

of the j resonant contribution. The entire K-matrix (described in Sect. 6.5.4), enters as only one of these terms with a single overall magnitude and phase relative to the rest of the contributions, in addition to the other parameters of the K-matrix model that are left free in the fit.

For the decay of a scalar meson, B, into three pseudoscalar mesons P_1, P_2, and P_3, via the decay of an intermediate resonance of arbitrary spin, R, $B \to R(P_1P_2)P_3$, this matrix element can be written in terms of a matrix element for the production process, a matrix element for the decay process, and a propagator, $T_R(m)$, for an intermediate state with mass m, as

$$F = \sum_{\lambda} \langle P_1 P_2 | R_\lambda \rangle \; T_R(m) \; \langle P_3 R_\lambda | B \rangle, \tag{6.3}$$

where, as the polarisation states of the intermediate resonance are not observed, there is the sum is over the helicity states, λ, of the intermediate resonance. This dynamical term can be written as a product of the invariant-mass lineshape, T, the angular distribution, Z, and the Blatt–Weisskopf barrier factors, X, that represent a correction to the amplitude due to the spatial extent of the intermediate resonance and the b-hadron,

$$F(m_{13}^2, m_{23}^2) = T(m_{13}) \cdot Z(\vec{p}, \vec{q}, L) \cdot X(p r_{\mathrm{BW}}, L) \cdot X(q r_{\mathrm{BW}}, L). \tag{6.4}$$

6.4.1 Blatt–Weisskopf Form Factors

Fundamental particles are pointlike, however bound states of quarks must have some finite spatial extent (analogous to the semi-classical impact parameter). Due to the potential well that this creates, the maximum angular momentum is limited by $2q$, the relative momentum of the decay particles in the resonance rest frame. Decaying particles moving slowly cannot generate sufficient angular momentum to conserve the spin of the resonance, and therefore these decays – both of the parent b-meson and the resonance – are suppressed, introducing an extra momentum dependence to the lineshape.

This additional dependence is introduced by assuming that the hadron forms a harmonic potential well [2, 3], and are included in the amplitude by multiplicative factors defined in terms of $z = q\, r_{\mathrm{BW}}$ (or $p\, r_{\mathrm{BW}}$),

$$\begin{aligned} L = 0 \;:\; & X(z) = 1\,, \\ L = 1 \;:\; & X(z) = \sqrt{\frac{1 + z_0^2}{1 + z^2}}\,, \\ L = 2 \;:\; & X(z) = \sqrt{\frac{z_0^4 + 3z_0^2 + 9}{z^4 + 3z^2 + 9}}\,, \end{aligned}$$

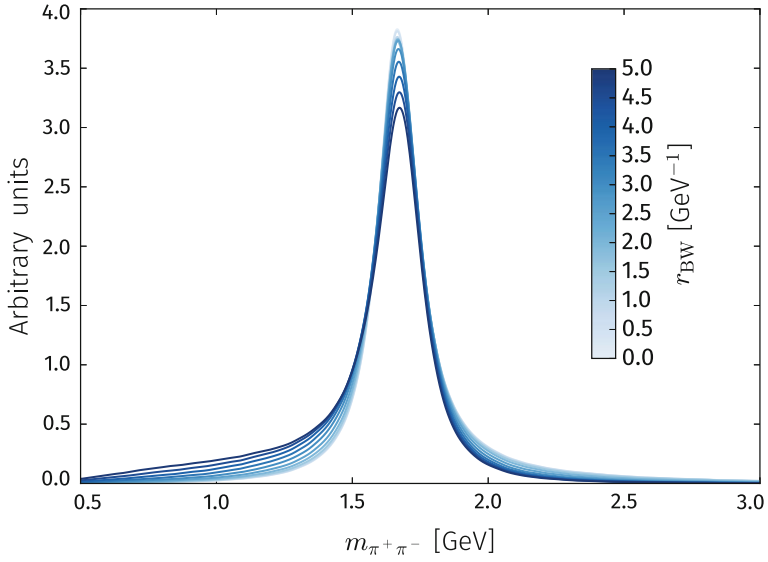

Fig. 6.2 Distribution of the $\rho_3(1690)$ resonance, modelled with a spin-3 relativistic Breit–Wigner, in $\pi^+\pi^-$ invariant mass for various values of the resonance Blatt–Weisskopf barrier radius

$$L = 3 \;:\; X(z) = \sqrt{\frac{z_0^6 + 6z_0^4 + 45z_0^2 + 225}{z^6 + 6z^4 + 45z^2 + 225}},$$
$$L = 4 \;:\; X(z) = \sqrt{\frac{z_0^8 + 10z_0^6 + 135z_0^4 + 1575z_0^2 + 11025}{z^8 + 10z^6 + 135z^4 + 1575z^2 + 11025}}. \tag{6.5}$$

where z_0 represents the value of z when $m = m_0$. The value of the barrier radius, r_{BW}, is often taken to be in range 2–4 GeV^{-1}. The effect of this choice on the invariant-mass distribution for the spin-3 $\rho_3(1690)$ resonance can be seen in Fig. 6.2.

An important point to note is that these distributions only result in the correct behaviour of the overall amplitude when combined with the explicit parameterisations of the angular distributions and mass-dependent width of the relativistic Breit–Wigner described in this Chapter (in the Particle Data Group review [4] these are the B' barrier factors), such that all parameters are evaluated in the correct reference frame.

6.4.2 Angular Distributions

The angular distributions in the cosine of the helicity angle, $\cos\theta_{13}$, result from the conservation of angular momentum between the resonance and the bachelor meson, and therefore from the spin of the intermediate resonance. As such these are in terms

of the Legendre polynomials that represent the eigenfunctions of angular momentum, which can be seen in Fig. 6.1.

Using the Zemach tensor formalism [5, 6], the angular probability distribution terms $Z(\vec{p},\vec{q})$ are given by

$$\begin{aligned}
L=0 &: Z(\vec{p},\vec{q}) = 1,\\
L=1 &: Z(\vec{p},\vec{q}) = -2\,\vec{p}\cdot\vec{q},\\
L=2 &: Z(\vec{p},\vec{q}) = \frac{4}{3}\left[3(\vec{p}\cdot\vec{q})^2-(|\vec{p}\,||\vec{q}\,|)^2\right],\\
L=3 &: Z(\vec{p},\vec{q}) = -\frac{24}{15}\left[5(\vec{p}\cdot\vec{q})^3-3(\vec{p}\cdot\vec{q})(|\vec{p}\,||\vec{q}\,|)^2\right],\\
L=4 &: Z(\vec{p},\vec{q}) = \frac{16}{35}\left[35(\vec{p}\cdot\vec{q})^4-30(\vec{p}\cdot\vec{q})^2(|\vec{p}\,||\vec{q}\,|)^2+3(|\vec{p}\,||\vec{q}\,|)^4\right].
\end{aligned} \tag{6.6}$$

The factors of pq form part of the Blatt–Weisskopf form factors described in Sect. 6.4.1.

6.4.3 Interference Effects

All modern amplitude analyses are performed via the construction of a quantitative model of the contributing amplitudes and their interferences, the parameters of which are inferred by some statistical procedure. However, it is instructive to investigate the qualitative features of the Dalitz plot, such that this may guide the physical interpretation of the models in Chap. 7.

The sensitivity to the relative phases of each resonant component arises from the interference terms in the amplitude. Considering a very simple amplitude model with only two contributing resonance components (in the same pair of daughter particles), total intensity (magnitude of the total amplitude squared) can be written as

$$\begin{aligned}
|\mathcal{A}|^2 &= |T_1(m^2)Z_1(\theta)+T_2(m^2)Z_2(\theta)|^2\\
&= Z_1^2[Re(T_1)^2+Im(T_1)^2]+Z_2^2[Re(T_2)^2+Im(T_2)^2]\\
&\quad +2Z_1Z_2[Re(T_1)Re(T_2)+Im(T_1)Im(T_2)],
\end{aligned} \tag{6.7}$$

where m is the invariant mass of the two daughter particles from the resonance decay, and θ is the corresponding helicity angle. The factors that do not depend on θ (such as the Blatt–Weisskopf form factors) have been subsumed into the definition of $T_i(m^2)$, and Z is real. The last term in this expression is the *interference* term, and gives sensitivity to the physical phase difference between the two contributions. Much like the individual resonance components, this interference term (in the absence of efficiency effects), has a helicity angle distribution proportional to the product of Legendre polynomials when the above expression is integrated over m^2. This has

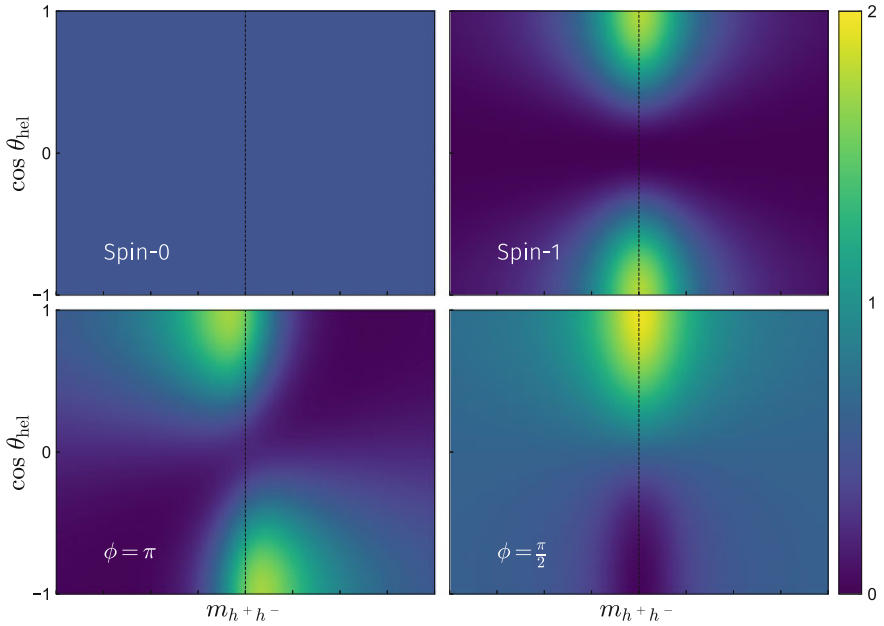

Fig. 6.3 Magnitude-squared of the total amplitude (z-axis), in the cosine of the helicity angle and di-hadron invariant mass, for interfering spin-0 (distributed flat in $m_{h^+h^-}$) and spin-1 (distributed with a relativistic Breit–Wigner in $m_{h^+h^-}$) components. The relative isobar phase, ϕ, is π in the bottom-left, and $\frac{\pi}{2}$ in the bottom-right. The magnitude-squared of the amplitude where the decay proceeds purely via the spin-0 contribution can be seen in the top-left, and in the top-right for the decay purely via a spin-1 resonance. Note that regardless of the relative phase, the projection on the di-hadron invariant-mass is the same, but the projection on the cosine of the helicity angle is modified

important consequences when inferring the properties, or existence, of intermediate resonances.

When the spins of two interfering resonances are different, the interference term from the products of the corresponding Legendre polynomials can be an odd function of $\cos\theta$, and therefore in these cases, when projected on to the invariant-mass axis (i.e., integrating across $\cos\theta$), the effect of the interference vanishes.[1] When projecting on to the helicity angle axis however, a structure appears that is sensitive to the relative isobar phases between the two resonances. An example of this, using toy data sampled from relativistic Breit–Wigner functions representing a broad spin-0 resonance interfering with a narrower spin-1 resonance, can be seen in Fig. 6.3, for two values of the relative isobar phase. Also of note is that this depends on the phase evolution of the relativistic Breit–Wigner: In the case of a relative isobar phase of π,

[1] For $B^+ \to \pi^+\pi^+\pi^-$, the symmetrisation of the amplitude by a folding of the Dalitz-plot results in this only being true at low mass for projection on the low-mass combination of oppositely charged pions (and high mass for the projection on the high-mass combination), as the full helicity range is not integrated over.

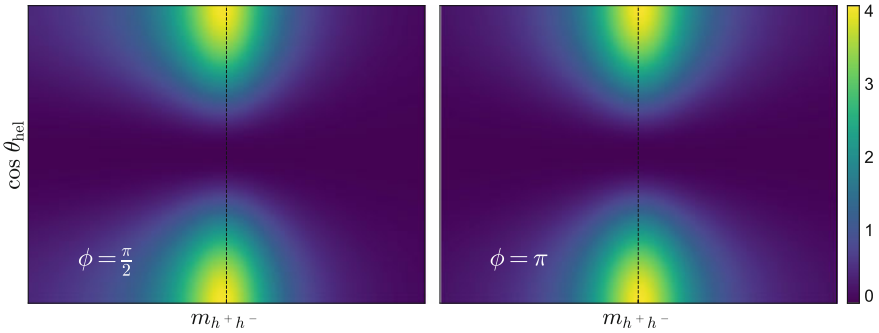

Fig. 6.4 Distributions in the cosine of the helicity angle and di-hadron invariant mass for two interfering (and overlapping in mass) spin-1 resonances of equal isobar magnitude, where the relative isobar phase, ϕ, is $\frac{\pi}{2}$ on the left, and π on the right. Note that regardless of the relative phase the projection on the cosine of the helicity angle is invariant, but the projection on the di-hadron invariant mass is modified

decays with low values of $\cos\theta$ preferentially occur above the pole mass, denoted by the dotted line, whereas decays with high values of $\cos\theta$ preferentially occur below the pole mass.

For two interfering resonances of the same spin, the interference term is always an even function of $\cos\theta$, and the opposite effect occurs. Projections on the helicity angle do not depend on the relative isobar phase, and instead projections on the invariant-mass distribution are sensitive to this phase. This is visible in Fig. 6.4, where similar projections are shown for two overlapping spin-1 resonances. When the relative isobar phase is zero or π, the maximum of the mass peak is consistent with the resonance pole mass (dotted line) in the invariant-mass projection. However, when this phase is $\pi/2$, a shift is observed in the position of the invariant-mass distribution relative to the pole mass, due to the constructive and destructive interference resulting from the phase evolution of the relativistic Breit–Wigner. This indicates that correct evaluation of the potential interference contributions from additional contributions is essential when measuring the properties of resonances, and that inspection of the structure in the cosine of the helicity angle and invariant-mass projection can be used to qualitatively interpret the effects of the interferences between various resonant contributions.

This is naturally more complicated when there are multiple interfering resonances of different spins, and hence in practice an automated statistical procedure is required to decouple these contributions (described in Sect. 6.6). However, when few contributions dominate is it often possible to observe these effects in real decays, as in the case of the analysis of the $B^+ \to \pi^+\pi^+\pi^-$ decay in Chap. 7.

6.5 Mass Distributions

The component of the amplitude that describes the evolution in the invariant mass of the resonance daughters, often known as the lineshape, is determined by the fundamental parameters of the resonance, such as its mass and width, and is also modulated by the presence of open channels in the same region. The mass lineshape also contains a complex phase, which in concert with the phase from the isobar coefficient determines the interference structure in the Dalitz plot.

Unlike for the angular distributions, enforcing physical constraints such as unitarity and analyticity in the lineshape is difficult. However, for a large number of resonances which are isolated and narrow, the relativistic Breit–Wigner is a sufficient approximation to the true distribution. In the analysis described in Chap. 7, these are used extensively, in addition to the unitarity-conserving K-matrix model for the $\pi\pi$ S-wave, and the Gounaris–Sakurai model for the $\rho(770)^{\circ}$.

6.5.1 Relativistic Breit–Wigner

The non-relativistic Breit–Wigner form arises from the Fourier transform into the frequency (or energy) domain of a damped driven harmonic oscillator, where the frequency at which the amplitude is at a maximum is known as the *resonant* frequency. This therefore is a very general physical phenomenon, which is also observed in the exponential decay law of an unstable particle from Fermi's golden rule, and as the phase-shift of a partial wave in non-relativistic scattering theory.

In quantum field theory, the Feynman rules for a massive intermediate vector resonance prescribe a propagator (disregarding the sum over intermediate polarisations)

$$BW_{\text{prop}} = \frac{i}{s - \Pi(s)} \tag{6.8}$$

where m is the mass of the propagator, s is the sum of the momenta of the incoming particles squared, and $\Pi(s) = m^2(s) + im(s)\Gamma(s)$ is the self-energy of the intermediate state. In general this self-energy is unknown for hadronic intermediate resonances. For isolated and narrow hadronic resonances, $m(s)$ can be well approximated by a constant.[2] Therefore, for resonant contributions, the relativistic Breit–Wigner lineshape used is

$$T(m) = \frac{1}{(m_0^2 - m^2) - i\, m_0 \Gamma(m)}\,, \tag{6.9}$$

[2]This is not the case for the $\rho(770)^{\circ}$ in particular, where a specific calculation has been performed to improve agreement with experimental data, described in Sect. 6.5.2. It is also possible to use dispersion theory techniques to estimate the mass dependence [7].

where m_0 is the mass of the resonance and the dependence of the decay width of the resonance on m is approximated by

$$\Gamma(m) = \Gamma_0 \left(\frac{q}{q_0}\right)^{2S+1} \left(\frac{m_0}{m}\right) X^2(q\, r_{\mathrm{BW}}) \,, \tag{6.10}$$

where Γ_0 is the nominal width of the resonance, S is the spin of the resonance, X is the Blatt–Weisskopf barrier factor, r is the barrier radius, q is (as before) the magnitude of the momentum of each of the resonance daughters in the resonance rest frame, and q_0 denotes the value of q when $m = m_0$.

6.5.2 Gounaris–Sakurai

For the $\rho(770)$ resonance (and often applied to the $\rho(1450)$ resonance), the functional form of the mass-dependent width has been explicitly calculated by Gounaris and Sakurai in Ref. [8], and hence this modification to the relativistic Breit–Wigner is known as the Gounaris–Sakurai model.[3] Here the lineshape is defined as

$$T(m) = \frac{1 + D \cdot \Gamma_0/m_0}{(m_0^2 - m^2) + f(m) - i\, m_0 \Gamma(m)} \,, \tag{6.11}$$

where

$$f(m) = \Gamma_0 \frac{m_0^2}{q_0^3} \left[q^2 \left[h(m) - h(m_0)\right] + \left(m_0^2 - m^2\right) q_0^2 \left.\frac{dh}{dm}\right|_{m_0} \right] , \tag{6.12}$$

q is the magnitude of the momentum of one of the daughter particles in the resonance rest-frame,

$$h(m) = \frac{2}{\pi} \frac{q}{m} \ln\left(\frac{m + 2q}{2m_\pi}\right) , \tag{6.13}$$

and

$$\left.\frac{dh}{dm}\right|_{m_0} = h(m_0) \left[(8q_0^2)^{-1} - (2m_0^2)^{-1}\right] + (2\pi m_0^2)^{-1} \,. \tag{6.14}$$

The normalisation condition at $T(0)$ fixes the parameter $D = f(0)/(\Gamma_0 m_0)$, and is found to be

$$D = \frac{3}{\pi} \frac{m_\pi^2}{q_0^2} \ln\left(\frac{m_0 + 2q_0}{2m_\pi}\right) + \frac{m_0}{2\pi\, q_0} - \frac{m_\pi^2 m_0}{\pi\, q_0^3} \,. \tag{6.15}$$

[3] This parameterisation disregards information about additional open channels, and as such its validity, particularly for precision mass measurements or for modelling the higher mass $\rho(1450)$ and $\rho(1700)$ resonances, is questioned by some authors [7].

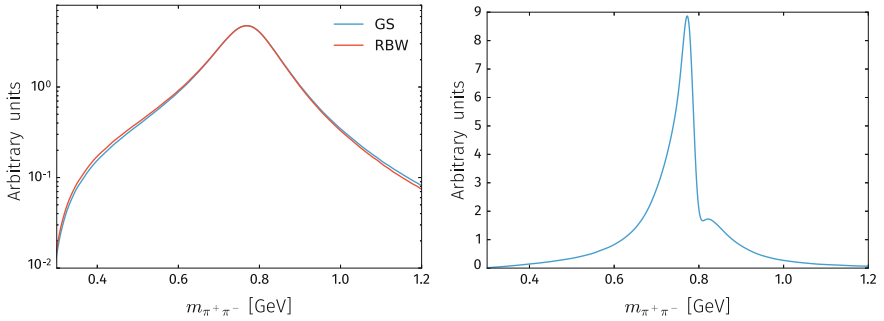

Fig. 6.5 Left: Relativistic Breit–Wigner (orange) and Gounaris–Sakurai (blue) models for the $\rho(770)^\circ$ invariant-mass shape, where the same values of the mass and with are used for both models. Right: The ρ–ω mixing model defined in Eq. 6.16

A comparison between this and the relativistic Breit–Wigner model for the $\rho(770)^\circ$ resonance can be seen in Fig. 6.5 (left).

$\rho-\omega$ Mixing Amplitude

In $B^+ \to \pi^+\pi^+\pi^-$, the $\pi^+\pi^-$ invariant-mass spectrum is dominated by a large $\rho(770)^\circ$ contribution. A distortion of this lineshape arises from the $B^+ \to \omega(\pi^+\pi^-)\pi^+$ decay, with the corresponding isospin-violating $\omega \to \pi^+\pi^-$ decay. Since the $\rho(770)^\circ$ and $\omega(782)$ are both vector states and overlap in $m(\pi^+\pi^-)$, the relative magnitude and phase of these strongly interfering contributions is included directly in a combined amplitude.

The combined ρ–ω mixing amplitude described in Refs. [9, 10] is modified to replace the relativistic Breit–Wigner with the Gounaris–Sakurai model,

$$A_{\rho-\omega} = A_\rho \left[\frac{1 + A_\omega \Delta |B| \exp(i\phi_B)}{1 - \Delta^2 A_\rho A_\omega} \right], \tag{6.16}$$

where A_ρ is the Gounaris–Sakurai $\rho(770)^\circ$ lineshape, A_ω is the relativistic Breit–Wigner $\omega(782)$ lineshape, $|B|$ and ϕ_B are the relative magnitude and phase of the production amplitudes of $\rho(770)^\circ$ and $\omega(782)$, and $\Delta = \delta\,(m_\rho + m_\omega)$, where δ governs the electromagnetic mixing of $\rho(770)^\circ$ and $\omega(782)$. When ignoring the small Δ^2 term in the denominator of Eq. 6.16, this is equivalent to the parameterisation described in Ref. [11].

From SU(3) symmetry, the $\rho(770)^\circ$ and $\omega(782)$ are expected to be produced coherently, giving $|B| \exp(i\phi_B) = 1$. In general δ is complex, although the imaginary part is expected to be small so this can be neglected. The theory prediction for δ is around 2 MeV [12], and previous analyses have found $|\delta|$ to be 2.15 ± 0.35 MeV [10] and 1.57 ± 0.16 MeV, and arg δ to be 0.22 ± 0.06 [11]. The distribution of this model in the di-pion invariant mass can be seen in Fig. 6.5 (right), under the assumption of coherent production.

6.5.3 Virtual Contributions

Virtual contributions, from the tail of off mass-shell B^{*0} decays can enter the $B^+ \to \pi^+\pi^+\pi^-$ Dalitz plot via the decay $B^+ \to B_v^{*0}(\pi^+\pi^-)\pi^+$. These are modelled as relativistic Breit–Wigner functions, with a pole mass corresponding to the true pole mass of the excited state. The exception to this is when calculating the q_0 parameter in Eq. 6.10, where, as the pole mass is outside of the kinematically allowed region, an effective mass term is used,

$$m_R^{\text{eff}}(m) = m_{\pi\pi}^{\text{min}} + (m_{\pi\pi}^{\text{max}} - m_{\pi\pi}^{\text{min}}) \left[1 + \tanh \left(\frac{m - \frac{m_{\pi\pi}^{\text{min}} + m_{\pi\pi}^{\text{max}}}{2}}{m_{\pi\pi}^{\text{max}} - m_{\pi\pi}^{\text{min}}} \right) \right]. \tag{6.17}$$

In principle, both scalar and vector B^{*0} resonances can contribute, where each of these appears similar to a exponential non-resonant term in the S or P wave, but entering the Dalitz plot from $m_{\pi\pi}^{\text{max}}$, rather than from $m_{\pi\pi}^{\text{min}}$ as is the case for conventional non-resonant components.

6.5.4 K-Matrix

Resonances are associated with poles in the S-matrix, and this alone provides the fundamental, model-independent description. In the special case of a narrow resonance, isolated from other resonances or open channels, there is a close correspondence with the peak observed in experiment (i.e., on the real axis) and the position of the pole – the lineshape of which is given by the relativistic Breit–Wigner distribution. In general however, the parameters of the relativistic Breit–Wigner are not a good representation of the true parameters of the resonance, as can be seen in the comparison between the model for two overlapping resonances using a K-matrix model and two relativistic Breit–Wigner lineshapes in Fig. 6.6.

For spin-1 (or higher) resonances decaying to two scalars, the relativistic Breit–Wigner is often a reliable description of the signal shapes, as these are mostly reasonably narrow and isolated. However, in the low di-pion mass region, there are a large number of broad overlapping scalar resonances, which exist in the presence of numerous decay channel openings that distort the lineshapes. Therefore a model is required that simultaneously respects unitarity when resonances interfere strongly, and when additional decay channels for the resonance are possible.

For the interfering resonant $K^{*0}(1430)$, $K^{*0}(800)$, and non-resonant structures in the $K\pi$ S-wave, the so-called LASS model [13] considerably improves agreement with data by enforcing unitarity in the interference via the phase shifts. Similarly, the Flatté model [14] for the $f_0(980)$ resonance, where the opening of the KK threshold (at 987 MeV for K^+K^- and 997 MeV for K^0K^0) distorts the lineshape in the $\pi^+\pi^-$ spectrum, likewise models the data well by accounting for the decays into KK and conserving unitarity.

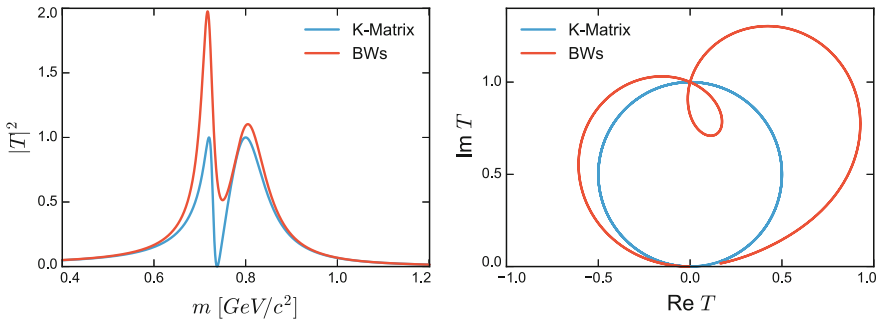

Fig. 6.6 Comparison between the naïve sum of relativistic Breit–Wigner functions (orange) and relativistic Breit–Wigner propagators within the K-matrix approach (blue), with equal isobar magnitude and phase, in intensity distribution in the di-hadron mass (left), and Argand evolution of the amplitude (right). The K-matrix amplitude remains within the unit circle, whereas the sum of relativistic Breit–Wigner lineshapes violates unitarity

In general, unitarity conserving amplitude models can be derived from the S-matrix formalism, where resonant contributions appear as poles in the S-matrix. The matrix S_{fi} can be defined as the projection of the initial state on the final state via the scattering operator S,

$$S_{fi} = \langle f|S|i\rangle = I + 2iT, \tag{6.18}$$

where the identity matrix, I, represents the trivial non-interacting component of the amplitude, and T contains all other scattering information. As the S-matrix is unitary, it then follows that the T-matrix is also unitary and the transition amplitude is bounded by a unit circle in the complex (Re, Im) plane. The factor of $2i$ is a convention that results in this circle being centred at $(0, i/2)$. For elastic processes the $\sqrt{s}$ evolution of the amplitude lies exactly on this circle, and for inelastic processes the amplitude exists strictly within the unit circle.

A Hermitian K-matrix and transition amplitude can then be defined as

$$\hat{K}^{-1} = \hat{T}^{-1} + i\rho, \qquad \hat{T} = (I - i\hat{K}\rho)^{-1}\,\hat{K}, \tag{6.19}$$

where the introduction of the phase-space factor, ρ, results in these being the Lorentz invariant quantities, $\hat{K}$ and $\hat{T}$, defined such that $T_{uv} \equiv \{\rho_u^{\dagger}\}^{\frac{1}{2}}\hat{T}_{uv}\{\rho_v\}^{\frac{1}{2}}$. For two-body channels the phase-space factor is

$$\rho_u = \sqrt{\left(1 - \frac{(m_{1u} + m_{2u})^2}{s}\right)\left(1 - \frac{(m_{1u} - m_{2u})^2}{s}\right)}, \tag{6.20}$$

where m_{1u} and m_{2u} are the rest masses of the two products. When this goes below the production threshold for a particular channel it is analytically continued via

the transformation $\rho_u \to i|\rho_u|$. The more complex parameterisations for multi-body channels can be seen in Ref. [15].

To use this formalism for the production of resonant states in B decays, a production-vector, P, is introduced, as described in Ref. [16]. The amplitude for scattering from the B decays into a specific final state, u, is then

$$\mathcal{F}_u = \sum_{v=1}^{n} [I - i\hat{K}\rho]^{-1}_{uv} \cdot \hat{P}_v \,, \tag{6.21}$$

where the sum is over all n intermediate states.

There is considerable freedom in the functional forms of K and P, other than that P must have the same pole structure as K. Here the convention of Ref. [15] is followed, and K is the sum over Breit–Wigner propagators for each pole, plus a slowly varying 'background' polynomial term,

$$\hat{K}_{uv}(s) = \left(\sum_{\alpha=1}^{N} \frac{g_u^{(\alpha)} g_v^{(\alpha)}}{m_\alpha^2 - s} + f_{uv}^{\text{scatt}} \frac{m_0^2 - s_0^{\text{scatt}}}{s - s_0^{\text{scatt}}} \right) f_{A0}(s) \,. \tag{6.22}$$

Here, m_α is the 'bare' pole mass of a resonant contribution; $g_u^{(\alpha)}$ and $g_v^{(\alpha)}$ are the couplings of the resonance α to the 'out', u, and, 'in', v, channels, respectively; f_{uv}^{scatt} is the coupling of the slowly varying component to the u and v channels; and m_0^2 and s_0^{scatt} are coefficients of the slowly varying component that are determined from scattering data. The matrix $\hat{K}$ is symmetric, such that it is Hermitian by construction. The 'Adler zero' term [17], $f_{A0}(s)$, suppresses the false *kinematical* singularity when s is below the $\pi^+\pi^-$ production threshold,

$$f_{A0}(s) = \frac{1\ \text{GeV}^2 - s_{A0}}{s - s_{A0}} \left(s - \frac{1}{2} s_A m_\pi^2 \right) , \tag{6.23}$$

where s_A and s_{A0} are constants of order unity.

The P-vector is defined analogously to the K-matrix term in Eq. 6.22,

$$\hat{P}_v(s) = \sum_{\alpha=1}^{N} \frac{\beta_\alpha g_v^{(\alpha)}}{m_\alpha^2 - s} + f_v^{\text{prod}} \frac{m_0^2 - s_0^{\text{prod}}}{s - s_0^{\text{prod}}} \,, \tag{6.24}$$

where β_α and f_v^{prod} are complex parameters that describe the production pole and slowly-varying components, and are to be left free in the fit, and s_0^{prod} is a constant. As in previous analyses [18], the P-vector appears without a term to suppress the kinematical singularity.

Table 6.1 K-matrix parameters quoted in Ref. [19], which are obtained from a global analysis of $\pi\pi$ scattering data by Anisovich and Sarantsev [15]. Only f_{1v} parameters are listed here, as only the di-pion contributions are observed. Masses, m_α, and couplings, $g_u^{(\alpha)}$, are given in GeV, while units of GeV^2 for s-related quantities are implied; s_0^{prod} is taken from Ref. [18]

α	m_α	$g_1^{(\alpha)}[\pi\pi]$	$g_2^{(\alpha)}[K\bar{K}]$	$g_3^{(\alpha)}[4\pi]$	$g_4^{(\alpha)}[\eta\eta]$	$g_5^{(\alpha)}[\eta\eta']$
1	0.65100	0.22889	−0.55377	0.00000	−0.39899	−0.34639
2	1.20360	0.94128	0.55095	0.00000	0.39065	0.31503
3	1.55817	0.36856	0.23888	0.55639	0.18340	0.18681
4	1.21000	0.33650	0.40907	0.85679	0.19906	−0.00984
5	1.82206	0.18171	−0.17558	−0.79658	−0.00355	0.22358
	s_0^{scatt}	f_{11}^{scatt}	f_{12}^{scatt}	f_{13}^{scatt}	f_{14}^{scatt}	f_{15}^{scatt}
	−3.92637	0.23399	0.15044	−0.20545	0.32825	0.35412
	s_0^{prod}	m_0^2	s_A	s_{A0}		
	−3.0	1.0	1.0	−0.15		

Fixed Parameters

The most commonly used set of parameters for the K-matrix scattering components that represent the complex 'bare' poles present in the K-matrix, as well as the coupling of these poles to the various final state, are those reported in Ref. [19]. These were obtained via private communication with the authors of Ref. [15] as the (then) latest values of their global fit to the available scattering data. These parameters are those used in Chap. 7, and are listed in Table 6.1.

Typical values for the other coefficients appearing in the K-matrix are $m_0^2 = 1\ \text{GeV}^2, s_0^{\text{scatt}} = -5\ \text{GeV}^2, s_A = 1$, and $s_{A0} = 0\ \text{GeV}^2$. There is also a free parameter in the production term in Eq. 6.24, s_0^{prod}, which in previous analyses of D meson decays has been found to be in the range −3 to 0 [18, 19].

Physical Interpretation

The K-matrix model (with the P-vector ansatz) described in the previous section can be thought of as some initial b-hadron decay, described by $\hat{P}$, into one of the five K-matrix channels, plus some other hadrons which are sufficiently decoupled via the isobar approximation - in this case a single π meson. This state is then propagated via the $[I - i\hat{K}\rho]^{-1}$ term to another of the five channels to form the final state (the addition of the identity element in this propagator term means that the 'intermediate' and final state can be the same), which is often referred to as 're-scattering'. In this analysis, only the $\pi^+\pi^-$ final state is observed, and therefore elements in the resulting matrix that describe other final states are discarded.

Elements of the K-matrix itself, describing the bare resonance poles and couplings to the various final states, can be entirely determined from coupled-channel analyses of scattering data, and these are assumed to universally propagate any state into any other. The P-vector describes the virtual 'intermediate' states produced by the b-hadron decay, and therefore is specific to each b-hadron decay. These have

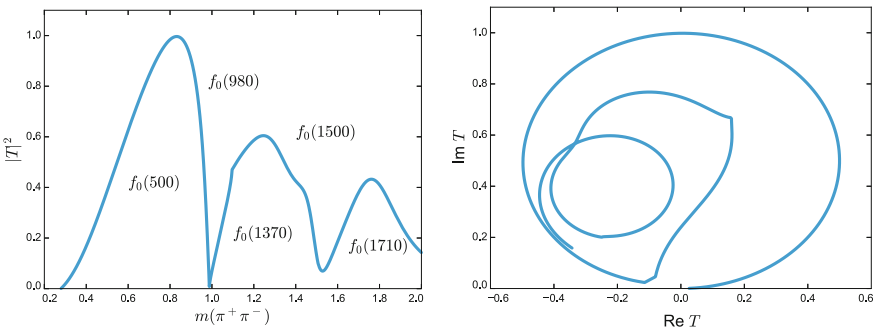

Fig. 6.7 **Left**: Absolute magnitude squared of the decay contribution to the $\pi^+\pi^-$ K-matrix, with the positions of the light scalars indicated. It is interesting to note that none of these features resemble a simple relativistic Breit–Wigner peak. **Right**: Argand diagram of the decay component of the $\pi^+\pi^-$ K-matrix. This is bounded by the unit circle, and elastic until approximately the $f_0(980)$ resonance

the same pole structure as the K-matrix, but otherwise there is no requirement on the functional form. Here the P-vector is chosen to have the same form as the components of the K-matrix, with similar pole and slowly-varying components. Specifically, there is no requirement to include any particular pole or slowly-varying component, and therefore inclusion of these is determined by the model selection procedure as with any other resonant contribution.

The physical transition probability and real and imaginary components of the amplitude of the K-matrix only term, given in Eq. 6.19, using parameters determined from the coupled channel analysis in Ref. [15], can be seen in Fig. 6.7. Despite not being included as an explicit pole, the $f_0(500)$ contribution is clear from this plot, and likely arises from the slowly-varying contributions.

6.6 Implementation Details

To extract the physical parameters described in the previous section, along with various derived parameters such as fit fractions and *CP*-asymmetries, the amplitude model must be constructed and fitted to the *b*-hadron decay data. To this end, the Laura++ amplitude analysis package is used [20]. This package also implements the efficiency, background, and other experimental corrections in order to obtain the best fit quality. There are also various implementation details specific to the analysis described in Chap. 7.

In the $B^+ \to \pi^+\pi^+\pi^-$ decay there are two identical (like-sign) pions in the final state, under exchange of which the amplitude is symmetric due to Bose symmetry. The pairs in which to define the amplitude are therefore arbitrary. In this case the two pairs of opposite-sign pions are selected via mass ordering, where the pair with the smaller invariant mass is given the label m_{low}, and the pair with the larger invariant

mass is labelled m_{high}. This results in a 'folding' of the conventional Dalitz-plot about $m_{\text{low}} = m_{\text{high}}$, and of the square Dalitz-plot about $\theta' = 0.5$.

Whilst the relative phases between amplitude contributions given by the isobar coefficients are physical, the absolute value of the phase has no meaning, and similarly with the absolute magnitudes of the isobar coefficients. Hence, the magnitude and phase of the dominant contribution (for $B^+ \to \pi^+\pi^+\pi^-$ this is the $\rho(770)^\circ$) are fixed to be 1 and 0, respectively, and all contributions are measured relative to this. When considering the *CP*-conjugate amplitude models, the phase of the dominant contribution is fixed to zero in each case, however the magnitude for one is left free in the fit to incorporate a *CP*-asymmetry in the dominant contribution.

6.6.1 Normalisation

The expression in Eq. 6.4 enters the total amplitude with a normalisation factor, $\mathcal{N}$, that ensures that the total integral of the component across the whole Dalitz plot is unity,

$$\mathcal{N} \int_{DP} F(m_{13}^2, m_{23}^2)\, m_{13}^2 m_{23}^2 = 1. \tag{6.25}$$

In Laura++, this integral is performed using Gauss-Legendre numerical integration, where weighted Legendre polynomials are used to approximate the total integral across the transformed domain of $[-1, 1]$. Typically $\mathcal{O}(1000)$ grid points are evaluated in each dimension, however when narrow resonances are present the integration mesh size may be too coarse to correctly evaluate the amplitude. In these cases, an adaptive binning scheme implements a finer mesh in the axis that the resonance is defined in (and in both axes where narrow resonances overlap). Integrals that represent the total 'rate' across the Dalitz plot, such as those in the denominator of Eq. 6.26, are also calculated in this way.

When F has no dependence on the resonance parameters (e.g., masses, widths are held constant), and only the isobar, c_j, parameters vary, $\mathcal{N}$ can be cached to improve overall execution time.

6.6.2 Efficiency

As true physical distributions are fitted to the distribution of events in the Dalitz plot, any variation in the experimental efficiency (i.e., the probability to observe a decay in a specific point in the phase space), would bias the parameters of the model that are extracted and the statistical significance of any particular component, and therefore such effects need to be corrected for.

Much like in the analysis described in Chap. 5, this is primarily achieved by large samples of simulated decays, with data-driven corrections for the particle

identification and level-0 trigger efficiencies. In Laura++ (for the analysis described in Chap. 7), the variation of the efficiency is expressed nonparametrically by a histogram in the square Dalitz-plot, which is smoothed by bin-by-bin cubic-spline interpolation.

The efficiency for each decay in the data, $\epsilon(m^2_{13}, m^2_{23})$, is obtained from the smoothed efficiency histogram, and enters in the definition of the normalised event-wise signal probability-density function,

$$\mathcal{P}_{\rm sig}(m^2_{13}, m^2_{23}) = \frac{|\mathcal{A}(m^2_{13}, m^2_{23})|^2 \epsilon(m^2_{13}, m^2_{23})}{\int_{\rm DP} |\mathcal{A}(m^2_{13}, m^2_{23})|^2 \epsilon(m^2_{13}, m^2_{23})\, dm_{13}\, dm_{23}}. \tag{6.26}$$

The Square Dalitz-Plot

In charmless three-body decays, intermediate resonances predominantly populate the regions around the edges of the conventional Dalitz plot. This effect is exacerbated in the observed distributions by the requirement of the trigger and reconstruction algorithms for a decay to have at least one high transverse-momentum track. Therefore, in an attempt to make the generation of simulated data as efficient as possible for a generic three-body decay, a transformation of the conventional Dalitz-plot, known as the *square* Dalitz-plot, is introduced, such that generating events uniformly in this transformed phase-space gives more weight to the edges of the conventional Dalitz-plot.

In addition to improving the MC generation efficiency, the uniform phase-space boundaries mean that implementing a binning scheme and performing efficiency corrections is considerably easier, as the boundaries no longer depend on the specific decay and bins can be easily aligned with the boundaries.

The square Dalitz-plot variables, m' and θ', are a re-scaling of one of the helicity angles and one of the invariant-mass pairs. There are therefore three such square Dalitz-plots for a three-body decay, where the helicity angle and invariant-mass pair are usually chosen to be those where the dominant resonant contributions are expected or to exploit a symmetry in the decay. These variables are defined such that, for m_{13},

$$m' \equiv \frac{1}{\pi} \arccos\left(2\frac{m_{13} - m^{\rm min}_{13}}{m^{\rm max}_{13} - m^{\rm min}_{13}} - 1\right), \tag{6.27}$$

$$\theta' \equiv \frac{1}{\pi}\theta_{13}, \tag{6.28}$$

which are in the range [0, 1], and similarly defined for the other two invariant-mass combinations.

For the analysis of $B^+ \to \pi^+\pi^+\pi^-$ described in Chap. 7, the square Dalitz-plot is chosen to be in m_{12}, and has the particularly useful property that the symmetrisation due to the two indistinguishable π mesons can be performed by folding about $\theta' = 0.5$.

6.6.3 Backgrounds

Background in the signal region used to select events for the Dalitz plot fit can arise from random combinations of hadrons from the event (combinatorial background), or where all final state hadrons are from a true b-hadron decay, but are otherwise mis-identified (cross-feed) or partially reconstructed. Regardless of their origin, the distributions of these background events in the Dalitz plot (conventional or square) is parameterised, much like the efficiency distributions, by a uniformly binned histogram with or without cubic-spline interpolation.

The probability of an event being background is constructed, using the distribution of background events over the Dalitz plot and the total number of background events in the data sample (which is most reliably estimated from a separate fit to the invariant mass distribution of the b-hadron), and enters the total likelihood in the same way as the efficiency corrected signal probability in Eq. 6.26,

$$\mathcal{P}_{\text{bkg}}(m^2_{13}, m^2_{23}) = \frac{\mathcal{B}(m^2_{13}, m^2_{23})}{\int_{\text{DP}} \mathcal{B}(m^2_{13}, m^2_{23})\, dm_{13}\, dm_{23}}, \tag{6.29}$$

where $\mathcal{B}(m^2_{13}, m^2_{23})$ is the background expectation at the point (m^2_{13}, m^2_{23}).

6.6.4 Parameter Inference

The aim of amplitude analysis is to extract the isobar parameters, c_j, that describe the relative magnitudes and interferences between the model components, and other parameters associated to individual resonances, such as masses and widths. Here, this is achieved via a maximum-likelihood fit.

Given an amplitude model probability density function (PDF), $\mathcal{P}(x;\theta)$, which is proportional to the probability that an observation, x, arises from a model P, defined in terms of the model parameters θ, the likelihood function of a vector of independent observations, $\vec{x} = (x_1, x_2, \ldots, x_i)$, can be formed,

$$\mathcal{L}(\vec{x};\theta) = \prod_{x_i} \mathcal{P}(x_i;\theta). \tag{6.30}$$

It follows that the parameters that maximise this likelihood, $\hat{\theta}$ describe a model that is most favoured by the observations.

In practice this is achieved via the non-linear optimisation routines provided by the MINUIT library [21], where instead minimisation is performed on the negative log-likelihood as this is more numerically stable (and as the logarithm is monotonically increasing function, a minimum in the negative log-likelihood coincides with a maximum in the likelihood).

Uncertainties

In most cases in high-energy physics, the maximum-likelihood estimator is unbiased, and asymptotically normal by the central limit theorem (i.e., the estimates are equal to the true parameter plus an uncertainty that is approximately normal, and that the uncertainty decays proportional to $1/\sqrt{N}$, where N is the size of the data).

If this is the case, then the variance, $\mathrm{Var}[\hat{\theta}]$, of a maximum-likelihood estimate of a parameter $\hat{\theta}$ follows the Cramér–Rao bound, which in the univariate case is

$$\mathrm{Var}[\hat{\theta}] \geq \frac{1}{I(\theta)}. \tag{6.31}$$

Here $I(\theta)$ is the Fisher information,

$$I(\theta) = -E_\theta \left[\frac{\partial^2 \log \mathcal{L}(x;\theta)}{\partial \theta^2} \right], \tag{6.32}$$

where E_θ denotes the expectation of θ, and $\mathcal{L}(x;\theta)$ is the univariate likelihood function. The maximum-likelihood estimator is these cases is also an efficient estimator, such that the Eq. 6.31 is an equality. The expectation value of θ can be estimated using the maximum-likelihood value of θ, $\hat{\theta}$, and therefore $\mathrm{Var}[\hat{\theta}]$ can be calculated from the second-derivative of $\mathcal{L}(x;\theta)$ at $\theta = \hat{\theta}$,

$$\mathrm{Var}[\hat{\theta}] = -\left(\frac{\partial^2 \log \mathcal{L}(x;\theta)}{\partial \theta^2} \right)\Bigg|_{\theta=\hat{\theta}}. \tag{6.33}$$

In amplitude analysis, the parameterisation of the models may violate the consistency assumptions that govern Eq. 6.33, resulting in biased estimates of the true parameters and their uncertainties (for example if there are large non-linear correlations between parameters, or the maximum-likelihood estimate of a parameter is near a physical boundary). Alternative methods for calculating the asymmetric uncertainty intervals and the covariance matrix involve scanning the profile likelihood under the assumption of normality, which is performed by MINOS [21].

One can also go one step further and obtain estimates for the statistical uncertainty on the parameters of interest by re-fitting the model on 'toy' data generated from the model, where the parameters are set to the maximum-likelihood estimates. The distribution of the central values of the refitted parameter estimates then gives the uncertainty on these parameters. This method is particularly useful for determining uncertainties on derived parameters, such as component fit fractions.

Another similar method that does not assume that the model replicates the data well involves forming a large number of 'bootstrapped' samples of the data, which have the same number of events but where the candidates are resampled with replacement [22]. The model is refitted to these bootstrapped distributions and the central values of the parameters used to estimate the uncertainty and bias of the original maximum-likelihood estimates.

6.6.5 Fit Fractions

For each contribution, j, in addition to the isobar parameters defined previously, one can also calculate its fractional contribution to the total amplitude,

$$FF_j = \frac{\int_{\mathrm{DP}} |c_j F_j(m_{13}^2, m_{23}^2)|^2 \, dm_{13}^2 \, dm_{23}^2}{\int_{\mathrm{DP}} |\mathcal{A}|^2 \, dm_{13}^2 \, dm_{23}^2}. \tag{6.34}$$

These *fit fractions* enable comparison between amplitude analyses that use different amplitude formalisms or parameterisations of the isobar coefficients, and in addition permit extraction of the quasi-two-body branching fractions involving the intermediate resonances. It is also useful to define the *interference* fit fractions, which express the net constructive or destructive interference contribution to the total amplitude,

$$FF_{i>j} = \frac{\int_{\mathrm{DP}} 2\mathrm{Re}[c_i c_j^* F_i F_j] \, dm_{13}^2 \, dm_{23}^2}{\int_{\mathrm{DP}} |\mathcal{A}|^2 \, dm_{13}^2 \, dm_{23}^2}. \tag{6.35}$$

Due to constructive and destructive interference, $\sum_j FF_j \neq 1$, however the sum of these and the interference fit fractions is unity.

It is important to note that given the efficiency correction described in Sect. 6.6.2, the isobar parameters extracted from the fit represent the true physical parameters, and therefore subsequent derived quantities need not correct for the efficiency variation across the phase-space.

6.6.6 Extracting CP-Violating Parameters

To extract parameters that are sensitive to CP-violation in the intermediate quasi-two-body decays, or in the interferences between them, additional terms are introduced to the isobar coefficients to parameterise this CP-violation, and the amplitude model must be fitted to CP-conjugate collision data. In the case of $B^+ \to \pi^+\pi^+\pi^-$, described in Chap. 7, charge conservation implies that this split can be performed by separating the data by the charge of the reconstructed B^+ meson, extracting parameters for $B^+ \to \pi^+\pi^+\pi^-$ and $B^- \to \pi^-\pi^-\pi^+$ decays separately.[4] Efficiencies in this case are as described in Sect. 6.6.2, but are separately calculated for B^+ and B^- to account for any detection asymmetry, and are applied separately to the corresponding model. A production asymmetry is also accounted for using a constant relative efficiency offset between the B^+ and B^- efficiency models, as this asymmetry has negligible correlation with the decay kinematics [24].

[4] This can also be done for neutral meson decays via specific intermediate resonances whose decays are quasi-flavour-specific, such as in the amplitude analysis of the $B^0 \to K_S^0\pi^+\pi^-$ decay, where CP-violation was observed in the $B^0 \to K^{*+}(892)(K_S^0\pi^+)\pi^-$ decay [23].

To account for potential CP-violation, the isobar parameters are modified such that they allow for differences between the B^+ and B^- amplitudes. For example, the Cartesian parameters are expressed as

$$c_\pm = x \pm \delta_x + i(y \pm \delta_y), \tag{6.36}$$

where taking the positive signs gives the B^+ decay isobar coefficient, and the negative signs give the B^- decay isobar coefficient. In the absence of CP-violation, $\delta_x = \delta_y = 0$.

A useful quantity that expresses the degree of CP-violation in a specific quasi-two-body decay is the CP-asymmetry, which using the Cartesian isobar coefficient convention is given by

$$\mathcal{A}_{CP} = \frac{|\bar{A}|^2 - |A|^2}{|\bar{A}|^2 + |A|^2} = -2\left[\frac{x\,\delta_x + y\,\delta_y}{x^2 + \delta_x^2 + y^2 + \delta_y^2}\right]. \tag{6.37}$$

This in essence gives the degree of CP-violation in the magnitude of the quasi-two-body contribution, but does not include information on the CP-violation in the interference between contributions, where the information is contained in the relative phases. The absolute phase difference between the B^+ and B^- amplitudes cannot be measured in the $B^+ \to \pi^+\pi^+\pi^-$, as the final state is not an eigenstate of CP. However, it is possible to observe CP-violation in the interference between two quasi-two-body contributions if the relative phases between these contributions are different in the B^+ and B^- amplitudes.

The branching fraction for a quasi-two-body contribution, $R_j\pi^+$, is calculated using an average of the B^+ and B^- fit-fractions,

$$\mathcal{B}(B^+ \to R_j(\pi^+\pi^-)\pi^+) = \mathcal{B}(B^+ \to \pi^+\pi^+\pi^-) \cdot FF_j^{CP}. \tag{6.38}$$

where FF_j^{CP} is the CP-conserving fit-fraction,

$$FF_j^{CP} = \frac{\int_{DP} |\bar{c}_j \overline{F}_j(m_{13}^2, m_{23}^2)|^2 + |c_j F_j(m_{13}^2, m_{23}^2)|^2 \, dm_{13}^2 \, dm_{23}^2}{\int_{DP} |\overline{\mathcal{A}}|^2 + |\mathcal{A}|^2 \, dm_{13}^2 \, dm_{23}^2}. \tag{6.39}$$

References

1. R.H. Dalitz, S.F. Tuan, The phenomenological description of K-nucleon reaction processes. Ann. Phys. **10**, 307 (1960). https://doi.org/10.1016/0003-4916(60)90001-4
2. J. Blatt, V.E. Weisskopf, *Theoretical nuclear physics* (Wiley, New York, 1952)
3. F. von Hippel, C. Quigg, Centrifugal-barrier effects in resonance partial decay widths, shapes, and production amplitudes. Phys. Rev. D **5**, 624 (1972). https://doi.org/10.1103/PhysRevD.5.624

4. Particle Data Group, C. Patrignani et al., Review of particle physics. Chin. Phys. **C40**, 100001 (2016) (2017 update). https://doi.org/10.1088/1674-1137/40/10/100001
5. C. Zemach, Three pion decays of unstable particles. Phys. Rev. **133**, B1201 (1964). https://doi.org/10.1103/PhysRev.133.B1201
6. C. Zemach, Use of angular-momentum tensors. Phys. Rev. **140**, B97 (1965). https://doi.org/10.1103/PhysRev.140.B97
7. P. Lichard, M. Vojik, An alternative parametrization of the pion form-factor and the mass and width of RHO(770), arXiv:hep-ph/0611163
8. G.J. Gounaris, J.J. Sakurai, Finite-width corrections to the vector-meson-dominance prediction for $\rho \to e^+e^-$. Phys. Rev. Lett. **21**, 244 (1968). https://doi.org/10.1103/PhysRevLett.21.244
9. W.M. Dunwoodie, Omega-RHO mixing parametrization, http://www.slac.stanford.edu/~wmd/omega-rho_mixing/omega-rho_mixing.note
10. P.E. Rensing, Single electron detection for SLD crid and multi-pion spectroscopy in $\mathrm{K}^- p$ interactions at 11 GeV/c. Ph.D. thesis, Stanford University, Stanford, CA, 1993 (Presented on 1993)
11. CMD-2 Collaboration, R.R. Akhmetshin et al., Measurement of $e^+e^- \to \pi^+\pi^-$ cross-section with CMD-2 around ρ meson. Phys. Lett. **B527**, 161 (2002). https://doi.org/10.1016/S0370-2693(02)01168-1, arXiv:hep-ex/0112031
12. S. Coleman, S.L. Glashow, Departures from the eightfold way: theory of strong interaction symmetry breakdown. Phys. Rev. **134**, B671 (1964). https://doi.org/10.1103/PhysRev.134.B671
13. D. Aston et al., A study of $K^-\pi^+$ scattering in the reaction $K^- p \to K^-\pi^+ n$ at 11 GeV/c. Nucl. Phys. B **296**, 493 (1988). https://doi.org/10.1016/0550-3213(88)90028-4
14. S.M. Flatté, Coupled-channel analysis of the $\pi\eta$ and KK systems near KK threshold. Phys. Lett. B **63**, 224 (1976)
15. V.V. Anisovich, A.V. Sarantsev, K matrix analysis of the ($I J^{PC} = 00^{++}$) -wave in the mass region below 1900 MeV. Eur. Phys. J. A **16**, 229 (2003). https://doi.org/10.1140/epja/i2002-10068-x. arXiv:hep-ph/0204328
16. I.J.R. Aitchison, K-matrix formalism for overlapping resonances. Nucl. Phys. A **189**, 417 (1972). https://doi.org/10.1016/0375-9474(72)90305-3
17. S.L. Adler, Consistency conditions on the strong interactions implied by a partially conserved axial-vector current. II. Phys. Rev. **139**, B1638 (1965). https://doi.org/10.1103/PhysRev.139.B1638
18. Focus Collaboration, J.M. Link et al., Dalitz plot analysis of D_s^+ and D^+ decay to $\pi^+\pi^-\pi^+$ using the K matrix formalism. Phys. Lett. **B585**, 200 (2004). https://doi.org/10.1016/j.physletb.2004.01.065, arXiv:hep-ex/0312040
19. BaBar Collaboration, B. Aubert et al., Improved measurement of the CKM angle γ in $B^\mp \to D^{(*)}K^{(*\mp)}$ decays with a Dalitz plot analysis of D decays to $K^0_S\pi^+\pi^-$ and $K^0_S K^+K^-$. Phys. Rev. **D78**, 034023 (2008). https://doi.org/10.1103/PhysRevD.78.034023, arXiv:0804.2089
20. T. Latham, The Laura++ Dalitz plot fitter, in *AIP Conference Proceedings*, vol. 1735 (2016) p. 070001. https://doi.org/10.1063/1.4949449, arXiv:1603.00752
21. F. James, M. Roos, Minuit: a system for function minimization and analysis of the parameter errors and correlations. Comput. Phys. Commun. **10**, 343 (1975). https://doi.org/10.1016/0010-4655(75)90039-9
22. B. Efron, Bootstrap methods: another look at the jackknife. Ann. Stat. **7**, 1 (1979). https://doi.org/10.1214/aos/1176344552
23. LHCb, R. Aaij et al., Amplitude analysis of the $B^0 \to K^0_s\pi^+\pi^-$ decay (In preparation)
24. LHCb, R. Aaij et al., Measurement of the $B^\pm$ production asymmetry and the CP asymmetry in $B^\pm \to J/\psi K^\pm$ decays, arXiv:1701.05501

Chapter 7
Amplitude Analysis of $B^+ \to \pi^+\pi^+\pi^-$

Charmless three-body b-meson decays to light hadrons proceed via various intermediate resonances. These decays in the Standard Model are mediated by tree-level and/or higher-order loop diagrams, where the interference between these amplitudes allows for direct CP violation. The dynamics of the $B^+ \to \pi^+\pi^+\pi^-$ decay is of particular interest, as the various overlapping low-mass $J^P = 0^+$ states are still little understood.

This chapter documents the amplitude analysis of the $B^+ \to \pi^+\pi^+\pi^-$ decay, using 3 fb^{-1} of LHCb Run 1 data. The magnitudes and relative phases of the intermediate resonances are reported for the B^+ and B^- decay, in addition to the branching fractions of the corresponding quasi-two-body decays.

7.1 Introduction

The phase-space of the $B^+ \to \pi^+\pi^+\pi^-$ decay is interesting to study for various reasons. Being a charmless decay, it is expected that Feynman diagrams for the production of some intermediate resonances have tree and loop diagram contributions of similar magnitude, therefore providing the potential for large CP-violation in decay. Furthermore, non-trivial strong-phase differences can be generated locally by the relative phases of interfering resonant structures, resulting in CP-violation varying across the phase-space.

Analysis of this decay also provides insight into the interactions of the lightest resonant states, such as the $f_0(500)$ and $f_0(980)$, which are still not well understood. The strongly interfering low-mass scalar states that decay to $\pi\pi$ form a large part of the 'non-resonant' amplitude component seen previously by other experiments [1], and therefore it is likely that the interaction between these and the other resonances have important consequences for the large CP-violation observed in this decay.

© Springer Nature Switzerland AG 2018

D. O'Hanlon, *Studies of* CP-*Violation in Charmless Three-Body* b-*Hadron Decays*,
Springer Theses, https://doi.org/10.1007/978-3-030-02206-8_7

The Dalitz-plot structure in $B^+ \to \pi^+\pi^+\pi^-$ is also a useful input to other measurements, such as the inference of the CKM angle α, using measurements of the $B^0 \to \pi^+\pi^-\pi^0$ decay [2], and the CKM angle γ, using combinations of various three-body charmless decays [3]. This family of decays has also been proposed for various direct tests of SU(3)-flavour symmetry in the Standard Model [4].

As $B^+ \to \pi^+\pi^+\pi^-$ is a charmless decay, its branching fraction is small, the world-average measurement being $(1.52 \pm 0.14) \times 10^{-5}$ [5]. However, with the high LHC cross-section for b-quarks, the number of events available for analysis is an order of magnitude greater than that at the B-factories, and with a significantly improved signal-to-background ratio.

7.1.1 *Input to a Measurement of γ*

Decays which have a substantial loop-mediated contribution can be affected by off mass-shell intermediate particles that do not appear in the Standard Model. As such, a comparison between the CKM angle γ measured in tree-dominated and loop-mediated decays is a sensitive test for 'new physics' (Fig. 7.1). Various measurements of γ using tree-dominated decays, such as those using $B \to D^{(*)}K^{(*)}$, have been performed [6–9], however those using loop-mediated decays have mostly been hindered by the low branching fractions of the necessary charmless decays and by unknown symmetry breaking factors. These factors are introduced by the use of the symmetry relations to cancel out so called 'penguin pollution', using similar final states. This penguin pollution arises where an additional weak phase is acquired from penguin diagram contributions carrying a different CKM phase to the tree-level diagram (for example if the dominant t-quark contribution exists in conjunction with a c-quark loop), introducing an unknown factor to the value of γ obtained if not properly controlled for, either experimentally or from theory input [10].

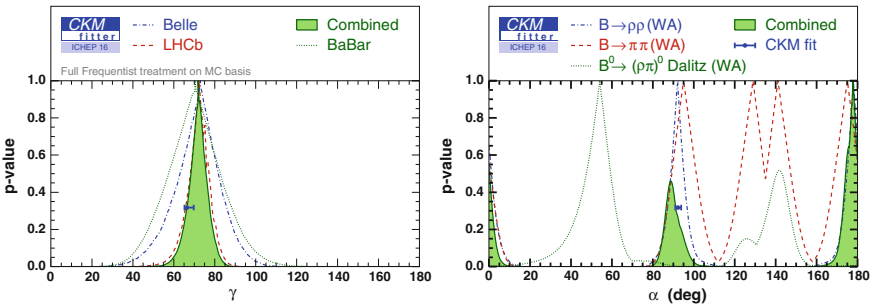

Fig. 7.1 Global CKM fit values (blue points) for the CKM angles γ (left) and α (right), without the direct measurements of corresponding angle; and p-values from the direct measurements (coloured contours) [9]

The most precise measurements of γ in loop-mediated decays have been using the two-body decays of $B \to \pi\pi, K\pi, KK$, but include unknown uncertainties either from SU(3) breaking, or from non-factorisable U-spin breaking contributions (although recent results imply that this approach can be robust for moderate magnitudes of the non-factorisable U-spin breaking contribution [11]). Additional measurements have also been performed exploiting the interference between particular intermediate resonances in three-body decays to extract the relative phases of the quasi-two-body amplitudes [12–14], but involve final states with a π^0 meson, which are difficult to reconstruct at LHCb.

One such proposal using the $B^+ \to \pi^+\pi^+\pi^-$ decay involves measuring the interference between a decay with a known weak phase contribution and other intermediate decays in the amplitude. Candidates for these decays are the tree-dominated $B^+ \to \chi_{c0}\pi^+$ and $B^+ \to \chi_{c2}\pi^+$ $b \to c\bar{c}$ decays, which each have a weak phase difference of zero. The $\chi_{c0,2}$ width is also such that non-neligible interference with other states in the region can occur. The difference between the phases for the for the B^+ and B^- amplitudes can be related back to γ (plus some additional penguin-driven weak phase), as the strong phases cancel under CP, by definition.

Initial investigations focussed on rate asymmetries in reduced regions of the Dalitz plot, under specific assumptions on the interfering components [15, 16]. However with a larger dataset, there is a clear additional benefit of constructing an amplitude model for the full Dalitz-plot to identify and measure these interfering phases directly as an additional tool to combat penguin pollution [2, 17]. In this way, a similar measurement, which uses the interference between the tree-dominated decay and isospin zero components (which in this case have a unique isospin amplitude, and therefore a unique strong phase) in the $B^+ \to \pi^+\pi^+\pi^-$ and $B^+ \to K^+\pi^+\pi^-$ decays, is proposed in Ref. [3]. Such measurements are impeded by the low branching fraction of the suppressed $B^+ \to \chi_{c0}\pi^+$ decay, which has not yet been observed.

7.1.2 Input to a Measurement of α

The CKM angle α is accessible in decays dominated by a $b \to u\bar{u}d$ tree-level transition (Fig. 7.1), however conventional modes for determining α, such as $B \to \pi\pi$ and $B \to \rho\rho$, have potentially sizeable loop-mediated contributions from penguin diagrams and additionally require the reconstruction of a final state with two π^0 mesons [5, 18].

The $B \to \rho\pi$ family of decays permit various strategies by which to measure α. One such measurement involves 'pentagonal' isospin relations between the charged and neutral $B \to \rho\pi$ decay amplitudes,

$$A^{+-} + A^{-+} + 2A^{00} = \sqrt{2}(A^{+0} + A^{0+}), \tag{7.1}$$

where A^{ij} represents the amplitude for the decay $B \to \rho\pi$ with ρ charge i, and π charge j. These amplitudes in general have contributions from $\Delta I = \frac{1}{2}, \frac{3}{2}$, and $\frac{5}{2}$, however penguin contributions arise only from the $\Delta I = \frac{1}{2}$ (neglecting the small

electroweak contribution to $\Delta I = \frac{5}{2}$). The amplitudes can therefore be combined to remove the $\Delta I = \frac{1}{2}$ component, and extract the CKM angle α as the phase between combinations of the charged and neutral decay amplitudes, A, and their CP-conjugates, $\bar{A}$,

$$\exp(2i\alpha) = \frac{\bar{A}^{+0} + \bar{A}^{0+}}{A^{+0} + A^{0+}} = \frac{\bar{A}^{+-} + \bar{A}^{-+} + 2\bar{A}^{00}}{A^{+-} + A^{-+} + 2A^{00}}. \tag{7.2}$$

From this it can be seen that one requires the $B^+ \to \rho^+\pi^0$ decay amplitude (and thereby reconstruct two π^0 mesons), in addition to the $B^+ \to \rho^0\pi^+$ decay amplitude from the analysis described in this Chapter, to measure the angle α in this way.

However, a time-dependent measurement of the $B^0 \to \rho\pi$ decay, and in particular, the interference between $B^0 \to \rho^\pm\pi^\mp$, $B^0 \to \rho^0\pi^0$ decays in the $B^0 \to \pi^+\pi^+\pi^0$ Dalitz-plot, permits direct extraction of α simultaneously with the relative strong-phase information [2, 19, 20]. This therefore does not require invoking isospin or SU(3) symmetry to subtract the weak-phase from penguin decays, and also is able to resolve α with a single discrete $\alpha \to \alpha + \pi$ ambiguity.

Whilst the $B^+ \to \pi^+\pi^+\pi^-$ decay does not, without assumptions regarding the penguin contributions, constrain any parameters in either formalism described above, experimental information on the resonant content of the $B^+ \to \pi^+\pi^+\pi^-$ phase-space informs the analysis of the $B^0 \to \pi^+\pi^-\pi^0$ decay phase-space. Moreover, accurate modelling of the dominant $\rho(770)$ contribution, plus the interfering resonant and non-resonant S-wave and $\omega(782)$ contributions, is essential for robust extraction of the CKM angle α in such an analysis [21, 22]. As such, the modelling efforts performed in the amplitude analysis of $B^+ \to \pi^+\pi^+\pi^-$ provides a valuable starting point for future measurements in this area.

7.1.3 Previous Measurements

The previous amplitude analyses of the $B^+ \to \pi^+\pi^+\pi^-$ decay performed by BaBar [1], much like for the other $B^+ \to h^+h^+h^-$ decays [23–25], hinted at sizable direct CP-violation in the quasi-two-body contributions. More recent model-independent analyses performed by LHCb, with an order of magnitude more signal events, showed large CP-asymmetries in specific phase-space regions (Fig. 7.2), along with a modest phase-space integrated asymmetry of 0.058 ± 0.014 [26]. To understand the mechanisms by which the pattern of CP-asymmetries arise, it is essential to understand the contributions from intermediate resonances and the interferences between them by constructing a model of the amplitude.

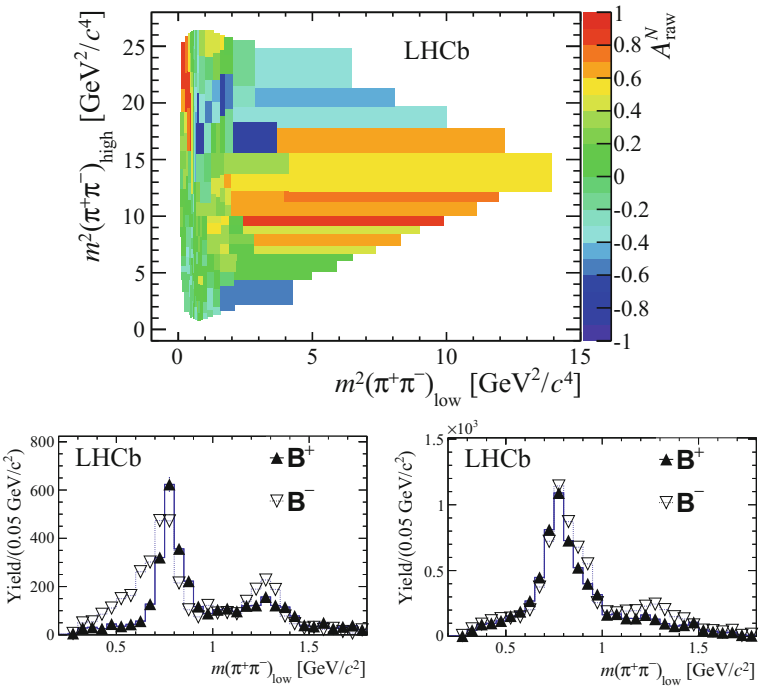

Fig. 7.2 Top: Binned raw *CP*-asymmetries from Ref. [26], where regions of large positive (red) and negative (blue) raw *CP*-asymmetry can be observed. Bottom: Projections on $m(\pi^+\pi^-)_{\rm low}$ of the B^+ and B^- distributions for negative (left) and positive (right) values of the helicity angle

7.1.4 Correspondence with Phenomenology

Various authors [22, 27, 28] stress the importance of the strong ρ–ω mixing, which is observed in the $\rho(770)^0$ region, on *CP*-asymmetries, and in particular, in inducing the observed sign flip in $\mathcal{A}_{CP}$ in this region [29]. Nevertheless, some methods used to obtain the phase-space integrated *CP*-asymmetry of the $B^+ \to \pi^+\pi^+\pi^-$ decay yield a sign opposite to that obtained in the LHCb analysis [30], whereas others result in a sign consistent with the experimental measurement [31]. This sign discrepancy is also observed in comparison between the experimental measurements and QCD factorisation, perturbative QCD, and soft-collinear effective theory calculations of the *CP*-asymmetry in the quasi-two-body $B^+ \to \rho(770)^0\pi^+$ decay [32]. Possible resolution of these discrepancies may be possible via final–state $\pi\pi \leftrightarrow KK$ rescattering effects, which are thought to play a significant role in the generation of the necessary strong phase difference for direct *CP*-violation in *B*-meson decays [33–35], or from neglecting the significant S-wave component at low $\pi\pi$ mass [31, 36].

The $B \to \pi\pi\pi$ family of decays also provide valuable input to perturbative QCD factorisation schemes [37], and recently significant progress has been made in

combining calculations of the $B \to \pi$ and $B \to \pi\pi$ form factors to provide a description of the entire $B^+ \to \pi^+\pi^+\pi^-$ phase-space [38, 39]. These result in predictions for the inclusive branching fraction in the $\rho(770)^0$ region which can be compared with experimental data model-independently. Additionally, promising improvements to the $B \to \pi\pi$ form-factor itself have also recently been made, incorporating finite-width effects for the dominant $B \to \rho$ decay, and the effect of higher mass ρ states, as effective non-resonant contributions to the $B \to \pi\pi$ form-factor [40, 41].

In addition to using SU(3) symmetry to extract the CKM angles from combinations of the decay amplitudes for B decays to three pseudoscalars, such quantities can be used to perform additional tests for anomalous SU(3) breaking effects beyond the Standard Model [4, 42, 43]. Initial indications from the phase-space integrated measurements imply that U-spin, and SU(3) breaking in general, in these three-body decays is large [4, 44], and therefore an analysis similar to that of two-body decays to extract the CKM angles may not be appropriate.

7.1.5 The Light Scalars

Understanding of the $J^P = 0^+$ resonances below 2 GeV is complicated by several factors. In general these states are broad and numerous, which results in a large degree of interference, distorting the shape in the $\pi^+\pi^-$ invariant-mass spectrum. This is further complicated by the opening of various decay channels in this region, where the drop in cross-section to the $\pi^+\pi^-$ final–state results in a further distortion of the lineshape [5]. Furthermore, there also exists a very broad low-mass enhancement now known as the $f_0(500)$ meson, which historically was not considered to be a bound state due to its large width [45]. It is also widely understood, via lattice QCD and other calculations, that the lowest mass glueball, a hadron with no valence quarks, also exists at low mass with the 0^{++} quantum numbers [46]. Due to these issues, the quark content of the light scalar resonances are unknown, however progress is being made in this area as more final states with a large number of signal decays are becoming experimentally accessible [47, 48].

Despite the lack of knowledge regarding the nature of these states, a reliable empirical description can be obtained using the K-matrix formalism with parameters obtained from global coupled-channel fits to historical scattering data. Phenomenological work in light of the BaBar amplitude analysis of $B^+ \to \pi^+\pi^+\pi^-$ indicates that, whilst individual scalar resonances are difficult to identify, these form an essential component of the overall decay amplitude, particularly below the $\rho(770)^0$ pole [36, 49, 50].

7.1.6 Analysis Strategy

This analysis aims to describe the $B^+ \to \pi^+\pi^+\pi^-$ phase-space with a combination of the K-matrix model for the $\pi^+\pi^-$ S-wave and a conventional isobar model for

the higher spin states.[1] To separate the signal events from background, a boosted decision-tree classifier is used, along with requirements on the information provided by the particle ID sub-detectors to suppress background from final state misidentification.

The fraction of signal in the Dalitz-plot fit cannot be well determined from the fit itself, and therefore a separate B^+-candidate invariant-mass fit is required. Furthermore, the different data selection categories have different efficiencies, and therefore the fraction of events that are selected in a particular category impact the overall efficiency, so these fractions are also determined from the invariant-mass fit.

The square Dalitz-plot efficiency map is primarily determined from fully simulated MC, with data-driven corrections used in the case of the particle ID and L0Hadron trigger efficiencies. The background shape in the Dalitz-plot fit is taken directly from the upper sideband in collision data, with modifications to account for contributions from $B^+ \to K^+\pi^+\pi^-$ and $B^0 \to \pi^+\pi^-$ decays.

The Dalitz-plot fit is then performed for B^+ and B^- decays simultaneously, where the model is selected by including components that sufficiently improve the model likelihood with respect to the data. The isobar parameters of the final fit result are reported, along with CP-asymmetries and fit fractions, and the K-matrix S-wave amplitude. Systematic uncertainties from the inputs to the Dalitz-plot fit are also calculated for all of the reported parameters. The results obtained from the Dalitz-plot fit are then compared to predictions from theoretical calculations.

7.2 Dataset and Selection

This analysis is performed on 1 fb^{-1} of 7 TeV and 2 fb^{-1} of 8 TeV centre-of-mass energy data collected by the LHCb detector in 2011 and 2012, respectively. This corresponds to approximately equal quantities of negative and positive dipole magnet polarity across the running periods, to cancel possible detector-induced charge asymmetries.

The data used in this analysis are pre-processed by the `Stripping21r1` and `Stripping21` `Bu2hhh_KKK_incl` lines for 2011 and 2012 data, respectively, which are written to the `Bhadron.mdst` stream. The requirements that are imposed on the signal candidates at this stage are listed in Table 7.1. These stripping requirements are made under the $B^+ \to K^+K^+K^-$ hypothesis, but include no particle identification requirements on the tracks and a large enough mass window such that the $B^+ \to \pi^+\pi^+\pi^-$ decay can be reconstructed from these candidates with negligible loss in efficiency.

Similar trigger requirements to the analysis described in Chap. 5 are used: `HadronTOS` or `GlobalTIS` at L0; `HltTrackAllL0` at HLT1; and the simple and boosted-decision-tree inclusive multi-body triggers at HLT2, for two and

[1] An equivalent analysis where the S-wave is also modelled with an isobar approach, and another where the S-wave is described model-independently, are the subject of separate LHCb investigations.

Table 7.1 Stripping selection requirements for B^+ candidates, where IP refers to the impact parameter, the distance between a vertex and an extrapolated track, and PV refers to a primary (pp) interaction vertex

Variable definition	Selection requirement
Track cuts	
Track transverse momentum	$p_{\mathrm{T}} > 100\,\mathrm{MeV}$
Track momentum	$p > 1500\,\mathrm{MeV}$
Minimum IP fit χ^2 w.r.t any PV	$\chi^2(\mathrm{IP})_{\mathrm{min}} > 1$
Track fit χ^2 per degree-of-freedom	$\chi^2_{\mathrm{trk}}/\mathrm{ndof} < 3$
Track ghost probability	$\mathrm{P(ghost)} < 0.5$
Track combination cuts	
Combined invariant mass	$5050 < m(K^+K^+K^-) < 6300\,\mathrm{MeV}$
Maximum pairwise distance of closest approach	$\mathrm{DOCA}_{\mathrm{max}} < 0.2\mathrm{mm}$
Sum of the track momenta	$\sum p > 20000\,\mathrm{MeV}$
Sum of the track transverse momenta	$\sum p_{\mathrm{T}} > 4500\,\mathrm{MeV}$
Sum of the mimimum IPs χ^2 w.r.t any PV	$\sum \chi^2_{\mathrm{IP}} > 500$
B^+ candidate cuts	
Cosine of the DIRA angle	$\cos\theta_{\mathrm{DIRA}} > 0.99998$
B^+ vertex and any PV distance fit χ^2	$\chi^2_{B^+-\mathrm{PV}} > 500$
B^+ vertex and any PV distance	$D_{B^+-\mathrm{PV}} > 3\mathrm{mm}$
B^+ vertex fit χ^2	$\chi^2_{B^+}\mathrm{vtx} < 12$
Minimum IP fit χ^2 w.r.t any PV	$\chi^2(\mathrm{IP})_{\mathrm{min}} < 10$
Transverse momentum	$p_{\mathrm{T}} > 1000\,\mathrm{MeV}$
PV constrained mass corrected for missing p_{T}	$4000 < m(B^+)^{\mathrm{Corr}}_{\mathrm{PV}} < 7000\,\mathrm{MeV}$

three-body decays. However, due to considerations made in Sect. 7.6.1, all figures in this chapter will pertain only to candidates which result in a positive L0Hadron trigger decision (TOS), unless otherwise specified.

To evaluate the signal efficiency, 4×10^6 $B^+ \to \pi^+\pi^+\pi^-$ filtered signal decay MC events are used, and to estimate the background rate and distribution, $B^+ \to K^+\pi^+\pi^-$ filtered signal decay MC is used. Here, only those events that pass the `Bu2hhh_KKK_incl` stripping line are saved, and each are generated flat in their corresponding square Dalitz-plots. This is in addition to standard MC samples for the other background categories. These simulated data samples are produced using running conditions typical of those during 2011 and 2012 detector operations [51].

7.2.1 Momentum Scale Calibration

This analysis makes use of world-average values for resonance masses and widths to identify and evaluate the magnitudes of resonant contributions. Therefore to minimise the systematic uncertainty resulting from this, proper calibration of the track

momentum is required. This calibration accounts for various effects related to the uncertainty on the dipole magnetic field map and alignment of the sub-detectors. This is carried out using a large sample of $J/\psi \to \mu^+\mu^-$ decays, resulting in a relative difference between the measured and world-average J/ψ mass of around 1×10^{-4} [52].

7.2.2 Decay-Tree Fitter

The Decay Tree Fitter algorithm (described in Sect. 4.9.5) is used to re-fit candidate decays under the $B^+ \to \pi^+\pi^+\pi^-$ mass hypothesis. The final–state pions are constrained to the world-average charged pion mass of 139.57 MeV, and for the Dalitz-plot fit, the conventional and square Dalitz-plot variables are calculated with the B^+ mass constrained to the world-average B^+ mass value, 5279.32 MeV, to ensure that the decays exist strictly within the kinematic limits. In both cases, the B^+ is constrained to originate from the primary vertex with the best χ^2_{IP}.

7.2.3 Mass Resolution

Due to the presence of narrow intermediate resonances, it is important to ensure that the experimental resolution in $m(\pi^+\pi^-)$ does not dominate the observed resonance width (and thus bias any parameters related to these resonances).

To investigate this effect, a study on simulated $B^+ \to \pi^+\pi^+\pi^-$ decay events is performed, where the stripping selection is applied, but otherwise no other selection cuts are imposed (other than requiring that the Decay-Tree Fitter converges). In bins of the $\pi^+\pi^-$ invariant mass the difference between the truth-level invariant mass, calculated from the true four-vectors, and the reconstructed invariant mass is computed. This is fitted with a double Crystal Ball distribution, where the means and widths of the central Gaussian distributions are shared, but where the tail parameters are independent. The width of the central Gaussian is then taken to be the experimental resolution in this bin. The results of this can be seen in Fig. 7.3 (left), which shows the variation of this resolution across the Dalitz plot in bins of $m_{\pi^+\pi^-}$. The narrow $\omega(782)$ is close to the $\pi^+\pi^-$ threshold at $m_{\text{PDG}} = 782.65$ MeV and with width $\Gamma_{\text{PDG}} = 8.49$ MeV, where the experimental resolution is sufficiently smaller than the natural width. For potential states at higher mass, such as the χ_{c0} at $m_{\text{PDG}} = 3.41475$ GeV, $\Gamma_{\text{PDG}} = 10.5$ MeV, the experimental resolution is a larger contribution, and as such a systematic related to this is assigned for models that include these components.

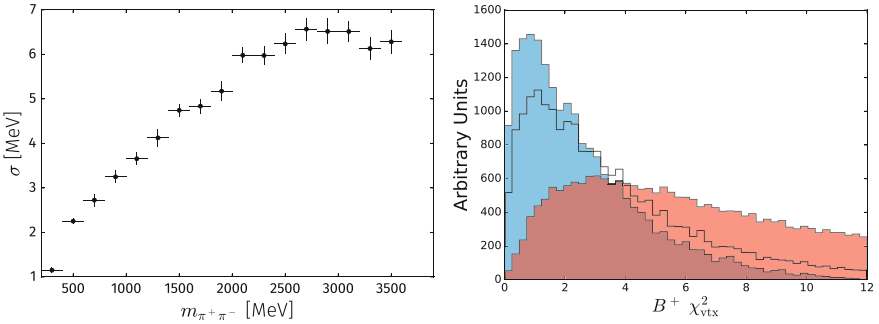

Fig. 7.3 Left: The variation of the $\pi^+\pi^-$ invariant mass resolution in bins of $m_{\pi^+\pi^-}$. Right: Distribution of B^+ vertex χ^2 for simulated $B^+ \to \pi^+\pi^+\pi^-$ decay events, for candidates in events with two signal candidates, where at least one candidate is a true signal decay. The two candidates are ordered by smaller (blue) or larger (red) B^+ vertex χ^2, and compared to the distribution for truth-matched decays (black)

7.2.4 Multiple Candidates Per Event

As the decay in this analysis is comparatively rare, it is unlikely that multiple true $B^+ \to \pi^+\pi^+\pi^-$ decays occur within an event. Nevertheless, multiple signal candidates in a single event can result from the reconstruction algorithms, either from duplicated tracks that correspond to the same true particle, or from candidates that are built from an overlapping subset of tracks. Candidates due to the first of these will be rejected by the dedicated 'clone killer' algorithms, and therefore most of the events with multiple candidates in this analysis are of the second kind, and can be discriminated via quantities such as the B^+ vertex fit consistency that enter the boosted decision-tree classifier. As can be inferred from Fig. 7.3, where B^+ candidates from $B^+ \to \pi^+\pi^+\pi^-$ signal MC events containing two candidates are ordered by B^+ vertex fit consistency and compared against the distribution for the true candidates, candidate arbitration via the quantities that enter the BDT tend to result in the selected candidate being signal-like.

A such, the 10% of events with multiple candidates that exist after the stripping selection is reduced to around 0.01% after the BDT selection, consistent with those rejected being more background-like. Multiple candidates in collision and simulated data that survive the requirement on the BDT receive no further treatment, to avoid biases [53].

7.2.5 Boosted Decision Tree

Much like in the analysis described in Chap. 5, the dominant background in the $B^+ \to \pi^+\pi^+\pi^-$ signal region is from incorrect association of non-signal tracks in

Table 7.2 Variables that enter the $B^+ \to \pi^+\pi^+\pi^-$ signal classifier, and whether these are reweighted in simulated data to match collision data

Variable	Reweighted
Minimum daughter PV χ^2_{IP}	Yes
B^+ p_{T} asymmetry	Yes
Pointing angle	Yes
B^+ p_{T}	Yes
B^+ PV DIRA	No
B^+ vertex fit χ^2	No
B^+ IP χ^2	No
B^+ flight distance χ^2	No

the event to a displaced vertex, and a similar strategy is employed here to reject this background with high efficiency. A classifier is trained using $B^+ \to \pi^+\pi^+\pi^-$ signal MC, generated flat in the square Dalitz-plot, and B^+ sideband $\pi^+\pi^+\pi^-$ collision data that passes the trigger and stripping requirements, where $m(B^+) > 5400\,\text{MeV}$ to avoid partially reconstructed and cross-feed backgrounds below the B^+ signal.

Input Variables

Variables are used that exhibit large differences between the signal and background, such as those that involve the reconstructed B^+ transverse momentum, vertex quality, and impact parameter with respect to the primary pp vertex. A list of these variables can be seen in Table 7.2, where the pointing angle is defined as

$$\theta_{\text{pointing}} = \frac{P_B \sin\theta_{\text{DIRA}}}{P_B \sin\theta_{\text{DIRA}} + \sum_i P_{h_i}}, \tag{7.3}$$

θ_{DIRA} is the angle between the reconstructed B^+ momentum and the displacement vector between the primary vertex and the B^+ decay vertex, and h_i for $i \in [1, 2, 3]$ refers to the three pions in the final state.

The p_{T} asymmetry is the asymmetry between the B^+ p_{T} and the p_{T} carried by the rest of the event, in a cone around the B^+ flight vector,

$$\mathcal{A}(p_{\text{T}}) = \frac{p_{\text{T}}^{B^+} - p_{\text{T}}^{\text{cone}}}{p_{\text{T}}^{B^+} + p_{\text{T}}^{\text{cone}}}. \tag{7.4}$$

This cone is defined in terms of its radius in pseudorapidity and azimuthal angle, (η, ϕ), as $R = \sqrt{(\Delta\eta)^2 + (\Delta\phi)^2}$. In this analysis a value of $R = 1.5$ is chosen.

The variables that are chosen to train the BDT to separate signal from background may have distributions in data that are not well replicated in simulation. If this is the case, the classifier may instead be identifying signal decays via this difference, rather than the true difference between signal and background in data. This results in a classifier with performance that is not replicated when it is applied to collision

data. Furthermore, evaluating the classifier on MC to calculate the signal efficiency results in biased distributions.

To avoid this problem, the variables that enter the BDT are reweighted to make them more similar to the signal data. This is performed using $B^+ \to K^+\pi^+\pi^-$ as a control mode, where sWeighted signal data and MC from this decay are used to train a gradient-boosted decision-tree reweighting algorithm [54]. To extract the sWeights, a fit is performed to the $B^+ \to K^+\pi^+\pi^-$ mode in collision data, where the trigger and loose particle identification requirements are applied, and the intermediate $B^+ \to \overline{D}^0(K^+\pi^-)\pi^+$ and $B^+ \to \overline{D}^0(\pi^+\pi^-)K^+$ decays vetoed. The same requirements are applied to the MC.

The variables that are reweighted in this way are the B^+ p_{T} and p, the daughter primary vertex fit χ^2, and the p_{T} asymmetry, in addition to the number of SPD hits (this quantity does not enter the BDT classifier, however it is used as a proxy for the event multiplicity and is useful for the MC efficiency corrections that follow). These variables are discrepant primarily due to the increased detector occupancy in collision data, and are similar between $B^+ \to \pi^+\pi^+\pi^-$ and $B^+ \to K^+\pi^+\pi^-$. This is expected, as most are properties of the event rather than the specific B^+ decay, and is confirmed by comparing the MC distributions in each case. No reweighting is performed for the daughter momenta, as these are parameterised directly in the efficiency maps. A comparison between these variables can be seen in Figs. 7.4 and 7.5, where the grey filled histogram is the background-subtracted $B^+ \to K^+\pi^+\pi^-$ data, the blue curve is unweighted $B^+ \to K^+\pi^+\pi^-$ signal MC, and the red curve is reweighted $B^+ \to K^+\pi^+\pi^-$ signal MC using the weights from the gradient-boosted reweighting algorithm (Fig. 7.6).

Training

An XGBoost [55] gradient-boosted decision-tree is used, trained using the Reproducible Experiment Platform [56] to compare potential alternative classifiers and to perform hyperparameter optimisation. Each iteration of the hyperparameter optimisation is performed using a random split of the data into training and testing sets to eliminate bias. For the final round of training, two classifiers are trained using even and odd event numbers to ensure that this split is reproducible when applied to the data sample used in the analysis, and, where an event was used to train the classifiers, the classification probability evaluated using the classifier trained on the other dataset (where this is not the case, such as for the collision data signal region, the classifier to use is chosen at random).

The receiver operating characteristic (ROC), the background rejection for a given value of the signal efficiency, is evaluated to estimate the performance of the classifier, which can be seen in Fig. 7.7 (top left). The area under this curve is approximately 0.987, which indicates good classification performance. Also in this figure is the signal efficiency and background rejection as a function of the cut on the BDT output, and the distribution of the signal and background test samples as a function of the classifier output.

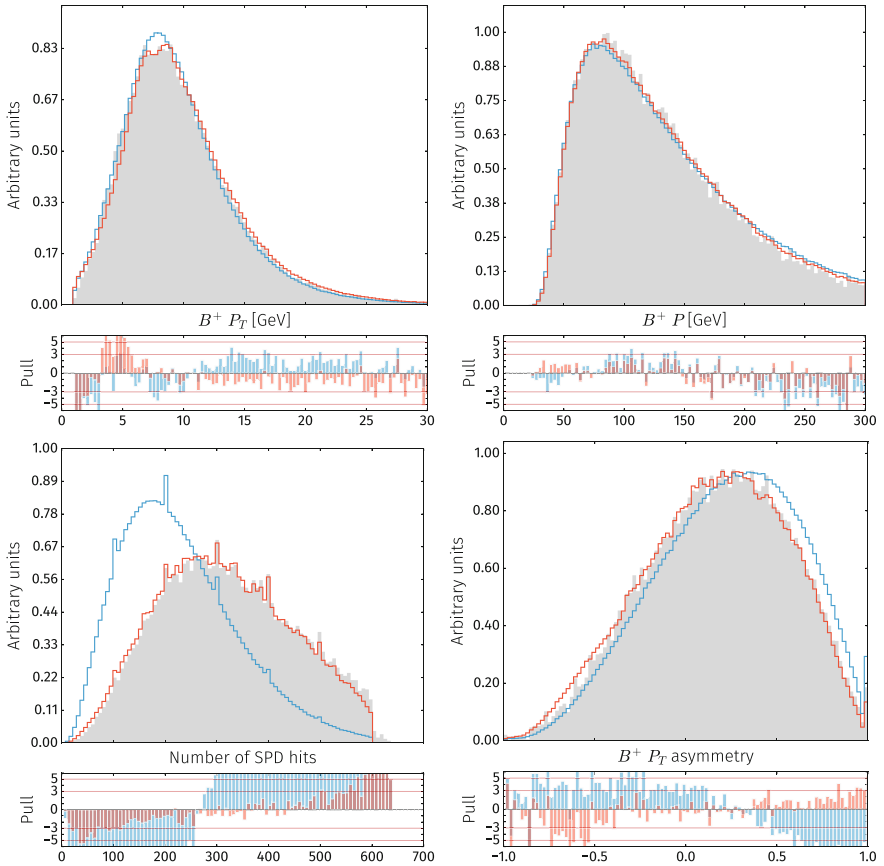

Fig. 7.4 Distributions of variables that enter the boosted decision-tree classifier (either individually or aggregated with other variables). The grey filled histogram is the background-subtracted $B^+ \to K^+\pi^+\pi^-$ data, the blue curve is unweighted $B^+ \to K^+\pi^+\pi^-$ signal MC, and the red curve is reweighted $B^+ \to K^+\pi^+\pi^-$ signal MC using the weights from the gradient-boosted reweighting algorithm

Optimisation of the BDT Requirement

The requirement on the classifier output for an amplitude analysis is motivated differently to that of a search or branching fraction analysis, such as that described in Chap. 5. Here, precision on the isobar parameter of the intermediate resonances is desired, which is a more complex requirement than the discovery significance or uncertainty on the total branching fraction. Despite this difference, toy studies performed in the context of the intermediate resonances observed in the $B^0_s \to K^0_S K\pi$ amplitude analysis [57], indicate that the signal purity multiplied by the approximate expected signal significance $(N_S/(N_S + N_B) \times N_S/\sqrt{N_S + N_B}$, where N_S (N_B) is

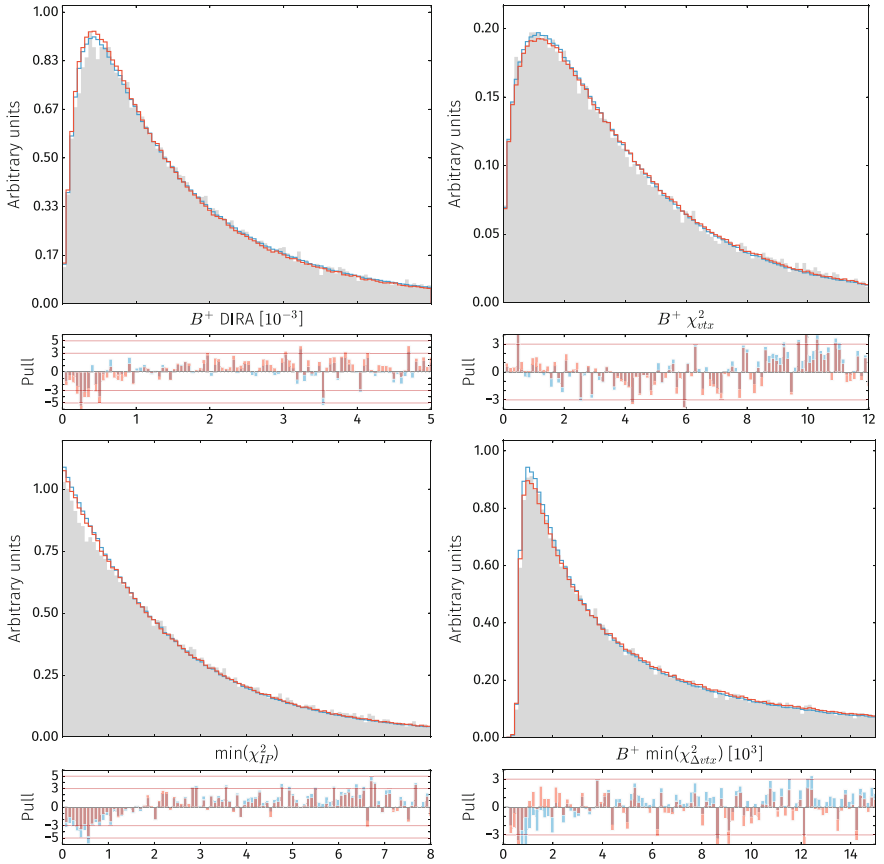

Fig. 7.5 Distributions of variables that enter the boosted decision-tree classifier (either individually or aggregated with other variables). The grey filled histogram is the background-subtracted $B^+ \to K^+\pi^+\pi^-$ data, the blue curve is unweighted $B^+ \to K^+\pi^+\pi^-$ signal MC, and the red curve is reweighted $B^+ \to K^+\pi^+\pi^-$ signal MC using the weights from the gradient-boosted reweighting algorithm

the expected signal (background) yield after a given cut) is a reasonable proxy for the precision on the parameters describing the dominant $B_s^0 \to K^{*0}(892)K$ decay.

The signal purity multiplied by the approximate expected signal significance as a function of the classifier output can be seen in Fig. 7.7 (top left), along with the signal efficiency from simulated signal data, the background rejection as estimated from the signal sideband in collision data, and the signal purity. Taking into account both figures-of-merit and the signal efficiency, candidates with classifier output less than 0.8 are rejected and not considered further. This requirement is approximately 90% efficient for signal and rejects approximately 98% of background in the signal region.

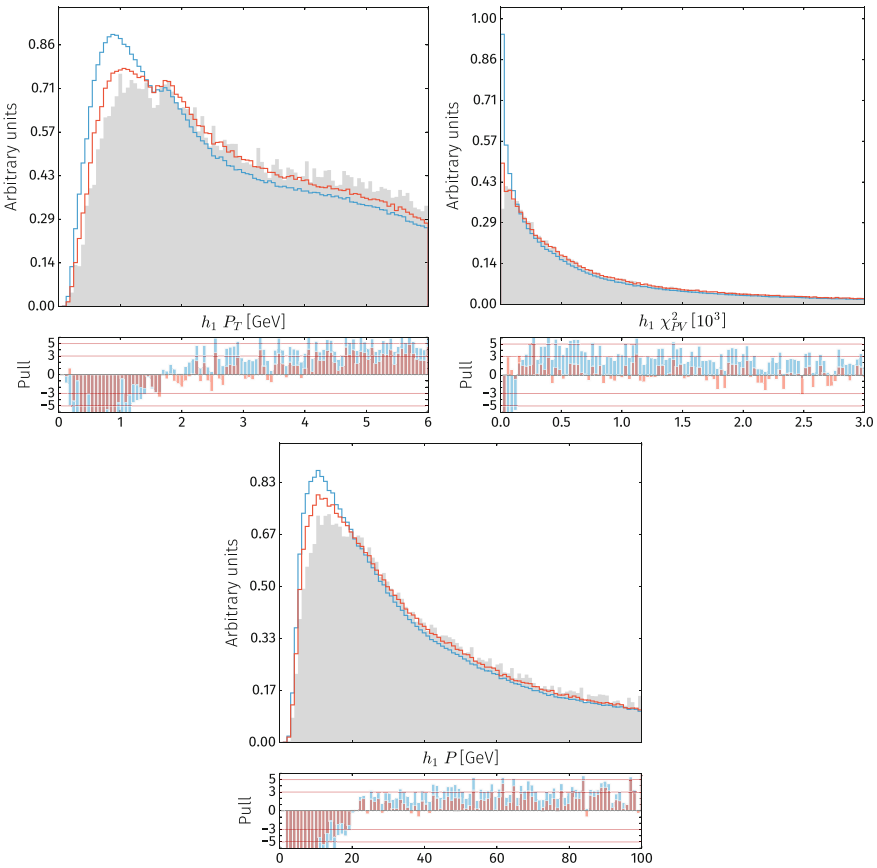

Fig. 7.6 Distributions of variables that enter the boosted decision-tree classifier (either individually or aggregated with other variables). The grey filled histogram is the background-subtracted $B^+ \to K^+\pi^+\pi^-$ data, the blue curve is unweighted $B^+ \to K^+\pi^+\pi^-$ signal MC, and the red curve is reweighted $B^+ \to K^+\pi^+\pi^-$ signal MC using the weights from the gradient-boosted reweighting algorithm

Optimisation of the Particle Identification Requirements

The selection requirements on the particle identification variables, the posterior probability of a particle being a pion (`ProbNNpi`) and the posterior probability of a particle being a kaon (`ProbNNK`), are also optimised using the signal purity multiplied by the expected signal significance. This figure-of-merit is calculated using the data-driven particle ID efficiencies and background rejection for each requirement, and the world-average relative branching fractions of the $B^+ \to \pi^+\pi^+\pi^-$ (signal) and $B^+ \to K^+\pi^+\pi^-$ (background) decays. The results of this optimisation, a scan over various values of the requirements on the posterior probabilities of the pion or kaon ID hypothesis, can be seen in Fig. 7.8. From these, cut values of `PROBNNpi`

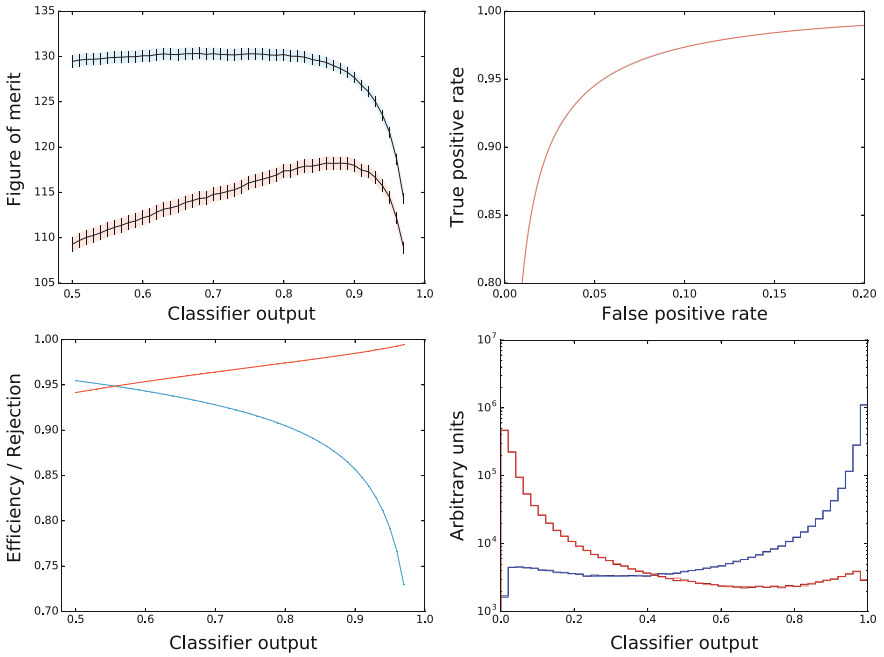

Fig. 7.7 Top left: Figures of merit corresponding to the approximate significance multiplied by the signal purity (red) and the approximate significance (blue). Top right: Classifier true-positive rate versus false-positive rate (the receiver operating characteristic) for the two classifier folds. Bottom left: Simulated signal efficiency (blue) and background rejection in the signal region (red). Bottom right: Distributions of classifier output for signal (blue) and background (red) for the two classifier folds (light and dark)

> 0.3 and PROBNNK < 0.1 are chosen, with a signal efficiency of around 50%, and mis-ID rate of around 2%.

7.3 Background

The distribution of low and high mass combinations of the opposite-sign pions, calculated without the constraint that the invariant mass of the decay products is equal to the B^+ mass, versus the reconstructed B^+ mass can be seen in Fig. 7.9. As the $\overline{D}^0$ veto is applied to the mass-constrained $m(\pi^+\pi^-)$ distributions, clear contributions from partially reconstructed decays with intermediate $\overline{D}^0$ contributions ($m(D^0) = 1864.83\,\text{MeV}$) can be observed at low $m(\pi^+\pi^+\pi^-)$, where the veto region is offset at this value of the reconstructed B^+ mass. A larger contribution from combinatorial background is expected at low $m(\pi^+\pi^+\pi^-)$, and in addition, broad distributions in $m(\pi^+\pi^-)$ at low $m(\pi^+\pi^+\pi^-)$ are associated

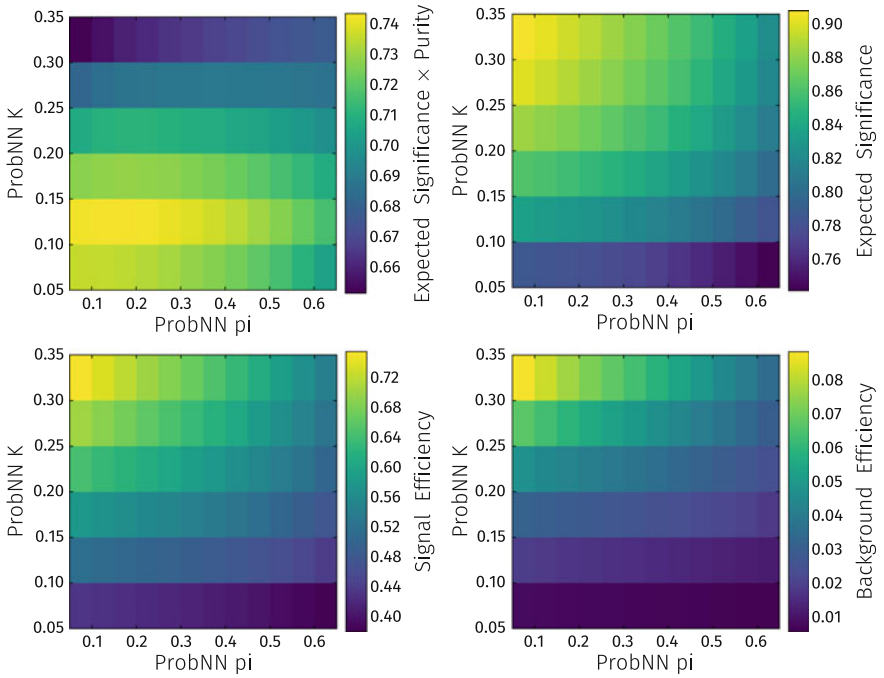

Fig. 7.8 Top: Figures of merit corresponding to the approximate significance multiplied by the signal purity (left) and the approximate significance (right). Bottom: Selection efficiency of the signal $B^+ \to \pi^+\pi^+\pi^-$ decay (left) and of $B^+ \to K^+\pi^+\pi^-$ background decay (right). Each are displayed as a function of the cut on the particle ID variables, where the corresponding cut is greater than the value on the x-axis, 'ProbNN pi', and less than the value on the y-axis, 'ProbNN K'

with partially reconstructed B^+ and B^0 meson decays, and those that vanish at $m(\pi^+\pi^+\pi^-) \approx 5227\,\text{MeV}$ associated with partially reconstructed decays from B_s^0 mesons. In the $m(\pi^+\pi^-)_{\text{High}}$ distribution a contribution from the $B^0 \to \pi^+\pi^-$ decay can be seen above $m(\pi^+\pi^+\pi^-) \approx 5420\,\text{MeV}$.

7.3.1 Cross-Feed Background

After the particle identification requirements are applied, the dominant source of mis-ID background is from the $B^+ \to K^+\pi^+\pi^-$ decay. Background from double or higher-order mis-identification, such as that from $B^+ \to K^+\pi^+K^-$ decays, is negligible (particularly as the branching fraction of the $B^+ \to K^+\pi^+K^-$ decay is some 30% of the signal decay).

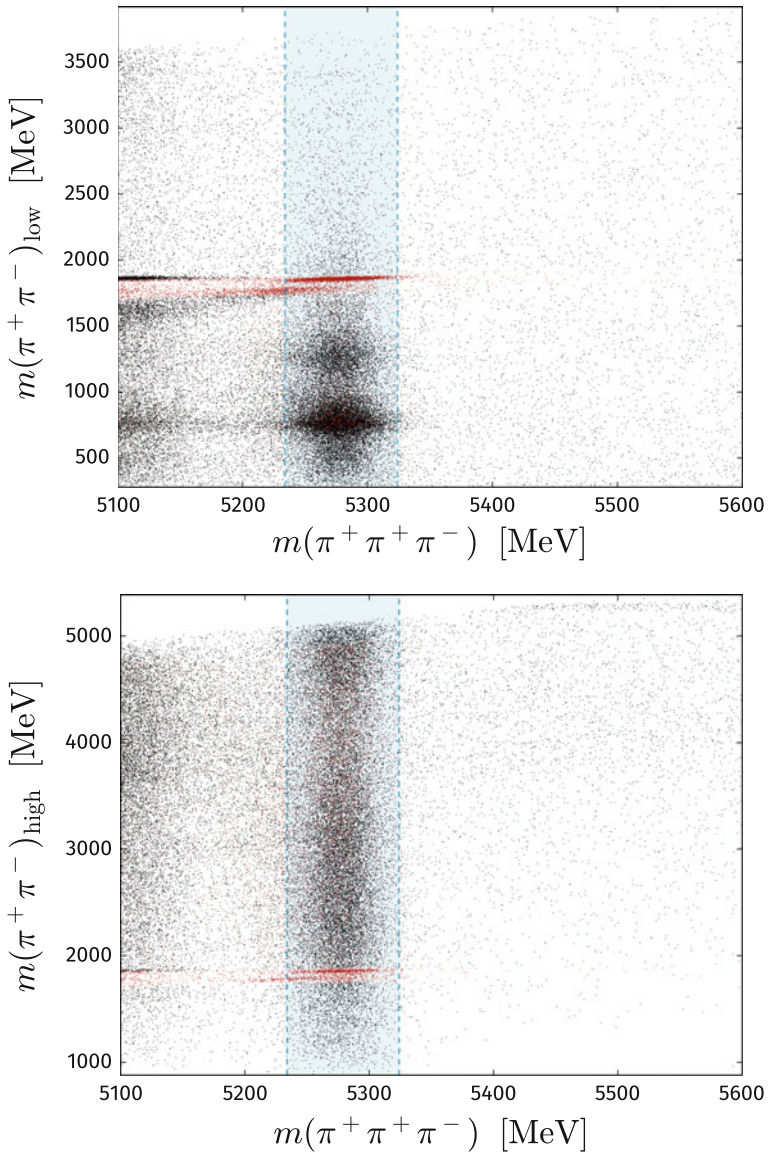

Fig. 7.9 Distribution of $B^+ \to \pi^+\pi^+\pi^-$ decay candidates in $\pi^+\pi^+\pi^+$ invariant-mass, versus low (top) and high (bottom) di-pion invariant-mass combinations for the full fit range, and for both trigger categories, where no B^+ mass constraint on the daughter pions is implemented. Events removed via the $\overline{D}^0$ veto are indicated in red, and the extent of the nominal Dalitz-plot fit signal region is indicated in blue

7.3.2 Partially Reconstructed Background

Potential partially-reconstructed background shapes in the $\pi^+\pi^+\pi^-$ invariant-mass spectrum are investigated using the RapidSim [58] package, which uses fixed order next-to-leading-logarithm calculations for the initial b-quark kinematical distributions at LHC energies. Subsequent hadronic decays are simulated using the ROOT class `TGenPhaseSpace`, which generates a flat distribution in an arbitrary phase-space, and the effects of LHCb detector acceptance and resolution are applied to the kinematical distributions of the decay products. Furthermore, unreconstructed decays involving neutral pions and alternative mass hypotheses can be implemented. This results in plausible physical distributions in $\pi^+\pi^+\pi^-$ invariant-mass before the effects of the analysis selection.

In addition to the branching fractions of potential partially-reconstructed background sources, there are additional factors that need to be applied to estimate the relative composition of the total partially-reconstructed background. Decays of Λ_b^0 baryons and B_s^0 mesons are scaled by their production fraction relative to B^+ mesons (factors of 0.480 ± 0.044 and 0.259 ± 0.015 [59, 60], respectively), decays with a proton in the final state are scaled by the $p \to \pi^+$ mis-ID rate of approximately 2% for the selection requirements in this analysis, and similarly, decays involving a mis-identified kaon are scaled by the mis-ID rate of approximately 1%.

Furthermore, to mimic the effect of the selection efficiency for final states with long lived intermediate particles, the ratio between the signal decay efficiency and the efficiency of fully simulated and selected 'proxy' modes are calculated as a correction factor to the relative branching fractions in Tables 7.3, 7.4 and 7.5. Simulated $B^+ \to K_S^0(\pi^+\pi^-)\pi^+$ data are used to estimate a K_S^0-meson and Λ-baryon rejection factor, and simulated $B^+ \to \overline{D}^0(\pi^+\pi^-)\pi^+$ data are used to estimate the rejection factor for charm hadrons. These rejection factors are found to be 0.1%, and 10%, respectively.

The decay $B_s^0 \to \pi^+\pi^-\pi^+\pi^-$ was observed in Ref. [61], but the branching fraction was not measured. The value used here, and reported in Table 7.3, is extrapolated from the $B^0 \to \rho^0(\pi^+\pi^-)\rho^0(\pi^+\pi^-)$ branching fraction, the measured $\rho^0\rho^0$ decay fraction, and the $B_s^0 \to \pi^+\pi^-\pi^+\pi^-$ yield, under the assumptions that the efficiencies are similar and the yield for $B_s^0 \to \pi^+\pi^-\pi^+\pi^-$ has no charm component.

The invariant-mass distribution of these sources of partially reconstructed background, incorporating their relative rejection factors with respect to the signal decay, can be seen Fig. 7.10. From this it can be seen that the dominant source of partially reconstructed background in the range [5100, 5600] MeV is charmless decays involving a $\rho^+ \to \pi^+\pi^0$ decay, where failing to reconstruct the π^0 results in the B^0 mass distribution shifting by at least $m(\pi^0)$; and B_s^0-meson decays via an intermediate charm meson, where a charged pion in the final state is not reconstructed, resulting in a shift of at least $m(\pi^+)$ from the true B_s^0 mass. Decays involving Λ_b^0 baryons, whilst having sizable branching fractions, are suppressed by the low proton mis-ID rate and the Λ_b^0 production fraction relative to B^+. Decays involving two unreconstructed pions, or a pion and a photon, have distributions that peak lower in mass than the range considered here.

Table 7.3 Branching fractions of potential partially reconstructed charmless background decays from B-mesons. All central values and uncertainties are taken from Ref. [5]. The branching fraction for $B^+ \to a_1(1260)^0(\pi^+\pi^-\pi^0)\pi^+$ is only that of $B^+ \to a_1(1260)^0\pi^+$, as the branching fraction of $a_1(1260)^0 \to \pi^+\pi^-\pi^0$ is unmeasured. The branching fraction of $B_s^0 \to \pi^+\pi^-\pi^+\pi^-$ is extrapolated from the yield obtained in Ref. [61]

Decay	Branching fraction $(\times 10^{-5})$
$B^+ \to \rho^+(\pi^+\pi^0)\rho^0(\pi^+\pi^-)$	2.40 ± 0.19
$B^+ \to \eta'(\rho^0(\pi\pi)\gamma)K^+$	2.05 ± 0.08
$B^+ \to a_1(1260)^0(\pi^+\pi^-\pi^0)\pi^+$	$2.0 \pm 0.6^\dagger$
$B^0 \to K_S^0(\pi^+\pi^-)\pi^+\pi^-$	1.80 ± 0.09
$B_s^0 \to K_S^0(\pi^+\pi^-)\pi^+\pi^-$	0.52 ± 0.14
$B^+ \to K_S^0(\pi^+\pi^-)\rho^+(\pi^+\pi^0)$	0.28 ± 0.05
$B^+ \to \eta(\pi^+\pi^-\pi^0)\pi^+$	0.11 ± 0.01
$B^0 \to \rho^0(\pi^+\pi^-)\rho^0(\pi^+\pi^-)$	0.09 ± 0.02
$B^+ \to \eta'(\rho^0(\pi\pi)\gamma)\pi^+$	0.08 ± 0.03
$B_s^0 \to \pi^+\pi^-\pi^+\pi^-$	$0.05 \pm 0.01^\dagger$
$B^+ \to \eta(\pi^+\pi^-\gamma)\pi^+$	0.017 ± 0.001
$B^+ \to \eta'(\pi^+\pi^-\pi^0)\pi^+$	< 0.05
$B^0 \to K_S^0(\pi^+\pi^-)\eta(\pi^+\pi^-\gamma)$	< 0.05
$B^0 \to K_S^0(\pi^+\pi^-)\eta'(\pi^+\pi^-\gamma)$	< 0.05
$B^0 \to K_S^0(\pi^+\pi^-)\eta'(\pi^+\pi^-\pi^0)$	< 0.05

Fit Contributions

The partially reconstructed background present in the fit region can be approximated by shapes corresponding to the decays listed in Table 7.6, and therefore simulated data (incorporating the full LHCb detector simulation and analysis selection) corresponding to these modes are used to obtain shapes that enter the B^+ invariant-mass fit to collision data. The world-average values of the $B^+ \to \rho^+\rho^0$ decay polarisation amplitudes show that the decay is dominated by the longitudinal component, $f_L = 0.950 \pm 0.016$ [8], and therefore the simulated $B^+ \to \rho^+\rho^0$ background events are generated with complete longitudinal polarisation. The $\eta' \to \rho^0\gamma$ decay in the decays of $B^+ \to \eta'(\rho^0(\pi\pi)\gamma)K^+$ and $B^+ \to \eta'(\rho^0(\pi\pi)\gamma)\pi^+$ is generated assuming the magnitudes of the positive and negative helicity amplitudes are equal, with a relative phase of zero.

7.3.3 Intermediate Charm Decays

The dominant source of correctly reconstructed charm background is the $B^+ \to \overline{D}^0(\pi^+\pi^-)\pi^+$ decay, which has a branching fraction of $(6.81 \pm 0.24) \times 10^{-6}$. The long lifetime of the weakly decaying D^0-meson results in a width narrow enough that

Table 7.4 Branching fractions of potential partially reconstructed background decays with an intermediate charm meson. All central values and uncertainties are taken from Ref. [5]

Decay	Branching fraction $(\times 10^{-5})$
$B^+ \to \overline{D}^0(\pi^+\pi^-\pi^0)\pi^+$	7.06 ± 0.49
$B_s^0 \to D_s^-(\pi^+\pi^-\pi^-)\pi^+$	3.27 ± 0.29
$B_s^0 \to D_s^{*-}(D_s^-(\pi^+\pi^-\pi^-)\gamma)\pi^+$	2.04 ± 0.52
$B^+ \to \overline{D}^0(\pi^+\pi^-)\rho^+(\pi^+\pi^0)$	1.90 ± 0.26
$B^0 \to D^-(\pi^-\pi^-\pi^+)\pi^+$	0.83 ± 0.07
$B^+ \to \overline{D}^{*0}(\overline{D}^0(\pi^+\pi^-)\pi^0)\pi^+$	0.74 ± 0.04
$B^+ \to \overline{D}^{*0}(\overline{D}^0(\pi^+\pi^-)\gamma)\pi^+$	0.26 ± 0.02
$B^+ \to D^-(\pi^-\pi^0)\pi^+\pi^+$	0.13 ± 0.01
$B^0 \to \overline{D}^0(\pi^+\pi^-)\pi^+\pi^-$	0.12 ± 0.01
$B^0 \to \overline{D}^0(\pi^+\pi^-)\pi^0$	< 0.05

Table 7.5 Branching fractions of potential partially reconstructed background decays from b-baryons. All central values and uncertainties are taken from Ref. [5]

Decay	Branching fraction $(\times 10^{-5})$
$\Lambda_b^0 \to \Lambda_c^+(pK^-\pi^+)\pi^-$	31.11 ± 3.01
$\Lambda_b^0 \to \Lambda_c^+(\Lambda(p\pi^-)\pi^+\pi^0)\pi^-$	22.2 ± 2.2
$\Lambda_b^0 \to \Lambda_c^+(pK_S^0(\pi^+\pi^-)\pi^0)\pi^-$	6.75 ± 0.71
$\Lambda_b^0 \to \Lambda_c^+(pK_S^0(\pi^+\pi^-))\pi^-$	5.36 ± 0.51
$\Lambda_b^0 \to p\pi^+K^-\pi^-$	5.11 ± 0.51
$\Lambda_b^0 \to \Lambda_c^+(\Sigma^0(\Lambda(p\pi^-)\gamma))\pi^-$	4.04 ± 0.40
$\Lambda_b^0 \to \Lambda_c^+(p\pi^+\pi^-)\pi^-$	2.2 ± 1.1
$\Lambda_b^0 \to p\pi^+\pi^-\pi^-$	2.13 ± 0.24

the interference with the rest of the amplitude is negligible, and a veto in the Dalitz plot can be performed with reasonable efficiency. Cross-feed decays, where $\overline{D}^0$ decays to $K^-\pi^+$ also exist, with a larger branching fraction of $(1.89 \pm 0.06) \times 10^{-4}$. After the PID requirements, this still results in a non-negligible structure in the $B^+ \to \pi^+\pi^+\pi^-$ Dalitz plot, so this is also vetoed. The veto is implemented by ensuring that the total $\overline{D}^0$ veto window in $m(\pi^+\pi^-)_{\text{low}}$ and $m(\pi^+\pi^-)_{\text{high}}$ is large enough to accommodate the cross-feed decay, where $1750 < m(\pi^+\pi^-) < 1890\,\text{MeV}$. This veto region can be seen in Fig. 7.11.

Decays via J/ψ and $\psi(2S)$ are suppressed by their small decay rate to hadrons, and by the small $B^+ \to J/\psi\pi^+$ and $B^+ \to \psi(2S)\pi^+$ branching fractions, resulting in a total branching fraction of around 1×10^{-9}, or smaller. So far no $B^+ \to \chi_{c0}\pi^+$ or $B^+ \to \chi_{c2}\pi^+$ decays have been observed (the previous BaBar analysis set limits on their contribution to $B^+ \to \pi^+\pi^+\pi^-$ decays [1]), so these decays could appear in the $B^+ \to \pi^+\pi^+\pi^-$ Dalitz plot. Despite being charmonia, the χ_{c0} and χ_{c2} have non-negligible natural widths ($\sim$ MeV) so can interfere strongly with the other resonances

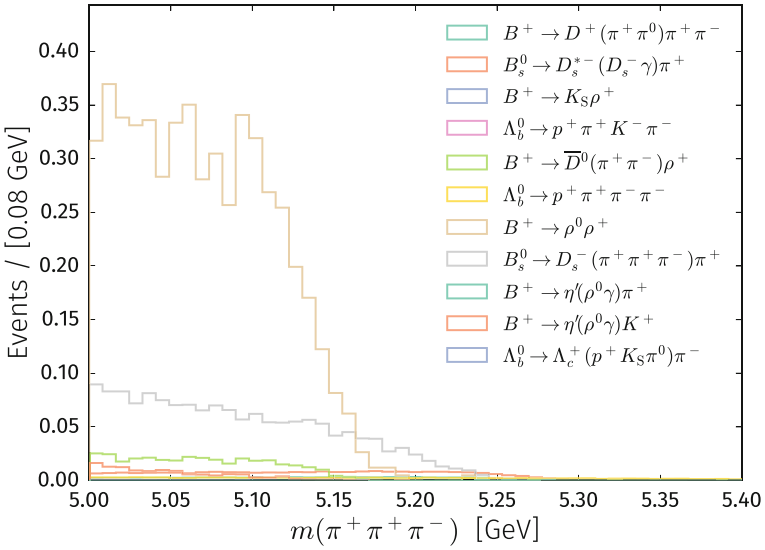

Fig. 7.10 Distributions of the ten largest sources of partially reconstructed background in the range [5.0, 5.4] GeV, as calculated with RapidSim, with relative weights as described in the text

Table 7.6 Partially reconstructed background modes present in the three-body invariant mass fit, using mass distributions from fully simulated data, and their corresponding fraction of the total partially reconstructed background component in the fit model

Decay	Fraction (%)
$B^0 \to \rho^0(\pi^+\pi^-)\rho^+(\pi^+\pi^0)$	38
$B_s^0 \to D_s^-(\pi^+\pi^-\pi^-)\pi^+$	20
$B^+ \to \eta'(\rho^0(\pi\pi)\gamma)K^+$	14
$B^+ \to \overline{D}^0(\pi^+\pi^-\pi^0)\pi^+$	12
$B^+ \to \eta'\pi^+$	6
$B^+ \to \eta\pi^+$	5
$\Lambda_b^0 \to p\pi^-\pi^+\pi^-$	2

present (this was observed with $B^+ \to \chi_{c0}K^+$ in the BaBar analysis of $B^+ \to K^+\pi^+\pi^-$ [23]), and such interference is one of the proposed avenues for a measurement of the CKM angle γ using this mode. As such, these resonances are considered as potential contributions in the Dalitz-plot analysis.

7.3.4 *Construction of the Dalitz-Plot Background Distributions*

The $B^+ \to \pi^+\pi^+\pi^-$ Dalitz-plot fit requires a model for the background in the fit region. For combinatorial background, this is informed by the upper sideband after

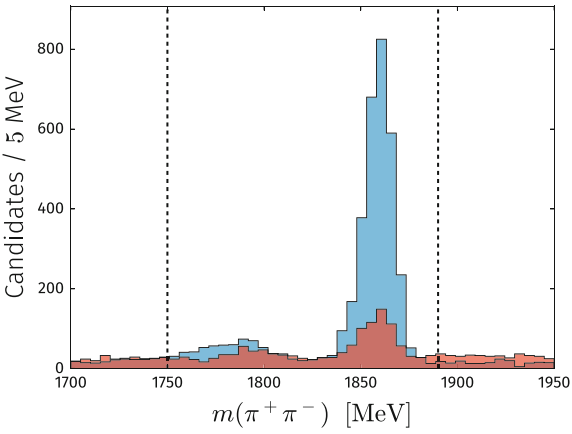

Fig. 7.11 Distribution in $m(\pi^+\pi^-)_{\text{low}}$ (blue) and $m(\pi^+\pi^-)_{\text{high}}$ (red) of the region around the $\overline{D}^0$ mass in the $B^+ \to \pi^+\pi^+\pi^-$ Dalitz-plot. The $\overline{D}^0$ veto window is indicated by the dashed black lines

the full selection is applied. The $B^+ \to K^+\pi^+\pi^-$ MC is used as a proxy for the small amount of $B^+ \to K^+\pi^+\pi^-$ cross-feed in the signal region, where the Dalitz-plot distribution is reweighted according to the distribution observed in the BaBar analysis.

Combinatorial Background

The sample of combinatorial background used in the Dalitz-plot fit is taken from the $5350 < m(\pi^+\pi^+\pi^-) < 6000\,\text{MeV}$ region, which is sufficiently far from the B^+ signal to avoid contamination from true signal decays, and avoids the presence of partially reconstructed backgrounds below the B^+ mass.

However, the variables used in the Dalitz-plot fit are obtained from a fit with a B^+ mass constraint, to ensure that the kinematic requirements are exactly satisfied. Far from the B^+ mass, in the region where the combinatorial background sample is taken, this B^+ mass constraint results in a distortion of the background Dalitz-plot distribution, as combinations that have a true invariant mass greater than the B^+ mass are compressed into the smaller phase-space. This results in a greater density of events in the higher mass regions of the background Dalitz-plot than is present in the signal region, and therefore is an unreliable model for the background in the signal region. Furthermore, this results in true two-body resonance decays that are combined with random high momentum tracks from the rest of the event populating incorrect regions of the background Dalitz-plot.

Whilst no variation of the kind expected from the B^+ mass constraint is observed in the background above the B^+ mass (see Figs. A.2, A.3 and A.4 in Appendix A), with increasing accumulations near the edges of the conventional Dalitz-plot, there is a variation of structure with increasing B^+ mass bin. To enable the use of the full mass range to inform the background model in the signal region whilst accounting for this variation, a Gaussian process model is fitted to the B^+ mass and square Dalitz-plot distributions in the sideband. A detailed description of this procedure can be found in Appendix A, and the result of which can be seen in Fig. 7.12.

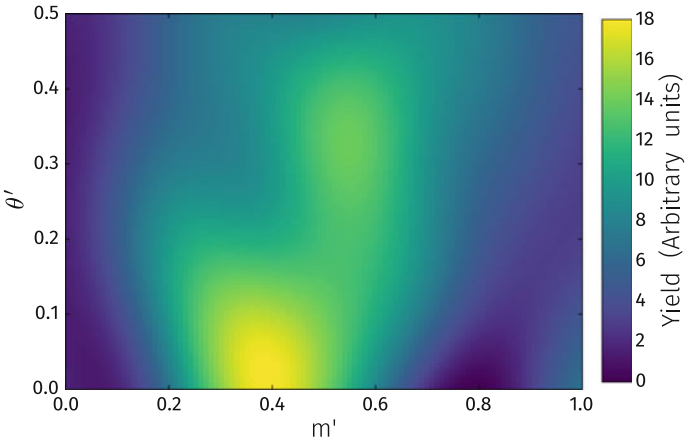

Fig. 7.12 Combinatorial background distribution entering the Dalitz-plot fit, obtained from the Gaussian-process fit procedure described in Appendix A

$B^0 \to \pi^+\pi^-$ Decay Background

One further complication for the combinatorial background sample is the presence of the $B^0 \to \pi^+\pi^-$ decay present in the $m(\pi^+\pi^+\pi^-) > 5450\,\text{MeV}$ sideband region, where a clear $B^0 \to \pi^+\pi^-$ peak is observed at high $m(\pi^+\pi^-)$ invariant mass from the combination of true $B^0 \to \pi^+\pi^-$ decay events with a random low-momentum π track from the rest of the event. As these events occur exclusively above the B^+ mass, they are not present in the Dalitz-plot fit signal region, and therefore must be removed for the combinatorial background sample to be a good representation of the background in the Dalitz-plot fit.

These events are removed from the background histogram by using the distribution of simulated $B^0 \to \pi^+\pi^-$ decays reconstructed as $B^+ \to \pi^+\pi^+\pi^-$, by combining the true $B^0 \to \pi^+\pi^-$ decay with a random track from the rest of the event. The distribution of these events in the square Dalitz-plot is subtracted from the combinatorial background histogram, with weights corresponding to the yield of $B^0 \to \pi^+\pi^-$ decays in the combinatorial background region, as obtained by an invariant mass fit to $m(\pi^+\pi^-)$ (as seen in Fig. 7.15). A similar procedure is performed for the small amount of $B^0 \to K^+\pi^-$ background also present.

The distribution in the square Dalitz-plot of the background subtracted $B^0 \to \pi^+\pi^-$ decay distribution, present in the sideband region, can be seen in Fig. 7.13, along with the corresponding distribution from MC. This indicates that the random π tracks from the simulated data are a reasonable match to those in collision data.

$B^+ \to K^+\pi^+\pi^-$ Decay Background

Despite the effectiveness of the particle ID requirements in removing the $B^+ \to K^+\pi^+\pi^-$ decay background, there is still a small amount of these events in the $B^+ \to \pi^+\pi^+\pi^-$ signal region, which may bias the Dalitz-plot fit. To mitigate this, $B^+ \to K^+\pi^+\pi^-$ MC events are weighted according to the Dalitz-plot model obtained

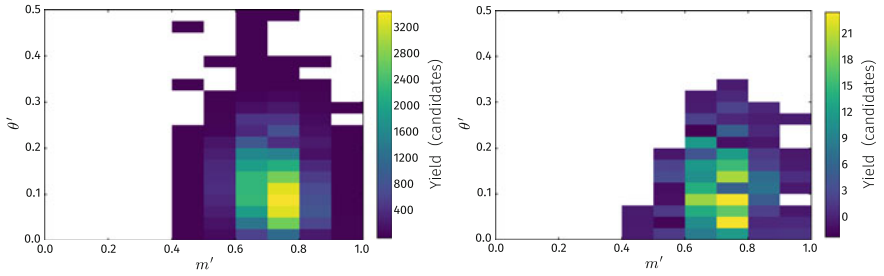

Fig. 7.13 Decays of $B^0 \to \pi^+\pi^-$ in the square Dalitz-plot for MC (left) and sWeighted data (right)

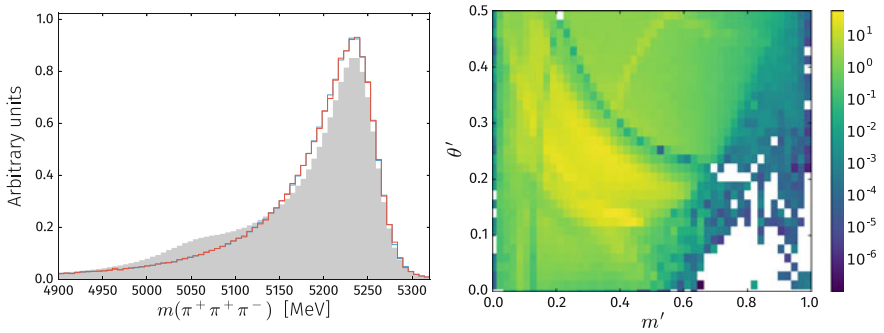

Fig. 7.14 Left: $B^+ \to K^+\pi^+\pi^-$ cross-feed background shapes in $\pi^+\pi^+\pi^-$ invariant mass from MC with no weights (grey filled histogram), with weights corresponding to PID efficiency (red histogram), and with weights corresponding to the BaBar Dalitz-plot model (blue histogram). Right: Folded square $B^+ \to \pi^+\pi^+\pi^-$ Dalitz plot with events corresponding to the $B^+ \to K^+\pi^+\pi^-$ background entering the Dalitz-plot fit, where the PID and Dalitz-plot weights are applied (the z-axis corresponds to the logarithm of bin content)

in the BaBar analysis [23]. This weighting is performed using Laura++, where the weights are produced given the probability from the decay amplitude model multiplied by the square Dalitz-plot Jacobian (as the $B^+ \to K^+\pi^+\pi^-$ MC events were generated flat in the square Dalitz-plot). These weights are then applied to the $B^+ \to K^+\pi^+\pi^-$ MC events reconstructed as $B^+ \to \pi^+\pi^+\pi^-$, and added to the total background histogram with weights corresponding to the number of $B^+ \to K^+\pi^+\pi^-$ events observed in the signal region from the B^+ invariant-mass fit (described in Sect. 7.4).

This model was obtained separately for B^+ and B^- candidates, and therefore the weights contain both the overall CP-asymmetry and the phase-space dependent CP-violating effects. The model obtained in Ref. [23] consists of the $K^*(892)^0$, $\rho(770)^0$, $\omega(782)$, χ_{c0}, $f_2(1270)$, $K_2^*(1430)^0$, and $f_0(1300)$ resonances modelled with relativistic Breit–Wigner lineshapes, the $K_0^*(1430)^0$ with the LASS model, the $f_0(980)$ with the Flatté model, and a flat scalar non-resonant component. The B^+-mass and Dalitz-plot distributions for the reweighted $B^+ \to K^+\pi^+\pi^-$ MC can be seen in Fig. 7.14.

$B^+ \to \eta'(\rho^0(\pi^+\pi^-)\gamma)K^+$ Decay Background

Due to the low energy of the photon produced in the $B^+ \to \eta'(\rho^0(\pi^+\pi^-)\gamma)K^+$ decay, this partially-reconstructed decay peaks close to the B^+ mass when reconstructed as $B^+ \to \pi^+\pi^+\pi^-$, and furthermore has a large branching fraction compared to the signal mode. As a result, a non-negligible number of events are present within the Dalitz-plot fit mass region. As such, this is also included as an explicit background in the Dalitz-plot fit, using the expected square Dalitz-plot distribution of the $B^+ \to \eta'(\rho^0(\pi^+\pi^-)\gamma)K^+$ decay, similar to the case of the $B^+ \to K^+\pi^+\pi^-$ decay background. It is assumed that decays of the η and η' other than via an intermediate $\rho^0 \to \pi^+\pi^-$ decay contribute negligibly.

The $\eta' \to \rho^0\gamma$ decay is assumed to proceed via positive and negative helicity amplitudes equally, and where relative phase between these amplitudes is zero. The resulting di-pion distribution compares well with previous measurements of this decay [62]. As such, the square Dalitz-plot distribution of these decays is used directly in the background model of the subsequent the Dalitz-plot fit.

7.4 Mass Fit

The B^+ invariant-mass fit is used to obtain the signal, combinatorial, and cross-feed background yields, which are inputs to the Dalitz-plot fit. Fits are also performed in the different running periods and trigger categories separately, as these are expected to have different signal to background ratios. The yields obtained are used to weight the contribution of each sample to the combined $B^+ \to \pi^+\pi^+\pi^-$ efficiency map. This fit is performed in the range 5120–5600 MeV to allow precise determination of the combinatorial background shape (the dominant source of background in the signal region). The yields of each contribution are subsequently scaled to the Dalitz-plot fit range of 5234–5324 MeV, around the world-average B^+ mass of $m(B^+) = 5279.32 \pm 0.14$ MeV.

In addition to the fit being performed separately for data collected in 2011 and 2012, the fit is also performed separately for those events where the signal B^+ decay fired the level-0 hadron trigger, 'TOS', and where the signal B^+ decay did not fire the level-0 hadron trigger (and subsequently was triggered by the rest of the event, either by the level-0 hadron trigger or another level-0 trigger), '!TOS'. These two trigger categories have different efficiency distributions in the $B^+ \to \pi^+\pi^+\pi^-$ phase-space, and therefore it is necessarily to determine the proportion of events that are obtained via each criterion. It is also expected that, due to the subsequent correlation of each trigger category with the B^+ momentum distribution, that the invariant-mass resolution of each is different.

Shape parameters, that describe the tails of the partially reconstructed background, $B^+ \to K^+\pi^+\pi^-$ cross-feed decay, and $B^+ \to \pi^+\pi^+\pi^-$ signal decay distributions, are fixed to the values obtained from a simultaneous fit to the simulated data sample for each distribution. The width parameters in the functions for the signal distributions

are free in the fit to data, and for and cross-feed are fixed to the values obtained in the simulated data. The mass parameters are permitted to vary, compared to the values obtained in simulation, by an additive value common to all distributions.

7.4.1 Signal and Cross-Feed-Background Models

The $B^+ \to \pi^+\pi^+\pi^-$ signal model is the sum of a Gaussian distribution,

$$G(m;\mu,\sigma) = \frac{1}{\sqrt{2\pi\sigma^2}} \exp\left[-\frac{(m-\mu)^2}{2\sigma^2}\right], \tag{7.5}$$

which parameterises the mass, m, in terms of a central value, μ, and a width, σ; and a Crystal Ball function, defined in Sect. 5.4.1. As in Chap. 5, the larger tails of the Crystal Ball distribution account for the radiation of one or more photons from the final state. An additional parameter, $f_{\rm G}$, determines the relative normalisations of the Crystal Ball and Gaussian functions in the total PDF. In the fit to collision data, all parameters except for the Gaussian mean and width are set to be equal to those in the fit to simulated data. This simulated data consists of a large number of $B^+ \to \pi^+\pi^+\pi^-$ decay candidates, generated flat in the square Dalitz-plot, and with the same running period and trigger categories as the fit to collision data.

The $B^+ \to K^+\pi^+\pi^-$ cross-feed decay is also modelled by the sum of a Gaussian and a Crystal Ball distribution, where in this case the Crystal Ball tail incorporates the broad spread in invariant-mass arising from the misassociation of the pion mass to a true kaon. Similarly, only the mean and width of the Gaussian distribution are permitted to float freely in the collision data fit.

Event Weights

In addition to the Dalitz-plot weights described in Sect. 7.3.4, instead of applying the particle ID requirements on the $B^+ \to K^+\pi^+\pi^-$ simulated data, the distributions are also weighted according to the efficiency of the particle ID requirements as obtained from PIDCalib package, which results in a similar shape modulation as imposing these requirements directly without the associated loss of data, and the use of the data-driven correction results in a more accurate distribution.

7.4.2 Partially-Reconstructed Background Model

The partially-reconstructed background components included in the B^+ mass fit are those listed in Table 7.6. Each is modelled by an ARGUS function numerically convolved with a Gaussian resolution function, as in Sect. 5.4.4. In the fit to collision data, all of the parameters of these models are fixed to the values obtained in the

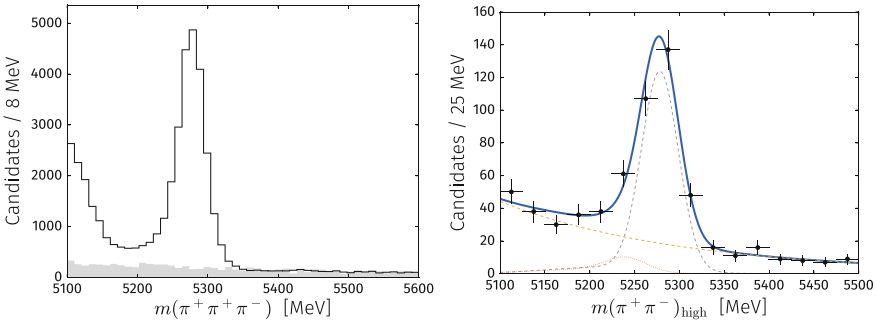

Fig. 7.15 Left: Selected right-sign (black histogram) and same-sign (shaded grey histogram) data, where the same-sign distribution is scaled according to the total combinatorial background yield in the invariant-mass fit. Right: Selected $B^0 \to \pi^+\pi^-$ events in $m(\pi^+\pi^-)_{\text{high}}$, and the projection of the auxiliary mass fit. The dashed grey curve is the $B^0 \to \pi^+\pi^-$ component, the dotted red curve is the $B^0 \to K^+\pi^-$ fit component, the dashed yellow curve is the combinatorial background component, and the blue curve is the total fit model

fit to simulated data, and the relative contributions fixed to their relative branching fractions multiplied by the corresponding efficiency.

7.4.3 Combinatorial Background

The combinatorial background component is modelled with an exponential function, with the parameter left floating. As a cross-check, to ensure that the shape of this component is physical and the partially reconstructed background model does not bias the shape, a sample of data corresponding to same-sign tracks is used. These are events with three like-sign pions with the same selection applied as the rest of the analysis. As no resonances decay to $\pi^+\pi^+$, this sample corresponds to random tracks from the rest of the event, however, as in the case of $B^0 \to \pi^+\pi^-$, backgrounds appearing in the $\pi^+\pi^+\pi^-$ invariant-mass spectrum may only be 'partially' combinatorial (with a true decay plus a random track), and therefore this sample is used only as a rough guide. The distributions of the right-sign and same-sign data can be seen in Fig. 7.15, where the distribution of the same-sign data is approximately linear in $m(\pi^+\pi^+\pi^+)$.

7.4.4 Background from $B^0 \to \pi^+\pi^-$

Above 5420 MeV, background from $B^0 \to \pi^+\pi^-$ decays appear (as noted in Sect. 7.3.4), where opposite-sign pions from a true $B^0 \to \pi^+\pi^-$ decay are combined with a random pion from the rest of the event. This manifests in $m(\pi^+\pi^+\pi^-)$ as a

Table 7.7 Yield of each component in the full invariant-mass fit range, split by running period and L0 trigger category. Uncertainties are statistical only

Category	2011		2012		Total
	TOS	!TOS	TOS	!TOS	
$B^+ \to \pi^+\pi^+\pi^-$	5002 ± 85	2636 ± 46	10214 ± 119	6310 ± 94	24163 ± 180
$B^+ \to K^+\pi^+\pi^-$	166 ± 18	97 ± 11	284 ± 31	197 ± 21	743 ± 81
Part. reco.	1195 ± 52	793 ± 49	2457 ± 75	1757 ± 72	6202 ± 126
Combinatorial	1189 ± 66	878 ± 36	2959 ± 99	2290 ± 94	7315 ± 155

shape that rises rapidly at around 5420 MeV, with a long tail extending to higher mass, and is included in the fit to data as a Crystal Ball function with parameters obtained from a fit to simulated $B^0 \to \pi^+\pi^-$ data. As this shape may bias the determination of the combinatorial background component, the yield is fixed in the $m(\pi^+\pi^+\pi^-)$ collision data fit by performing an auxiliary fit to the B^0 region in the unconstrained $m(\pi^+\pi^-)$ spectrum, the result of which can be seen in Fig. 7.15. This fit also includes a component for $B^0 \to K^+\pi^-$, the yield of which is fixed to the ratio of efficiencies multiplied by the ratio of branching fractions. The yield of these components can be found in Table 7.9.

7.4.5 Results

The invariant-mass fits to $m(\pi^+\pi^+\pi^-)$ data, for the two running periods and two trigger categories can be seen in Fig. 7.16, where the projections of the total fit model and individual components are indicated. The fitted yields of the signal and background components can be found in Table 7.7 for the full fit range, and Table 7.8 for the mass range corresponding to the Dalitz-plot fit. The value of the mass shift between collision data and MC is on average approximately $m_{\text{Data}} - m_{\text{MC}} = 4\,\text{MeV}$, and consistent between each category. When B^+ and B^- data are fitted separately, the asymmetry in the combinatorial background yield is consistent with zero.

7.5 Efficiency Map

The overall selection efficiency is computed as a function of the square Dalitz-plot, defined in Sect. 6.6.2, which is used to correct the signal data in the Dalitz-plot fit to its true physical distribution. The efficiency map is comprised of several contributions, the largest of which is calculated as a ratio of the distribution of selected MC events and the initial MC generated flat in the same square Dalitz-plot. This distribution

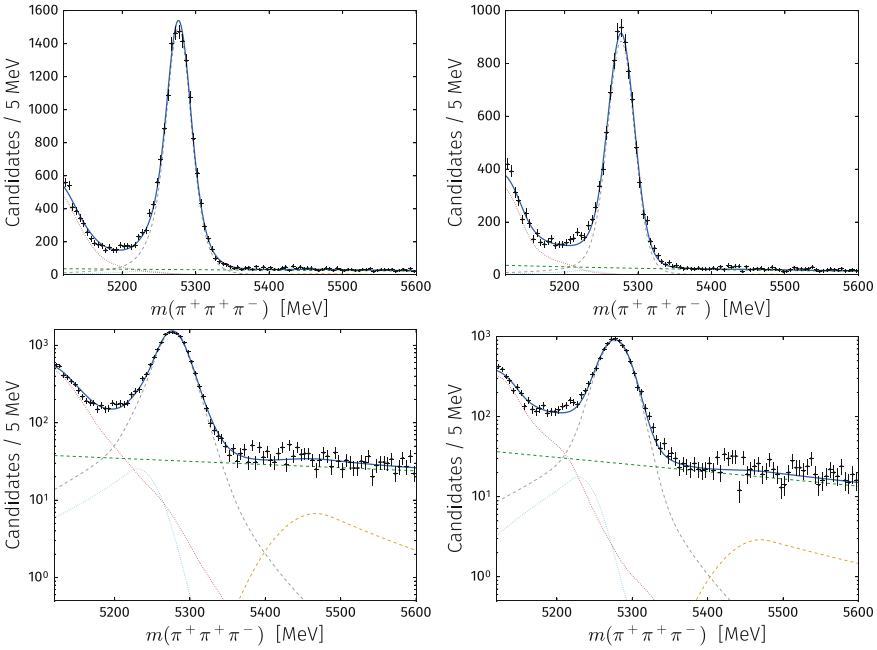

Fig. 7.16 Data and fit model projections for TOS (left) and !TOS (right) categories, and the same categories with logarithmic y-axes (bottom). In each case the solid blue curve is the total fit model, the dashed grey curve the $B^+ \to \pi^+\pi^+\pi^-$ signal model, the light-blue dotted curve is the $B^+ \to K^+\pi^+\pi^-$ cross-feed background model, the dashed green curve is the combinatorial background model, the red dotted curve is the partially reconstructed background component, and the dashed yellow curve is the $B^0 \to \pi^+\pi^-$ component

Table 7.8 Yield of each component in the amplitude analysis signal region of 5234 to 5324 MeV, split by running period and L0 trigger category. Uncertainties are statistical only

Category	2011		2012		Total
	TOS	!TOS	TOS	!TOS	
$B^+ \to \pi^+\pi^+\pi^-$	4391 ± 75	2334 ± 41	9071 ± 106	5585 ± 83	21382 ± 159
$B^+ \to K^+\pi^+\pi^-$	50 ± 5	25 ± 3	88 ± 10	53 ± 6	216 ± 23
Part. reco.	22 ± 1	20 ± 1	51 ± 2	44 ± 2	137 ± 3
Combinatorial	170 ± 9	149 ± 6	470 ± 16	413 ± 17	1203 ± 26

is subsequently corrected to account for known disagreements between the MC and the signal data in the kinematical and event-based variables. First, a correction to level-0 hadron TOS efficiency is applied, and lastly the efficiency is multiplied by the particle identification efficiency.

Table 7.9 Yield of each component in the fit to the unconstrained $m(\pi^+\pi^-)_{\text{high}}$ distribution around the B^0 mass

Category	2011		2012		Total
	TOS	!TOS	TOS	!TOS	
$B^0 \to \pi^+\pi^-$	65 ± 10	19 ± 6	123 ± 14	70 ± 11	277 ± 21
$B^0 \to K^+\pi^-$	5 ± 10	4 ± 6	18 ± 14	6 ± 10	33 ± 21

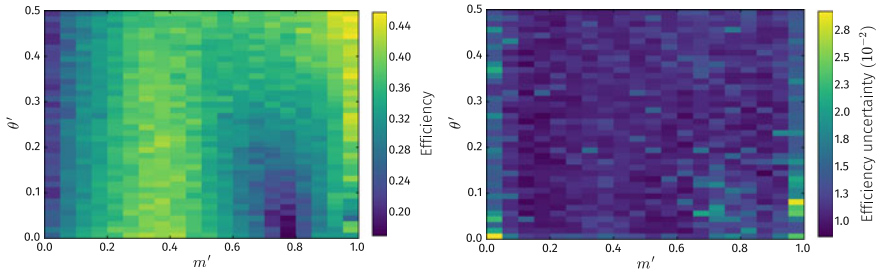

Fig. 7.17 Particle ID efficiency (left) and absolute uncertainty on the particle ID efficiency (right) for B^+ decays, in the square Dalitz-plot

Uncertainties on this efficiency map are calculated via statistical bootstrap using the overall corrected event-by-event efficiencies, and thereby correlations between the various sources of uncertainty on the methods described in this section, and correlations between bins in the efficiency map, are accounted for. As such, figures in this section that contain uncertainties on the individual components in the efficiency description are only an indication of the uncertainty on the corresponding contribution, and do not enter the final measurement.

7.5.1 Particle Identification

As noted in Chap. 5, particle identification efficiency is not well reproduced in the simulated data, and therefore this efficiency as a function of the square Dalitz-plot is determined using a data-driven technique implemented in the `PIDCalib` package, described in Chap. 4. This efficiency is obtained as a function of track p, p_{T}, and the number of tracks in the event, and combined to form the overall PID efficiency for an MC decay, separately for B^+ and B^- decays. An example of this PID efficiency is shown in Fig. 7.17.

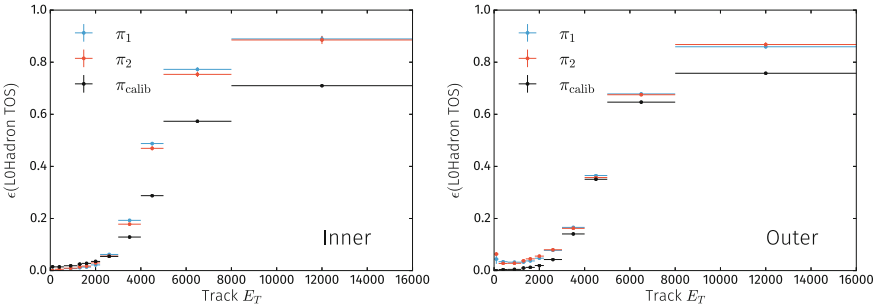

Fig. 7.18 Per track efficiency of the L0Hadron TOS trigger decision for $B^+ \to \pi^+\pi^+\pi^-$, as a function of track transverse energy, E_T, for 2012 MC (coloured points) and 2012 calibration data (black points), for inner (left) and outer (right) HCAL regions. The shape of this distribution is driven primarily by the energy resolution of the HCAL, but also due to the association of an HCAL deposit defined online with the transverse energy of a particle track defined offline. The curve does not saturate at 1 due to the different requirements on the number of SPD hits for the TOS and TIS trigger lines

7.5.2 *Level-0 Trigger Correction*

The efficiency of the level-0 hadron trigger used in this analysis is not well reproduced by the simulated data, and therefore a correction is calculated using pions from a $D^{*+} \to D^0(K^-\pi^+)\pi^+$ control mode. The TOS efficiencies of the pion tracks in the control mode collision data are calculated using the TISTOS method (see Sect. 4.8.4), using events that are both TOS and TIS triggered, in bins of track transverse momentum at the HCAL $z-$position. A comparison between the calibration data efficiency and efficiency from $B^+ \to \pi^+\pi^+\pi^-$ MC (also calculated using the TISTOS method, to account for biases in the efficiency due to the selection requirements) can be seen in Fig. 7.18. The MC is reweighted according to the previously described weights, to account for the mismatch between data and MC in the overall event multiplicity. The cause of the residual discrepancy is likely to be due to calorimeter ageing, where radiation damage results in an efficiency decrease in the calorimeter cells as a function of time and the total particle flux, which is constant across a running period in the simulated data, and more generally a difference between the simulated and real energy deposits in the HCAL.

The efficiencies of the MC decays are calculated such that at least one of the signal decay tracks fires the level-0 hadron trigger, and this efficiency is used to correct the square Dalitz-plot efficiency of the signal mode. A correction is also applied to correct for nearby signal particles contributing to the same hadron-calorimeter cluster. In addition, a complementary correction is applied to the MC that does not fire the level-0 hadron trigger, but where any trigger is fired by objects from the rest of the event. An example of this correction can be seen in Fig. 7.19, where the correction particularly impacts the upper edge of the conventional Dalitz-plot.

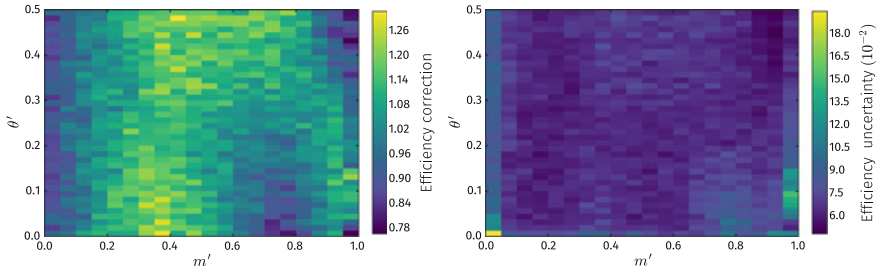

Fig. 7.19 Correction to the MC L0Hadron TOS efficiency for B^+ decays in the square Dalitz-plot

7.5.3 *Disagreement Between MC and Collision Data*

As noted in Sect. 7.2.5, there is some disagreement between other variables used (either directly or indirectly) in this analysis between the MC and collision data. These effects must be corrected to determine accurately the total selection efficiency of the signal data. These variables include inputs to the BDT classifier, but also the distribution of the number of hits in the silicon pre-shower detector, which is indicative of the event multiplicity. In addition to variables directly used in the BDT, the particle-ID efficiency in particular depends on the event multiplicity, and therefore correcting for this difference results in increased accuracy of the data-driven correction described above. An efficiency correction to the MC is computed using the weights from the gradient-boosted reweighting algorithm, and this correction particularly impacts the high $m(\pi^+\pi^-)_{\text{high}}$ corner of the conventional Dalitz-plot, where the total efficiency is low.

7.5.4 *Combined Efficiency Maps*

The overall efficiency for each data taking period and trigger category, is computed as a function of the square Dalitz-plot, taking into account the geometrical efficiency, the stripping and selection efficiency, and the PID and L0 corrections. The binning scheme of the efficiency maps is required to be fine compared to the scale of the resonant structure, but coarse enough such that the statistical uncertainty is small compared to the central value. In this analysis, a binning scheme corresponding to 20 bins in m', uniformly in the range [0, 1], and 40 bins in θ', uniformly in the range [0, 0.5]. The combined efficiency can be seen in Fig. 7.20 for B^+ and B^- decays.

A significant accumulation of reconstructed candidates arises at the corner of the square Dalitz-plot, corresponding to events with high-momentum decay products with a large amount of final-state radiation, which is an effect compounded by the Decay-Tree Fitter mass constraint. This is a real physical effect, however this region is removed from the data and efficiency distributions (with a negligible loss of signal

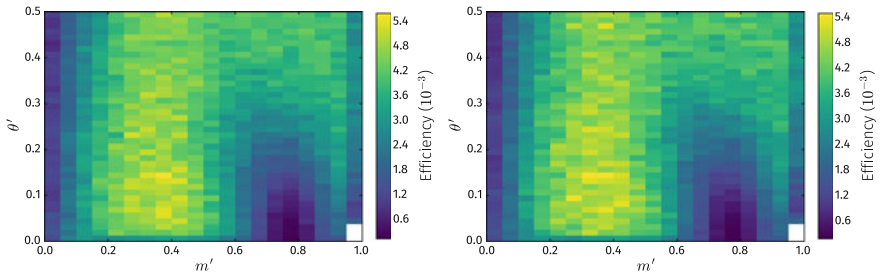

Fig. 7.20 Combined square Dalitz-plot efficiency distributions for B^+ (left) and B^- (right) decays

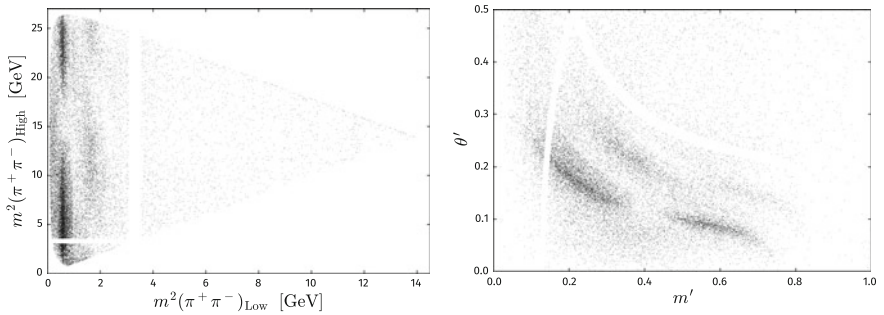

Fig. 7.21 Distributions of selected events in the conventional (left) and square (right) $B^+ \to \pi^+\pi^+\pi^-$ Dalitz plot, for both trigger categories combined. Each are folded to represent the symmetrised amplitude, and in each case the depleted bands are due to the $\overline{D}^0$ veto

candidates) to avoid biasing the cubic spline interpolation of the overall efficiency description.

7.6 Amplitude Fit

The amplitude fit is performed using the Laura++ package [63], and takes as input from the previous sections the number of signal candidates, the number of background candidates and their distribution(s), the efficiency of the signal in the square Dalitz-plot, and the mass-constrained conventional Dalitz-plot variables of selected collision data in the signal region (corresponding to [5234, 5324] MeV). The distributions of these selected events in the conventional and square Dalitz-plots can be seen in Fig. 7.21. From these, clear contributions can be seen due to the $\rho(770)^0$ and $f_2(1270)$ resonances, observed in the previous BaBar analysis of this mode [1].

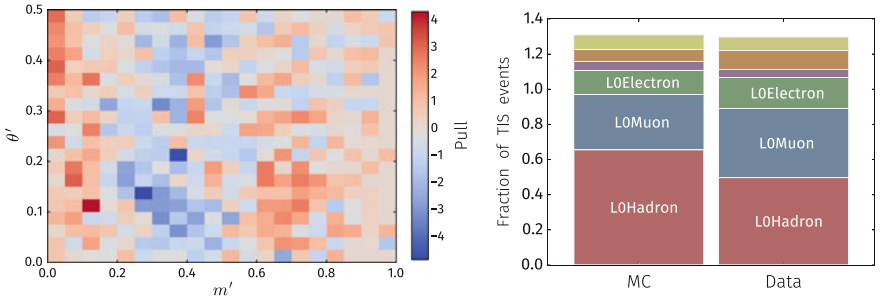

Fig. 7.22 Left: Difference between the efficiency corrected and background subtracted yields in the square Dalitz-plot, for the TOS and !TOS data categories, divided by their uncertainty. Right: Fraction of candidates via each trigger line, where any L0 trigger fired independently of a decision resulting from the signal candidate (TIS), for data and MC. Here the unlabelled categories are L0Photon (yellow), L0DiMuon (purple), and L0ElectronHi (orange). These fractions do not sum to unity, as it is possible for an event to satisfy the requirements of more than one trigger line simultaneously

7.6.1 Comparison Between TOS and !TOS Data

The $B^+ \to \pi^+\pi^+\pi^-$ data is acquired via two trigger pathways: trigger-on-signal (TOS), where the $B^+ \to \pi^+\pi^+\pi^-$ signal decay results in a positive L0Hadron trigger decision; and independently-of-signal (TIS), where the signal decay does not result in a positive L0Hadron trigger decision, but is present in an event where a physics trigger is fired. The efficiency for the TOS data can be calculated directly from simulated signal decays, with a data-driven efficiency correction. The efficiency of data collected via TIS and not TOS (!TOS) can also be calculated using simulated signal decays, and the effect of the signal decay not resulting in a positive L0Hadron decision corrected using a similar data-driven correction. However in this case the decay which resulted in a positive trigger decision is not known, and such a correction cannot be applied. It is assumed that such a decision is uncorrelated with respect to the signal decay, which is likely to be true for level-0 triggers that do not involve the HCAL (L0Muon, L0DiMuon, L0Electron, and L0Photon). However, the majority of TIS trigger decisions in $B^+ \to \pi^+\pi^+\pi^-$ data are via the L0Hadron trigger (Fig. 7.22 (right)).

As such, the TOS efficiency is assumed to be more robust than that of the !TOS sample. The pull (the difference in central value divide by the overall uncertainty) between the background subtracted and efficiency corrected data distributions for the TOS and !TOS samples can be seen in Fig. 7.22. Broad regions where there is substantial disagreement between the two datasets are observed in low θ' at around $m' = 0.4$ and 0.7, and furthermore, a χ^2 test between the two samples results in a p-value of approximately 4 Gaussian standard-deviations, implying a statistically significant difference.

As a result of this comparison, the nominal fit results (and all further investigations in this chapter, unless otherwise specified) will be computed using the TOS sample only, and the !TOS sample results investigated as a cross-check in Sect. 7.8.

7.6.2 Model Selection

The importance of including the correct resonant components in an amplitude model is exemplified in Sect. 6.4.3, where it can be seen that interference between the resonant components can significantly affect the parameters extracted from the fit to data. It is therefore important to have a robust procedure to select these model components, to ensure that the resulting parameters of interest are unbiased.

Contributions from the $\rho(770)^0$, $\omega(782)$, and S-wave are included in the model by default, where the $\rho(770)^0$ and $\omega(782)$ are modelled with the combined ρ–ω mixing model as described in Sect. 6.5.2 (and unless otherwise specified, '$\rho(770)^0$' as a model component will refer to this combined model). The S-wave is modelled with the K-matrix model, as described in Sect. 6.5.4. Additional resonances that are considered in the model are listed in Table 7.10, which are those that are established by more than one experiment, and have observed decays to the $\pi^+\pi^-$ final state.

Fit Quality Metric

An overall measure of the fit quality of one model with respect to another is the change in likelihood, $\Delta \log \hat{\mathcal{L}}$, between the two models (and $\sqrt{-2\Delta \log \hat{\mathcal{L}}}$ is the approximate Gaussian significance between them). This does not take into account the number of degrees-of-freedom that can be different between each potential model, however, at this stage all additional model components contribute at most four degrees-of-freedom (six when masses and widths are floated), and therefore the likelihoods are compared directly.[2]

A method of regularising the negative log-likelihood minimisation directly, such as that proposed in Ref. [65], using the least-absolute-shrinkage and selection operator (LASSO) technique for L_1 regularisation, was investigated. This technique penalises model component magnitudes, according to a tunable regularisation parameter, via the sum of the absolute differences between the data and model values, and as such those components that do not sufficiently improve the fit quality asymptotically tend to zero. In this case, the magnitudes obtained using a LASSO modification to the likelihood did not differ substantially to those obtained with unpenalised minimisation, however these techniques appear better suited to analyses with a greater number of decay products and therefore a much larger configuration space [66].

[2]The Akaike information criterion [64], which in the limit of infinite data is $2k - 2\log\hat{\mathcal{L}}$, where k is the number of model parameters and $\hat{\mathcal{L}}$ the maximised likelihood value, does allow the number of parameters to be taken into account, but here only represents a scaling of $\log\hat{\mathcal{L}}$.

Table 7.10 Resonances included in the model selection procedure, and their mass and width parameters as used in this analysis. These are resonances which are established by more than one experiment, and have observed decays to the $\pi^+\pi^-$ final state

Resonance	Spin	Mass (MeV)	Width (MeV)
$f_2(1270)$	2	1275.5 ± 0.8	$186.7^{+2.2}_{-2.5}$
$f_2(1430)$	2	1430	100
$\rho^0(1450)$	1	1465 ± 25	400 ± 60
$f_2'(1525)$	2	1525 ± 5	73^{+6}_{-5}
$f_2(1565)$	2	1562 ± 13	134 ± 8
$\rho_3(1690)^0$	3	1686 ± 4	186 ± 14
$\rho^0(1700)$	1	1720 ± 20	250 ± 100
$\rho_3(1990)$	3	1982 ± 14	188 ± 24
$f_4(2050)$	4	2018 ± 11	237 ± 18
$f_0(2100)$	0	2101 ± 7	224 ± 22
$\rho^0(2150)$	1	2155 ± 21	320 ± 70
χ_{c0}	0	3414.75 ± 0.31	10.5 ± 0.6
χ_{c2}	2	3556.20 ± 0.09	1.93 ± 0.11

Strategy

In this analysis, a fit is first performed where all potential components are included, such that any interferences that favourably impact fit quality occur, and the negative log-likelihoods from this procedure are used to estimate the importance of each component in the model. This provides a baseline which is then further investigated in an ad-hoc way, incorporating higher-order modifications to the fit model, such as free masses and widths. Potential components are those which have been observed to decay to $\pi^+\pi^-$ (and where the branching fraction, if known, is $\gtrsim 10^{-4}$), and have been established by two or more experiments. In practice this comprises various light unflavoured resonances, and some higher-mass $c\bar{c}$ resonances.

Components that do not have a significant effect on the model parameters are removed, to reduce spurious correlations and mitigate an artificial reduction in precision on the parameters of interest. These removed components are then considered as a contribution to the overall systematic uncertainty in Sect. 7.7. The fits presented here are performed $\mathcal{O}(100)$ times with randomised initial parameters, generated uniformly in the range $[-10, 10]$, to ensure that a global minimum is reached.

The model selection strategy used in this analysis is therefore as follows:

- An approximate reference $\Delta \log \mathcal{L}$ value is obtained by performing a fit with all plausible components. All resonance parameters are fixed to their world-average values at this stage.
- Contributions with a $\Delta \log \mathcal{L}$ with respect to the baseline model of less than 5 are removed.
- Resonance parameters, such as the relative $\rho-\omega$ magnitude and phase, and masses and widths of certain dominant resonances, are floated to investigate any corresponding improvements in fit quality.

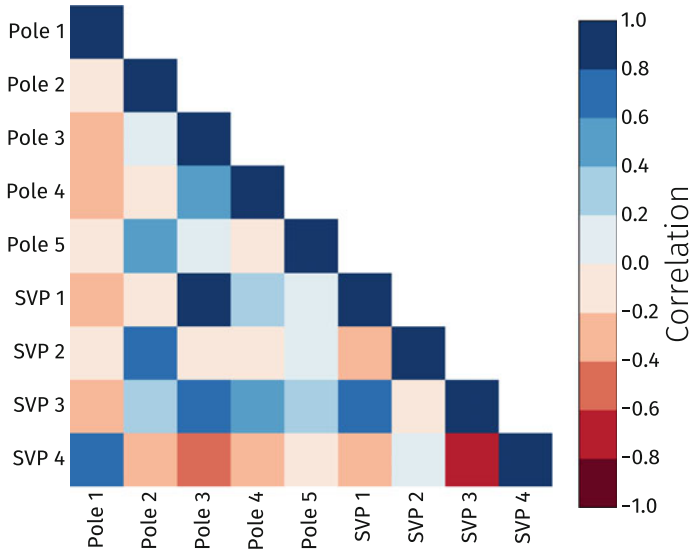

Fig. 7.23 Linear correlation between the magnitude of the isobar coefficients corresponding to potential K-matrix components within the $B^+ \to \pi^+\pi^+\pi^-$ amplitude model, used to guide the model selection procedure

- Improvements to the fit via modifications to the fixed parameters of the K-matrix and variation of the Blatt–Weisskopf radius are then considered, where further variation of these parameters beyond the best-fit value are considered as a systematic effect in Sect. 7.7. Additional contributions to the model are also considered here, such as the inclusion of additional non-resonant components of spin-0 or 1, or virtual contributions.
- The current best fit at this stage will be taken as the nominal model. Contributions removed previously are individually added back in to investigate whether there is a significant difference in their $\Delta \log \mathcal{L}$ with respect to this now optimised model. Any contribution where the greatest of these two $\Delta \log \mathcal{L}$ values is between 10 and 20 units are added or removed, where appropriate, to study systematic effects.
- Finally, as a cross-check, scans in resonance mass and width are performed for potential latent contributions of spin-0, 1, 2, 3, and 4, to ensure that no significant resonant structure is unaccounted for in the final best-fit model. These studies are documented in Sect. 7.8.

K-Matrix Parameters

Due to the significant degree of correlation (see Fig. 7.23) between the K-matrix model parameters, it is not suitable to use this procedure to gain an understanding of the significance of these contributions. As the poles represent couplings to known physical processes, these are kept in their entirety. Furthermore, all but the last (SVP 5) slowly-varying parts are also kept, at the cost of some fit stability and an overall

Table 7.11 The change in log-likelihood, evaluated with respect to the corresponding baseline model in each case, when the indicated component is removed. The model configurations are as indicated in the text. Light to dark green indicates larger to smaller positive differences in log-likelihood with respect to the baseline, and light to dark red indicates smaller to larger negative differences in log-likelihood with respect to the baseline

Component	$\Delta \log \mathcal{L}_1$	$\Delta \log \mathcal{L}_2$	$\Delta \log \mathcal{L}_3$	$\Delta \log \mathcal{L}_4$	$\Delta \log \mathcal{L}_5$
$f_2(1270)$	259.51	–	–	–	
$\rho(1450)^0$	177.50	–	–	–	
$\rho_3(1690)^0$	49.27	–	–	–	
$\rho(1700)^0$	18.42	21.34	21.37	21.60	9.57
$\rho_3(1990)$	12.01	15.03	8.81	12.96	10.04
$f_4(2050)$	8.51	6.07	6.45	5.57	7.17
$f_2(1430)$	8.23	10.73	–	12.33	12.50
$f_2(1565)$	7.53	10.77	7.06	16.01	13.00
$f_0(2100)$	6.77	5.38	2.50	4.21	1.87
$f_2'(1525)$	1.24	–	–	–	
χ_{c2}	3.62	–	–	–	
χ_{c0}	1.16	–	–	–	
Baseline	−48548.32	−48542.50	−48542.82	−48542.90	−48562.83

increase in parameter uncertainty. The fifth slowly-varying parameter is almost entirely correlated with numerous other K-matrix parameters (which additionally results in significant instability in the fit convergence), and therefore can be removed from the model at no detriment to the analysis.

Baseline Results

The change in $\log \mathcal{L}$, when removing a specific component, relative to the baseline fit where all components are included, $\Delta \log \mathcal{L}_1$, can be seen for various potential contributing resonances in Table 7.11.

Pairwise Removal

If two or more resonances are highly correlated (for example when there is strong interference and they are nearby in mass), the maximum-likelihood fit may be able to compensate for the loss of one of these correlated components by modifying the parameters of the other contribution(s). In such a case, the overall change in $\log \mathcal{L}$ may be under-estimated by considering resonance components individually, and as such removing two components which are individually not significant could result in an undesirably significant change in fit quality.

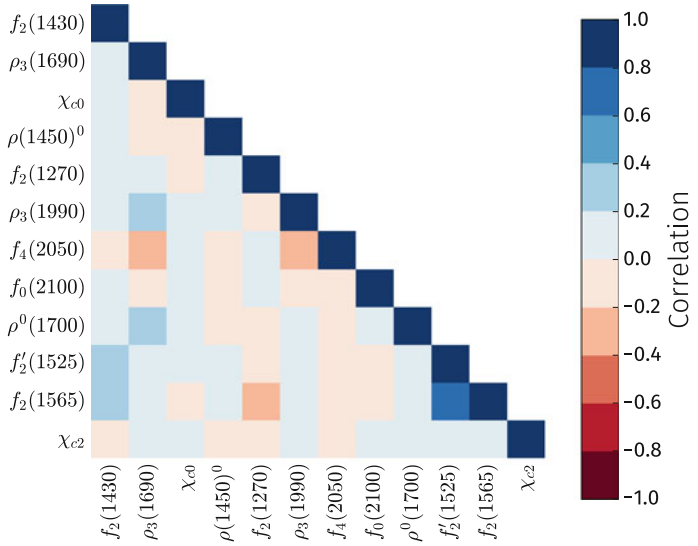

Fig. 7.24 Linear correlation between the magnitude of the isobar coefficients corresponding to additional potential resonances within the $B^+ \to \pi^+\pi^+\pi^-$ amplitude model, used to guide the model selection procedure

In an attempt to mitigate this effect, the correlation matrix for the initial baseline fit, Fig. 7.24, described in the previous section is inspected for components that are significantly ($\gtrsim 20\%$) correlated. These components are removed in a pairwise fashion, and the change in $\log \mathcal{L}$ calculated. This allows identification of those resonances by which, even though individually they do not meet the initial criteria for inclusion into the model, one must be included to avoid the combined deficit in $\log \mathcal{L}$.

These values can be seen in Table 7.12, for the pairs of resonances which are significantly correlated. In principle this procedure could also be performed with combinations of an arbitrary number of resonances, however Fig. 7.24 indicates that this is unnecessary. From this it can be seen that none of changes in $\log \mathcal{L}$ are significantly different from the sum of those presented in Table 7.11, and therefore do not strongly contradict the conclusions obtained using the individual $\Delta \log \mathcal{L}$ values.

Fit Fractions

Inspection of the total fit fraction and fit fractions of each resonance are a useful indicator of model robustness. A model with a small ($\lesssim 50\%$) or large ($\gtrsim 150\%$) total fit fraction implies that large destructive or constructive interference is occurring, indicative of a likely unphysical fine-tuning effect between the resonant contributions to achieve better agreement with the data. As such, any model that satisfies these conditions is rejected. The absolute fit fractions of each component (diagonal elements) and absolute interference fit fractions (off diagonal elements) can be seen in Fig. 7.25 (left) for the overall baseline model. These interference fit fractions are shown as a proportion of the overall fit fractions in Fig. 7.25 (right), of the component

Table 7.12 The change in log-likelihood, with respect to the initial baseline model, when removing the pairs of components listed

Components	$\Delta \log \mathcal{L}$
$f_2(1430)$ and $f_2(1565)$	17.38
$\rho_3(1990)$ and $f_4(2050)$	25.78
$f_2'(1525)$ and $f_2(1565)$	15.39
Baseline	−48548.32

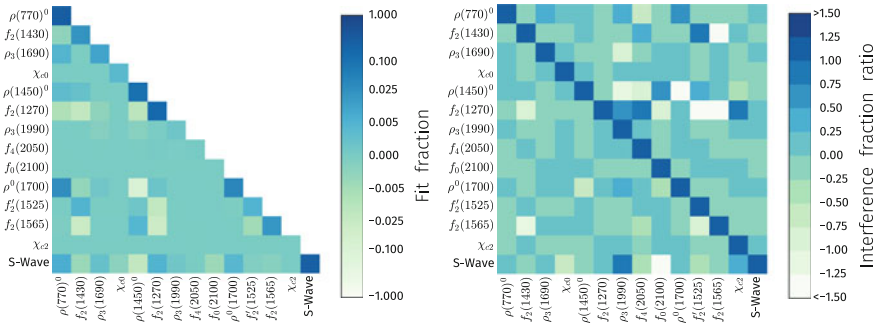

Fig. 7.25 Left: Absolute fit fractions (diagonal) and interference fit fractions (below diagonal). Right: Interference fit fractions as a proportion of the overall fit fraction of the component listed on the x-axis (below diagonal) and as a proportion of the component listed on the y-axis (above diagonal)

listed on the x-axis (below diagonal) and as a proportion of the component listed on the y-axis (above diagonal). From these it can be seen that no large cancellation is mediated by spuriously large interference between the model components.

Additional Investigations

It is often of some use to float the masses and widths of the dominant model components. Whilst the momentum scale calibration mitigates any experimental bias on the resonance mass parameters, the world-average mass values can be inconsistent with the values observed, due to the difference between the true pole mass of the resonance (a model-independent quantity) and the parameter that appears in the relativistic Breit–Wigner (or similar) model. Similarly, different formalisms used for the modification of the line-shape due to (angular) momentum conservation, such as the values of the Blatt–Weisskopf barrier radii, are also correlated with the resonance mass as it appears in the isobar model.

A second set of fits is performed where the components with $\Delta \log \mathcal{L}_1 < 5$ are removed, and the dominant $\rho(770)^0$ mass and width are floated to improve the fit quality. The corresponding changes in $\log \mathcal{L}$ when components are removed in this configuration, relative to the baseline fit with all components where $\Delta \log \mathcal{L}_1 < 5$, are denoted as $\Delta \log \mathcal{L}_2$. In addition to the floating $\rho(770)^0$ mass and width, the $f_2(1270)$

mass was floated at this stage, where removals with respect to this configuration are denoted as $\Delta \log \mathcal{L}_4$.

When certain resonances are removed from the fit where the $f_2(1270)$ mass is floated, the value of the mass parameter converges to a systematically lower value than either the world-average value or the value obtained from the baseline fit. The most significant shift is observed when the $f_2(1430)$ is removed, and furthermore, the $f_2(1270)$ mass in the baseline fit is highly correlated with the $f_2(1430)$ isobar coefficients. Here it is expected that interference effects from resonances other than those with the same spin will cancel out when integrating over the helicity angle, and therefore an unaccounted for $f_2(1430)$ contribution could subsequently bias the parameters of the $f_2(1270)$ model (and thereby bias overall model projections in m_{Low} and m_{High}).

A set of fits are performed where the $\rho(770)^0$ and $f_2(1430)$ mass and width are left free, and the change in log-likelihood when removing individual resonances for this configuration, $\Delta \log \mathcal{L}_3$, are listed in Table 7.11. It can be seen that floating the $f_2(1430)$ mass and width, in addition to those of the $\rho(770)^0$, results in a global increase in the significance of all potential model components, as well as an improvement in the $\Delta \log \mathcal{L}$ of the fit with all components of around 12.5 units (compared to an improvement of only around 3.6 units where the $f_2(1270)$ mass is floated).

Non-resonant and Virtual Contributions

In the previous BaBar analysis of $B^+ \to \pi^+\pi^+\pi^-$ [1], a significant non-resonant S-wave component was observed, with a fit fraction of approximately 35%. It is reasonable that this non-resonant component can be accommodated via the non-resonant terms in the K-matrix model, and therefore an additional component of the form described in Ref. [1] is unnecessary. Nevertheless, a component corresponding to

$$A(m_{\text{low}}, m_{\text{high}}) = c_{\text{nr}} \left(e^{-\alpha_{\text{nr}} m_{\text{high}}} + e^{-\alpha_{\text{nr}} m_{\text{low}}} \right), \tag{7.6}$$

where α_{nr} is a parameter that determines the shape of the non-resonant distribution, and c_{nr} is a normalisation term, is tested in the optimised model. The value $\alpha_{\text{nr}} = 0.28 \pm 0.06\,\text{GeV}^{-2}$ was obtained in Ref. [1], and is fixed here. The difference in the negative log-likelihood between the best fit containing this component and the optimised model is $\Delta \log \mathcal{L} = 32$, however these fits have a fit fraction in excess of 150% for both the B^+ and B^- models, with a non-resonant fit-fraction of around 40% and a K-matrix fit-fraction of around double the value of the optimised model. As such, these are unphysical, and inclusion of an additional non-resonant component is not considered further.

A similar broad contribution can arise from virtual B^{*0} decays, which are modelled using the tail of a relativistic Breit–Wigner function, as per the description in Sect. 6.5.3. Like the above, this is also added to the optimised model, and the difference in fit quality is $\Delta \log \mathcal{L} = 18$. The B^{*0} component comprises 2.1%(1.2%) of the total B^+ (B^-) fit fraction, and results in a slightly reduced S-wave fit fraction, and an increased $\rho(770)^0$ CP-asymmetry. As this improvement in fit quality is not significant, this will not be included in the final model, but will be considered as a source of systematic uncertainty in Sect. 7.7.

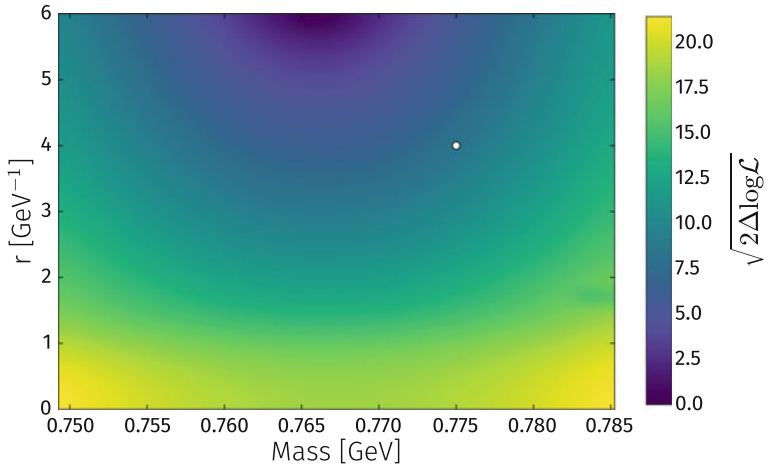

Fig. 7.26 Likelihood scan for the nominal fit, where the resonance Blatt–Weisskopf barrier radius and $\rho(770)^0$ mass is varied. The change in likelihood is evaluated with respect to the minimum (and therefore a smaller z-value is better), and the white point indicates the values in the nominal fit model

Blatt–Weisskopf Barrier Radii

The Blatt–Weisskopf barrier factor is an essential component of the amplitude formalism, however the radius parameter is process dependent and not easily obtained model independently. As such, this parameter is often fixed to a reasonable value (2–5 GeV^{-1}) and varied to investigate the systematic uncertainty introduced. It is also possible to leave the radius parameter floating in the fit, however this is correlated with the mass parameter of each resonance, and as such floating masses and widths in addition to the barrier radius causes complications (both for fit stability and for interpretation of the resulting values).

A scan of radius parameters versus the $\rho(770)^0$ mass can be seen in Fig. 7.26, where it can be observed that the overall minimum is located at large values of the radius parameter, r, but far from the world-average $\rho(770)^0$ mass[3] of $m_{\text{PDG}} = 775.26 \pm 0.25$ MeV. When the $\rho(770)^0$ mass is constrained with a Gaussian function to the world-average value, the values of the parameters obtained in the nominal fit (the white point in Fig. 7.26), are not significantly far from the minimum when the $\rho(770)^0$ mass is held constant. As a measurement of the $\rho(770)^0$ mass is not the primary interest of this analysis, a Gaussian constraint on the mass and width will be applied in the final fit.

[3] In Ref. [5], measurements are separated by the ρ charge and production mechanism, where it is noted that significant a discrepancy arises between the values obtained via each production mechanism, ultimately due to the large width of the ρ. Nevertheless, it is noted in Ref. [5] that, in principle, the cleanest measurements are obtained from e^+e^- scattering.

Production Vector Adler Zero

In principle, an Adler zero term (Eq. 6.23) can also be applied to the production vector in the K-matrix model, in addition to the K-matrix components, to suppress the false kinematical singularity at low $m_{\pi\pi}$. By convention this is not performed, as doing so has been found to impact fit quality negatively. This is also true in this analysis, where addition of an Adler zero to the P-vector results in a best-fit log-likelihood value around 25 units away from the fit where no such term is included.

Final Model and Fit Configuration

The components included in the final optimised model are listed in Table 7.13. The mass and width of the $\rho(770)^0$ are constrained according to Gaussian distributions defined by the world-average values and their corresponding uncertainty. Freeing the parameters of other resonances did not significantly increase fit quality. The resonance Blatt–Weisskopf barrier radius is fixed to a value of $4\,\text{GeV}^{-1}$, and the value of s_0^{prod} in the K-matrix model is fixed to $-3\,\text{GeV}^2$. No additional non-resonant components or virtual contributions are present. To obtain the nominal best fit results, the fit is performed 1000 times with initial parameters sampled uniformly in the range $[-10, 10]$ and the fit with the greatest log-likelihood selected.

Multiple Solutions

Due to the numerous interacting components in amplitude models, particularly those with broad overlapping states, it is not uncommon for the fit to converge to multiple nearby minima in the likelihood function when initialised with random parameter values. These can result in fits that converge to the same parameters, within their statistical uncertainty, or genuinely distinct solutions that are difficult for the fit to determine between.

In this analysis, the distribution of the difference in the log-likelihood between the best fit value and values for fits within $\Delta \log \mathcal{L} < 10$ can be seen in Fig. 7.27. The fraction of fits generated with randomised starting parameters that converge with the

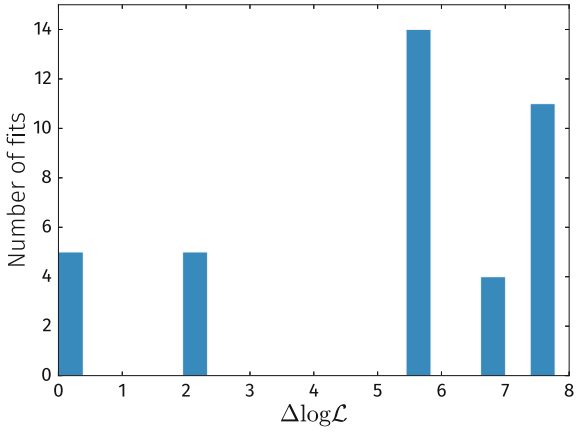

Fig. 7.27 Distribution of the difference in the log-likelihood between the best fit value and values for fits within $\Delta \log \mathcal{L} < 10$

Table 7.13 List of resonant contributions present in the nominal model. The models for the $\rho(770)^0$ and $\omega(782)$, denoted with '†' are included as a single $\rho-\omega$ mixing model, described in Sect. 6.5.2. Here, 'GS' indicates the Gounaris–Sakurai model, and 'RBW' indicates the relativistic Breit–Wigner

Resonance	Spin	Model
S-wave	0	K-matrix
$\rho(770)^0$	1	GS†
$\omega(782)$	1	RBW†
$f_2(1270)$	2	RBW
$f_2(1430)$	2	RBW
$\rho(1450)^0$	1	RBW
$\rho_3(1690)^0$	3	RBW
$\rho(1700)^0$	1	RBW

most minimal negative log-likelihood is only around 0.5%, however this behaviour is consistent with what is observed in the convergence of the fits to pseudoexperiments generated from the nominal model, and therefore is likely due to the high degree of correlation between the K-matrix parameters impeding the fit progress. The solution closest to the minimum corresponds to a change in the log-likelihood of approximately 2.3 units, and the second closest solution corresponds to a change of approximately 5.5 units.

In general, the isobar parameters obtained in each of these fits are comparable. Argand plots of the isobar parameters which are the most discrepant between each fit can be seen in Fig. 7.28, where the B^+ (B^-) parameters for the nominal fit correspond to blue solid (dashed) ellipses, the parameters for the fit converging 2.3 units of $\log\mathcal{L}$ away from the minimum are shown as green solid (dashed) ellipses, and the parameters for the fit converging 5.5 units away are shown as solid (dashed) red ellipses. In each case, the area of the ellipse corresponds to a 68% confidence interval. In general, the additional solutions give a smaller overall B^+ fit fraction, with an increased total S-wave fit fraction and reduced $\rho_3(1390)$ and $\rho(1700)^0$ fit fractions. The *CP*-asymmetries are largely unchanged, as the additional solutions generally represent variations in the phase rather than the magnitude of the resonant contributions, and additionally the B^- parameters appear robust.

7.6.3 Results

The isobar parameters for the final model can be found in Table 7.14, and corresponding fit-fractions and *CP*-asymmetries in Table 7.15. The floating parameters for the combined $\rho-\omega$ mixing model can be found in Table 7.16. In each case the uncertainties are statistical only, obtained from fits to pseudoexperiments. Argand

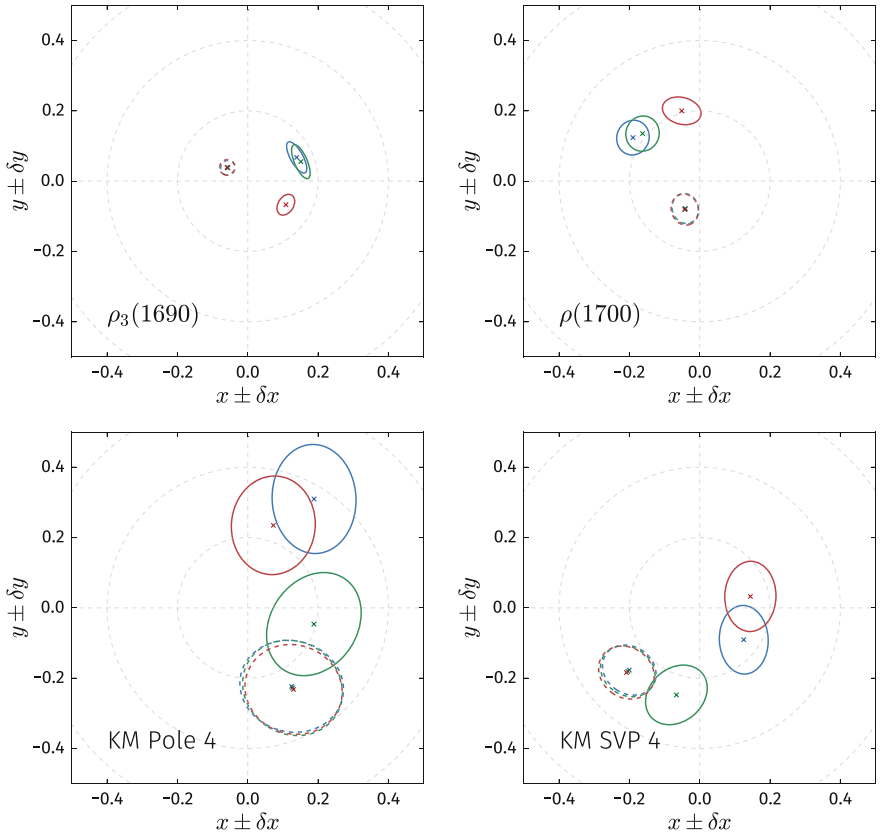

Fig. 7.28 Argand plots of the most discrepant isobar parameters between the fits closest to the minimal negative log-likelihood. Parameters of the B^+ (B^-) amplitude in the nominal fit correspond to blue solid (dashed) ellipses, the parameters for the fit converging 2.3 units away from the minimum are shown as green solid (dashed) ellipses, and the parameters for the fit converging 5.5 units away are shown as solid (dashed) red ellipses. In each case, the area of the ellipse corresponds to a 68% confidence interval around the central value (denoted as 'x')

plots of the real and imaginary components of the isobar parameters can be found in Appendix B.

Fit Projections

Projections of the nominal fit model on the data can be found in Figs. 7.29, 7.30, 7.31 and 7.32 for the invariant-mass pairs, and in Figs. 7.33, 7.34, 7.35 and 7.36, for the cosine of the helicity angle. These plots also contain the projection of the total background component and the individual model components. These projections correspond to the total Dalitz-plot, as well as projections in restricted interesting regions in m_{low}:

- The region below the $\rho(770)^0$, dominated by S-wave, where $m_{\text{low}} < 0.62\,\text{GeV}$.

Table 7.14 Cartesian isobar coefficients extracted from the final fit. Uncertainties are statistical only

Component	x	y	δ_x	δ_y
$\rho(770)^0$	1	0	-0.040 ± 0.016	0
$f_2(1270)$	-0.013 ± 0.020	-0.130 ± 0.016	0.216 ± 0.018	0.382 ± 0.018
$f_2(1430)$	-0.037 ± 0.015	0.007 ± 0.011	0.058 ± 0.015	-0.039 ± 0.012
$\rho(1450)^0$	-0.061 ± 0.020	-0.116 ± 0.026	-0.389 ± 0.020	-0.027 ± 0.028
$\rho_3(1690)^0$	0.041 ± 0.009	0.053 ± 0.011	0.098 ± 0.009	0.015 ± 0.014
$\rho(1700)^0$	-0.115 ± 0.017	0.023 ± 0.018	-0.074 ± 0.019	0.101 ± 0.020
KM Pole 1	-0.128 ± 0.032	0.237 ± 0.044	-0.198 ± 0.031	-0.275 ± 0.046
KM Pole 2	-0.006 ± 0.055	0.018 ± 0.058	-0.212 ± 0.068	-0.008 ± 0.056
KM Pole 3	0.236 ± 0.060	0.087 ± 0.062	-0.031 ± 0.057	0.391 ± 0.069
KM Pole 4	0.157 ± 0.057	0.043 ± 0.065	0.032 ± 0.057	0.266 ± 0.071
KM Pole 5	-0.265 ± 0.073	-0.013 ± 0.077	-0.063 ± 0.075	-0.434 ± 0.080
KM SVP 1	-0.288 ± 0.055	0.004 ± 0.052	-0.026 ± 0.061	-0.371 ± 0.048
KM SVP 2	0.038 ± 0.051	0.054 ± 0.052	-0.114 ± 0.056	0.021 ± 0.065
KM SVP 3	-0.032 ± 0.082	0.203 ± 0.068	-0.332 ± 0.085	0.082 ± 0.074
KM SVP 4	-0.038 ± 0.034	-0.134 ± 0.042	0.163 ± 0.036	0.043 ± 0.036

Table 7.15 Component fit fractions, FF, and *CP* asymmetries, $\mathcal{A}_{CP}$, extracted from the final fit. Uncertainties are statistical only

Component	B^+ FF (%)	B^- FF (%)	$\mathcal{A}_{CP}$ (%)
$\rho(770)^0$	67.37 ± 1.27	55.14 ± 1.20	-4.10 ± 1.70
$\omega(782)$	0.62 ± 0.06	0.52 ± 0.07	0.78 ± 7.87
$f_2(1270)$	7.08 ± 0.91	18.81 ± 1.44	49.85 ± 5.66
$f_2(1430)$	0.10 ± 0.09	0.67 ± 0.30	76.83 ± 23.95
$\rho(1450)^0$	15.07 ± 1.86	6.90 ± 1.07	-31.98 ± 9.37
$\rho_3(1690)^0$	1.61 ± 0.27	0.28 ± 0.10	-67.59 ± 11.15
$\rho(1700)^0$	3.46 ± 0.82	0.46 ± 0.26	-73.90 ± 13.51
KM Pole 1	7.27 ± 1.52	15.97 ± 2.74	42.38 ± 10.34
KM Pole 2	3.19 ± 2.30	2.58 ± 2.05	-4.64 ± 42.36
KM Pole 3	18.20 ± 6.91	9.80 ± 4.48	-24.52 ± 28.19
KM Pole 4	8.86 ± 4.40	3.91 ± 3.16	-33.58 ± 39.00
KM Pole 5	20.72 ± 8.95	13.04 ± 5.93	-17.07 ± 30.13
KM SVP 1	15.69 ± 5.55	12.51 ± 3.96	-5.41 ± 24.89
KM SVP 2	0.78 ± 1.50	1.46 ± 1.52	35.65 ± 49.45
KM SVP 3	14.38 ± 8.01	6.28 ± 4.89	-34.11 ± 40.64
KM SVP 4	1.61 ± 1.29	4.28 ± 1.48	49.84 ± 25.08
Total S-wave	16.52 ± 0.86	22.04 ± 0.92	-21.44 ± 26.11

Table 7.16 Parameters of the $\rho-\omega$ mixing model from the final fit. Uncertainties are statistical only

Parameter	Value
B^- magnitude	0.960 ± 0.109
B^+ magnitude	0.945 ± 0.103
B^- phase	0.192 ± 0.116
B^+ phase	-0.152 ± 0.115

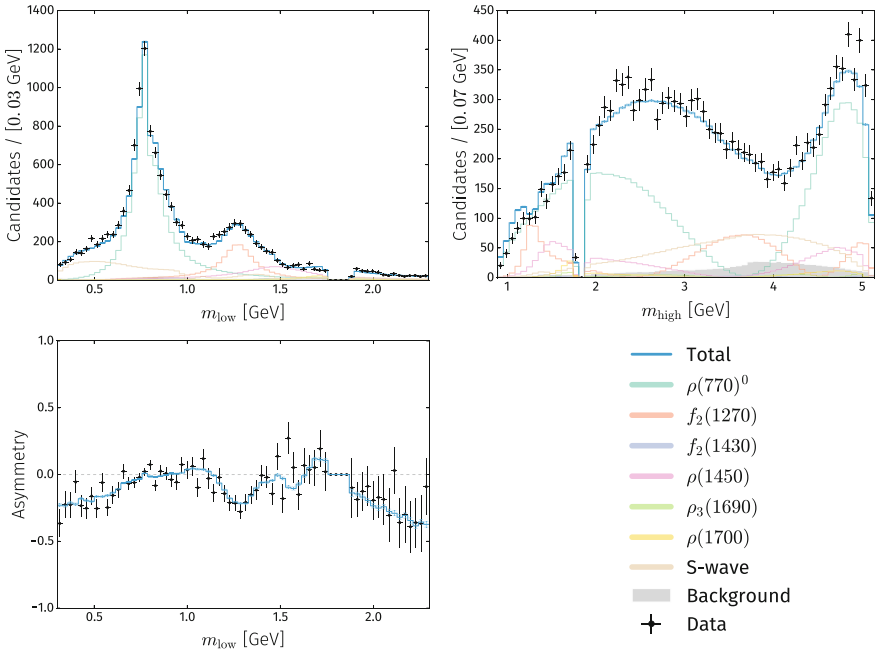

Fig. 7.29 Data and model projections for the lower section of m_{low} (top left) and the asymmetry in this range as a function of m_{low} (bottom left), the full range of m_{high} (top right), and the legend for the fit projections presented in this section (bottom right)

- The $\rho(770)^0$ and $\omega(782)$ region, where $0.62 < m_{\text{low}} < 0.92\,\text{GeV}$.
- The $f_2(1270)$ region, where $0.92 < m_{\text{low}} < 1.62\,\text{GeV}$.
- The region above the $f_2(1270)$ and below the $\overline{D}^0$ veto, $1.50 < m_{\text{low}} < 1.74\,\text{GeV}$.
- The region above the $\overline{D}^0$ veto, $1.9 < m_{\text{low}} < 3.6\,\text{GeV}$.
- The region around the χ_{c0}, where $3.3 < m_{\text{low}} < 3.5\,\text{GeV}$.

For the plots of the helicity angle, in addition to these regions, the region above and below the $\rho(770)^0$ pole is also shown. Here it is possible to identify the effect that the evolution of the strong (Breit–Wigner) phase associated with the $\rho(770)^0$ resonance has on the CP-asymmetry, as a function of the helicity angle. In addition to the $\overline{D}^0$

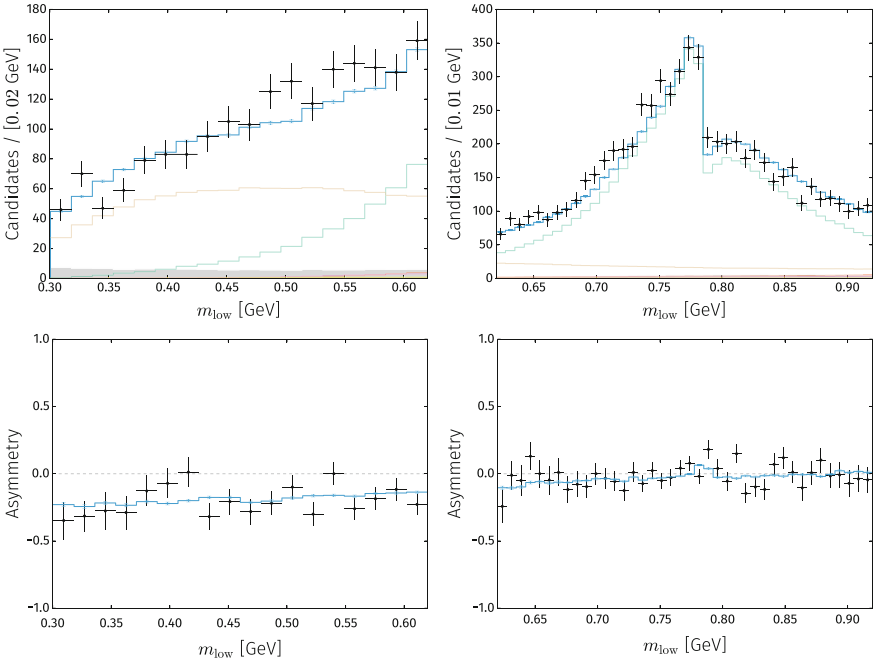

Fig. 7.30 Data and model projections in m_{low} for the region below the $\rho(770)^0$ (top left) and in the $\rho(770)^0$ (top right) region; and the asymmetry in these ranges as a function of m_{low} in each region (bottom)

veto, plots of $\cos\theta_{\text{hel}}$ also exhibit a deficit at high $\cos\theta_{\text{hel}}$ due to the symmetrisation of the Dalitz plot, which is more evident at high m_{low}.

Some components in the model exhibit a large CP-asymmetry, and in addition have a non-negligible correlation with other components. This is true for the $f_2(1270)$ and $f_2(1430)$, and the $\rho(1450)^0$ and $\rho(1700)^0$. As such, the CP-asymmetries of these components are presented as two-dimensional contours in Fig. 7.37.

7.6.4 S-Wave Amplitude

It is possible to visualise the evolution of the (unsymmetrised) S-wave amplitude as a function of $m(\pi^+\pi^-)$ by plotting the K-matrix model magnitude and phase. This can be found in Fig. 7.38. The dominant contribution is from the broad $f_0(500)$ at low mass, where there is very little phase variation. A sharp decrease in the amplitude at around 1 GeV is characteristic of the $f_0(980)$ contribution, along with a rapid phase rotation. More complex behaviour is seen in the region of the overlapping $f_0(1370)$, $f_0(1500)$ and $f_0(1710)$ resonances, uncharacteristic of a simple relativistic Breit–Wigner evolution. There is large CP-violation the magnitude of S-wave at low

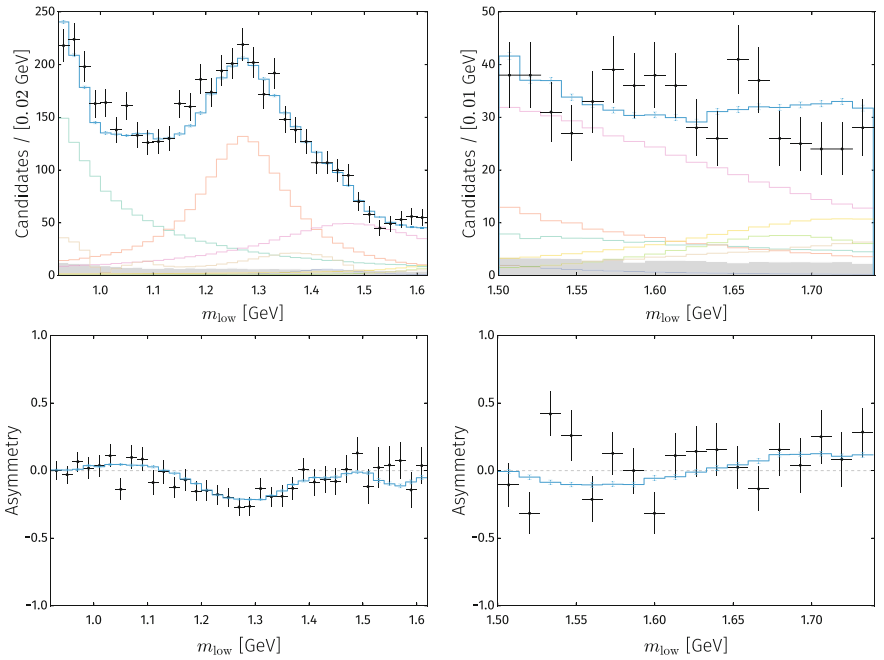

Fig. 7.31 Data and model projections in m_{low} for the region around the $f_2(1270)$ (top left) and in region below the $\overline{D}^0$ veto (top right); and the asymmetry in these ranges as a function of m_{low} in each region (bottom)

$m(\pi^+\pi^-)$, which changes sign around the $f_0(980)$ pole, and decreases to zero at higher $m(\pi^+\pi^-)$. The relative phase between the B^+ and B^- component S-wave component is negligible below the $f_0(980)$ pole (and the $K\overline{K}$ threshold), after which these phases diverge substantially, before converging again at high $m(\pi^+\pi^-)$.

7.7 Systematic Uncertainties

Systematic uncertainties are divided into 'experimental systematics', that arise from the experimental procedure of selecting the signal decays and the calculation of their efficiency, and 'model systematics', that arise from inherent uncertainties in the modelling of the $B^+ \to \pi^+\pi^+\pi^-$ amplitude. This distinction is motivated by the observation that, due to the complexities of constructing and fitting amplitude models to data, the systematic uncertainties driven by the amplitude fit are often significantly larger than, but uncorrelated with, those driven by the rest of the analysis procedure.

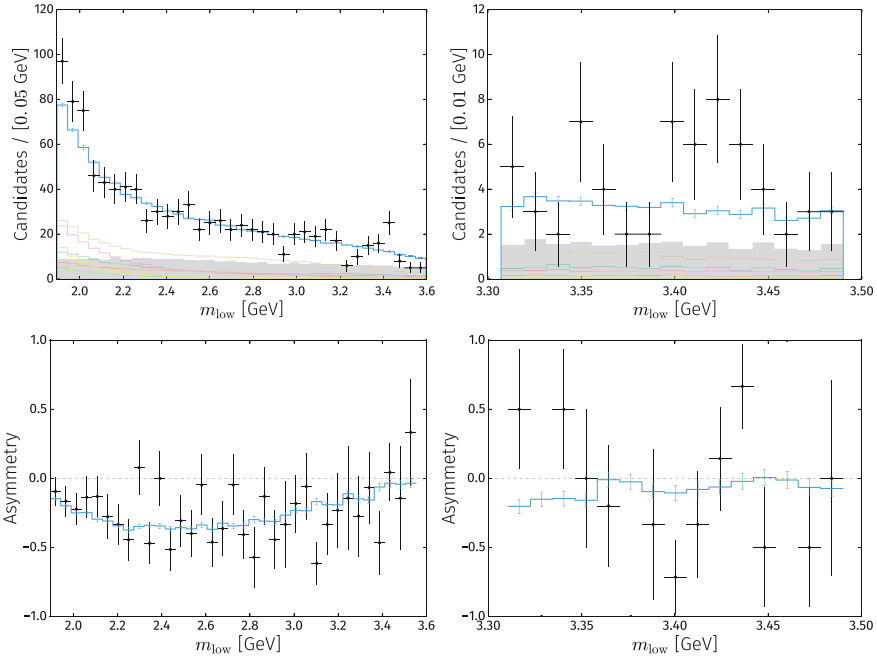

Fig. 7.32 Data and model projections in m_{low} for the region above the $\overline{D}^0$ veto (top left) and in region around the χ_{c0} (top right); and the asymmetry in these ranges as a function of m_{low} in each region (bottom)

7.7.1 Experimental Systematics

Experimental systematics are dominated by the uncertainty on the overall signal and background yields, background distributions in the Dalitz-plot fit, and the statistical uncertainty on the variation of the efficiency across the square Dalitz-plot. Also considered here are systematics from the $\overline{D}^0$ veto and the bias on each parameter in the amplitude fit as calculated from toy pseudoexperiments. The total systematic uncertainties due to the experimental procedure are given in Tables 7.17 and 7.18, along with the contributions from the various sources listed in this section. Uncertainties on the cartesian isobar coefficients are reported later in Table 7.21.

Mass Fit

Parameters that are fixed in the nominal invariant mass fit are varied according to their uncertainties and the resulting change in extracted yield used to assign a systematic uncertainty. The exponential function used to model the combinatorial background is replaced with a linear function, and the Gaussian convolved ARGUS function used for the partially reconstructed background replaced with a nonparametric kernel density-estimate. No such model variation is used for the signal or cross-feed, as the precision on the model shapes afforded from the large number of simulated decays

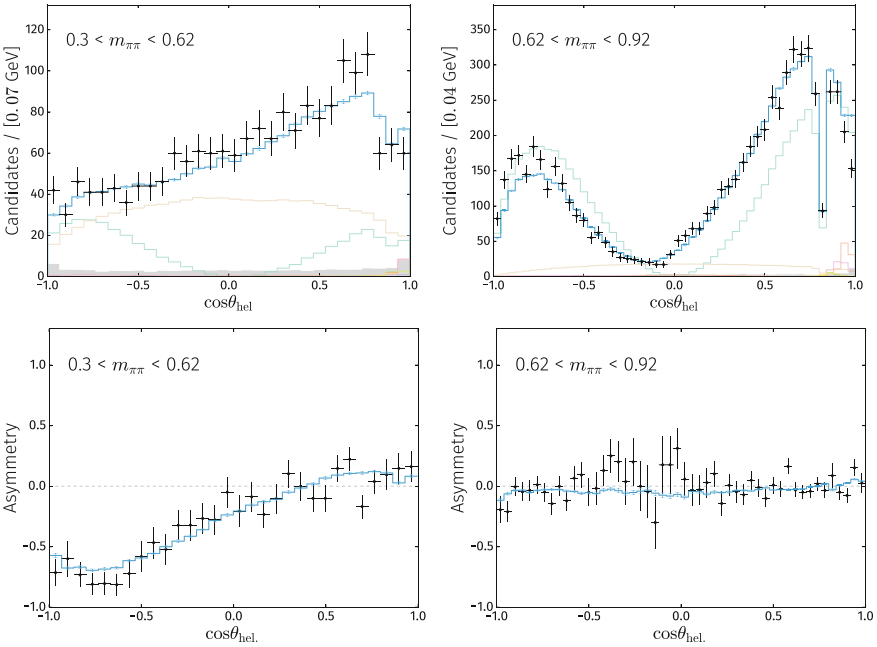

Fig. 7.33 Data and model projection of $\cos\theta_{\rm hel}$ for the region below the $\rho(770)^0$ (top left), and in the $\rho(770)^0$ (top right) region; and the asymmetry in these ranges as a function of $\cos\theta_{\rm hel}$ in each region (bottom)

renders any variation of the shape from the model itself negligible. The asymmetries in the background contributions obtained from the mass fit are also varied according to their uncertainties.

The subsequent systematic uncertainty is added in quadrature to the statistical uncertainty on the signal and background yields obtained from the invariant-mass fit, and is propagated through to the Dalitz-plot fit.

Efficiency Distribution

The uncertainty on the efficiency map due to the statistical uncertainty on the distribution of simulated events is calculated using the statistical bootstrap procedure: the Dalitz-plot fit is performed using an ensemble of efficiency maps, each calculated via resampling, with replacement, of the simulated data. Any spread in the fitted parameter values extracted from the fits that minimise the negative log-likelihood is therefore due to the statistical uncertainty of the efficiency maps. In addition, a systematic uncertainty is also calculated from the statistical uncertainty on the PID and L0Hadron trigger efficiency calibration, and systematic uncertainty is assigned based on the variation of the number of bins in the square Dalitz-plot efficiency map. The pion detection asymmetry, $\mathcal{A}^{\pi}_{\rm det}$, has previously been measured by LHCb to be consistent with zero at the per-mille level [67], and therefore no systematic uncertainty is assigned here.

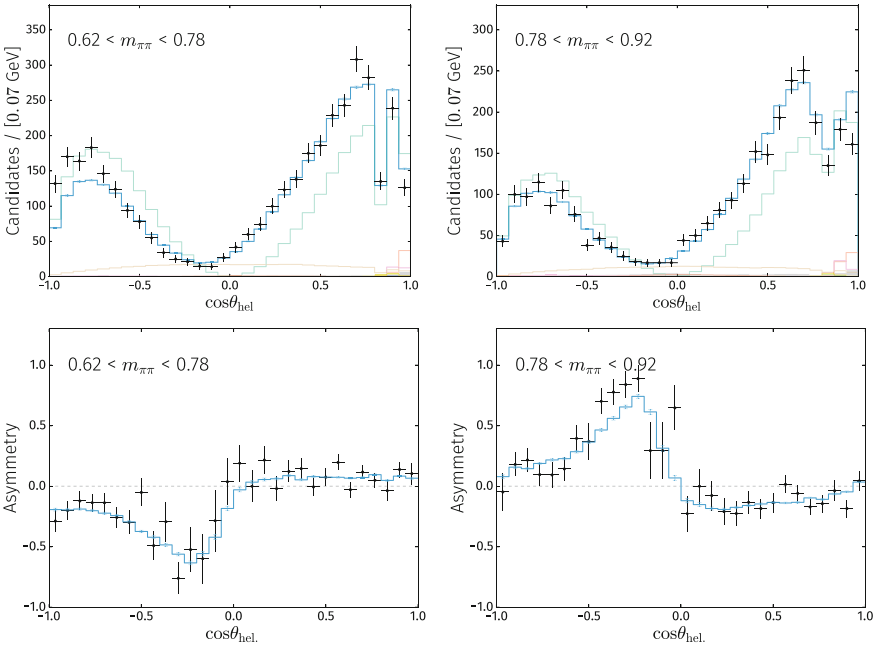

Fig. 7.34 Data and model projection of $\cos\theta_{\rm hel}$ in the $\rho(770)^0$ region, below (top left) and above (top right) the $\rho(770)^0$ pole mass; and the asymmetry in these ranges as a function of $\cos\theta_{\rm hel}$ in each region (bottom)

Veto

The $\overline{D}^0$ veto window is enlarged to the range [1725, 1915] MeV to investigate possible systematic effects resulting in incomplete removal of intermediate charm contributions. As this necessitates re-acquiring the $B^+ \to \pi^+\pi^+\pi^-$ yield, it also affects the three-body invariant-mass fit, where the background models are also updated to take into account the effect of the larger veto. Background distributions in the Dalitz plot are also modified.

Dalitz-Plot Background

The model parameters for the combinatorial background distribution (including those that control the subtraction of $B^0 \to \pi^+\pi^-$ and $B^0 \to K^+\pi^-$ decays), and the distribution of $B^+ \to \eta' K^+$ decay background are varied according to their quoted statistical uncertainty, and the resulting variation in the parameters from the fit that minimises the negative log-likelihood in each case taken to be the resulting uncertainty. The $B^+ \to K^+\pi^+\pi^-$ decay distribution is sufficiently well known using the BaBar model that such variation is negligible compared to the overall uncertainty on the yield, so this is not considered further.

The uncertainty introduced by the $(m_{\rm low}, m_{\rm high}, m_{\pi^+\pi^+\pi^-})$ binning when fitting the Gaussian process to the combinatorial background is taken into account in the

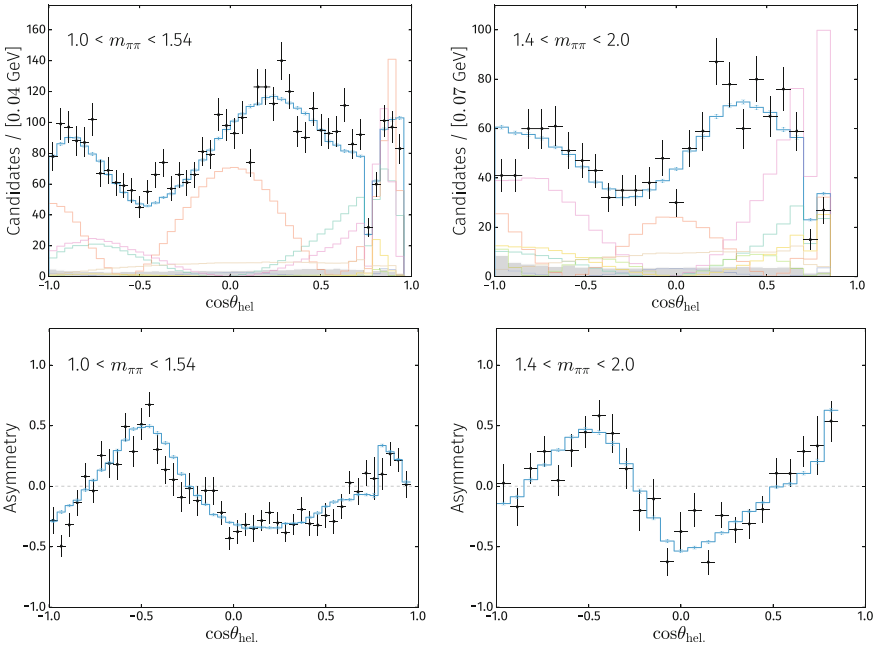

Fig. 7.35 Data and model projection of $\cos\theta_{\rm hel}$ for the $f_2(1270)$ region (top left), and above the $f_2(1270)$ region (top right); and the asymmetry in these ranges as a function of $\cos\theta_{\rm hel}$ in each region (bottom)

statistical uncertainty obtained from the Gaussian process. However, the distribution of the $B^0 \to \pi^+\pi^-$ and $B^0 \to K^+\pi^-$ decay in $m_{\pi^+\pi^+\pi^-}$ is imperfectly modelled by MC. Therefore the yield of $B^0 \to \pi^+\pi^-$ and $B^0 \to K^+\pi^-$ in bins of $m_{\pi^+\pi^+\pi^-}$ is obtained directly from a fit to data, and a systematic obtained based on the deviation of the fitted amplitude parameters in this case with respect to the nominal fit values. The distribution in $m_{\rm low}$ and $m_{\rm high}$ is modelled by MC, as in the nominal fit.

7.7.2 *Production Asymmetry*

The production asymmetry of B^+ mesons at the LHC has been measured by LHCb [67] to be $(-0.41 \pm 0.50) \times 10^{-2}$ at 7 TeV, and $(-0.53 \pm 0.33) \times 10^{-2}$ at 8 TeV, which are consistent with zero. This asymmetry is introduced as a global asymmetry between the B^+ and B^- efficiency maps, with a value sampled from a Gaussian with mean and width corresponding to the LHCb measurement. The resulting variation in the parameters obtained from fits using these efficiencies is negligible, and therefore no systematic is assigned.

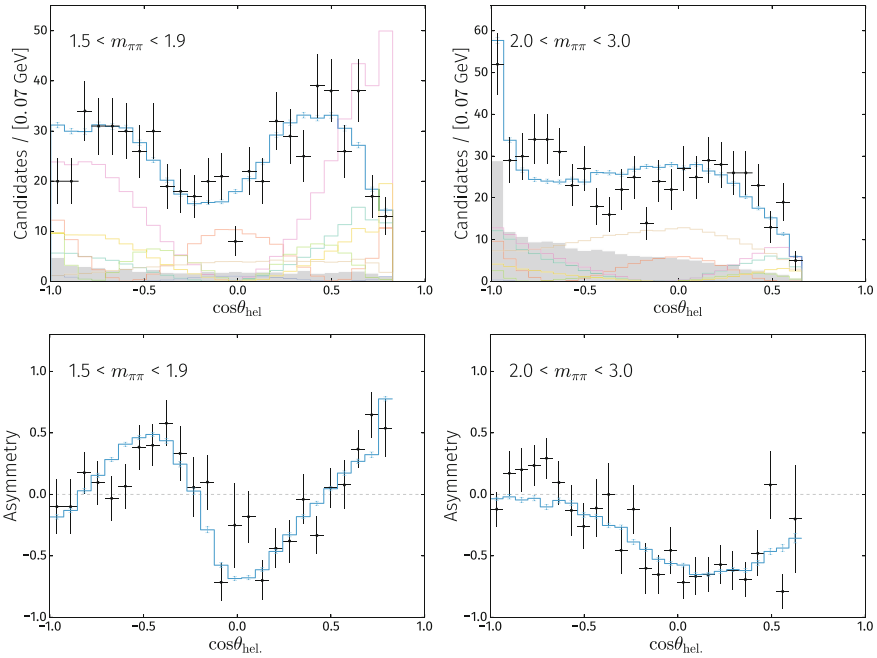

Fig. 7.36 Data and model projection of $\cos\theta_{\rm hel}$ for the $\rho_3(1690)^0$ region (top left), and above the $\rho_3(1690)^0$ region (top right); and the asymmetry in these ranges as a function of $\cos\theta_{\rm hel}$ in each region (bottom)

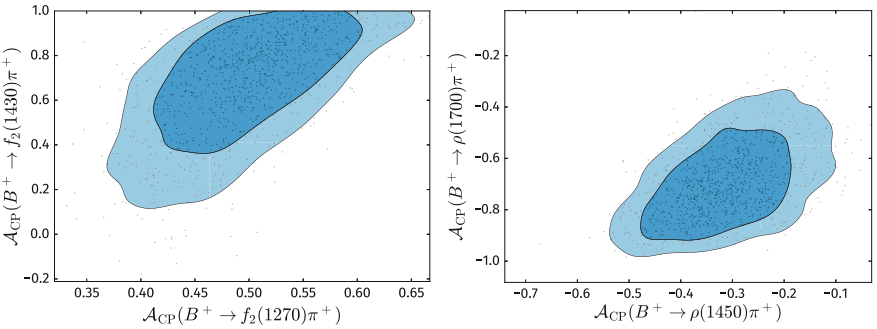

Fig. 7.37 Two dimensional distributions of the *CP*-asymmetries of $f_2(1270)$ and $f_2(1430)$ (left), and $\rho(1450)^0$ and $\rho(1700)^0$ (right), with statistical uncertainties only. Black points are the result from fits to pseudoexperiments, and the blue contours are 68% (dark) and 90% (dark plus light) intervals

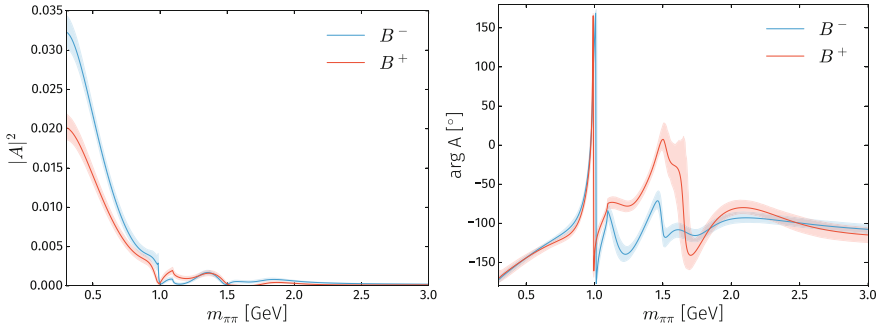

Fig. 7.38 Amplitude squared (left) and phase (right) of the K-matrix component of the $B^+ \to \pi^+\pi^+\pi^-$ amplitude, for B^+ (red) and B^- (blue) decays. Here, the phase of the B^- component is shifted by $+110°$ for legibility, and the error bands are 68% confidence intervals, incorporating statistical uncertainties only

7.7.3 Model Systematics

The radius of the Blatt–Weisskopf barrier factor for the resonance decay is not floated in the fit to data, and therefore a systematic uncertainty is assigned here. This systematic is the maximum absolute change with respect to the nominal value of each model parameters, when fits are performed at radius values of 3, 5, or 6 GeV^{-1}. Values outside these ranges have likelihood values significantly far away from that of the nominal fit such that it is possible to exclude them from consideration.

Similarly, the value for the s_0^{prod} parameter in the K-matrix is also not floated in the fit to data, but is dependent on the production process and therefore this results in a systematic uncertainty. In this case the systematic on the parameter values is taken to be the maximum change with respect to the nominal values in fits performed with s_0^{prod} values of 1, 2, 4, or 5 GeV^2.

The $f_2(1430)$ component was included in the model primarily to improve fit quality in the $f_2(1270)$ region, and therefore a systematic uncertainty is assigned on all parameters other than those relating to the $f_2(1430)$, corresponding to the change with respect to the nominal fit values when the $f_2(1430)$ is removed. Furthermore, the components of the K-matrix with the smallest magnitudes, pole 2 and SVP 2, are also removed and a systematic assigned based on the variation of the parameters.

The subsequent absolute systematics on the fit fractions, and CP-asymmetries can be seen in Tables 7.19, 7.20, respectively, where the total is the sum in quadrature of the systematics from all sources of model systematics. These uncertainties are assumed to be drawn from Gaussian distributions, where the values indicate the 68% interval around the central value. Uncertainties on the cartesian isobar coefficients are reported later in Table 7.21.

Table 7.17 Systematic uncertainties on the fit fractions from experimental sources. 'Total' is the sum in quadrature of the systematics from each source of amplitude model uncertainty

Component	Fit bias (10^{-2})		Bkg. models (10^{-2})		$\overline{D}^0$ veto (10^{-2})		Mass fit (10^{-2})		Efficiency (10^{-2})		Total (10^{-2})	
	Positive	Negative	Positive	Negative	Positive	Negative	Positive	Negative	Positive	Negative	Positive	Negative
$\rho(770)^0$	0.04	0.27	0.30	0.12	0.38	0.02	0.04	0.05	3.07	0.36	3.11	0.47
$\omega(782)$	0.01	0.01	< 0.01	< 0.01	< 0.01	< 0.01	< 0.01	< 0.01	0.01	0.01	0.01	0.01
$f_2(1270)$	0.02	0.03	0.07	0.10	0.17	0.10	< 0.01	< 0.01	0.54	1.56	0.57	1.57
$f_2(1430)$	0.04	0.04	0.01	0.02	0.03	0.04	< 0.01	< 0.01	0.10	< 0.01	0.12	0.05
$\rho(1450)^0$	0.30	0.12	0.30	0.07	0.70	0.12	0.05	< 0.01	4.99	0.43	5.06	0.46
$\rho_3(1690)^0$	0.01	0.05	0.02	0.01	0.04	0.01	< 0.01	< 0.01	0.32	0.14	0.32	0.15
$\rho(1700)^0$	0.25	0.17	0.10	0.02	0.74	0.01	0.01	< 0.01	1.01	0.18	1.29	0.24
Total S-wave	< 0.01	< 0.01	0.11	0.12	0.16	0.24	< 0.01	0.05	2.99	1.75	3.00	1.77

Table 7.18 Systematic uncertainties (10^{-2}) on the *CP*-asymmetries from experimental sources. 'Total' is the sum in quadrature of the systematics from each source of amplitude model uncertainty

Component	Fit bias	Background models	$\overline{D}^0$ veto	Mass fit	Efficiency	Total
$\rho(770)^0$	0.19	0.22	0.44	0.07	1.75	1.83
$\omega(782)$	0.64	0.23	0.69	0.07	1.98	2.21
$f_2(1270)$	0.28	0.31	0.79	0.03	0.72	1.15
$f_2(1430)$	8.55	1.92	4.02	0.25	19.44	21.70
$\rho(1450)^0$	0.16	0.74	1.41	0.08	15.61	15.69
$\rho_3(1690)^0$	5.01	0.76	0.28	0.01	6.43	8.19
$\rho(1700)^0$	6.75	1.27	3.94	0.03	19.09	20.67
Total S-wave	0.03	1.92	1.09	0.36	4.18	4.74

Table 7.19 Systematic uncertainties on the fit fractions resulting from variations of the amplitude model. 'Total' is the sum in quadrature of the systematics from each source of amplitude model uncertainty

Component	Model variation $\left(10^{-2}\right)$		Barrier radius $\left(10^{-2}\right)$		s_0^{prod} $\left(10^{-2}\right)$		Total $\left(10^{-2}\right)$	
	Positive	Negative	Positive	Negative	Positive	Negative	Positive	Negative
$\rho(770)^0$	0.28	1.90	2.97	0.81	2.34	0.22	3.80	2.07
$\omega(782)$	0.04	0.03	0.01	0.02	0.00	0.03	0.04	0.05
$f_2(1270)$	3.99	6.16	0.40	0.51	0.10	0.02	4.01	6.19
$f_2(1430)$	0.02	0.37	0.03	0.12	0.00	0.01	0.03	0.39
$\rho(1450)^0$	1.99	0.94	0.83	0.01	1.26	0.05	2.50	0.94
$\rho_3(1690)^0$	0.35	0.25	0.12	0.00	0.06	0.00	0.37	0.25
$\rho(1700)^0$	0.18	0.22	0.47	0.10	0.47	0.00	0.68	0.24
Total S-wave	3.01	2.51	0.28	0.40	1.04	0.13	3.20	2.54

Table 7.20 Systematic uncertainties (10^{-2}) on the *CP*-asymmetries resulting from variations of the amplitude model. 'Total' is the sum in quadrature of the systematics from each source of amplitude model uncertainty

Component	Model variation	Barrier radius	s_0^{prod}	Total
$\rho(770)^0$	1.57	1.66	2.01	3.04
$\omega(782)$	3.14	1.60	0.53	3.57
$f_2(1270)$	8.68	0.98	0.53	8.75
$f_2(1430)$	5.46	2.28	0.18	5.92
$\rho(1450)^0$	9.36	2.74	4.34	10.68
$\rho_3(1690)^0$	14.56	2.19	0.85	14.75
$\rho(1700)^0$	10.46	9.07	3.31	14.23
Total S-wave	54.81	4.41	2.67	55.05

7.8 Cross-Checks

As the Dalitz-plot fit results should be independent of the precise B^+ mass window chosen, the window is reduced to the range [5249, 5309] MeV (approximately twice the expected width of the B^+ signal peak in each direction), and the expected number of signal and background events scaled correspondingly. The efficiency maps are also recomputed, as a tighter B^+ window affects the momentum distribution of the final state particles. It is also expected that the fit-fractions and CP-asymmetries will be consistent when performing the fit using various sub-categories of the data. As such, the fit is performed separately for 2011 and 2012 data, and results consistent with those found in the nominal fit are obtained.

Latent Model Components

In Sect. 7.6.2, well-established resonances are introduced into the model with their world-average masses and widths. However it is possible that resonances that are not well established by other experiments are present in the $B^+ \to \pi^+\pi^+\pi^-$ signal data. Furthermore, it may be possible that large uncertainties are present on the parameters of otherwise established states, and therefore these are not identified when introduced into the model with these parameters fixed to their world-average values. As such, a generic search is performed for additions to the model with various mass, width, and spin hypotheses. The variation in $\sqrt{\Delta \log \mathcal{L}}$ for these scans can be found in Fig. 7.39, where in each bin in a fit is performed with the nominal model plus an additional component of the indicated mass, width, and spin, and the change in $\log \mathcal{L}$ is evaluated with respect to the value found for the nominal fit model.

Artefacts in this procedure are expected to arise due to imperfect efficiency modelling, for example at the edges of the Dalitz plot, presenting as additional broad components. This can be seen in Fig. 7.39, for all spin hypotheses. Additionally, a better fit quality can be achieved by including a narrow resonance at approximately 2 GeV, for several spin hypotheses. Such a resonance is not consistent with those listed in Ref. [5], and a narrow resonance at intermediate mass would be easily identified in data from scattering experiments. As such, this is assumed to be unphysical, and is likely due to mis-modelling of the efficiency or background distributions above the $\overline{D}^0$ veto, or from candidates in the tail of the $\overline{D}^0$ resonance surviving the veto.

Alternative Resonance Models

Despite decisions motivated by the change in fit likelihood described in Sect. 7.6.2, it is interesting to see what effect a 'worse' model has on the final results of the Dalitz-plot fit. In this case, the $\rho-\omega$ mixing model is replaced by separate Gounaris–Sakurai and relativistic Breit–Wigner models for the $\rho(770)^0$ and $\omega(782)$ resonances, respectively, and results consistent with the nominal fit are obtained.

In addition, the Zemach spin tensor formalism summarised in Sect. 6.4.2 is not guaranteed to conserve angular momentum, particularly for high-mass high-spin states. An alternative is the 'relativistic' Rarita–Schwinger spin tensor formalism, where angular momentum is enforced by construction, and as such may result in a

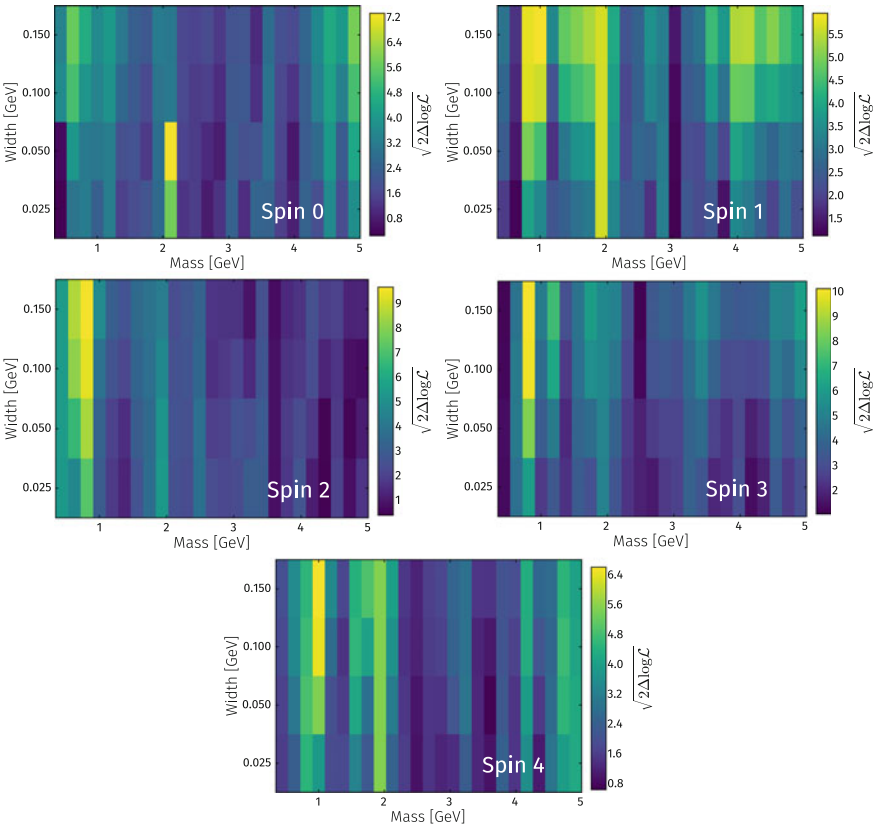

Fig. 7.39 Likelihood relative to the nominal fit result for the masses and widths of additional resonances of spin-0 (top left), spin-1 (top right), spin-2 (middle left), spin-3 (middle right), and spin-4 (bottom)

better representation of the data.[4] This results in a modification of the spin factors compared to the Zemach formalism, and amplitude model parameters and fit projections using the Rarita–Schwinger formalism with the nominal model obtained in Sect. 7.6.2 can be found in Appendix C.

[4]This is not a given, as there is still significant ambiguity in the ad-hoc Blatt–Weisskopf factors. The radius parameter of which may in practice account for any discrepancy introduced by using an 'incorrect' spin formalism.

7.9 Results

The final results for the CP-asymmetries, branching fractions, and isobar parameters are given in this section, incorporating all systematic uncertainties. Isobar parameters can be seen in Table 7.21, and fit fractions and CP-asymmetries in Table 7.22. The central values for the interference fit fractions can be seen in Fig. 7.40. Furthermore, the CP-conserving fit fractions are presented in Table 7.23, along with the product branching fractions of the $B^+ \to R(\pi^+\pi^-)\pi^+$ decays, where R is an intermediate resonance, using the world-average $B^+ \to \pi^+\pi^+\pi^-$ branching fraction of $1.52 \pm 0.14 \times 10^{-5}$.

Where the branching fraction to $\pi^+\pi^-$ is known, these product branching fractions can be converted into quasi-two body branching fractions. The $\rho(770)^0$ decays 100% to $\pi^+\pi^-$, to the level of precision required here, and therefore,

$$\mathcal{B}(B^+ \to \rho(770)^0\pi^+) = (9.26 \pm 0.14 \pm 0.25 \pm 0.35 \pm 0.85) \times 10^{-6}, \quad (7.7)$$

using $\mathcal{B}(\omega(782) \to \pi^+\pi^-) = (1.53^{+0.11}_{-0.13})\%$,

$$\mathcal{B}(B^+ \to \omega(782)\pi^+) = (5.66 \pm 0.40 \pm 0.10 \pm 0.40 \pm 0.52^{+0.48}_{-0.41}) \times 10^{-6}, \quad (7.8)$$

using $\mathcal{B}(f_2(1270) \to \pi^+\pi^-) = (\frac{2}{3} \times 84.2^{+2.9}_{-0.9})\%$, where the factor of $\frac{2}{3}$ is from isospin conservation,

$$\mathcal{B}(B^+ \to f_2(1270)\pi^+) = (3.60 \pm 0.24 \pm 0.30 \pm 1.37 \pm 0.33^{+0.04}_{-0.12}) \times 10^{-6}, \quad (7.9)$$

and using $\mathcal{B}(\rho_3(1690)^0 \to \pi^+\pi^-) = (23.6 \pm 1.3)\%$,

$$\mathcal{B}(B^+ \to \rho_3(1690)^0\pi^+) = (0.58 \pm 0.08 \pm 0.14 \pm 0.19 \pm 0.05 \pm 0.03) \times 10^{-6}, \quad (7.10)$$

In each case, the uncertainties are statistical, from the experimental procedure, from the amplitude model, from the uncertainty on the branching fraction of $B^+ \to \pi^+\pi^+\pi^-$, and from the uncertainty on the resonance decay branching fraction, respectively.

The fit fraction for the $\omega(782)$ component in the combined $\rho-\omega$ mixing model is calculated by isolating the $\omega(782)$ contribution in the overall magnitude of the amplitude squared,

$$|A_{\rho\omega}|^2 = \frac{|A_\rho|^2}{|1 - \Delta^2 A_\rho A_\omega|^2}\left[1 + 2\mathrm{Re}(A_\omega \exp(i\phi_B))\Delta|B| + |A_\omega|^2\Delta^2|B|^2\right], \quad (7.11)$$

where the symbols have the same meaning as in Sect. 6.5.2. From Eq. 6.34 it follows that the fit fraction for the $\omega(782)$ component is

Table 7.21 Cartesian isobar coefficients extracted from the final fit. Uncertainties are statistical, from the experimental procedure, and from the amplitude model, respectively

Component	x	y	δ_x	δ_y
$\rho(770)^0$	1	0	$-0.040 \pm 0.016 \pm 0.017 \pm 0.029$	0
$f_2(1270)$	$-0.013 \pm 0.020 \pm 0.009 \pm 0.019$	$-0.130 \pm 0.016 \pm 0.020 \pm 0.032$	$0.216 \pm 0.018 \pm 0.058 \pm 0.062$	$0.382 \pm 0.018 \pm 0.060 \pm 0.073$
$f_2(1430)$	$-0.037 \pm 0.015 \pm 0.001 \pm 0.009$	$0.007 \pm 0.011 \pm 0.004 \pm 0.012$	$0.058 \pm 0.015 \pm 0.010 \pm 0.014$	$-0.039 \pm 0.012 \pm 0.021 \pm 0.013$
$\rho(1450)^0$	$-0.061 \pm 0.020 \pm 0.024 \pm 0.030$	$-0.116 \pm 0.026 \pm 0.055 \pm 0.054$	$-0.389 \pm 0.020 \pm 0.032 \pm 0.017$	$-0.027 \pm 0.028 \pm 0.067 \pm 0.059$
$\rho_3(1690)^0$	$0.041 \pm 0.009 \pm 0.010 \pm 0.017$	$0.053 \pm 0.011 \pm 0.030 \pm 0.025$	$0.098 \pm 0.009 \pm 0.027 \pm 0.019$	$0.015 \pm 0.014 \pm 0.034 \pm 0.019$
$\rho(1700)^0$	$-0.115 \pm 0.017 \pm 0.023 \pm 0.017$	$0.023 \pm 0.018 \pm 0.006 \pm 0.012$	$-0.074 \pm 0.019 \pm 0.037 \pm 0.031$	$0.101 \pm 0.020 \pm 0.013 \pm 0.021$
KM Pole 1	$-0.128 \pm 0.032 \pm 0.017 \pm 0.332$	$0.237 \pm 0.044 \pm 0.018 \pm 0.343$	$-0.198 \pm 0.031 \pm 0.009 \pm 0.219$	$-0.275 \pm 0.046 \pm 0.038 \pm 0.509$
KM Pole 2	$-0.006 \pm 0.055 \pm 0.017 \pm 0.086$	$0.018 \pm 0.058 \pm 0.036 \pm 0.245$	$-0.212 \pm 0.068 \pm 0.065 \pm 0.090$	$-0.008 \pm 0.056 \pm 0.062 \pm 0.240$
KM Pole 3	$0.236 \pm 0.060 \pm 0.026 \pm 0.195$	$0.087 \pm 0.062 \pm 0.104 \pm 0.206$	$-0.031 \pm 0.057 \pm 0.024 \pm 0.176$	$0.391 \pm 0.069 \pm 0.149 \pm 0.392$
KM Pole 4	$0.157 \pm 0.057 \pm 0.016 \pm 0.246$	$0.043 \pm 0.065 \pm 0.086 \pm 0.264$	$0.032 \pm 0.057 \pm 0.005 \pm 0.134$	$0.266 \pm 0.071 \pm 0.126 \pm 0.533$
KM Pole 5	$-0.265 \pm 0.073 \pm 0.032 \pm 0.172$	$-0.013 \pm 0.077 \pm 0.140 \pm 0.281$	$-0.063 \pm 0.075 \pm 0.018 \pm 0.246$	$-0.434 \pm 0.080 \pm 0.211 \pm 0.404$
KM SVP 1	$-0.288 \pm 0.055 \pm 0.034 \pm 0.066$	$0.004 \pm 0.052 \pm 0.084 \pm 0.225$	$-0.026 \pm 0.061 \pm 0.054 \pm 0.233$	$-0.371 \pm 0.048 \pm 0.136 \pm 0.219$
KM SVP 2	$0.038 \pm 0.051 \pm 0.010 \pm 0.129$	$0.054 \pm 0.052 \pm 0.015 \pm 0.225$	$-0.114 \pm 0.056 \pm 0.036 \pm 0.126$	$0.021 \pm 0.065 \pm 0.057 \pm 0.227$
KM SVP 3	$-0.032 \pm 0.082 \pm 0.110 \pm 0.303$	$0.203 \pm 0.068 \pm 0.026 \pm 0.187$	$-0.332 \pm 0.085 \pm 0.178 \pm 0.422$	$0.082 \pm 0.074 \pm 0.018 \pm 0.452$
KM SVP 4	$-0.038 \pm 0.034 \pm 0.024 \pm 0.246$	$-0.134 \pm 0.042 \pm 0.016 \pm 0.174$	$0.163 \pm 0.036 \pm 0.034 \pm 0.134$	$0.043 \pm 0.036 \pm 0.030 \pm 0.322$

Table 7.22 Component fit fractions, FF, and *CP* asymmetries, $\mathcal{A}_{CP}$, extracted from the final fit. Uncertainties are statistical, from the experimental procedure, and from the amplitude model, respectively

Component	B^+ FF (%)	B^- FF (%)	$\mathcal{A}_{CP}$ (%)
$\rho(770)^0$	$67.37 \pm 1.27 \pm 3.11 \pm 3.80$	$55.14 \pm 1.20 \pm 0.47 \pm 2.07$	$-4 \pm 2 \pm 2 \pm 3$
$\omega(782)$	$0.62 \pm 0.06 \pm 0.01 \pm 0.04$	$0.52 \pm 0.07 \pm 0.01 \pm 0.05$	$1 \pm 8 \pm 2 \pm 4$
$f_2(1270)$	$7.08 \pm 0.91 \pm 0.57 \pm 4.01$	$18.81 \pm 1.44 \pm 1.57 \pm 6.19$	$50 \pm 6 \pm 1 \pm 9$
$f_2(1430)$	$0.10 \pm 0.09 \pm 0.12 \pm 0.03$	$0.67 \pm 0.30 \pm 0.05 \pm 0.39$	$77 \pm 24 \pm 22 \pm 6$
$\rho(1450)^0$	$15.07 \pm 1.86 \pm 5.06 \pm 2.50$	$6.90 \pm 1.07 \pm 0.46 \pm 0.94$	$-32 \pm 9 \pm 16 \pm 11$
$\rho_3(1690)^0$	$1.61 \pm 0.27 \pm 0.32 \pm 0.37$	$0.28 \pm 0.10 \pm 0.15 \pm 0.25$	$-68 \pm 11 \pm 8 \pm 15$
$\rho(1700)^0$	$3.46 \pm 0.82 \pm 1.29 \pm 0.68$	$0.46 \pm 0.26 \pm 0.24 \pm 0.24$	$-74 \pm 14 \pm 21 \pm 14$
Total S-wave	$16.52 \pm 0.86 \pm 3.00 \pm 3.20$	$22.04 \pm 0.92 \pm 1.77 \pm 2.54$	$-21 \pm 26 \pm 5 \pm 55$

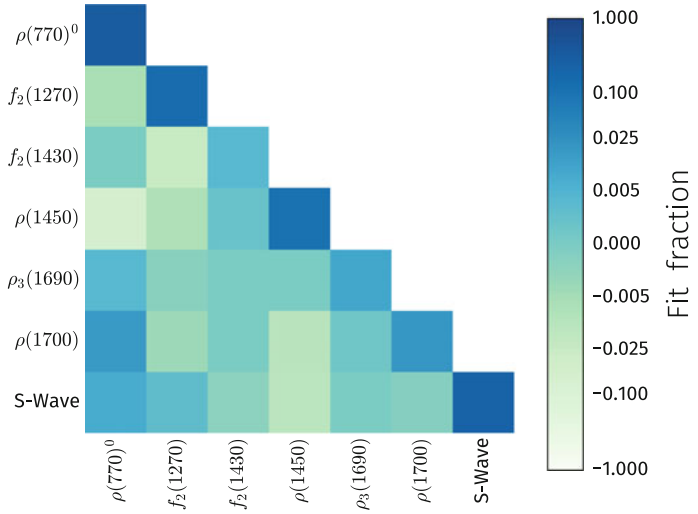

Fig. 7.40 Fit fractions (diagonal elements) and interference fit fractions (below diagonal elements) for the final model. The z-scale is linear in the range $[-0.005,\ 0.005]$

$$\mathrm{FF}_\omega = \mathrm{FF}_{\rho\omega} \int_{\mathrm{DP}} |A_\omega|^2 \Delta^2 |B|^2 \, dm_{13}^2 \, dm_{23}^2, \tag{7.12}$$

Table 7.23 *CP*-conserving fit-fractions and corresponding quasi-two-body product branching fractions for contributing resonances. Uncertainties are statistical, from the experimental procedure, from the amplitude model, and from the uncertainty on the total branching fraction of $B^+ \to \pi^+\pi^+\pi^-$, respectively

Resonance	FF (10^{-2})	BF (10^{-6})
$\rho(770)^0$	$60.89 \pm 0.91 \pm 1.65 \pm 2.28$	$9.26 \pm 0.14 \pm 0.25 \pm 0.35 \pm 0.85$
$\omega(782)$	$0.57 \pm 0.04 \pm 0.01 \pm 0.04$	$0.09 \pm 0.01 \pm 0.02 \pm 0.01 \pm 0.01$
$f_2(1270)$	$13.29 \pm 0.88 \pm 1.11 \pm 5.07$	$2.02 \pm 0.13 \pm 0.17 \pm 0.77 \pm 0.19$
$f_2(1430)$	$0.40 \pm 0.16 \pm 0.07 \pm 0.22$	$0.06 \pm 0.02 \pm 0.01 \pm 0.03 \pm 0.01$
$\rho(1450)^0$	$10.74 \pm 1.01 \pm 2.61 \pm 1.10$	$1.63 \pm 0.15 \pm 0.40 \pm 0.17 \pm 0.15$
$\rho_3(1690)^0$	$0.90 \pm 0.13 \pm 0.23 \pm 0.30$	$0.14 \pm 0.02 \pm 0.03 \pm 0.05 \pm 0.01$
$\rho(1700)^0$	$1.87 \pm 0.41 \pm 0.56 \pm 0.31$	$0.28 \pm 0.06 \pm 0.09 \pm 0.05 \pm 0.03$
S-wave	$19.44 \pm 0.61 \pm 2.76 \pm 2.33$	$2.95 \pm 0.09 \pm 0.42 \pm 0.35 \pm 0.27$

where $\mathrm{FF}_{\rho\omega}$ is the total $\rho-\omega$ mixing model fit fraction, and the integral is calculated across the full Dalitz-plot defined in terms of m^2_{13} and m^2_{23}.

7.9.1 Upper Limits

Upper limits are set on the contributions from $B^+ \to \chi_{c0}\pi^+$ and $B^+ \to \chi_{c2}\pi^+$ decays. A likelihood scan is performed over possible *CP*-conserving fit fractions and integrated from zero to 90 (95)% of the total to obtain a Bayesian credible limit, which can be seen in Fig. 7.41, where the light blue region indicates the 90% credible region and the sum of the light and dark blue regions indicates the 95% credible region.

The limits on the fit fractions correspond to limits on the quasi-two-body branching fractions of

$$\mathcal{B}(B^+ \to \chi_{c0}\pi^+) < 6.2\ (6.8) \times 10^{-6}, \tag{7.13}$$

$$\mathcal{B}(B^+ \to \chi_{c2}\pi^+) < 2.8\ (3.4) \times 10^{-6}, \tag{7.14}$$

at 90 (95)% confidence, where only statistical uncertainties are incorporated, and where values of $\mathcal{B}(\chi_{c0} \to \pi^+\pi^-) = (8.33 \pm 0.35) \times 10^{-3}$ and $\mathcal{B}(\chi_{c2} \to \pi^+\pi^-) = (2.33 \pm 0.12) \times 10^{-3}$ have been used [5]. These improve on the current upper-limits

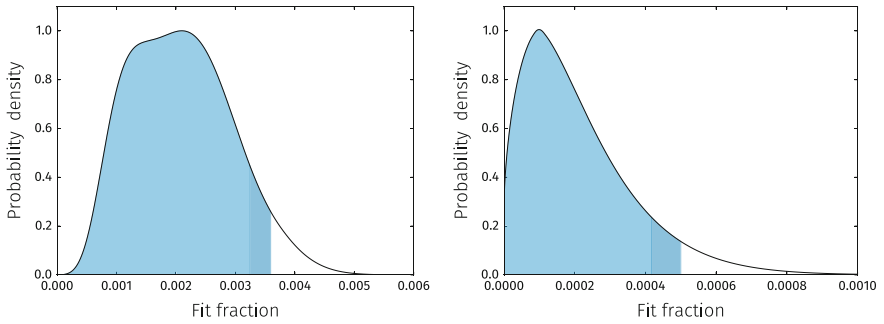

Fig. 7.41 Profile likelihood for the *CP*-conserving fit fraction of $B^+ \to \chi_{c0}\pi^+$ (left) and $B^+ \to \chi_{c2}\pi^+$ (right) decay contributions to the $B^+ \to \pi^+\pi^+\pi^-$ phase-space. The light blue regions indicate the 90% credible region and the sum of the light and dark blue regions indicate the 95% credible region

by factors of approximately two and seven, for the χ_{c0} and χ_{c2} decay limits respectively.

7.10 Discussion

The amplitude analysis of $B^+ \to \pi^+\pi^-\pi^-$ has uncovered several interesting features of the intermediate decay dynamics, in particular with their relation to the large *CP*-violation observed in the previous model-independent analysis.

$\rho(770)^0$

Some discrepancy between the $\rho(770)^0$ mass observed in data and the mass in the $\rho(770)^0$ model can be observed in Fig. 7.30. The mass used in the model is the world-average mass, and therefore it is likely that this is due to experimental effects, or imperfect modelling of the $\rho(770)^0$. Whilst the Gounaris–Sakurai parameterisation is an improvement over the relativistic Breit–Wigner, this model still does not take into account the effects of the higher mass $\rho(1450)^0$ and $\rho(1700)^0$ contributions, which can affect the model shape. Furthermore, it has been shown that unaccounted for P-wave rescattering contributions can affect the observed value of the $\rho(770)^0$ mass [35].

The striking feature of the $\rho(770)^0$ region is that the *CP*-asmmetry for the $\rho(770)^0$ (that is, the degree of *CP*-violation carried in the magnitude of the $\rho(770)^0$ component) is consistent with zero, within experimental precision. By inspecting the projections of $\cos\theta_{\text{hel}}$ (Fig. 7.34), one can see a large positive *CP*-asymmetry below the $\rho(770)^0$ pole, and a correspondingly large negative *CP*-asymmetry above the $\rho(770)^0$ pole, which is therefore a function of the evolution of the strong phase of the $\rho(770)^0$ resonance. This indicates that the *CP*-asymmetry in this region arises as a result of the interference between the $\rho(770)^0$ and the S-wave, and an effect similar to that proposed in Ref. [36] is observed.

$\rho_3(1690)^0$

Production of the $\rho_3(1690)^0$ has not previously been observed in a B-meson decay (and is the first observation of a spin-3 state in a B-meson decay to light hadrons). However, in this analysis it is found to be a necessary contribution to the amplitude.

Additionally, the existence of an intermediate $\rho_3(1690)^0$ contribution to the $B^+ \to \pi^+\pi^-\pi^-$ decay amplitude indicates that the same is plausible for $B^0 \to \pi^+\pi^-\pi^0$. This has a non-negligible effect on the Snyder–Quinn method of obtaining the CKM angle α using an amplitude analysis of this decay. Previous preliminary work on this by LHCb indicated that neglecting latent ρ contributions, specifically the higher spin $\rho_3(1690)^0$, results in a bias in the value of α obtained [68]. However, when a $\rho_3(1690)^0$ contribution *is* present in this amplitude, increased precision on α can be obtained due to the interference between the $\rho_3(1690)^0$ and the other ρ components.

S-Wave and the K-Matrix Model

This analysis indicates that the K-matrix model results in an excellent description of the S-wave contribution at low $\pi^+\pi^-$ invariant mass. The K-matrix approach does introduce a larger number of degrees-of-freedom than in an equivalent isobar model, but this is outweighed by the significant increase in fit quality. Ambiguities in the K-matrix formalism as applied to B decays, such as the Adler-zero term in the production vector, are disfavoured by the fit. The agreement of the K-matrix model with the S-wave observed in $B^+ \to \pi^+\pi^-\pi^-$ indicates that the structure of the S-wave observed in scattering experiments is similar to that in B-decays, and in particular no additional contributions corresponding to speculative states are observed.

Significant CP-violation is observed in the magnitude of the S-wave contribution at low $m(\pi^+\pi^-)$, the sign of which changes at around the $f_0(980)$ pole, possibly as a result of $\pi\pi \leftrightarrow KK$ rescattering [34]. No CP-violation is observed in the phase of the S-wave below the $f_0(980)$ pole, after which the phase motion diverges significantly, and remains different for B^+ and B^- decays throughout the $f_0(1370)$–$f_0(1500)$ region.

The K-matrix formalism depends on legacy scattering data, and whilst this data is unlikely to updated in the near future, contemporary advances in fitting methodologies and modelling of resonance components, in particular the $f_0(500)$, could improve the fit quality of this and similar methods. Furthermore, the successes of unitarity-conserving methods such as the K-matrix for S-wave states indicates that, in future updates to this analysis, unitarity-conserving models for higher spin contributions, notably the $\rho(770)^0$, $\rho(1450)^0$, and $\rho(1700)^0$, should be seriously considered.

7.10.1 Comparison with the Model-Independent Analysis

With the model presented here, it is possible to infer how the features in the CP-asymmetry plot in Fig. 7.2 arise, and a comparison between the model-independent result and the result of the model constructed in this analysis can be seen in Fig. 7.42.

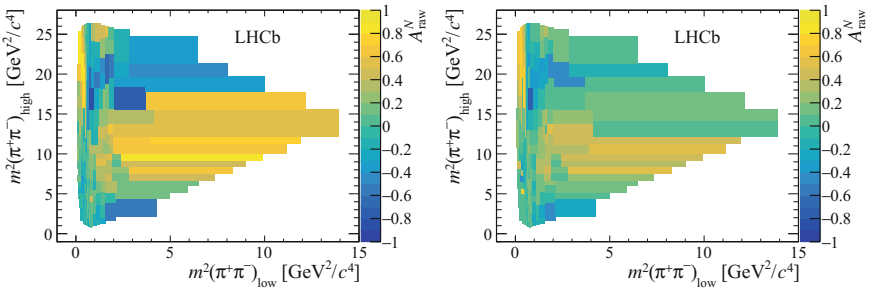

Fig. 7.42 Left: Binned raw *CP*-asymmetry from Ref. [26], where regions of large positive (yellow) and negative (blue) raw *CP*-asymmetry can be observed. Right: Binned *CP*-asymmetry from the model obtained in this analysis

The asymmetry below 1 GeV$^2/c^4$ in $m^2(\pi^+\pi^+)_{\text{low}}$, and the rapid change between positive and negative asymmetry in this region, is attributable to the interference between the $\rho(770)^0$ and S-wave. Between 1 and 2 GeV$^2/c^4$ in $m^2(\pi^+\pi^+)_{\text{low}}$, the large negative asymmetry is driven by the $f_2(1270)$ contribution, and the large negative asymmetry between 2 and 4 GeV$^2/c^4$ in $m^2(\pi^+\pi^+)_{\text{low}}$ is dominated by the *CP*-asymmetry in the $\rho_3(1690)^0$ contribution.

7.10.2 Comparison with Phenomenological Predictions

Comparison of the total amplitude model with theoretical calculations is not feasible, however numerous predictions have been made for the quasi-two-body $B^+ \to \rho\pi^+$ branching fractions and *CP*-asymmetries (where ρ in this case represents the $\rho(770)^0$, $\rho(1450)^0$, or $\rho(1700)^0$), which this dataset permits the most precise measurements of to-date. A comparison of the experimental values and theoretical predictions can be found in Table 7.24. Comparing branching fractions and *CP*-asymmetries neglects much of the nuance in the different approaches with regards to the evolution of the *CP*-asymmetry across the phase-space (and, in addition, some published after the BaBar analysis use this as input), however it is clear that some match the experimental data better than others. Those based on PQCD and SCET consistently predict a central value corresponding to a moderate negative *CP*-asymmetry for the $B^+ \to \rho(770)^0\pi^+$ decay, whereas the experimental measurements are small. The result obtained in Ref. [31], with a more careful use of the factorisation hypothesis (used in the PQCD and QCDF methods) and incorporation of interference with non-resonant contributions, results in a more realistic central value of the *CP*-asymmetry, but with uncertainties that result in it being inconsistent with the experimental results. Predictions involving the higher-mass ρ states from Ref. [69] are in good agreement, and predictions for the quasi-two-body branching fractions match the experimental results better than those of the *CP*-asymmetries, in general.

Table 7.24 Comparison of predicted and experimental product branching fractions and *CP*-asymmetries for $B^+ \to \rho(770)^0\pi^+$ (denoted ρ), $B^+ \to \rho(1450)^0\pi^+$ (denoted ρ'), and $B^+ \to \rho(1700)^0\pi^+$ (denoted ρ''). The techniques employed by the references listed are perturbative QCD (PQCD), QCD factorisation (QCDF), soft-collinear effective theory (SCET), and heavy meson chiral perturbation theory (ChPT) with the factorisation approximation. Superscripts denote two solutions found in the fits performed in Ref. [70], which have significantly different charm penguin contributions

Method	$\mathcal{B}(\rho)$ (10^{-6})	$\mathcal{A}_{CP}(\rho)$ (%)	$\mathcal{B}(\rho')$ (10^{-6})	$\mathcal{A}_{CP}(\rho')$ (%)	$\mathcal{B}(\rho'')$ (10^{-6})	$\mathcal{A}_{CP}(\rho'')$ (%)
This work	9.26 ± 0.96	-4 ± 4	1.63 ± 0.48	-32 ± 21	0.28 ± 0.12	-74 ± 28
BaBar [1]	$8.1^{+1.4}_{-1.8}$	18^{+9}_{-16}	$1.4^{+0.6}_{-0.9}$	-6^{+36}_{-49}	–	–
PQCD [30]	$8.84^{+1.91}_{-1.69}$	$-27.5^{+2.98}_{-3.66}$	–	–	–	–
PQCD [69]	–	–	$0.815^{+0.146}_{-0.132}$	-29^{+4}_{-3}	$0.281^{+0.063}_{-0.066}$	-35^{+4}_{-6}
QCDF [32]	$8.7^{+3.2}_{-1.9}$	$-9.8^{+11.9}_{-10.5}$	–	–	–	–
QCDF [71]	$11.9^{+7.8}_{-7.9}$	$4.1^{+19.2}_{-18.9}$	–	–	–	–
SCET^1 [70]	$10.7^{+1.2}_{-1.1}$	$-10.8^{+13.1}_{-12.7}$	–	–	–	–
SCET^2 [70]	$7.9^{+0.8}_{-0.8}$	$-19.2^{+15.6}_{-13.5}$	–	–	–	–
ChPT/Fact. [31]	$7.3^{+0.4}_{-0.4}$	$5.9^{+1.2}_{-1.0}$	–	–	–	–

7.11 Summary

An amplitude model of the charmless $B^+ \to \pi^+\pi^+\pi^-$ decay is constructed using 3 fb^{-1} of Run 1 LHCb data, allowing for *CP*-violation. The broad low-mass S-wave structures are modelled with the unitarity-conserving K-matrix model, and no additional spin-0 components are necessary to achieve a good fit to the data. The $\rho(770)^0$ and $\omega(782)$ are fitted with a model that combines the Gounaris–Sakurai model for the $\rho(770)^0$ and a relativistic Breit–Wigner model for the $\omega(782)$, and directly parameterises their relative magnitude and phase. The rest of the resonant contributions in the nominal model, the $f_2(1270)$, $f_2(1430)$, $\rho(1450)^0$, $\rho_3(1690)^0$, and $\rho(1700)^0$, are included as relativistic Breit–Wigner models of corresponding spin.

Isobar parameters are reported for all resonant contributions, for B^+ and B^-, and indicate *CP*-violation in the relative magnitudes and phases of various resonances, most notably the $f_2(1270)$ and $\rho_3(1690)^0$. The total branching fractions of the resonant contributions are reported, using the *CP*-averaged fit-fractions, and *CP*-asymmetries are calculated from the magnitude of the isobar parameters for each contribution. No evidence is seen for the $B^+ \to \chi_{c0}\pi^+$ and $B^+ \to \chi_{c2}\pi^+$ decays, and appropriate upper limits are set.

References

1. BaBar collaboration, B. Aubert et al., Dalitz plot analysis of $B^+ - > \pi^+\pi^+\pi^-$ Decays. Phys. Rev. **D79**, 072006 (2009). https://doi.org/10.1103/PhysRevD.79.072006, arXiv:0902.2051
2. A.E. Snyder, H.R. Quinn, Measuring CP asymmetry in $B \to \rho\,\pi$ decays without ambiguities. Phys. Rev. D **48**, 2139 (1993)
3. R.E. Blanco, C. Gobel, R. Mendez-Galain, Measuring the CP violating phase gamma using $B^+ - > \pi^+\pi^+\pi^-$ and $B^+ - > K^+\pi^+\pi^-$ decays. Phys. Rev. Lett. **86**, 2720 (2001). https://doi.org/10.1103/PhysRevLett.86.2720. arXiv:hep-ph/0007105
4. D. Xu, G.-N. Li, X.-G. He, Large SU(3) breaking effects and CP violation in B^+ decays into three charged octet pseudoscalar mesons. Int. J. Mod. Phys. A **29**, 1450011 (2014). https://doi.org/10.1142/S0217751X14500110. arXiv:1307.7186
5. Particle Data Group, C. Patrignani et al., Review of particle physics. Chin. Phys. **C40**, 100001 (2016). https://doi.org/10.1088/1674-1137/40/10/100001, http://pdg.lbl.gov/. 2017 update
6. LHCb collaboration, Measurement of the CKM angle γ from a combination of $B \to DK$ analyses. http://cdsweb.cern.ch/search?p=LHCb-CONF-2017-004&f=reportnumber&action_search=Search&c=LHCb+Conference+ContributionsLHCb-CONF-2017-004
7. LHCb collaboration, R. Aaij et al., Measurement of the CKM angle γ from a combination of LHCb results. JHEP **12**, 087 (2016). https://doi.org/10.1007/JHEP12(2016)087, arXiv:1611.03076
8. Y. Amhis et al., Averages of b-hadron, c-hadron, and τ-lepton properties as of summer 2016. arXiv:1612.07233
9. J. Charles et al., Current status of the standard model CKM fit and constraints on $\Delta F = 2$ new physics. Phys. Rev. **D91**(7), 073007 (2015). https://doi.org/10.1103/PhysRevD.91.073007, arXiv:1501.05013
10. K. Lingel, T. Skwarnicki, J.G. Smith, Penguin decays of B mesons. Ann. Rev. Nucl. Part. Sci. **48**, 253 (1998). https://doi.org/10.1146/annurev.nucl.48.1.253. arXiv:hep-ex/9804015
11. LHCb collaboration, R. Aaij et al., Determination of γ and $-2\beta_s$ from charmless two-body decays of beauty mesons. Phys. Lett. **B739**(1) (2015). https://doi.org/10.1016/j.physletb.2014.12.015, arXiv:1408.4368
12. BaBar collaboration, J.P. Lees et al., Amplitude analysis of $B^0 \to K^+\pi^-\pi^0$ and evidence of direct CP violation in $B \to K^*\pi$ decays. Phys. Rev. **D83**, 112010 (2011). https://doi.org/10.1103/PhysRevD.83.112010, arXiv:1105.0125
13. M. Ciuchini, M. Pierini, L. Silvestrini, New bounds on the CKM matrix from $B \to K\pi\pi$ Dalitz plot analyses. Phys. Rev. D **74**, 051301 (2006). https://doi.org/10.1103/PhysRevD.74.051301. arXiv:hep-ph/0601233
14. M. Gronau, D. Pirjol, A. Soni, J. Zupan, Improved method for CKM constraints in charmless three-body B and B(s) decays. Phys. Rev. D **75**, 014002 (2007). https://doi.org/10.1103/PhysRevD.75.014002. arXiv:hep-ph/0608243
15. G. Eilam, M. Gronau, R.R. Mendel, Large CP asymmetries in $B^+ - > \eta_{(c)}(\chi_{c0})\pi^+$ from $\eta_{(c)}(\chi_{c0})$ width. Phys. Rev. Lett. **74**, 4984 (1995). https://doi.org/10.1103/PhysRevLett.74.4984. arXiv:hep-ph/9502293
16. N.G. Deshpande, G. Eilam, X.-G. He, J. Trampetic, The nonresonant Cabibbo suppressed decay $B^+ - > \pi^+\pi^+\pi^-$ and signal for CP violation. Phys. Rev. D **52**, 5354 (1995). https://doi.org/10.1103/PhysRevD.52.5354. arXiv:hep-ph/9503273
17. I. Bediaga, R.E. Blanco, C. Gobel, R. Mendez-Galain, A Direct measurement of the CKM angle gamma. Phys. Rev. Lett. **81**, 4067 (1998). https://doi.org/10.1103/PhysRevLett.81.4067. arXiv:hep-ph/9804222
18. P.F. Harrison, H.R. Quinn, *The Babar Physics Book: Physics at an Asymmetric B Factory* (SLAC report, Stanford Linear Acceleration Center, 1998)
19. Y. Nir, H.R. Quinn, Learning about the Cabibbo-Kobayashi-Maskawa matrix from *CP* asymmetries in B^0 decays. Phys. Rev. D **42**, 1473 (1990)

20. Y. Grossman, H.R. Quinn, Removing discrete ambiguities in *CP* asymmetry measurements. Phys. Rev. D **56**, 7259 (1997). https://doi.org/10.1103/PhysRevD.56.7259. arXiv:hep-ph/9705356
21. J. Tandean, S. Gardner, Nonresonant contributions in $B^0 \to \rho\pi$ decay. Phys. Rev. D **66**, 034019 (2002). https://doi.org/10.1103/PhysRevD.66.034019. arXiv:hep-ph/0204147
22. O.M.A. Leitner, X.-H. Guo, A.W. Thomas, Direct CP violation in $B^+ - > \pi^+\pi^+\pi^-$: Determination of alpha without discrete ambiguity. Eur. Phys. J. C **31**, 215 (2003). https://doi.org/10.1140/epjc/s2003-01332-0. arXiv:hep-ph/0211003
23. BaBar collaboration, B. Aubert et al., Evidence for Direct CP Violation from Dalitz-plot analysis of $B^\pm \to K^\pm\pi^\mp\pi^\pm$. Phys. Rev. **D78**, 012004 (2008). https://doi.org/10.1103/PhysRevD.78.012004, arXiv:0803.4451
24. A. Belle, Garmash et al., Evidence for large direct CP violation in $B^+ - > \rho(770)^0 K^+$ from analysis of the three-body charmless $B^+ - > \pi^+\pi^+\pi^-$. Phys. Rev. Lett. **96**, 251803 (2006). https://doi.org/10.1103/PhysRevLett.96.251803, arXiv:hep-ex/0512066
25. BaBar collaboration, J.P. Lees et al., Study of CP violation in Dalitz-plot analyses of $B^+ - > K^+K^-K_s^0$, $B^+ - > K^+K^+K^-$, and $B^+ - > K_s^0 K_s^0 K^+$. Phys. Rev. **D85**, 112010 (2012). https://doi.org/10.1103/PhysRevD.85.112010, arXiv:1201.5897
26. LHCb collaboration, R. Aaij et al., Measurement of CP violation in the three-body phase space of charmless $B^\pm$ decays. Phys. Rev. **D90**, 112004 (2014). https://doi.org/10.1103/PhysRevD.90.112004, arXiv:1408.5373
27. X.-H. Guo, O.M.A. Leitner, A.W. Thomas, Enhanced direct CP violation in $B^+ - > \rho\pi^+$. Phys. Rev. D **63**, 056012 (2001). https://doi.org/10.1103/PhysRevD.63.056012. arXiv:hep-ph/0009042
28. G. Lü et al., CP violation for $B \to \rho^0(\omega)V \to \pi^+\pi^-V$ in QCD factorization. Phys. Rev. D **90**, 034014 (2014). https://doi.org/10.1103/PhysRevD.90.034014
29. C. Wang, Z.-H. Zhang, Z.-Y. Wang, X.-H. Guo, Localized direct CP violation in $B^\pm \to \rho^0(\omega)\pi^\pm \to \pi^+\pi^-\pi^\pm$. Eur. Phys. J. C **75**, 536 (2015). https://doi.org/10.1140/epjc/s10052-015-3757-2. arXiv:1506.00324
30. Y. Li, A.-J. Ma, Z.-J. Xiao, W.-F. Wang, Quasi-two-body decays $B_{(s)} \to P\rho \to P\pi\pi$ in perturbative QCD approach. arXiv:1612.05934
31. H.-Y. Cheng, C.-K. Chua, Z.-Q. Zhang, Direct CP violation in charmless three-body decays of B mesons. Phys. Rev. D **94**, 094015 (2016). https://doi.org/10.1103/PhysRevD.94.094015. arXiv:1607.08313
32. H.-Y. Cheng, C.-K. Chua, Revisiting charmless hadronic $B(u, d)$ decays in QCD factorization. Phys. Rev. D **80**, 114008 (2009). https://doi.org/10.1103/PhysRevD.80.114008. arXiv:0909.5229
33. H.-Y. Cheng, C.-K. Chua, A. Soni, Final state interactions in hadronic b decays (2005).https://doi.org/10.1103/PhysRevD.71.014030/Phys.Rev.D71014030
34. J.H. Alvarenga, Nogueira et al., CP violation: Dalitz interference, CPT, and final state interactions. Phys. Rev. D **92**, 054010 (2015). https://doi.org/10.1103/PhysRevD.92.054010. arXiv:1506.08332
35. I. Bediaga, P.C. Magalhães, Final state interaction on $B^+ \to \pi^-\pi^+\pi^+$. arXiv:1512.09284
36. B. Bhattacharya, M. Gronau, J.L. Rosner, CP asymmetries in three-body $B^\pm$ decays to charged pions and kaons. Phys. Lett. B **726**, 337 (2013). https://doi.org/10.1016/j.physletb.2013.08.062. arXiv:1306.2625
37. H.-Y. Cheng, C.-K. Chua, Branching fractions and direct CP violation in charmless three-body decays of B mesons. Phys. Rev. D **88**, 114014 (2013). https://doi.org/10.1103/PhysRevD.88.114014. arXiv:1308.5139
38. S. Kränkl, T. Mannel, J. Virto, Three-body non-leptonic B decays and QCD factorization. Nucl. Phys. B **899**, 247 (2015). https://doi.org/10.1016/j.nuclphysb.2015.08.004. arXiv:1505.04111
39. R. Klein, T. Mannel, J. Virto, K.K. Vos, CP violation in multibody B decays from QCD factorization. arXiv:1708.02047
40. S. Cheng, A. Khodjamirian, J. Virto, $B \to \pi\pi$ Form factors from light-cone sum rules with B-meson distribution amplitudes. arXiv:1701.01633

41. S. Cheng, A. Khodjamirian, J. Virto, Timelike-helicity $B \to \pi\pi$ form factor from light-cone sum rules with dipion distribution amplitudes. arXiv:1709.00173
42. B. Bhattacharya et al., Charmless B→PPP decays: The fully-symmetric final state. Phys. Rev. D **89**, 074043 (2014). https://doi.org/10.1103/PhysRevD.89.074043. arXiv:1402.2909
43. X.-G. He, G.-N. Li, D. Xu, SU(3) and isospin breaking effects on $B \to PPP$ amplitudes. Phys. Rev. D **91**, 014029 (2015). https://doi.org/10.1103/PhysRevD.91.014029. arXiv:1410.0476
44. D. Xu, G.-N. Li, X.-G. He, U-spin analysis of CP violation in B^- decays into three charged light pseudoscalar mesons. Phys. Lett. B **728**, 579 (2014). https://doi.org/10.1016/j.physletb.2013.12.040. arXiv:1311.3714
45. J.R. Pelaez, From controversy to precision on the sigma meson: a review on the status of the non-ordinary $f_0(500)$ resonance. Phys. Rept. **658**, 1 (2016). https://doi.org/10.1016/j.physrep.2016.09.001, arXiv:1510.00653
46. W. Ochs, The Status of Glueballs. J. Phys. **G40**, 043001 (2013). https://doi.org/10.1088/0954-3899/40/4/043001. arXiv:1301.5183
47. LHCb collaboration, R. Aaij et al., Analysis of the resonant components in $B^{\overline{0}} \to J/\psi\pi^+\pi^-$. Phys. Rev. **D87**, 052001 (2013). https://doi.org/10.1103/PhysRevD.87.052001, arXiv:1301.5347
48. LHCb collaboration, R. Aaij et al., Dalitz plot analysis of $B^0 \to D^{\overline{0}}\pi^+\pi^-$ decays. Phys. Rev. **D92**, 032002 (2015). https://doi.org/10.1103/PhysRevD.92.032002, arXiv:1505.01710
49. J.-P. Dedonder et al., S-, P- and D-wave final state interactions and CP violation in $B^+ -> \pi^+\pi^+\pi^-$. Acta Phys. Polon. B **42**, 2013 (2011). https://doi.org/10.5506/APhysPolB.42.2013. arXiv:1011.0960
50. Z.-H. Zhang, X.-H. Guo, Y.-D. Yang, CP violation in $B^\pm \to \pi^\pm\pi^+\pi^-$ in the region with low invariant mass of one $\pi^+\pi^-$ pair. Phys. Rev. D **87**, 076007 (2013). https://doi.org/10.1103/PhysRevD.87.076007. arXiv:1303.3676
51. A. Puig, The LHCb trigger in 2011 and 2012, LHCb-PUB-2014-046. http://cdsweb.cern.ch/search?p=LHCb-PUB-2014-046&f=reportnumber&action_search=Search&c=LHCb+Reports
52. LHCb collaboration, R. Aaij et al., Precision measurement of D meson mass differences. JHEP **06**, 065 (2013). https://doi.org/10.1007/JHEP06(2013)065, arXiv:1304.6865
53. P. Koppenburg, Statistical biases in measurements with multiple candidates. arXiv:1703.01128
54. A. Rogozhnikov, Reweighting with boosted decision trees (2015). http://arogozhnikov.github.io/2015/10/09/gradient-boosted-reweighter.html
55. T. Chen, C. Guestrin, XGBoost: A scalable tree boosting system, CoRR (2016). arxiv:1603.02754
56. T. Likhomanenko et al., Reproducible experiment platform. J. Phys. Conf. Ser. **664**, 052022 (2015). https://doi.org/10.1088/1742-6596/664/5/052022, arXiv:1510.00624
57. T. Gershon, T. Latham, R. Silva Coutinho, Selection optimisation for Dalitz-plot analyses. http://cdsweb.cern.ch/search?p=LHCb-INT-2015-003&f=reportnumber&action_search=Search&c=LHCb+Internal+NotesLHCb-INT-2015-003
58. G.A. Cowan, D.C. Craik, M.D. Needham, RapidSim: an application for the fast simulation of heavy-quark hadron decays. Comput. Phys. Commun. **C214**, 239 (2017). https://doi.org/10.1016/j.cpc.2017.01.029, arXiv:1612.07489
59. LHCb collaboration, R. Aaij et al., Measurement of b hadron production fractions in 7 TeV pp collisions. Phys. Rev. **D85**, 032008 (2012). https://doi.org/10.1103/PhysRevD.85.032008, arXiv:1111.2357
60. LHCb collaboration, Updated average f_s/f_d b-hadron production fraction ratio for 7 TeV pp collisions. http://cdsweb.cern.ch/search?p=LHCb-CONF-2013-011&f=reportnumber&action_search=Search&c=LHCb+Conference+ContributionsLHCb-CONF-2013-011
61. LHCb collaboration, R. Aaij et al., Observation of the $B^0 \to \rho^0\rho^0$ decay from an amplitude analysis of $B^0 -> (\pi^+\pi^-)(\pi^+\pi^-)$ decays. Phys. Lett. **B747**, 468 (2015). https://doi.org/10.1016/j.physletb.2015.06.027, arXiv:1503.07770
62. H. Albrecht et al., Measurement of $\eta' -> \pi^+\pi^-\gamma$ *in* $\gamma\gamma$ collisions. Phys. Lett. B **199** (1987). https://doi.org/10.1016/0370-2693(87)90953-1

63. T. Latham, The Laura++ Dalitz plot fitter. AIP Conf. Proc. **1735** , 070001 (2016). https://doi.org/10.1063/1.4949449, arXiv:1603.00752
64. H. Akaike, A new look at the statistical model identification. IEEE Trans. Autom. Control **19**, 716 (1974)
65. B. Guegan, J. Hardin, J. Stevens, M. Williams, Model selection for amplitude analysis. JINST **10**, P09002 (2015). https://doi.org/10.1088/1748-0221/10/09/P09002. arXiv:1505.05133
66. P. d'Argent et al., Amplitude analyses of $D^0 \to \pi^+\pi^-\pi^+\pi^-$ and $D^0 \to K^+K^-\pi^+\pi^-$ decays. arXiv:1703.08505
67. LHCb collaboration, R. Aaij et al., Measurement of the $B^\pm$ production asymmetry and the CP asymmetry in $B^\pm \to J/\psi K^\pm$ decays. Phys. Rev. **D95**, 052005 (2017). https://doi.org/10.1103/PhysRevD.95.052005, arXiv:1701.05501
68. O. Deschamps, P. Perret, A. Robert, The sensitivity on α of LHCb using a time dependent Dalitz plot analysis of the $B_d \to 3\pi$ channel. http://cdsweb.cern.ch/search?p=LHCb-2005-024.CERN-LHCb-2005-024&f=reportnumber&action_search=Search&c=LHCb+ReportsLHCb-2005-024.CERN-LHCb-2005-024
69. Y. Li, A.-J. Ma, W.-F. Wang, Z.-J. Xiao, Quasi-two-body decays $B_{(s)} \to P\rho'(1450)$, $P\rho''(1700) \to P\pi\pi$ in the perturbative QCD approach. arXiv:1704.07566
70. W. Wang, Y.-M. Wang, D.-S. Yang, C.-D. Lu, Charmless two-body $B(B_s) \to VP$ decays in soft-collinear-effective-theory. Phys. Rev. D **78**, 034011 (2008). https://doi.org/10.1103/PhysRevD.78.034011. arXiv:0801.3123
71. M. Beneke, M. Neubert, QCD factorization for $B \to PP$ and $B \to PV$ decays. Nucl. Phys. B **675**, 333 (2003). https://doi.org/10.1016/j.nuclphysb.2003.09.026. arXiv:hep-ph/0308039

Chapter 8
Summary

This thesis documents studies of CP-violation in charmless three-body b-hadron decays, using data corresponding to 3fb^{-1} of luminosity from Run 1 of the LHCb experiment at the Large Hadron Collider. These studies are performed following a search for previously unobserved suppressed b-baryon decays, and by constructing an amplitude model of the $B^+ \to \pi^+\pi^+\pi^-$ decay.

Searches for previously unobserved Λ_b^0 and Ξ_b-baryon decays to a Λ-baryon and two charged light-hadrons are performed, in an effort to investigate CP-violation in the baryon sector, provide information on hadronisation in b-baryon decays, and identify decay modes suitable for future amplitude analyses. The decays of $\Lambda_b^0 \to \Lambda K^+\pi^-$ and $\Lambda_b^0 \to \Lambda K^+K^-$ are observed, with absolute branching fractions of

$$\mathcal{B}(\Lambda_b^0 \to \Lambda\, K^+\pi^-) = (5.6 \pm 0.8 \pm 0.8 \pm 0.7) \times 10^{-6}\,,$$
$$\mathcal{B}(\Lambda_b^0 \to \Lambda\, K^+K^-) = (15.9 \pm 1.2 \pm 1.2 \pm 2.0) \times 10^{-6}\,,$$

where uncertainties are statistical, systematic, and from the uncertainty on the normalisation branching fraction, respectively. Upper limits are set on all other decay modes. The phase-space integrated CP-asymmetries of these decays are also measured, and found to be

$$\mathcal{A}_{CP}(\Lambda_b^0 \to \Lambda K^+\pi^-) = -0.53 \pm 0.23 \pm 0.11\,,$$
$$\mathcal{A}_{CP}(\Lambda_b^0 \to \Lambda K^+K^-) = -0.28 \pm 0.10 \pm 0.07\,,$$

where uncertainties are statistical and systematic, respectively.

These correspond to the first observations of these decay modes, in addition to some of the first measurements of CP-violation in a charmless three-body b-baryon decay. These measurements have a significant statistical component to their overall uncertainty, and therefore future updates using Run 2 data (of which an additional $2.6\,\text{fb}^{-1}$ has already been collected) will result in increased precision.

© Springer Nature Switzerland AG 2018

D. O'Hanlon, *Studies of* CP-*Violation in Charmless Three-Body* b-*Hadron Decays*,
Springer Theses, https://doi.org/10.1007/978-3-030-02206-8_8

An amplitude analysis of the $B^+ \to \pi^+\pi^+\pi^-$ decay mode is also performed, where significant CP-violation in specific regions of the three-body phase space was observed previously. An amplitude model is constructed using the unitarity-conserving K-matrix model to describe the S-wave component of the amplitude, a dedicated mixing model for the $\rho(770)^0$ and $\omega(782)$ contributions, and conventional relativistic Breit–Wigner models for the higher-spin resonances present in the decay. Contributions from numerous intermediate resonances are observed, and the total branching fractions involving resonances with known branching fractions to $\pi^+\pi^-$ are found to be

$$\begin{aligned}
\mathcal{B}(B^+ \to \rho(770)^0\pi^+) &= (9.26 \pm 0.14 \pm 0.25 \pm 0.92) \times 10^{-6}, \\
\mathcal{B}(B^+ \to \omega(782)\pi^+) &= \left(5.66 \pm 0.40 \pm 0.10 \pm 0.40^{+0.70}_{-0.66}\right) \times 10^{-6}, \\
\mathcal{B}(B^+ \to f_2(1270)\pi^+) &= \left(3.60 \pm 0.24 \pm 0.30 \pm 1.37^{+0.33}_{-0.35}\right) \times 10^{-6}, \\
\mathcal{B}(B^+ \to \rho_3(1690)^0\pi^+) &= (0.87 \pm 0.13 \pm 0.22 \pm 0.29 \pm 0.10) \times 10^{-6},
\end{aligned}$$

where in each case, the uncertainties are statistical, from the experimental procedure, from the amplitude model, and from the uncertainty on the resonance and $B^+ \to \pi^+\pi^+\pi^-$ branching fractions, respectively.

Furthermore, CP-violation is permitted for each component in the model, and the most significant quasi-two-body CP-asymmetries are found to be

$$\begin{aligned}
\mathcal{A}_{CP}(B^+ \to f_2(1270)\pi^+) &= (50 \pm 6 \pm 1 \pm \ \ 9)\%, \\
\mathcal{A}_{CP}(B^+ \to \rho_3(1690)^0\pi^+) &= (-68 \pm 11 \pm 8 \pm 15)\%,
\end{aligned}$$

where uncertainties are statistical, from the experimental procedure, and from the amplitude model, respectively. These results are consistent with, and more precise than, the previous BaBar analysis of this decay [1].

When investigating the evolution of the S-wave amplitude across the Dalitz plot, significant CP-violation is also observed in the relative phase between the B^+ and B^- components. Asymmetry in the $\rho(770)^0$ region also confirms that the behaviour of the S-wave in this decay is a key ingredient in the observed pattern of CP-violation.

Reference

1. BaBar collaboration, B. Aubert et al., Dalitz plot analysis of $B^0_s \to \bar{D}^0 K^-\pi^+$ decays. Phys. Rev. **D79**, 072006 (2009). https://doi.org/10.1103/PhysRevD.79.072006. arXiv:0902.2051

Appendix A
$B^+ \to \pi^+\pi^+\pi^-$ Combinatorial Background Model

In the analysis described in Chap. 7, a Gaussian process model is used to describe the combinatorial background. A Gaussian process is a statistical model where each point in a space is associated with a normally distributed random variable. This implies that any linear combination of model estimates is also a Gaussian, yielding a closed form expression for the model at an arbitrary point in the input space. Fortunately, to avoid having to fit an infinite number of Gaussian functions, Gaussian processes can be completely determined by the functional form of their covariance matrix. As such, it is possible to obtain model estimates in a large number of dimensions with relatively few parameters (those defining the form of the covariance function), and using these extrapolate the behaviour of the model with reliable estimates of the uncertainty. Furthermore, these parameters can easily be extracted directly from the data, which gives Gaussian processes an advantage over other non-parametric models, such as kernel density estimates and piecewise spline interpolation.

In a Gaussian process fit, parameters are extracted that describe the functional form of the covariance between two arbitrary points. One such function is the squared-exponential,

$$k(x_i, x_j) = \sigma_f^2 \exp\left(-\frac{(x_j - x_i)^2}{2l^2}\right), \tag{A.1}$$

where σ_f and l are *hyper*parameters that determine the absolute magnitude of the covariance, and scale in x over which points co-vary, respectively. The Gaussian process for a vector of outputs y is then defined as

$$y \sim \mathcal{N}(0, K), \tag{A.2}$$

where the covariance matrix,

$$K = \begin{bmatrix} k(x_0, x_0) & k(x_1, x_0) & \dots & k(x_n, x_0) \\ k(x_0, x_1) & k(x_1, x_1) & \dots & k(x_1, x_n) \\ \vdots & \vdots & \ddots & \vdots \\ k(x_0, x_n) & k(x_1, x_n) & \dots & k(x_n, x_n) \end{bmatrix}, \tag{A.3}$$

© Springer Nature Switzerland AG 2018

D. O'Hanlon, *Studies of* CP-*Violation in Charmless Three-Body* b-*Hadron Decays*,
Springer Theses, https://doi.org/10.1007/978-3-030-02206-8

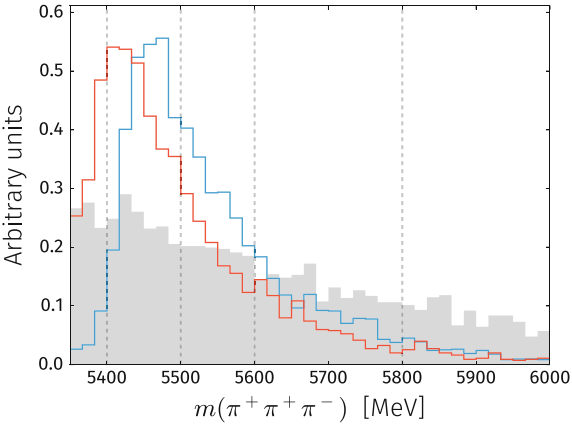

Fig. A.1 Distribution in $m(\pi^+\pi^+\pi^-)$ of the uncorrected collision data (grey shaded histogram), and simulated $B^0 \to \pi^+\pi^-$ (blue histogram) and $B^0 \to K^+\pi^-$ (orange histogram) decays, where a charged pion is taken from the rest of the event. Bin boundaries used in the analysis are indicated with dashed grey lines

is given between each entry in the vector of inputs, x, using the covariance function, k, defined above. The conditional probability of a new output, (with true value y_*), at a new input, x_*, given the previously observed data, y, is a Gaussian distribution,

$$P(y_*|y) \sim \mathcal{N}(K_* K^{-1} y,\ K_{**} - K_* K^{-1} K_*^T), \tag{A.4}$$

where $K_* = [k(x_*, x_0), k(x_*, x_1), \cdots, k(x_*, x_n)]$, and $K_{**} = k(x_*, x_*)$. The best estimate for y is the mean of this distribution,

$$\hat{y}_* = K_* K^{-1} y, \tag{A.5}$$

and the uncertainty is the square-root of the variance,

$$\mathrm{Var}(y_*) = K_{**} - K_* K^{-1} K_*^T. \tag{A.6}$$

The log-likelihood for this construction, can then be used to determine the hyper-parameters, $\theta = [\sigma_f, l]$,

$$\log p(y|x, \theta) = -\frac{1}{2} y^T K^{-1} y - \frac{1}{2} \log |K| - \frac{n}{2} \log 2\pi. \tag{A.7}$$

The hyperparameters can then be inferred by maximising the likelihood, or obtained via marginalisation using suitable priors and Markov-chain Monte-Carlo.

A.1 Use in the $B^+ \to \pi^+\pi^+\pi^-$ Analysis

It is observed that the Dalitz-plot background distribution above the B^+ mass, after the full selection is applied, varies as a function of $m(B^+)$, and therefore this is unlikely to reliably describe the background in the signal region. It is assumed that the

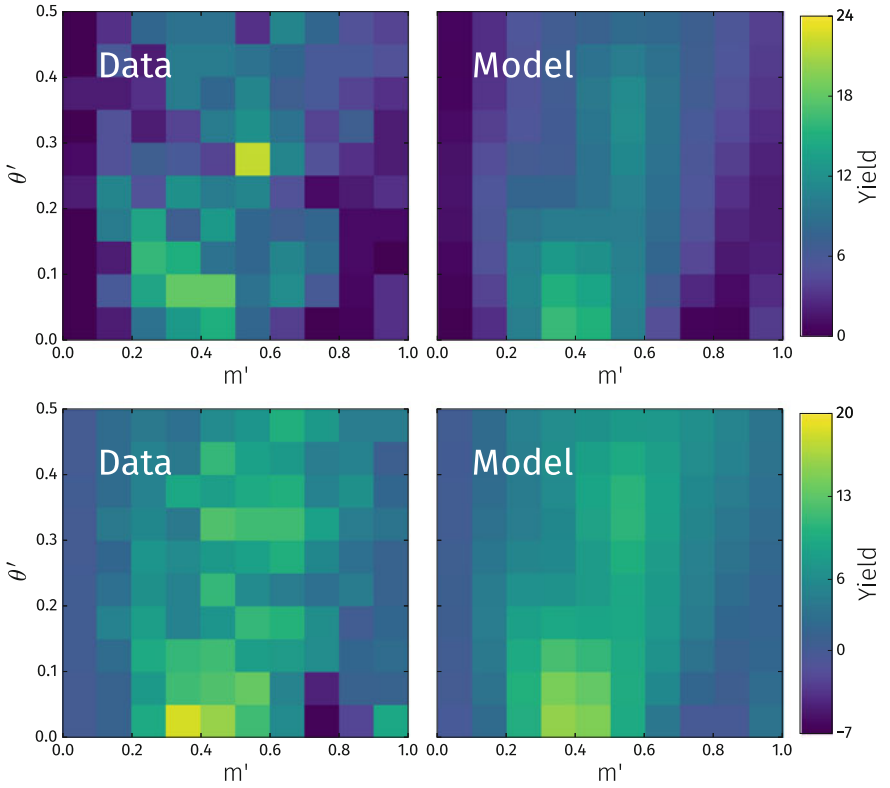

Fig. A.2 Corrected data (left) and model (right) square Dalitz-plot distributions for the mass bin [5350, 5400] MeV (top) and [5400, 5500] MeV (bottom)

region closest to the true B^+ mass best represents the background in the signal region, however due to the tight requirements on the BDT classifier this region contains few events. To reduce the statistical uncertainty on the background distribution, a Gaussian process is used to parameterise the combinatorial background yield as a function of the reconstructed B^+ mass and the two square Dalitz-plot variables. This model is then extrapolated into the signal region to form the background model that enters the Dalitz-plot fit.

The sideband of the fully selected collision data in the region [5350, 6000] MeV is split into five bins, with boundaries corresponding to [5350, 5400, 5500, 5600, 5800, 6000] MeV. The events in these bins in mass are further binned in the square Dalitz-plot, with 10 uniform bins in each of m' and θ' (with ranges of [0, 1] and [0, 0.5], respectively). Similar is done for simulated $B^0 \to \pi^+\pi^-$ and $B^0 \to K^+\pi^-$ decay data, and the expected yield of these events in each bin subtracted from that of the collision data histogram, using the yield extracted from the fit to the unconstrained $m(\pi^+\pi^-)_{\text{high}}$ distribution described in Sect. 7.4.4. Normalised distributions of these components in $m(\pi^+\pi^+\pi^-)$ can be seen in Fig. A.1.

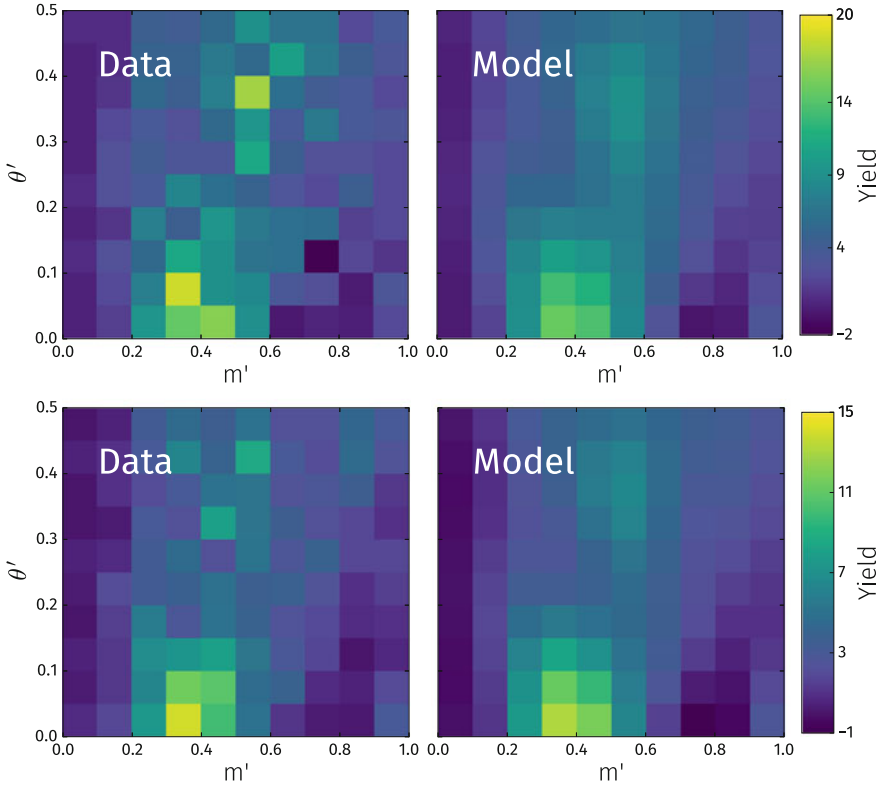

Fig. A.3 Corrected data (left) and model (right) square Dalitz-plot distributions for the mass bin [5500, 5600] MeV (top) and [5600, 5800] MeV (bottom)

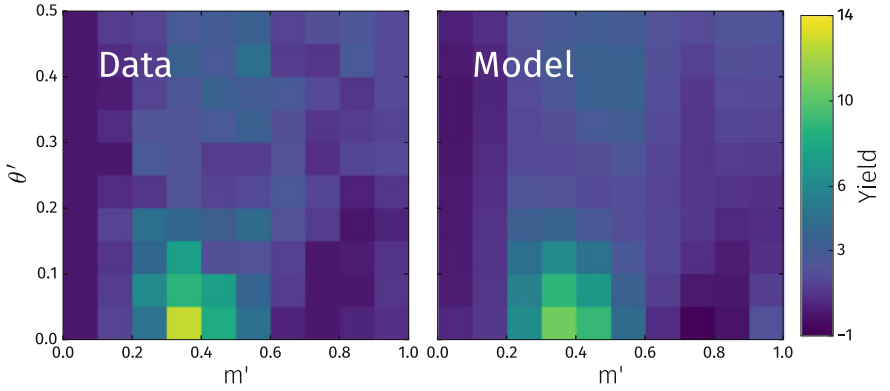

Fig. A.4 Corrected data (left) and model (right) square Dalitz-plot distributions for the mass bin [5800, 6000] MeV

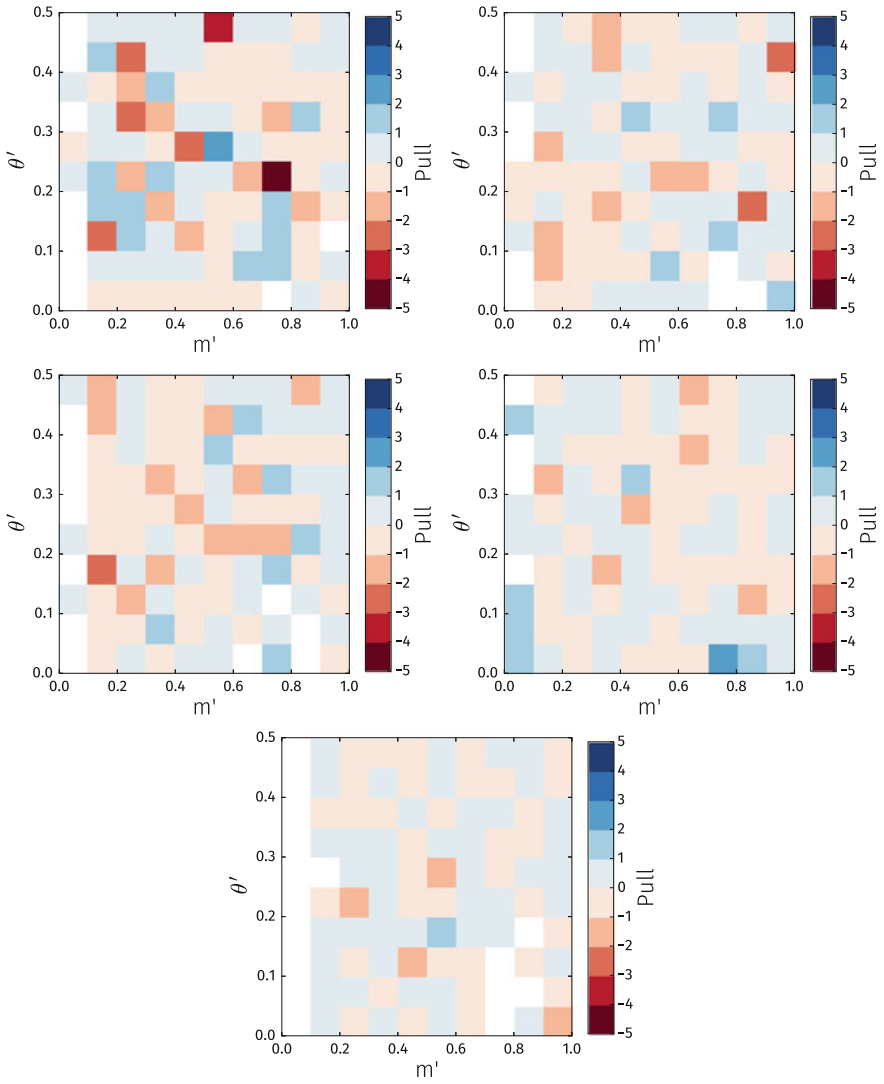

Fig. A.5 Pull distributions for the square Dalitz-plots in mass bins [5350, 5400] (top left), [5400, 5500] (top right), [5500, 5600] (mid left),[5600, 5800] (mid right), [5800, 5600] (bottom)

The corrected background distribution is then fitted with a three-dimensional Gaussian process, with a squared-exponential covariance function, using the GPy package [1]. The square Dalitz-plots for the background data and the Gaussian process model in bins of $m(\pi^+\pi^+\pi^-)$ can be seen in Figs. A.2, A.3 and A.4. Here, negative yields in some bins are caused by mismodelling of the $B^0 \to \pi^+\pi^-$ and $B^0 \to K^+\pi^-$ decay mass distributions in MC. Pull distributions that correspond to

each of these can be found in Fig. A.5, and the resulting background model, evaluated at $m(\pi^+\pi^+\pi^-) = 5279\,\text{MeV}$ can be seen in Fig. 7.12.

Reference

1. GPy, GPy: A Gaussian process framework in python, http://github.com/SheffieldML/GPy (since 2012)

Appendix B
Isobar Parameters

This appendix contains further information relating to results obtained for the isobar parameters fitted in the analysis of $B^+ \to \pi^+\pi^+\pi^-$ described in Chap. 7.

B.1 Argand Plots

The complex isobar parameters can be displayed in terms of the magnitude and phase relative to the reference $\rho(770)^0$ component, for the B^+ and B^- amplitudes. These can be found in Figs. B.1, B.2, B.3 and B.4, with 68% confidence intervals. *CP*-violation is indicated by a difference in the magnitudes between the B^+ and B^- coefficient, and/or in a difference between the phases (both displayed here relative to the $\rho(770)^0$ component). As the *CP*-asymmetry corresponds only to the difference in the magnitudes of the B^+ and B^- decay contributions, these figures contain additional information regarding *CP*-violation in the relative phases.

© Springer Nature Switzerland AG 2018

D. O'Hanlon, *Studies of* CP-*Violation in Charmless Three-Body* b-*Hadron Decays*,
Springer Theses, https://doi.org/10.1007/978-3-030-02206-8

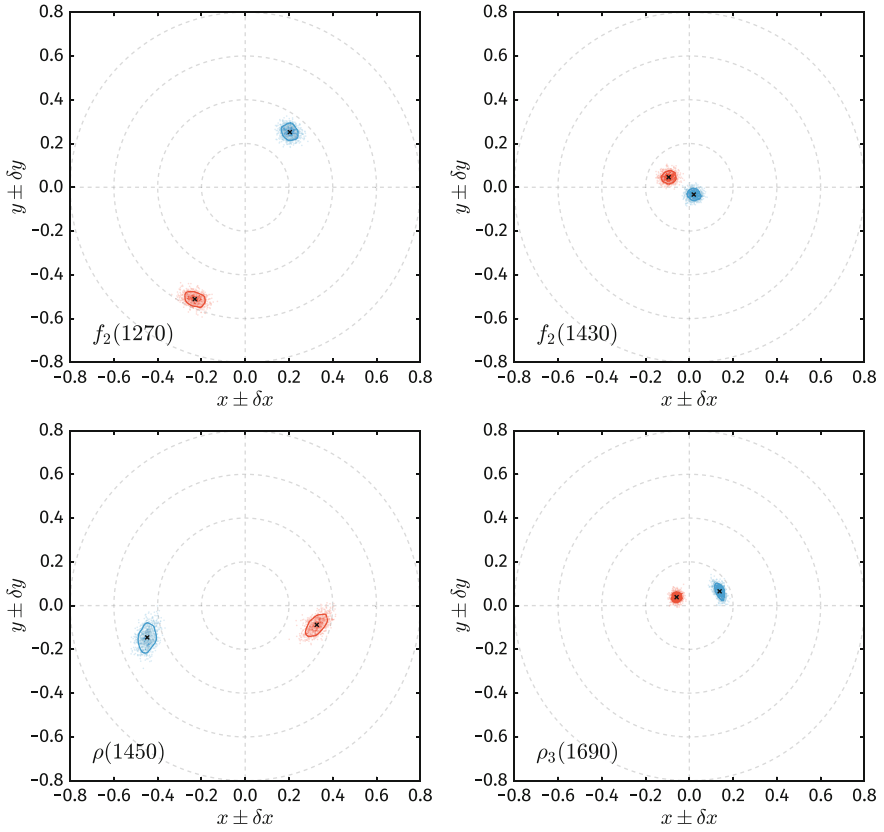

Fig. B.1 Argand plots of isobar coefficients from pseusodexperiments sampled from the final model, for B^+ (blue) and B^- (orange). The contours are a 2D kernel density estimate and enclose a 68% confidence interval around the central value (black cross), with statistical uncertainties only

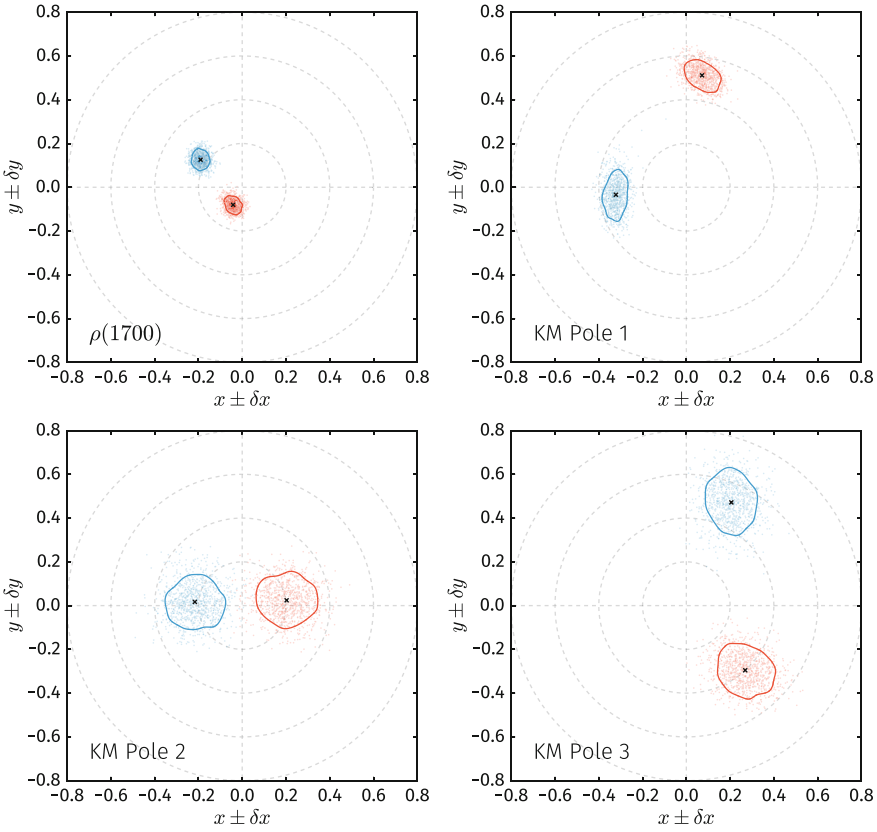

Fig. B.2 Argand plots of isobar coefficients from pseusodexperiments sampled from the final model, for B^+ (blue) and B^- (orange). The contours are a 2D kernel density estimate and enclose a 68% confidence interval around the central value (black cross), with statistical uncertainties only

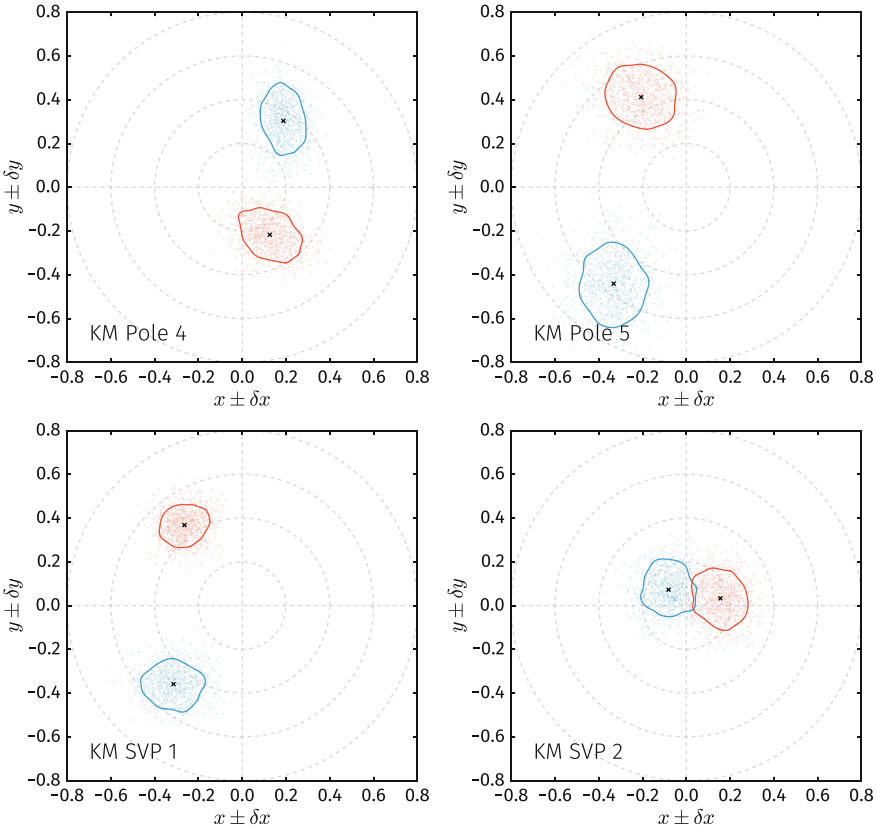

Fig. B.3 Argand plots of isobar coefficients from pseusodexperiments sampled from the final model, for B^+ (blue) and B^- (orange). The contours are a 2D kernel density estimate and enclose a 68% confidence interval around the central value (black cross), with statistical uncertainties only

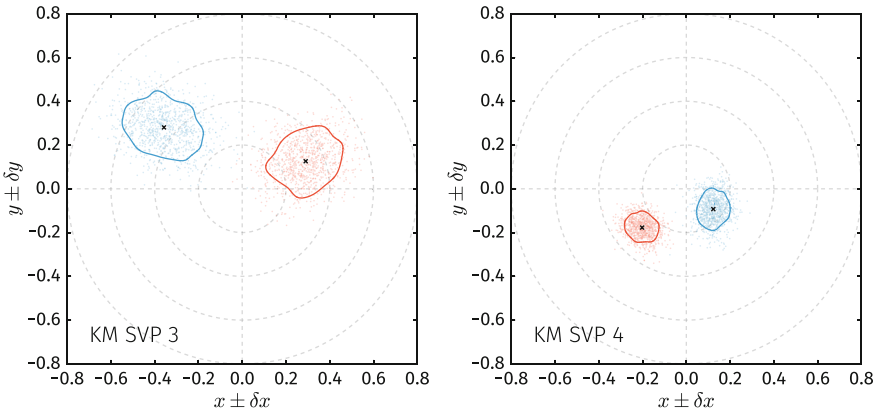

Fig. B.4 Argand plots of isobar coefficients from pseusodexperiments sampled from the final model, for B^+ (blue) and B^- (orange). The contours are a 2D kernel density estimate and enclose a 68% confidence interval around the central value (black cross), with statistical uncertainties only

Appendix C
Rarita–Schwinger Formalism

The Zemach tensor formalism, used to derive the expressions in Sect. 6.4.2, is a non-relativistic prescription for calculating the angular distributions of the decay products. In this formalism, the 'spin' amplitude, which results from a sum over the intermediate unobserved polarisation states, is necessarily a Lorentz scalar, and therefore takes the same value regardless of the frame it is evaluated in.

However, this construction enforces that the spin amplitude is maximal when the b-hadron momentum vector and resonance spin axis are aligned, in contrast to enforcing that the amplitude is maximal when the spin axis of the resonance is aligned with the orbital angular momentum axis of the b-hadron decay, which conserves angular momentum by construction. This effect is large when the Lorentz boost of the b-hadron decay products is large, and therefore scales like a relativistic correction to the angular term in the amplitude.

In the Rarita–Schwinger spin tensor formalism [1], three conditions are required of the integral-spin polarisation tensors to conserve angular momentum and to reduce the total number of degrees of freedom to only those permitted by the available z-projections of the spin. Firstly, the polarisation of a state must be orthogonal to the momentum vector of that state,

$$p^{\mu}\epsilon_{\mu\nu} = 0, \tag{C.1}$$

secondly, that the polarisation tensor is invariant under exchange of index,

$$\epsilon_{\mu\nu} = \epsilon_{\nu\mu}, \tag{C.2}$$

and finally, that the polarisation tensor is traceless

$$g^{\mu\nu}e_{\mu\nu} = 0. \tag{C.3}$$

© Springer Nature Switzerland AG 2018

D. O'Hanlon, *Studies of* CP-*Violation in Charmless Three-Body* b-*Hadron Decays*,
Springer Theses, https://doi.org/10.1007/978-3-030-02206-8

C.1 Spin-1

The orbital angular momentum tensor for a two particle $L = 1$ system can be constructed by projecting the momentum vector of the state on to its polarisation tensor,

$$L^{\mu}(p, q) = -P^{\mu\nu} q_{\nu}, \tag{C.4}$$

where $P^{\mu\nu}$ is the projection operator for spin-1,

$$P^{\mu\nu} = \sum_{s_z} \epsilon^{\mu}(p, s_z)\epsilon^{*\nu}(p, s_z) = -g^{\mu\nu} + \frac{p^{\mu} p^{\nu}}{M^2}, \tag{C.5}$$

which projects any 4-vector onto the spin-1 subspace spanned by ϵ^{μ}.

For a decay $B \to R(P_1 P_2) P_3$, where B is a scalar, P are pseudoscalars, and R a vector, the total spin amplitude is equal to the product of the amplitudes of the two quasi-two-body decays. In this case, as $L = S = 1$, these both involve the spin-1 projection operator

$$\langle R P_3 | \mathcal{M}_{\mathcal{B}} | B \rangle = \sum_{s_z} L_{\mu}(p_B, q_B) \cdot P^{\mu\nu}(p_B) \epsilon^{*}_{\nu}(p, s_z), \tag{C.6}$$

and

$$\langle P_1 P_2 | \mathcal{M}_{\mathcal{R}} | R \rangle = \sum_{s_z} \epsilon_{\nu}(p_R, s_z) \cdot L^{\nu}(p_R, q_R), \tag{C.7}$$

(as the orbital tensor L is already in the spin-1 subspace, by construction). Here, q is the difference between the final state momenta for the B decay, q_B, and the intermediate resonance decay, q_R, and p their sum.

Therefore,[1]

$$T = \langle P_1 P_2 | \mathcal{M}_{\mathcal{R}} | R \rangle \cdot \langle R P_3 | \mathcal{M}_{\mathcal{B}} | B \rangle, \tag{C.8}$$

$$= L_{\mu}(p_B, q_B) P^{\mu\nu}(p_B) L^{\nu}(p_R, q_R) \sum_{s_z} \epsilon^{*}_{\nu}(p_B, s_z) \cdot \epsilon_{\nu}(p_R, s_z), \tag{C.9}$$

$$= L_{\mu}(p_B, q_B) P^{\mu\nu}(p_B) L^{\nu}(p_R, q_R) P_{\mu\nu}(p_R). \tag{C.10}$$

As $L_{\mu} P^{\mu\nu} = L^{\nu}$ (a projection of an orbital tensor into its own subspace leaves it invariant), then this can be re-written as

$$T = L_{\mu}(p_B, q_B) L^{\nu}(p_R, q_R). \tag{C.11}$$

[1] The Clebsch–Gordan coefficient pre-factors arising from the use of the Wigner–Eckart theorem are ignored here, as the total amplitude is normalised separately per Sect. 6.6.1.

Using Eq. C.5, these can be written in terms of the final state momenta, a, b, and c, as,

$$\begin{aligned} L_\mu(p_B, q_B) &= -P_{\mu\nu}q^\nu = g_{\mu\nu}q^\nu - p_\mu \frac{p^\nu q_\nu}{m_B^2} \\ &= [c-(a+b)]_\mu - [c+(a+b)]_\mu \frac{m_c^2 - m_R^2}{m_B^2}, \end{aligned}$$

and

$$\begin{aligned} L^\mu(p_R, q_R) &= -P^{\mu\nu}q_\nu = g^{\mu\nu}q_\nu - p^\mu \frac{p_\nu q^\nu}{m_R^2} \\ &= [a-b]^\mu - [a+b]^\mu \frac{m_a^2 - m_b^2}{m_R^2}. \end{aligned}$$

and therefore

$$\begin{aligned} L_\mu(p_B, q_B)L^\mu(p_R, q_R) &= \left(0, \vec{p}\left(1 - \frac{m_c^2 - m_R^2}{m_{ab}^2}\right)\right) \times (0, \vec{q}) \\ &= \vec{p_B} \cdot \vec{q_R} \left(\frac{m_B^2 + m_R^2 - m_c^2}{m_B^2}\right) \\ &= p_B q_R \cos\theta_{\text{hel}} \sqrt{(1 + p_R^2/m_R^2)}. \end{aligned}$$

C.2 Higher Spin

The resulting angular variables from the Rarita–Schwinger prescription can be cast into multiplicative correction factors to those terms present in Sect. 6.4.2. These are expressed in terms of ζ, the ratio between the momentum of the 2-body system and the mass of the resonance, m_R, $\zeta = |\vec{p}|/m_R$, the momentum of the bachelor in the b-hadron rest frame, p^*, and the momentum of one of the resonance daughters in the resonance rest frame, q.

$$\begin{aligned} L = 0 &: Z'(\vec{p}, \vec{q}) = 1, \\ L = 1 &: Z'(\vec{p}, \vec{q}) = p^* q \sqrt{1 + \zeta^2}, \\ L = 2 &: Z'(\vec{p}, \vec{q}) = (p^* q)^2 \left(1 + \frac{2\zeta^2}{3}\right), \\ L = 3 &: Z'(\vec{p}, \vec{q}) = (p^* q)^3 \sqrt{1 + \zeta^2} \left(1 + \frac{2}{5}\zeta^2\right), \\ L = 4 &: Z'(\vec{p}, \vec{q}) = (p^* q)^4 \left(\frac{8}{35}\zeta^4 + \frac{40}{35}\zeta^2 + 1\right). \end{aligned}$$

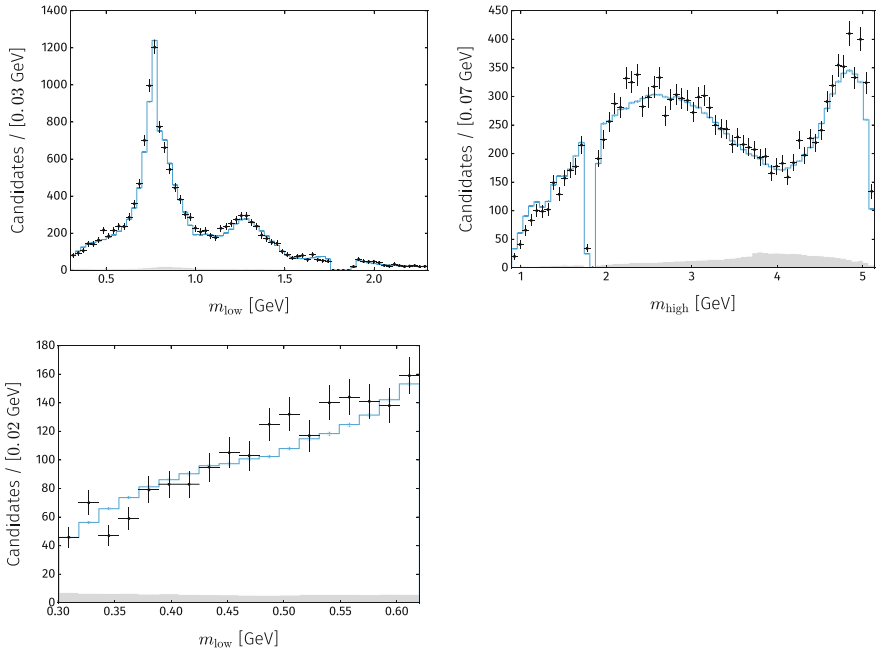

Fig. C.1 Data and model projections for the lower section of m_{low} (top left) and for the region below the $\rho(770)^0$ (bottom), the full range of m_{high} (top right)

The first three of these appear in Ref. [2], and the last were derived during the LHCb analysis of $B^0 \to \overline{D}^0\pi^+\pi^-$ [3].

C.3 Results for $B^+ \to \pi^+\pi^+\pi^-$

The results obtained from the final amplitude model described in Sect. 7.6.2, where the Rarita–Schwinger tensor formalism is used instead of the Zemach formalism for the spin terms, are presented in this section. No further modification of the model is performed (in particular, the momentum of the bachelor hadron in the resonance rest frame, p, is used in the Blatt–Weisskopf barrier factor), and uncertainties are statistical only.

The negative log-likelihood for the best of 1000 fits with random initial parameters is −48473.2, which is approximately 29 units worse than the nominal fit in Sect. 7.6.2. Fit projections of this model on the TOS data can be seen in Figs. C.1, C.2, C.3 and C.4, and the values of the fit parameters can be seen in Tables C.1, C.2 and C.3.

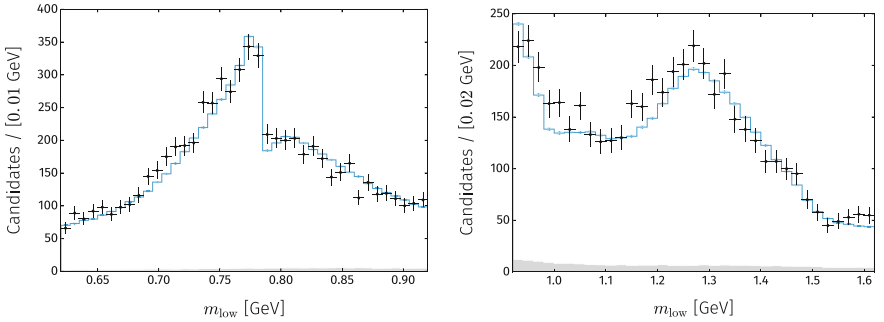

Fig. C.2 Data and model projections in m_{low} for the region around the $\rho(770)^0$ (left) and in the $f_2(1270)$ (right) region

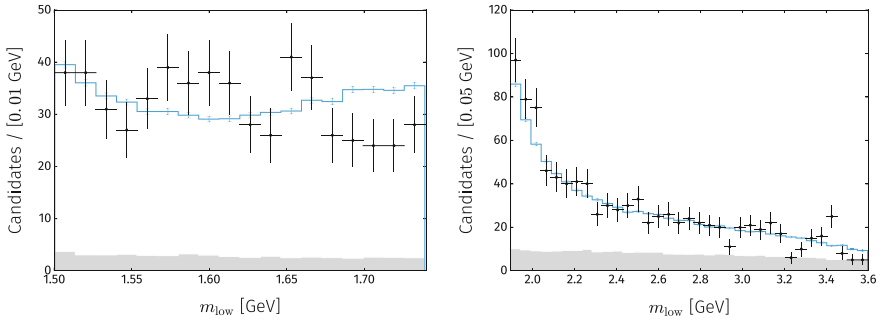

Fig. C.3 Data and model projections in m_{low} for the region below the $\overline{D}^0$ veto (left); and above the $\overline{D}^0$ veto (right)

Fig. C.4 Data and model projections in m_{low} for the region around the χ_{c0}

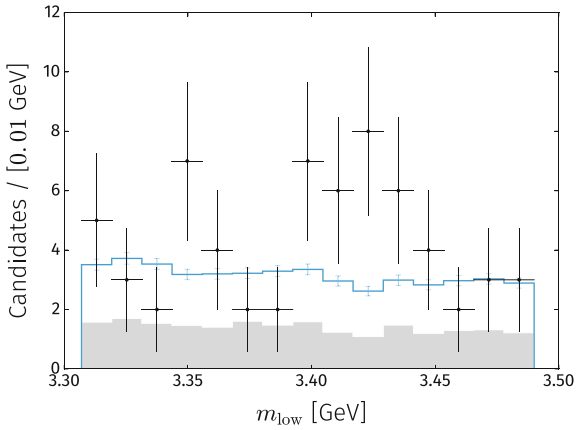

Table C.1 Component fit fractions, FF, and *CP* asymmetries, $\mathcal{A}_{CP}$, extracted from the fit using the Rarita–Schwinger spin formalism. Uncertainties are statistical only

Component	B^+ FF (%)	B^- FF (%)	$\mathcal{A}_{CP}$ (%)
$\rho(770)^0$	76.79 ± 1.35	57.38 ± 1.16	-8.82 ± 1.19
$\omega(782)$	0.72 ± 0.03	0.64 ± 0.08	—
$f_2(1270)$	5.33 ± 0.43	17.65 ± 1.24	57.57 ± 3.93
$f_2(1430)$	1.23 ± 0.28	0.30 ± 0.20	-57.01 ± 20.58
$\rho(1450)^0$	26.94 ± 1.94	10.12 ± 1.75	-40.72 ± 9.56
$\rho(1700)^0$	4.57 ± 1.05	0.62 ± 0.27	-73.72 ± 12.36
$\rho_3(1690)^0$	1.29 ± 0.23	0.84 ± 0.29	-15.51 ± 14.22
KM Pole 1	3.84 ± 0.57	12.84 ± 2.84	57.93 ± 8.34
KM Pole 2	4.16 ± 2.48	4.46 ± 2.91	9.16 ± 44.62
KM Pole 3	21.71 ± 3.75	5.60 ± 2.86	-55.09 ± 16.58
KM Pole 4	14.34 ± 3.59	2.06 ± 2.45	-72.21 ± 19.70
KM Pole 5	46.32 ± 8.91	10.64 ± 5.77	-59.04 ± 13.82
KM SVP 1	20.24 ± 6.20	7.78 ± 3.07	-39.75 ± 17.34
KM SVP 2	2.66 ± 2.68	1.89 ± 1.72	-11.28 ± 36.35
KM SVP 3	19.91 ± 5.71	3.12 ± 2.44	-70.06 ± 18.84
KM SVP 4	0.86 ± 0.80	3.59 ± 1.18	64.83 ± 24.09
Total S-wave	17.02 ± 0.90	20.16 ± 1.07	-52.86 ± 12.06

Table C.2 Cartesian isobar coefficients extracted from fit using the Rarita–Schwinger spin formalism. Uncertainties are statistical only

Component	x	y	δ_x	δ_y
$\rho(770)^0$	1 ± 0	1 ± 0	0.085 ± 0.011	0 ± 0
$\rho(1450)^0$	-0.392 ± 0.023	-0.218 ± 0.021	-0.008 ± 0.016	-0.218 ± 0.018
$f_2(1430)$	-0.017 ± 0.014	-0.068 ± 0.009	-0.068 ± 0.012	-0.025 ± 0.011
$\rho(1700)^0$	-0.124 ± 0.015	0.044 ± 0.015	-0.120 ± 0.017	-0.051 ± 0.014
$\rho_3(1690)^0$	0.042 ± 0.012	0.024 ± 0.008	-0.034 ± 0.012	0.105 ± 0.010
$f_2(1270)$	0.156 ± 0.016	0.351 ± 0.013	-0.017 ± 0.013	-0.127 ± 0.012
KM Pole 1	-0.133 ± 0.027	-0.206 ± 0.041	-0.090 ± 0.035	0.225 ± 0.032
KM Pole 2	-0.241 ± 0.039	-0.035 ± 0.062	0.013 ± 0.069	-0.010 ± 0.037
KM Pole 3	0.050 ± 0.036	0.356 ± 0.049	0.200 ± 0.047	0.113 ± 0.043
KM Pole 4	0.134 ± 0.043	0.246 ± 0.061	0.156 ± 0.046	0.074 ± 0.038
KM Pole 5	-0.226 ± 0.044	-0.466 ± 0.063	-0.323 ± 0.061	-0.083 ± 0.051
KM SVP 1	-0.124 ± 0.038	-0.283 ± 0.046	-0.305 ± 0.055	0.001 ± 0.035
KM SVP 2	-0.162 ± 0.054	-0.054 ± 0.050	-0.023 ± 0.048	0.036 ± 0.061
KM SVP 3	-0.295 ± 0.061	0.148 ± 0.051	-0.086 ± 0.051	0.191 ± 0.058
KM SVP 4	0.114 ± 0.024	0.039 ± 0.035	-0.048 ± 0.040	-0.122 ± 0.022

Table C.3 Parameters of the $\rho-\omega$ mixing model floated in the fit with the Rarita–Schwinger spin formalism. Uncertainties are statistical only

Parameter	Value
B^- magnitude	0.979 ± 0.061
B^+ magnitude	0.845 ± 0.105
B^- phase	0.196 ± 0.117
B^+ phase	-0.193 ± 0.140

References

1. V. Filippini, A. Fontana, A. Rotondi, Covariant spin tensors in meson spectroscopy. Phys. Rev. D **51**, 2247 (1995). https://doi.org/10.1103/PhysRevD.51.2247
2. Particle Data Group, J. Beringer et al., Review of particle physics. Phys. Rev. **D86**, 010001 (2012) (2013 partial update for the 2014 edition), http://pdg.lbl.gov/. https://doi.org/10.1103/PhysRevD.86.010001
3. LHCb collaboration, R. Aaij et al., Dalitz plot analysis of $B_s^0 \to \overline{D}^0 \pi^+ \pi^-$ decays. Phys. Rev. **D92**, 032002 (2015). https://doi.org/10.1103/PhysRevD.92.032002, arXiv:1505.01710